TWO-PHOTON IMAGING OF GLIAL ION AND WATER HOMEOSTASIS IN HEALTH AND DISEASE

Alexander S. Thrane & Vinita Rangroo Thrane

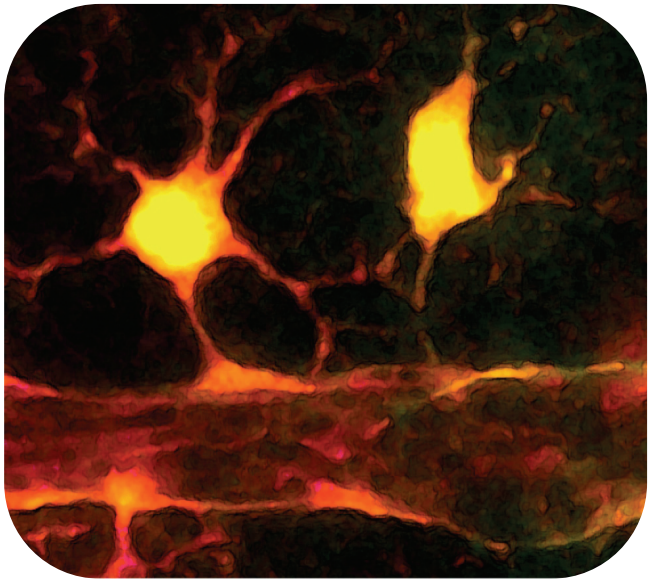

Supervisors:
Prof. Erlend A. Nagelhus
Prof. Maiken Nedergaard

Letten Centre, Institute of Basic Medical Sciences & Centre for Molecular Medicine Norway
Faculty of Medicine
University of Oslo
Norway

Center for Translational Neuromedicine
Division of Glial Therapeutics
Department of Neurosurgery
University of Rochester
USA

2013

Series of dissertations submitted to the
Faculty of Medicine, University of Oslo
No. 1573

ISBN 978-82-8264-531-7

Cover: Inger Sandved Anfinsen.
Printed in Norway: AIT Oslo AS.

Produced in co-operation with Akademika publishing.
The thesis is produced by Akademika publishing merely in connection with the thesis defence. Kindly direct all inquiries regarding the thesis to the copyright holder or the unit which grants the doctorate.

TABLE OF CONTENTS

1. ACKNOWLEDGMENTS

'In my own view, some advice about what should be known, about what technical education should be acquired, about the intense motivation needed to succeed, and about the carelessness and inclination toward bias that must be avoided is far more useful than all the rules and warnings of theoretical logic.' Santiago Ramòn y Cajal in 'Advice for a Young Investigator' (1916).

This thesis is the result of our combined work at the Center for Translational Neuromedicine in Rochester, NY, and at the Letten Centre in Oslo.

We would like to express our deepest gratitude for all those who made this work possible. First, we would like to thank our families for their unwavering support, including Berit, Vijay, Kumud, Per, Bente, Rytik, Camilla and Hannibal. Second, we would like to thank our supervisors Erlend A. Nagelhus and Maiken Nedergaard for their invaluable advice, numerous discussions, and long hours of hard work helping shape this thesis. Third, we would like to thank all the colleagues and collaborators that helped us both in Oslo and Rochester, including Michael J. Chen, Nathan A. Smith, Justin Chang, Maria L. Cotrina, Qiwu Xu (Jim), Ning Kang, Nanhong Lou, Takahiro Takano, Takumi Fujita, Fushun Wang, Lane Bekar, Salvador Pena, Arnulfo Torres, Yonghong Liao, Douglas Zeppenfeld, Benjamin Plogg, Jeffrey Iliff, Thiyagarajan Meenakshisundaram, Rashid Deane, Arthur Cooper, Abdelatiff Benraiss, Weiguo Peng, Gry F. Vindedal, Scott Kennedy, Phillip M. Rappold, Nadia N. Haj-Yasein, David Wang, Georg A. Gundersen, Rune Enger, Torgeir Holen, Øyvind Skare, Johannes P. Helm, Anna E. Thoren, Vidar Jensen, Øyvind Hvalby, Arne Klungland and Ole P. Ottersen.

This work was sponsored by PhD stipends from IMB (A.S.T.) and from MLS (V.R.T.), and also Fulbright scholarships for both of the candidates.

2. ABSTRACT

The vital role of glial cells in the nervous system has only been revealed relatively recently as these cells are electrically silent. Technical advances that allow direct visualization of glial activity have therefore been paramount to the recent glial renaissance. One such technique, two-photon laser scanning microscopy (2PLSM), forms the basis of our thesis. 2PLSM offers the necessary spatial and temporal resolution to study glial cells in intact living brain. Exploiting the strengths of 2PLSM, we chose to examine key roles of glial water and ion homeostasis in health and disease. Our first study (**Paper I**) delineated a novel aquaporin-4 (AQP4) mediated glial signaling pathway that is activated in response to hypo-osmotic brain edema, and which may contribute to the high mortality of this condition. In the second study (**Paper II**) we showed that AQP4 plays a crucial role in oxygen microdistribution during cortical spreading depression (CSD), a wave of tissue depolarization closely linked to migraine. In the next study (**Paper III**), we found that general anesthetics directly suppress astrocyte calcium signals, and this effect may explain some of the sedative effects of these drugs. In **Paper IV** we explored the paravascular circulation of cerebrospinal fluid (CSF) through brain, and found that this compartment served both as a highway for selective lipid transport and signal mediation between astrocytes. In **Paper V** we used 2PLSM to show a pathological activation of microglia in the advanced stages of hepatic encephalopathy (HE), which may be linked to the development of fatal brain edema in severe cases of this condition. Finally, in **Paper VI** we use a congenital disorder of ammonia handling to show that the immediate neurotoxicity of ammonia is mediated by a direct short-circuiting of astrocyte potassium buffering. This secondarily causes an impairment of inhibitory neurotransmission, and is not related to astrocyte swelling as was previously hypothesized. Blocking the downstream accumulation of chloride in neurons using Na^+-K^+-$2Cl^-$ cotransporter subtype-1 (NKCC1) inhibitor bumetanide, we were able to reverse ammonia neurotoxicity and thus develop a clinically relevant therapy. Taken together, using *in vivo* 2PLSM imaging we were able to elucidate important roles of glial cells in normal brain function and debilitating neurological disorders.

3. ABBREVIATIONS

$\Delta F/F_0$ - change in fluorescence normalized to time 0
1PLSM - one-photon laser scanning microscopy
2PLSM - two-photon laser scanning microscopy
AM - acetoxymethyl
Aqp4 - aquaporin-4 gene
AQP4 - aquaporin-4 protein
ATP – adenosine triphosphate
BAPTA - 1,2-bis(o-aminophenoxy)ethane-N,N,N',N'-tetraacetic acid
BBB - blood-brain barrier
CNS - central nervous system
CSD - cortical spreading depression
CSF - cerebrospinal fluid
DAPC - dystrophin-associated protein complex
E_{GABA} - GABA reversal potential
eGFP - enhanced green fluorescent protein
EPSP - excitatory post-synaptic potential
FITC - fluorescein isothiocyanate
GABA - γ-aminobutyric acid
GFAP - glial fibrillary acidic protein
Gln - glutamine
Glu - glutamate
Glt1 - glutamate transporter 1 gene
GLT1 - glutamate transporter 1 protein
GS - glutamine synthetase
HE - hepatic encephalopathy
ICP - intracranial pressure
ISM - ion-sensitive microelectrode
IP_3 - inositol-1,4,5-triphosphate
IP_3R2 - IP_3 receptor 2
KCC2 - K^+-$2Cl^-$ cotransporter-2
KO – knock-out
$[K^+]_o$ - extracellular potassium concentration
mRNA - messenger ribonucleic acid
mGluR5 - metabotropic glutamate receptor 5
MSO - L-methionine sulfoximine
NH_4^+ - ammonium
NH_3 - ammonia
$[NH_4^+]_o$ - extracellular ammonium concentration
NAD^+ - nicotinamide adenine dinucleotide
NADH - reduced NAD^+
NKA - Na^+-K^+-ATPase
NKCC1 - Na^+-K^+-$2Cl^-$ cotransporter-1
NMR – nuclear magnetic resonance
$Otc^{spf\text{-}ash}$ - ornithine transcarbamylase deficient mouse with sparse-fur and abnormal skin and hair
ROI - region of interest
RVD - regulatory volume decrease
shRNA - short hairpin ribonucleic acid
Slc12a2 – NKCC1 gene
V_m - membrane potential
WT - wild-type

4. LIST OF PAPERS

PAPER I
Thrane AS, Rappold PM, Fujita T, Torres A, Bekar LK, Takano T, Peng W, **Rangroo Thrane V**, Enger R, Haj-Yasein NN, Skare Ø, Holen T, Klungland A, Ottersen OP, Nedergaard M and Nagelhus EA. *Critical role of aquaporin-4 (AQP4) in astrocytic Ca2+ signaling events elicited by cerebral edema.* Proc Natl Acad Sci. 2011;108 (2):846-51. (A.S.T., P.M.R. and T.F. are joint first authors, commented upon in Nat Rev Neurosci, February 2011).

PAPER II
Thrane AS, Takano T, **Rangroo Thrane V**, Wang F, Peng W, Ottersen OP, Nedergaard M and Nagelhus EA. *In vivo NADH fluorescence imaging indicates effect of aquaporin-4 deletion on oxygen microdistribution in cortical spreading depression*. **Resubmitted after review to J Cereb Blood Flow Metab**. (A.S.T., T.T. and V.R.T are joint first authors)

PAPER III
Thrane AS, Rangroo Thrane V, Zeppenfeld D, Lou N, Xu Q, Nagelhus EA and Nedergaard M. *General anesthesia selectively disrupts astrocyte calcium signaling in the awake mouse cortex.* Proc Natl Acad Sci. 2012; 109(46):18974-9. (A.S.T. and V.R.T are joint first authors)

PAPER IV
Rangroo Thrane V, **Thrane AS,** Plog B, Thiyagarajan M, Gundersen GA, Iliff J, Deane R, Nagelhus EA, and Nedergaard M. *Paravascular microcirculation facilitates rapid lipid transport and astrocyte signaling in the brain*. **Submitted to Nat Neurosci.** (V.R.T and A.S.T. are joint first authors)

PAPER V
Rangroo Thrane V, Thrane AS, Chang J, Alleluia V, Nagelhus EA and Nedergaard M. *Real-time analysis of microglial activation and motility in hepatic and hyperammonemic encephalopathy.* Neuroscience. 2012; 220:247-55. (V.R.T and A.S.T. are joint first authors)

PAPER VI
Rangroo Thrane V, Thrane AS, Wang F, Cotrina ML, Smith NA, Chen M, Kang N, Fujita T, Nagelhus EA and Nedergaard M. *Ammonia compromises astrocyte potassium buffering and impairs neuronal inhibition without causing swelling in vivo*. **Pending resubmission after review to Nat Med.** (V.R.T and A.S.T. are joint first authors)

5. INTRODUCTION

"What is the function of glial cells in neural centers? The answer is still not known, and the problem is even more serious because it may remain unsolved for many years to come until physiologists find direct methods to attack it." Santiago Ramon-y Cajal

These words by Cajal rang very true in both his day and for the century that followed (Ransom et al. 2003). Because scientists did not possess adequate tools to directly explore the functions of glial cells, they were quickly forgotten amidst the vast array of data accumulated on neurons, where electrophysiology provided concrete endpoints to study. Like many other discoveries in science, the realization of the importance of glial cells coincided with the invention and subsequent application of new techniques to the field. One such technique that has gained momentum since the 1990s is two-photon laser scanning microscopy (2PLSM) (Denk et al. 1990), and this is the primary method of investigation used in our thesis. Imaging in live animals has traditionally been dominated by techniques such as functional magnetic resonance imaging and positron emission tomography, which have relatively poor temporal and anatomical (spatial) resolution (Lauritzen 2005; Schafer et al. 2012). High-resolution analyses have, on the other hand, been restricted to light and electron microscopy in fixed tissue sections or slices. Thus, high temporal and anatomical resolution has long been incompatible with analyses of living animals (Misgeld and Kerschensteiner 2006). The introduction of 2PLSM changed this, and now allows anatomical structures as small as dendritic spines to be studied in living brains over days and even weeks (Holtmaat et al. 2009). 2PLSM studies in intact animals thus allow investigators to address important biological questions in clinically relevant manner, significantly shortening the distance from bench to bedside (Dirnagl 2006).

Glial cells are by far the most numerous cell-type in the brain, outnumbering neurons 10:1 (Ransom et al. 2003). However, until around 30 years ago glial cells were only thought to act as a form of glue providing structural support for neurons. Glial involvement in normal brain function and their roles in neurological disorders is therefore a relatively new field of research. Additionally, studies that increase our understanding of glial cells are highly salient for the general field of neuroscience, as they can open up a completely new set of therapeutic targets for brain disorders (Nedergaard et al. 2010; Verkhratsky et al. 2012b). Glial cells have already been

implicated in a number of diseases, including stroke, epilepsy, Alzheimer, Parkinson, spinal cord injury, traumatic brain injury, brain edema, macular edema and migraine (Fuhrmann et al. 2010; Manley et al. 2000; Reichenbach et al. 2007; Takano et al. 2007; Tian et al. 2005; Verkhratsky et al. 2012b). They have also been shown to have key roles in regulating physiological parameters critical for neuronal function, such as extracellular potassium ($[K^+]_o$) and other ion homeostasis, volume regulation, neurotransmitter recycling, cerebral blood flow and energy metabolism (Attwell et al. 2010; Caesar et al. 2008; Haj-Yasein et al. 2012; Kirischuk et al. 2012; Mathiesen et al. 2012; Nedergaard and Verkhratsky 2012; Paulsen et al. 1988b; Pellerin et al. 2007; Takano et al. 2006; Wang et al. 2012a). More studies focusing on how glial cells can generate and influence central nervous system (CNS) disorders are therefore clearly needed. Our thesis aims to use the advantages of 2PLSM to help address this 'glial knowledge gap' with the hope of elucidating novel therapeutic approaches.

Two-photon imaging using femtosecond-pulsed lasers

Before introducing the neurobiological background for our thesis studies, we first want to review the central aspects of 2PLSM imaging. Starting with the basic principles of fluorescence imaging – light is a form of electromagnetic radiation that can be described as both a particle, called a photon, or a wave. The wavelength of light describes its energy content; the shorter the wavelength the higher the energy of individual photons. Fluorescence imaging relies on the interaction of light with a molecule that then absorbs the light energy, raising the molecule to a higher energy (excited) state. The molecule, called a fluorochrome, then loses some energy through mechanical vibration, before emitting the rest of its energy as a new photon and returning to its basal 'unexcited' state. The emitted photon is always of lower energy (red-shifted) compared to the exciting photon due to the energy lost in vibration (Christensen and Nedergaard 2011). In a biological setting, relevant fluorochromes are frequently bonded to macromolecules to attain desired chemical properties, such as lipid solubility, and are then called fluorophores (Paredes et al. 2008).

The resolution of traditional light microscopy has been significantly improved with the advent of the laser, which is an acronym for 'light amplification by stimulated emission of radiation' (Maiman 1960). In laser scanning microscopy, a collimated (parallel rays) coherent (in phase) beam of monochromatic (only 1 wavelength) photons is scanned across the specimen of interest, usually in a raster

pattern using galvanometric mirrors (Duemani Reddy et al. 2008). However, an early issue with laser scanning microscopy was that extensive light excitation occurred above and below the focal point of the microscope, introducing noise to the collected image. This issue was greatly improved by the introduction of confocal laser scanning microscopy, where a strategically placed pinhole effectively cuts out all light emitted from outside the focal point. The pinhole also gives confocal microscopy its other important feature; the ability to collect optical sections from the specimen. However, the major issue with confocal microscopy that has made it largely incompatible with *in vivo* studies is the large amount of light energy delivered to the tissue both in and around the focal point (Misgeld and Kerschensteiner 2006). Another aspect of this problem, is that due to light scattering at the wavelength required to excite biologically relevant fluorophores confocal microscopy is unable penetrate tissue much deeper than 50 µm (Christensen and Nedergaard 2011).

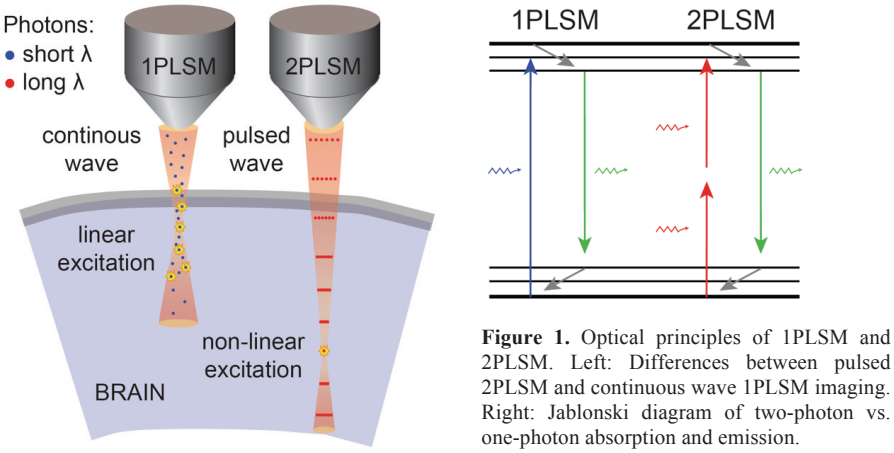

Figure 1. Optical principles of 1PLSM and 2PLSM. Left: Differences between pulsed 2PLSM and continuous wave 1PLSM imaging. Right: Jablonski diagram of two-photon vs. one-photon absorption and emission.

Although theoretically conceived almost a century ago, 2PLSM was only made possible in the 1990s through the development of powerful femtosecond pulsed lasers (Denk et al. 1990). 2PLSM is based on the principle that if a pulsed laser emits a high enough concentration of photons, 2 or more photons may excite the same molecule simultaneously. Denk et al. were the first to successfully apply this concept to laser scanning microscopy (Denk et al. 1990). Since multiple photons are used to excite the target, each individual photon can have a relatively low energy, i.e. long wavelength **(Fig. 1)**. This has several advantages over conventional confocal

microscopy in that the longer wavelengths used, frequently in the infrared band (800-1000 nm), achieve much deeper tissue penetration (500-1000 um) and exert much less photodamage (injury due to light) (Helmchen and Denk 2005). The latter issue becomes even more important when conducting fluorescent imaging, as the fluorophores used can generate free radicals when excessively stimulated by light causing phototoxicity (Bestvater et al. 2002; Christensen and Nedergaard 2011). Finally, the transfer of light energy in 2PLSM is non-linear, and only in the focal point of the beam will a critical concentration of photons be achieved sufficient to excite (or damage) the tissue **(Table 1)**. This means that 2PLSM has inherent optical sectioning and noise reduction properties, and thus does not require a pinhole to block out-of focus light as with confocal microscopy.

Table 1. Summary of the salient 2PLSM and 1PLSM parameters.

	2PLSM	**1PLSM**
Laser wave	Pulsed	Continuous
Wavelength	800-1000 nm	400-600 nm
Tissue penetration	500-1000 um	20-50 um
Excitation	Non-linear	Linear
Phototoxicity	Limited to focal point	Entire cone of light
Emission	All photons useful	Out-of-focus photons generate noise
XY resolution	½ λ (e.g. 450 nm)	½ λ (e.g. 250 nm)
Z resolution	λ (e.g. 900 nm)	λ (e.g. 500 nm)

Neuroglia – more than just glue

The major difference between glial cells and neurons are that glia lack electrical excitability and therefore cannot fire action potentials. The lack of an easily measurable form of activity in glia is also one of the major reasons for the previously neurocentric focus of brain research (Ransom et al. 2003). The term glia was first coined by Rudolf L. K. Virchow (1821-1902), who thought that glia were a connective tissue 'glue' whose function was to provide structural support to neurons. Later, in 1851, Heinrich Müller made the first drawing of a glial cell in the retina, now known as the Müller cell. In the spinal cord, Jakob Henle was the first to describe star-like 'stellate cells,' which we now know as astrocytes. These findings were later elaborated upon by numerous eminent histopathologists, including Camillo Golgi (1843-1926) and Santiago Ramón y Cajal (1852-1934) (Verkhratsky and Butt 2007). We now know that glia are a heterogeneous group of cells that can generally

be divided into macro- and micro-glia on the basis of morphology. The latter cell type is of mesenchymal origin and migrates to the brain in embryology, differentiating to become the resident immune-cell of the CNS (Kettenmann et al. 2011). Macroglial cells are of ectodermal origin and the sub-types include oligodendrocytes in the CNS and Schwann cells in PNS, which both provide the myelin sheath to neuronal axons (Barres 2008). However, the most numerous macroglial cell type and the major focus of our thesis are astrocytes. These complex and heterogeneous cells perform many of the essential homeostatic functions that the more specialized neurons cannot perform **(Fig. 2)** (Matyash and Kettenmann 2010). Astrocytes are capable of complex signaling and recent discoveries have led many to suspect that these cells may play an active role in CNS signal transmission (Agulhon et al. 2008).

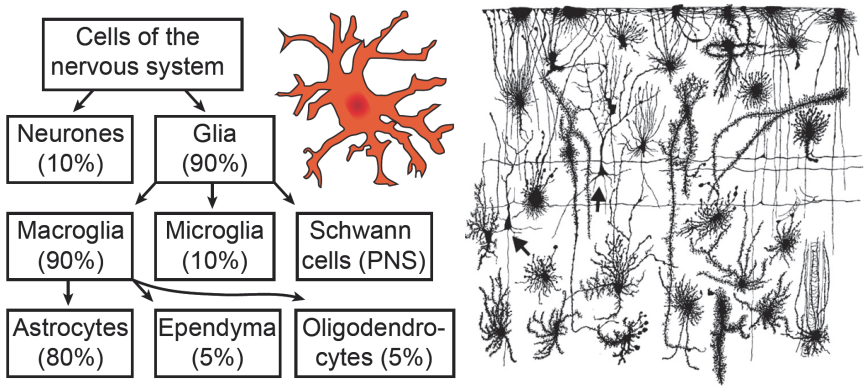

Figure 2. Cellular composition of the CNS and PNS. Left: Overview of the different cell types and their relative proportions in the human nervous system. Right: Early illustrations of cellular heterogeneity in the brain created using the silver impregnation method. Modified from Retzius, Biologische Untersuchungen, 1894.

Astrocytes – stars of the brain

Astrocytes were named because of their star-like appearance, owing primarily to their high expression of cytoskeletal glial-fibrillary acidic protein (GFAP) (Ransom et al. 2003). Astrocytes can be divided up into two main subgroups, stellate and radial (elongated) cells. Stellate astrocytes in the grey matter are called protoplasmic astrocytes, and in the white matter fibrous astrocytes (Matyash and Kettenmann 2010). Radial astrocytes are further divided into Müller cells (in the retina) and Bergmann glia (in the cerebellum) (Nimmerjahn et al. 2009; Reichenbach et al. 2007). Radial astrocytes, apart from those in retina and cerebellum, are commonly present

during development in the brain and are thought to be involved in neural migration (Regan 2007). Protoplasmic astrocytes are the cell-type seen most frequently in the cerebral cortex of adults, and our thesis focuses primarily on this sub-group (Oberheim et al. 2012). Astrocytes, although named after their star-like appearance in early histological preparations, are in fact more bush-like, and extend a multitude of fine processes that almost entirely fill a 3-dimesional domain **(Fig. 3)**. This astrocyte domain usually encompasses thousands of synapses, multiple blood vessels and usually does not overlap with neighboring astrocyte domains except during pathological conditions such as epilepsy (Oberheim et al. 2008). Astrocyte processes that extend to synapses are termed peri-synaptic and those extending to blood vessels are called perivascular endfoot processes (Simard and Nedergaard 2004). Astrocytes are thus strategically located in a domain-structure that can integrate local synaptic activity with metabolic supply from the blood (Oberheim et al. 2008). Moreover, because the extracellular space is of very limited size in the CNS, astrocytes are also ideally constructed to influence both the content and volume of the extracellular space locally, regulating neurotransmitter and ion concentrations (Thorne and Nicholson 2006).

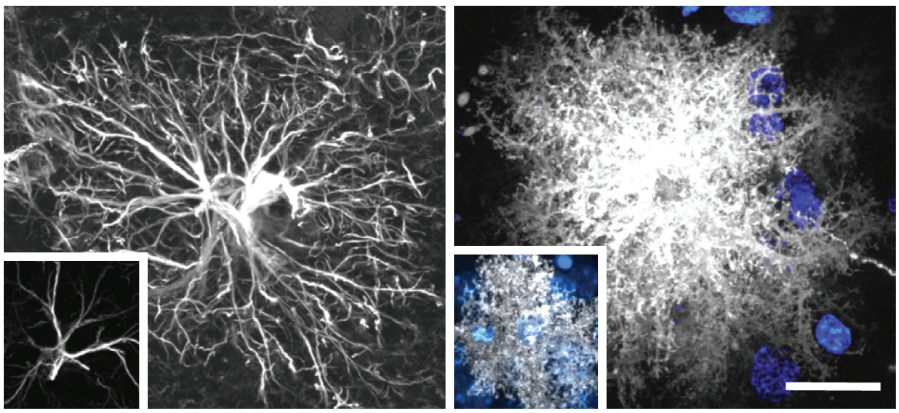

Figure 3. Astrocyte complexity distinguishes advanced nervous systems. Left: GFAP-stained protoplasmic astrocytes from mouse (inset) and human, illustrating the dramatic increase in the complexity of these cells through evolution. Right: Mouse (inset) and human astrocytes labeled with intracellular dye reveals a more 'bush' than 'star'-like structure compared to GFAP staining. Scale bar 20 um. Modified with permission from Oberheim et al. 2009.

Finally, astrocytes are extensively coupled to each other via gap-junctions, thus forming a vast syncytium of cells. Recent research has indicated that this may

help astrocytes act as effective conduits for redistributing metabolites or ions between active and inactive synapses (Giaume et al. 2010; Rouach et al. 2008). All of these anatomic specializations would lead one to suspect that highly developed astrocytes might be a pre-requisite for more complex nervous systems. Interestingly, glial complexity increases much more steeply than neuronal complexity from lower to higher species, perhaps indicating that highly evolved astrocytes are necessary to cope with high synapse densities (Oberheim et al. 2006). Additionally, some disease states in brain and retina are characterized by a reduction in the glia/neuron ratio early in the disease, perhaps indicating that common neurological disorders are primary gliopathies (Verkhratsky et al. 2012b).

There has been a vast increase in our understanding of the subset of channels and receptors expressed by astrocytes in recent years. Notably, astrocytes express abundant channels and transporters for potassium (e.g. inward rectifying K^+ channel Kir4.1, Na^+-K^+-ATPase, NKA), sodium, chloride, water (e.g. aquaporin-4, AQP4), metabolites (e.g. monocarboxylate transporters), amino acids (e.g. system N transporter 1, SN1) and neurotransmitters (e.g. glutamate transporter 1, GLT1) (Kirischuk et al. 2012; Lovatt et al. 2007; Paulsen et al. 1988b). These membrane proteins are principally involved in what we now believe to be key astrocyte functions, including $[K^+]_o$ buffering, neurotransmitter clearance and recycling at the synapse (especially glutamate and γ-aminobutyric acid, GABA), cerebral blood flow regulation, water transport and feeding neurons with lactate via the glucose-lactate shuttle (Bak et al. 2006; Haj-Yasein et al. 2012; Iliff et al. 2012; Paulsen et al. 1988a; Pellerin et al. 2007; Takano et al. 2006). Additionally, immunogold and *in situ* studies have indicated that astrocytes might be capable of directly influencing synaptic processing via vesicular or non-vesicular (e.g. connexin hemichannel) neurotransmitter release, or so-called 'gliotransmission' (Bezzi et al. 2004; Hamilton and Attwell 2010; Jourdain et al. 2007; Zhang et al. 2004). In conclusion, several lines of evidence indicate that astrocytes can actively modulate neuronal function and thus regulate information transmission in the CNS, perhaps coupling this to local metabolic factors (Attwell et al. 2010). These seminal observations have led to a revision of the classical neurocentric view of the synapse, and prompted the inclusion of astrocytes into a 'tripartite synapse' (Araque et al. 1999). Our thesis seeks to extend this work and use 2PLSM to address two related ways that astrocytes can influence synaptic function: the control of extracellular ion and volume homeostasis.

Astrocyte water homeostasis and AQP4

A tightly regulated water homeostasis is essential for normal brain function (Amiry-Moghaddam and Ottersen 2003). An excessive influx of water into the brain parenchyma will cause swelling, called brain edema. Because the brain is enclosed in a rigid cranium this swelling will raise intracranial pressure, which can then set up a vicious cycle where venous drainage from the brain is compressed and pressure rises further until the brain herniates through the base of the skull. Brain edema is therefore associated with significant mortality and morbidity, and current treatments are unfortunately limited to only partially effective and quite old approaches such as hyperosmotic infusions or corticosteroids (Grande and Romner 2012).

Water can be transported through biological membranes via several mechanisms. Initially, water transport was thought to occur exclusively through passive diffusion directly through the lipid bilayer. However, this assumption was dispelled through Nobel Prize winning work by Peter Agre and co-authors, who isolated an ancient family of membrane channels in erythrocytes that are highly permeable to water (Preston and Agre 1991; Preston et al. 1992). Subsequent work has shown that almost all animals and plants express a family of water channels, called aquaporins, and to date no less than 12 isoforms have been identified in mammals (Agre et al. 2004). More recently, it has also been shown that membrane transporters (e.g. EEAT) and ion channels can contribute to active and passive water flux (MacAulay and Zeuthen 2010), and these critical observations also need to be incorporated to generate a comprehensive model of transmembrane water transport **(Fig. 4)**.

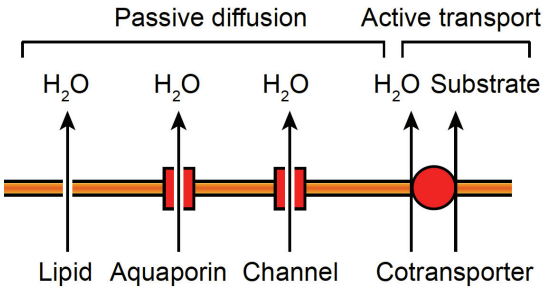

Figure 4. Multiple pathways for water transport across the lipid bilayer. Aquaporins and several types of ion channels can increase plasma membrane H_2O permeability. Most cotransporters also move H_2O with every cycle of substrate transport.

Aquaporins are a family of transmembrane proteins that selectively permeate water, and can thus increase water flux across cell membranes manifold (King et al. 2004). Water transport across aquaporins is mediated by osmotic gradients, and hence diffusion is passive and bi-directional. A sub-group of aquaporins also permeate other substances in addition to water, such as urea, ammonia or glycerol, but the physiological role of this metabolite permeability is incompletely understood (King et al. 2004). Aquaporins are expressed in a range of tissues including blood (erythrocytes), kidney (renal tubules), lens, retina and brain. The principal types of aquaporins expressed in brain are AQP1 (choroid plexus epithelial cells), and AQP4 (astrocytes and ependymocytes) (Agre et al. 2004). Some aquaporins appear capable of gating the degree of water permeability (e.g. AQP2 via vasopressin in kidney) (Moeller et al. 2011). However, it is somewhat controversial whether AQP4 is capable of gating. Several studies have indicated that phosphorylation of different sites on the AQP4 molecule can increase or decrease water permeability (e.g. in response to glutamate, erythropoietin, vasopressin and potassium) (Gunnarson et al. 2009; Gunnarson et al. 2008; Illarionova et al. 2010; Moeller et al. 2009; Niermann et al. 2001; Song and Gunnarson 2012). However, subsequent structural determinations have contradicted these observations (Mitsuma et al. 2010).

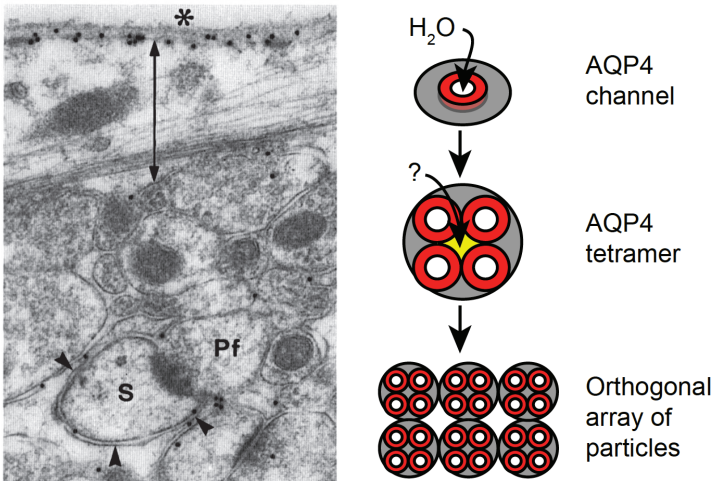

Figure 5. AQP4 expression in astrocytes is polarized to endfeet and peri-synaptic processes. Left: Immunogold labeling for AQP4 (black dots) showing sub-pial endfeet and peri-synaptic enrichment. Modified with permission from Nielsen et al. 1997. Right: Individual AQP4 channels permeate water. 4 AQP4 channels can assemble into tetramers, which have central pore that may permeate other molecules. Numerous AQP4 tetramers join together into orthogonal arrays of particles that almost completely cover astrocyte endfoot membranes.

AQP4, which is the main aquaporin explored in our thesis, is expressed to such a large extent by astrocytes that formations of AQP4 proteins clustered in so-called orthogonal arrays of particles can be seen by freeze fracture EM to cover almost the entire surface of astrocyte processes **(Fig. 5)** (Rash et al. 2004). AQP4 is thought to be permeable primarily to water, and no other solutes, although there is some debate whether the central pore formed between tetramers can act as a gas-channel (Fang et al. 2002; Wang et al. 2007; Wang and Tajkhorshid 2010). Additionally, AQP4 is selectively enriched in distinct subcellular domains, including perivascular endfeet and peri-synaptic processes, indicating that AQP4 may have a role in dissipating osmotic gradients generated near the synapses to the vasculature **(Fig. 6)** (Amiry-Moghaddam et al. 2003a; Binder et al. 2006; Frydenlund et al. 2006; Nagelhus et al. 1999; Nielsen et al. 1997). The peri-vascular localization of AQP4 in brain is controlled by the dystrophin-associated protein complex (DAPC), and disruption of this complex in a mouse model of myotonic dystrophy is associated with a loss of the perivascular enrichment (Amiry-Moghaddam et al. 2004; Frigeri et al. 2001; Vajda et al. 2004). However, a recent study that AQP4 anchoring mechanism may differ between macroglial cell types (Enger et al. 2012).

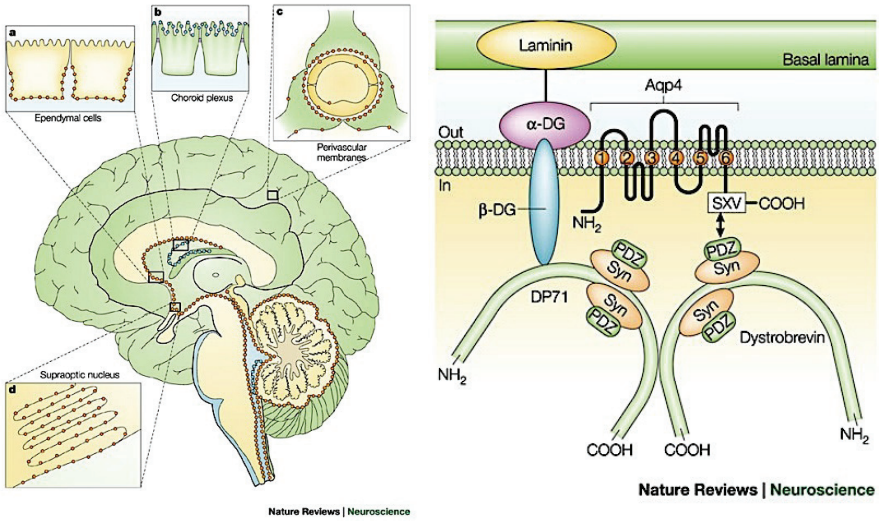

Figure 6. The subcellular localization of AQP4 is ensured by the DAPC-complex. Left: Illustration showing the expression pattern of AQP1 (blue) and AQP4 (red) in the human brain. Right: AQP4 is anchored to distinct membrane domains in astrocytes via the DAPC-complex. Adapted with permission from Amiry-Moghaddam and Ottersen 2003.

AQP4 has been implicated in the pathophysiology of a range of CNS disorders, including hypo-osmotic brain edema, stroke, epilepsy, hydrocephalus, migraine, and meningitis (Amiry-Moghaddam et al. 2003b; Binder et al. 2004; Binder et al. 2006; Manley et al. 2000; Padmawar et al. 2005; Papadopoulos et al. 2004; Papadopoulos and Verkman 2005). Constitutive *Aqp4* knock-out (KO) mice have for instance been shown to have reduced hypo-osmotic brain edema and reduced stroke infarct size, which is hypothesized to be related to decreased astrocyte swelling and secondary dysfunction (Manley et al. 2000). A glia-specific *Aqp4* KO has also recently been created, and observations from these animals are strikingly similar to constitutive KO, indicating that most of the functional AQP4 is expressed in astrocytes and not e.g. endothelial cells (Haj-Yasein et al. 2011c). Although there is an expanding literature exploring AQP4 functions in the CNS, several critical questions remain unanswered, including: 1) Are all forms of astrocyte swelling AQP4-dependent, or is this phenotype only evident in cell culture or acute brain slices from young animals? 2) Does AQP4 play a role in astroglial signaling through sensitizing these cells to small volume changes near the synapse or blood vessels? 3) Does AQP4 mediate astrocyte volume changes at the level of the individual cell or is the role of AQP4 instead to facilitate more global water and cerebrospinal fluid (CSF) flux (Iliff et al. 2012)? 4) Does AQP4 only permeate water or can it also act as a gas channel to for instance O_2? Because this is a rapidly evolving field, the current thesis has restricted itself to addressing only a subset of these questions.

Astrocyte regulation of $[K^+]_o$ homeostasis in the brain

Rapid and efficient potassium homeostasis is vital in maintaining normal neuronal function, and is thought to be one of the primary functions of astrocytes (Kofuji and Newman 2004). Interestingly, the blood-brain barrier (BBB) is highly impermeable to potassium ions, ensuring that $[K^+]_o$ in the CNS is regulated internally and is minimally affected by systemic fluctuations (Hansen et al. 1977). Astrocytes have multiple passive and active potassium transport mechanisms, and similar to most mammalian cells the potassium gradient is largely responsible for their negative (more so than neurons, ~85 mV) membrane potential (Kofuji and Newman 2004). Moreover, astroglia including Müller cells likely have a much greater permeability to and capacity for buffering $[K^+]_o$ than neurons, although this permeability may be

restricted to functional micro-domains (Newman et al. 1984; Walz 2000). Astrocyte potassium buffering is thought to be divided into two main mechanisms: local potassium uptake and spatial buffering (**Fig. 7**) (Kimelberg and Nedergaard 2010; Kofuji and Newman 2004).

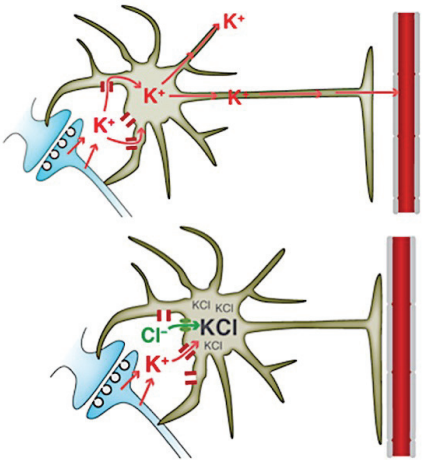

Figure 7. Two proposed mechanisms for astrocyte potassium homeostasis. Top: Potassium spatial buffering involves astrocyte uptake of increased potassium from the synaptic cleft down its electrochemical gradient to the vasculature. This mechanism is thought to involve potassium channel Kir4.1 and potentially AQP4. Bottom: Local potassium accumulation coupled with sodium pumping and sodium/chloride cotransport to remove excess K^+ released from neuronal activity. This mechanism is thought to involve NKCC1 / KCC2 and the NKA. Modified with permission from Kimelberg and Nedergaard 2010.

Ion pumps, cotransporters or potassium channels can all mediate local potassium uptake. This mechanism is thought to be temporary and the influxed potassium ions are eventually released back into the extracellular space, restoring the ionic composition of the various cellular compartments. Cotransporters and ion pumps usually couple K^+ influx to anion (e.g. Cl^-) influx or cation (e.g. Na^+) efflux, to maintain electroneutrality. The NKA pump and (Na^+)-K^+-Cl^- cotransporters are thought to be the main proteins responsible for short-term buffering of increases in $[K^+]_o$ following neuronal activity (Andersson et al. 2004; Kofuji and Newman 2004; Miyakawa-Naito et al. 2003; Olson et al. 1986; Xiong and Stringer 2000). The NKA exports $3Na^+$ and imports $2K^+$ causing it to be mildly electrogenic (hyperpolarizing the membrane potential, V_m) and is sensitive to inhibition by several drugs, such as the plant-toxins ouabain and digitalis. Previous studies have indicated that the astroglial isoform of NKA is more effective in buffering $[K^+]_o$ than the neuronal isoform (Grisar et al. 1983; Reichenbach et al. 1987). (Na^+)-K^+-Cl^- cotransporters move all relevant ions in an electroneutral manner, and are highly expressed in secretory epithelia and ependymal cells, and to a lesser extent in both neurons and astrocytes (Delpire et al. 1999; Rivera et al. 2005). There are several important types

of (Na^+)-K^+-$2Cl^-$ cotransporters, including Na^+-K^+-Cl^- cotransporter-1 (NKCC1) expressed at a high level in early development when it imports Cl^-, and K^+-$2Cl^-$ cotransporter-2 (KCC2) expressed later in development when it exports Cl^-. The ontogenic expression patterns of these two cotransporters are thought to represent a developmental switch in the action of GABA, from depolarizing in early development to hyperpolarizing in adulthood (Rivera et al. 2005; Rivera et al. 1999). NKCC1 but not KCC2 is highly sensitive to low doses of the clinically used diuretic bumetanide, whilst both transporters are inhibited by the diuretic furosemide (Kimelberg 1987; Kofuji and Newman 2004).

The second mechanism for astroglial for potassium clearance is spatial buffering (Chen and Nicholson 2000; Xiong and Stringer 2000). This mechanism entails astrocytes redistributing local increases in $[K^+]_o$ from areas of high neuronal activity through the gap junction-coupled astrocyte syncytium to areas of less activity with lower $[K^+]_o$. The driving force for the potassium current is the difference between the local potassium equilibrium potential (E_K) and the glial syncytium membrane potential (V_m) (Chever et al. 2010; Djukic et al. 2007; Haj-Yasein et al. 2011a; Heuser et al. 2012; Karowski and Proenza 1977; Nagelhus et al. 2004; Newman et al. 1984). Potassium siphoning is a variant of spatial buffering that involves redistribution of increased $[K^+]_o$ to specific subcellular compartments due to polarized potassium channel expression, such as in retinal Müller cells (Newman 1985; Newman et al. 1984). One of the main advantages of this mechanism is that it allows the redistribution of potassium ions with little increases in potassium inside individual astrocytes. However, though this model provides an astrocyte-specific mechanism for buffering $[K^+]_o$, there are many faults with the theory including the lack of a sufficiently strong electrochemical gradient to push a potassium current between astrocytes (Meeks and Mennerick 2007). In the brain the potassium channel subtype Kir4.1 is highly enriched in astrocytes, where it has a polarized expression similar to AQP4, principally being present in endfeet and peri-synaptic membranes. It therefore seems likely that there is some functional coupling between potassium and water homeostasis in these specialized astrocyte membrane domains (Amiry-Moghaddam et al. 2003b; Chever et al. 2010; Djukic et al. 2007; Nagelhus et al. 1999; Strohschein et al. 2011). Any spillover or siphoning of excess potassium beyond the local uptake at the individual synapse is thought to be a hallmark of pathology or an artifact of experimental preparations (e.g. epilepsy or spreading depression) (Kofuji

and Newman 2004). Potassium homeostasis in the brain is a controversial topic and further studies are clearly warranted to help ascertain the relative importance of the various mechanisms involved in $[K^+]_o$ buffering.

Cortical spreading depression (CSD) and migraine

CSD is a self-propagating wave of depolarization and neurodepression that spreads through cortical grey matter at a slow rate of 2-5 mm min^{-1} (Lauritzen 2001; Leao 1947). Waves of CSD can be evoked in experimental animals by intense neuronal stimulation, local application of potassium or tissue injury (Takano and Nedergaard 2009).

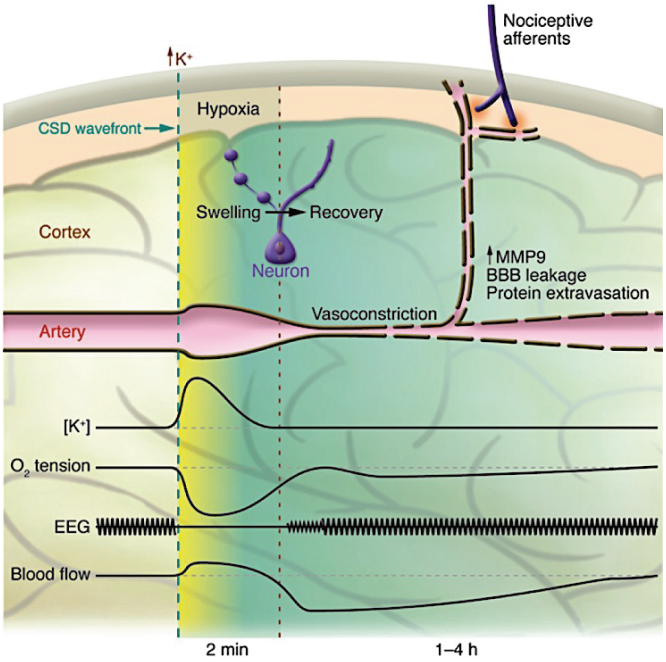

Figure 8. Model of migraine pathophysiology. The illustration shows a human cortex with a wave of CSD spreading across it. The CSD wave itself (yellow) is accompanied by neurodepression (decreased electrocorticogram amplitude), depolarization (increased $[K^+]_o$), hyperemia, hypoxia and will typically manifest as visual phenomena called an *aura*. This period is followed by prolonged oligemia, slow restoration of neuronal activity and activation of trigeminal nociceptive afferents causing the characteristic headache (green). Modified with permission from Takano et al. 2009.

CSD has been closely linked to the pathophysiology of migraine headaches, where sufferers often experience a phenomenon called *aura* that manifests as sensory phenomena (e.g. scintillation-scotoma). These phenomena show a slow somato- or retino-topic spread across the cortex that is of an equivalent velocity to CSD

(Lauritzen et al. 2011). As the 'aura wave' subsides, the patient typically begins to experience throbbing headaches, which is thought to be related to secondary meningeal vasodilation with activation of trigeminal nociceptive afferents **(Fig. 8)** (Takano and Nedergaard 2009). However, the characteristic wave of depressed neuronal (electrocorticogram) activity seen during CSD is present in a very narrow zone of cortex, and thus cannot be detected non-invasively with external electroencephalogram electrodes in humans (Lauritzen et al. 2011). When functional imaging is used to measure cerebral blood flow during migraine attacks investigators again observe a brief and variable hyperemia (more prominent in anesthetized animals) followed by a characteristically slow wave of cortical oligemia (Lauritzen 1994; Tfelt-Hansen and Koehler 2011). Finally, using more invasive recordings investigators have shown that human cortex is capable of generating and sustaining CSD waves following injury or experimental stimulation (Lauritzen 1994). Taken together, CSD is therefore likely to be a fundamental property of all densely packed nervous tissue, both animal and human.

CSD is characterized by an increase in $[K^+]_o$ of more than 50 mM, and re-establishing the transmembrane potassium gradient thus presents a unique metabolic challenge for the brain parenchyma (Takano et al. 2007). Additionally, other electrolyte gradients are critically altered, with $[Ca^{2+}]_o$ decreasing from 1.2 to 0.1 mM, $[Cl^-]_o$ decreasing from 120 to 70 mM and $[Na^+]_o$ decreasing from 150 to 60 mM (Lauritzen et al. 2011). CSD waves are usually self-terminating and do not cause permanent brain injury (Takano et al. 2007). However, in the context of severe cortical injury (e.g. traumatic brain injury or stroke), so-called peri-infarct or anoxic depolarizations can be observed that persist and increase the area of brain that is permanently damaged (Lauritzen et al. 2011). Interestingly, when fluorocitrate is used to selectively injure astroglial by inhibiting the Krebs cycle this also causes CSD to induce irreversible neuronal dysfunction (Largo et al. 1997; Paulsen et al. 1987). The predilection for migraine attacks to originate in the striate (V1) cortex in humans may therefore relate directly to the relatively lower astrocyte-to-neuron ratio in this area (Lauritzen et al. 2011).

To study this metabolic strain we chose to employ reduced nicotinamide adenine dinucleotide (NADH) imaging, which relies on the natural auto-fluorescence of NADH but not NAD^+ **(Fig. 9)**. NADH is critical co-enzyme in cellular metabolism, which is generated from NAD^+ (reduction) during glycolysis, and to a larger extent

from Krebs cycle, and is used by the mitochondrial respiratory chain (oxidation). When used in conjunction with 2PLSM, NADH imaging can thus be used to generate detailed maps of local tissue red-ox state, where increased NADH signal intensity is a sensitive proxy of tissue hypoxia (Kasischke et al. 2011). Interestingly, NADH fluorescence in neuropil is highest in astrocytes, almost precisely outlining the entire cells (including processes), whilst showing little overlap with mitochondrial staining (Kasischke et al. 2004). NADH imaging during CSD or hypoxemia reveals sharply defined cylindrical perivascular regions of high oxygen tension (low NADH signal) and irregularly shaped interspersed watershed regions of low oxygen tension (high NADH signal) (Kasischke et al. 2011; Takano et al. 2007). The steep sigmoidal NADH-pO_2 curve with a p_{50} for O_2 of 3.4 mmHg explains the sharp border between high and low NADH signal intensity in perivascular and watershed regions, respectively (Kasischke et al. 2011).

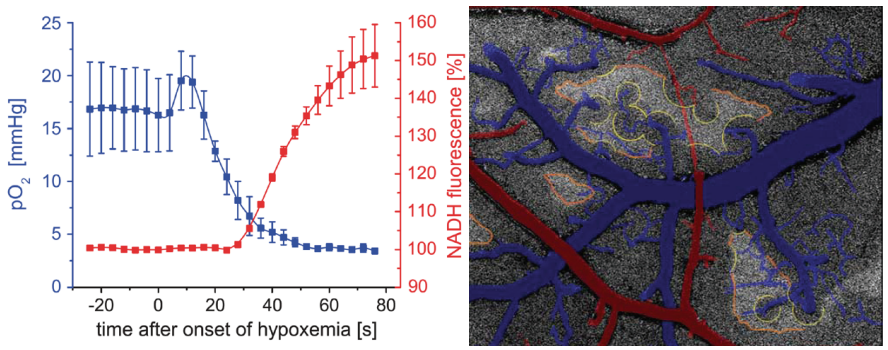

Figure 9. 2PLSM imaging of tissue red-ox state using NADH fluorescence. Left: NADH, but not NAD^+, is fluorescent and serves as a sensitive proxy of tissue hypoxia in the brain. Right: NADH imaging reveals increased NADH indicative of tissue hypoxia in geometrically shaped microwatershed regions of mouse cortex during brief and mild hypoxemia. Arteries and veins are pseudo-colored in red and blue, respectively. Modified with permission from Kasischke et al. 2011.

Using *in vivo* 2PLSM NADH imaging Takano et al. in 2007 made a set of key observations regarding the micro-distribution of oxygen in CSD. The authors observed that in watershed areas tissue hypoxia causes and coincides with CSD, and critical hypoxia in these regions causes swelling along with dendritic spine distortion in neurons, but not astrocytes (Takano et al. 2007). The extent of astrocyte swelling is still somewhat more debated, but the much clearer swelling in neurons shown in this and other studies at least indicates that astrocyte volume regulation is much tighter (from unpublished observations *in situ*) (Risher et al. 2012) (Takano et al. 2007; Zhou

et al. 2010). More importantly, the NADH observations made by Takano et al. indicate that the self-propagating nature of the CSD wave might stem from a primary energy failure (i.e. NKA failure). This energy failure seems most likely to stem from excess energy consumption than from inadequate supply, as blood flow actually increases during the early phase of CSD. However, what sets up the CSD wave in the first place is a bit more uncertain. The wave itself is preceded by propagating field oscillations in glial and neuronal V_m, indicating that CSD might be initiated by neuronal hyperexciteability similar to seizures (Larrosa et al. 2006). Additionally, genetic analysis of patients with familial hemiplegic migraine has revealed mutations in genes encoding calcium channels (e.g. $Ca_v2.1$), the astrocytic Na^+-K^+-ATPase and sodium channels (e.g. SCN1) linked to maintaining V_m (Leo et al. 2011; Takano and Nedergaard 2009). In conclusion, CSD presents a unique metabolic challenge for astrocytes and neurons alike, and the self-sustaining slow propagation of the CSD wave appears to be caused by a vicious cycle of excess oxygen consumption, watershed hypoxia and a secondary failure of potassium homeostasis (Takano et al. 2007).

Calcium signaling in astrocytes

The advent of calcium imaging using chemical calcium indicators (e.g. Fluo-3) was one of the major breakthroughs that alerted investigators to the active role of glia in brain information processing. It was known through histological studies since the 1980s that astrocytes express a subset of glutamate receptors (Bowman and Kimelberg 1984; Kettenmann et al. 1984). However, it was not until 1990 that Cornell-Bell et al. observed that cultured astrocytes are able to respond to locally applied glutamate by generating wide-spreading waves of elevated intracellular calcium (Cornell-Bell et al. 1990). This observation was critical to subsequent glial research because it showed that astrocytes have the ability to directly sense synaptic activity. Subsequently, co-cultures of astrocytes and neurons were used to show that astrocytes are not just able to respond, but also to alter neuronal signaling through intracellular calcium signals (Nedergaard 1994; Parpura et al. 1994). Finally, these observations of bidirectional astrocyte communication with neurons were validated in more intact preparations (acute hippocampal slices and retinal preparations) (Kang et al. 1998; Newman and Zahs 1998). More recent work has also indicated that in response to the activation of glutamatergic and purinergic receptors or alterations of

local ion concentrations astrocytes may be able to release neurotransmitters into the synaptic cleft, either via vesicular or non-vesicular mechanisms (e.g. connexin hemichannels) (Hamilton and Attwell 2010; Kang et al. 1998; Simard et al. 2003; Torres et al. 2012; Wang et al. 2012a; Wang et al. 2012b). This extensive astroglial signaling at the level of the individual synapse led to the development of the 'tripartite synapse' model, which incorporates an astrocytic process into the basic unit of information processing (Araque et al. 1999).

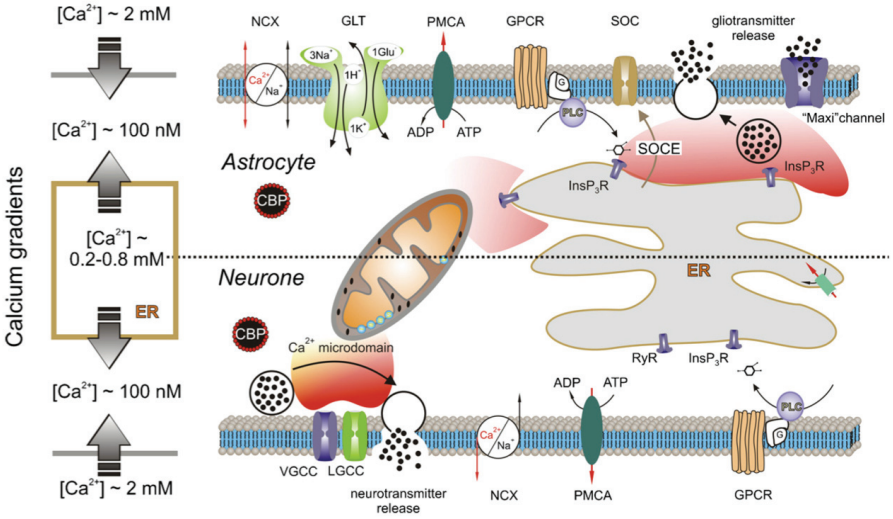

Figure 10. Illustration of the molecular mechanisms governing intracellular calcium in astrocytes and neurons. Abbreviations: CBP: Ca2+-binding protein; ER: endoplasmic reticulum; GLT: glutamate transporter; GPCR: G-protein coupled receptor; $InsP_3R$: inositol-1,4,5-trisphosphate receptor; LGCC: ligand-gated Ca2+ channel; NCX: sodium–calcium exchanger; PMCA: plasmalemmal Ca2+ ATP-ase; RyR: ryanodine receptor; SERCA: sarco(endo)plasmic reticulum Ca2+ ATP-ase; SOC: store-operated Ca2+ channel; VGCC: voltage-gated Ca2+ channel; 'Maxi' channel: high-permeability plasmalemmal channels (such as connexins or pannexins or P2X7 receptors or volume-regulated anion channels) that can act as a pathway for non-exocytotic gliotransmitter release. Modified with permission from Nedergaard et al. 2010.

Intracellular transients of free ionized calcium (Ca^{2+}) are an old form of cellular signaling that is present even in bacteria, and likely co-evolved with the use of adenosine triphosphate (ATP) as the primary intracellular energy source (Dominguez 2004). Intracellular calcium is tightly regulated in all mammalian cell types, and a rapid increase in this ion is used to among other things to mediate programmed cell-death (apoptosis) (Parpura and Verkhratsky 2012). Astrocytic calcium signals appear to derive primarily from endoplasmic reticulum (ER), where

the concentration of calcium is ~1000x higher than in the cytoplasm. Upon activation of metabotropic G_q-coupled G-protein coupled receptors, phospholipase C cleaves phosphatidylinositol-4,5-bisphosphate in plasmalemma, releasing inositol-1,4,5-trisphosphate (IP_3) to the cytosol and diacylglycerol in the membrane. IP_3-dependent calcium release from the ER via the IP_3 receptor type 2 (IP_3R2) is thought to be the major pathway of calcium signaling in astrocytes; as opposed to neurons where voltage gated calcium channels mediate vesicular neurotransmitter release **(Fig. 10)** (Nedergaard et al. 2010). However, it is possible that smaller IP_3-independent calcium signals in the small processes trigger IP_3 signaling in so-called calcium-induced calcium release (Arcuino et al. 2002). IP_3-independent mechanisms for calcium influx in astrocytes include plasmalemmal calcium channels (e.g. Cav1) and/or transporters (e.g. Na^+-Ca^{2+}-exchanger) (Nedergaard et al. 2010).

Intracellular calcium transients are known to propagate as waves throughout a network of astrocytes joined by gap junctions (composed of two connexons), which is termed the astrocytic syncytium (Rouach et al. 2008). There are a number of mechanisms thought to be involved in calcium wave propagation, including the diffusion of Ca^{2+} or IP_3 through gap junctions and paracrine ATP release activating neighboring metabotropic P2Y receptors (Verkhratsky et al. 2012a). Astrocytic calcium waves as observed *in vitro* and *in situ* propagate relatively slowly compared to axonal signals (4-20 $\mu m\ s^{-1}$ vs. 10-100 $m\ s^{-1}$) (Hartline and Colman 2007). For this reason, some authors would argue that astrocytic calcium waves may be too slow or could generate noise if they were to modulate individual synaptic events (Agulhon et al. 2008). Conversely, this temporal difference may indicate that astrocyte calcium transients are responsible for the integration of neuronal activity over a larger temporal (seconds) and spatial (thousands of synapses) scale, which is more relevant for neurovascular coupling (Iadecola and Nedergaard 2007).

Through the application of 2PLSM to calcium imaging, investigators have recently been able to explore astrocyte calcium signals in intact living brains. In one of the seminal *in vivo* studies Wang et al. showed that physiological sensory stimulation (in the form of air-puffing whiskers) is able to elicit a coordinated calcium response that followed neuronal firing in the stimulated area of somatosensory cortex (Wang et al. 2006). The magnitude of this sensory-evoked astrocytic calcium response was directly correlated with the neuronal response and depended on

activation of G_q-coupled metabotropic glutamate receptor 5 (mGluR5). Subsequent *in vivo* studies have elaborated on this observation, and shown that other forms of sensory stimulation (e.g. hindlimb electroshock), as well as local agonist application or stimulated neuromodulator release (e.g. acetylcholine and norepinephrine) can also elicit calcium activity in cortical astrocytes (Bekar et al. 2008; Navarrete et al. 2012; Takata et al. 2011; Winship et al. 2007). Astrocytes thus appear able to respond to several types of physiologically relevant signals *in vivo*.

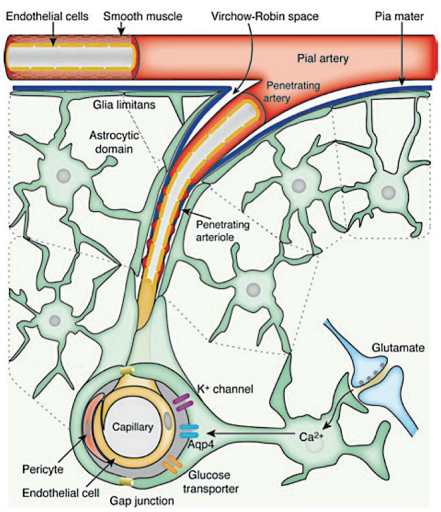

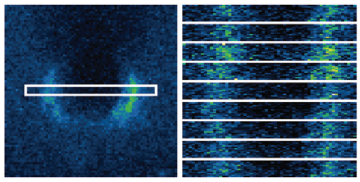

Figure 11. Astrocytic regulation of blood flow via calcium signals. Left: Illustration of the hypothetical role of astrocytes in connecting neuronal demand with blood flow supply via calcium signaling. Adapted with permission from Iadecola and Nedergaard, 2007. Right: Serial 2PLSM images taken at 3 s intervals of a cerebral arteriole showing functional hyperemia and associated calcium activity (pseudocolored rhod-2 intensity) in the awake mouse cortex (unpublished).

Since *in vitro* and *in situ* work showed astrocyte-neuronal signaling is inherently bidirectional, the next question would be what neuronal changes do astrocyte calcium signals elicit *in vivo*. Unfortunately, on this critical issue the literature is quite divided. The previously discussed 'tripartite synapse' model states that astrocyte calcium activity triggers gliotransmitter release, which may in turn modulate neuronal activity (Araque et al. 1999). However, data that directly questions some of the key observations underpinning this model has emerged more recently (Agulhon et al. 2010; Agulhon et al. 2008; Nedergaard and Verkhratsky 2012; Sun et al. 2013). Another critical function for astroglial calcium transients is mediating neurovascular coupling (functional hyperemia) **(Fig. 11)**. Stimulating astrocyte calcium transients or experimentally increasing intracellular calcium using uncaging triggers brisk vascular responses. However, both the type of response (vasodilation or constriction) and the mechanisms implicated are currently under intense debate, as

different experimental paradigms have generated divergent results (e.g. pre-constricted blood vessels in brain slice vs. *in vivo*) (Attwell et al. 2010; Iadecola and Nedergaard 2007; Lauritzen et al. 2012; Takano et al. 2006).

There are several important questions regarding astrocyte calcium signaling that remain unanswered. First, can we trust the data from *in situ* studies of young animals or are hippocampal slices not as good a model study astrocytes as it has been for neurons (Sun et al. 2013)? Second, *in vivo* imaging has a much higher signal-to-noise ratio for calcium recordings and is often acquired at a lower temporal resolution (e.g. 1-10 Hz frame rate). This raises the question of whether we are in fact detecting all the relevant calcium signals or looking in the right places (e.g. soma v.s. processes). Two *in situ* studies have recently shown that short lasting low amplitude calcium transients in the processes occur even in response to individual synaptic events (Di Castro et al. 2011; Panatier et al. 2011). More recently, high-speed 2PLSM set-ups developed primarily for neuronal calcium imaging are breaching this barrier, allowing frame rates of up to 1000 Hz (Chen et al. 2011). Third, does neuronal activity generate multiple astrocytic calcium waves, and if so do these have different kinetics and functions (Torres et al. 2012)? Fourth, are we imaging deep enough in the cortex? Whisker activation principally stimulates layer IV, and we may be simply observing an axially propagated response in the more superficial layers. Finally, one major problem with the *in vivo* literature to date is that, with the exception of two studies, it has been carried out using anaesthetized animals, where neuronal activity is known to be significantly depressed (Greenberg et al. 2008). These two preliminary studies of calcium signaling in awake animals revealed profoundly different spontaneous and evoked activity patterns. These included synchronized 'bursts' (instead of waves) across hundreds of astrocytes and a much higher level of spontaneous activity (Dombeck et al. 2007; Nimmerjahn et al. 2009). Exploring calcium signaling in astrocytes in awake animals would no doubt give a more physiological view of how astrocytes signal and perhaps provide some more definitive answers to whether or how astrocytes can sense and modulate synaptic transmission.

Cerebrospinal fluid microcirculation in the brain

In most tissues of the body, a parallel lymphatic circulation accompanies blood vessels and supports normal hemodynamic function by resorbing interstitial fluid,

carrying immune cells and transporting lipids (Schmid-Schonbein 1990). The brain, however, is one of the few organs to be entirely devoid of an anatomically distinct lymphatic system. Through the selective barrier properties of the BBB, the composition of the CNS microenvironment is regulated very separately from the rest of the body (Abbott 2004). It has long been thought that CSF might serve the role of peripheral lymph in the CNS. Macroscopically, CSF circulates rapidly from the choroid plexi in the ventricles where it is produced and diffuses through the brain parenchyma by convective bulk flow, before being resorbed by the arachnoid granulations into venous sinuses **(Figure 12)** (Abbott 2004; Aukland and Reed 1993; Sakka et al. 2011). However, the extracellular space in the brain is extremely narrow and very tortuous, meaning that any bulk flow through this anatomical space should be much slower than the interstitial fluid diffusion rates we observe (0.1-0.3 μL min^{-1} g^{-1}) (Thorne and Nicholson 2006).

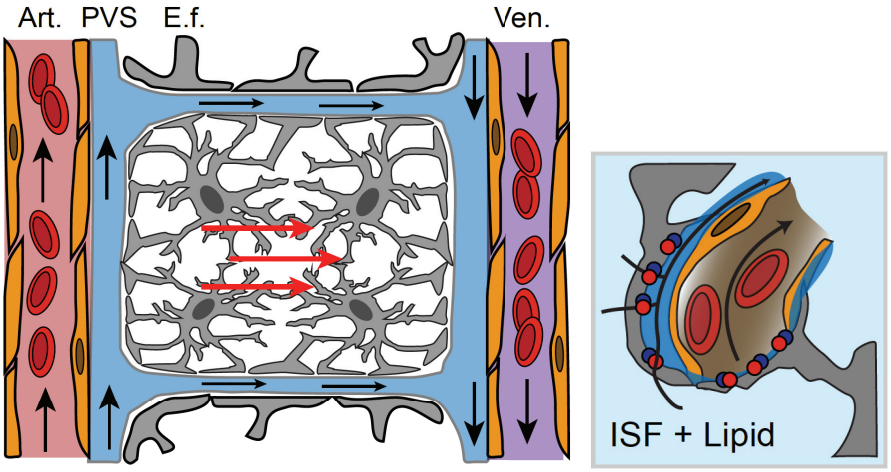

Figure 12: Paravascular CSF circulation in neuropil. Left: Macroscopic CSF circulation, illustrating para-arterial (Art., red) and para-venous (Ven., purple) PVS (blue) ensheathed by astrocyte endfoot (e.f.) processes. Paravascular CSF flow mediates convective bulk flow of interstitial fluid through the narrow and tortuous extracellular space. Right: Microscopic view of paravascular circulation of interstitial fluid (ISF) and lipids through putative transporters in glial endfeet.

These observations have led investigators to suggest that 'highways' for more rapid CSF flow through the parenchyma must exist, and the two most likely candidates are the para-axonal and paravascular pathways. The former is more highly developed in species with bigger axons, but diffusion-weighted MRI has also revealed that water flux along axons is a major pathway in the human brain (Abbott 2004;

Mori et al. 2009). Several groups have illustrated the latter pathway since the 1800s by injecting various tracer molecules (e.g. horseradish peroxidase) injected into the brain parenchyma, ventricles or subarachnoid CSF and performing serial histological sectioning. This method causes the tracer to strikingly outline a paravascular space (PVS) ensheathing the cerebral vasculature, although the choice of tracer determines how completely the vasculature will be outlined (Abbott 2004; Cserr et al. 1981; Cserr et al. 1986; Rennels et al. 1990; Szentistvanyi et al. 1984). Interestingly, a recent 3D EM reconstruction has revealed that astrocyte endfeet provide a complete ensheathment of cerebral blood vessels, ensuring the patency of this paravascular compartment (Mathiisen et al. 2010).

The paravascular CSF pathway was recently revisited by Iliff et al., who used 2PLSM to demonstrate that a range of water-soluble tracers and deuterated water (^2H_2O) itself pass rapidly along the separate anatomical space between astrocyte endfeet and the blood vessel wall *in vivo* (Iliff et al. 2012). The PVS is largest near the pial surface, where it is called the Virchow-Robin space, and becomes progressively narrower before almost disappearing at the capillary level (Abbott 2004). Interestingly, Iliff et al. also showed that water flow through this pathway was 70% slowed by deletion of *Aqp4*, indicating that one of the major roles of this protein could be facilitating CSF microcirculation **(Fig. 13)**. It therefore appears that the brain has a distinct pathway for the microcirculation of water and water-soluble compounds. However, another major function of peripheral lymph is the transport of lipids from the gut to the liver and peripheral organs. Despite grey and white matter being composed of 38 and 58 % lipid, respectively (O'Brien and Sampson 1965a; O'Brien and Sampson 1965b), the BBB is largely impermeable to peripheral lipids and lipoproteins (Leoni et al. 2010). The essential lipids needed for myelin or synaptic membranes therefore need to be produced within the CNS (Mauch et al. 2001). Interestingly, astrocytes have been shown to orchestrate this vital process, by producing cholesterol and high-density lipoprotein-like molecules (Fagan and Holtzman 2000). The addition of fatty acid residues (palmitoylation) has important functions during neurodevelopment and synaptic plasticity (Fukata and Fukata 2010). Astrocyte lipid clearance to the blood is also likely to be important, and for instance cholesterol is cleared by conversion to 24S-OH-cholesterol (cerebrosterol), making it BBB permeable (Bjorkhem 2007). CSF is rich in astrocyte-produced lipoproteins, and mutations in genes related to this process (e.g. ApoE) have been linked to

neurodegenerative conditions such as Alzheimer disease (Leoni and Caccia 2011; Leoni et al. 2010; Riddell et al. 2008). Taken together, observations regarding lipid metabolism in the CNS indicate the existence of astrocyte-neuronal lipid (or cholesterol) shuttle, where astrocytes feed neurons with the necessary lipid for synaptic membranes (Nieweg et al. 2009). An important question that is unanswered in current literature is therefore whether the PVS serves as a conduit for rapid lipid as well as water microcirculation through the brain parenchyma.

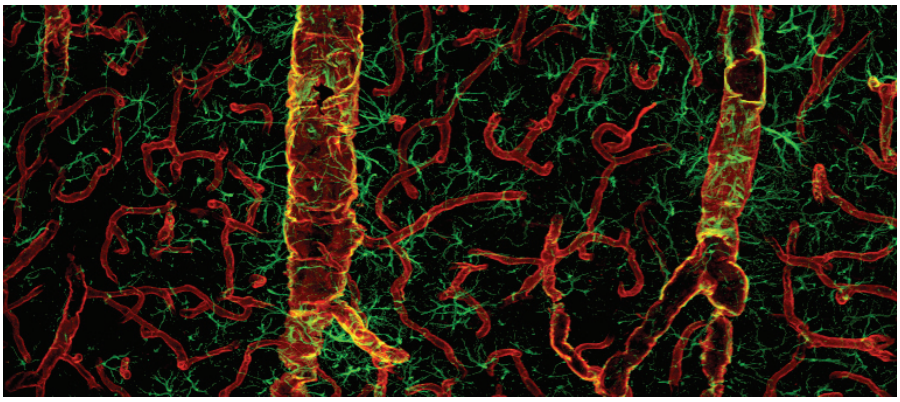

Figure 13. Immunofluorescence micrograph of AQP4 and GFAP expression in the mouse cortex. Modified from Simard et al. 2003.

Microglia - the double-edged sword of CNS immunity

Microglia are a cell type that has come into focus relatively recently. They are the innate immune cells of the CNS and are of mesenchymal origin. Microglia are derived from peripheral macrophages and migrate to the brain during early development (Chan et al. 2007; Verkhratsky and Butt 2007). The function of microglia has been described as a 'double-edged sword,' as they have the capability of being both protective and harmful in health and disease. Under physiological conditions, microglia exist in the 'resting state,' which is morphologically characterized by the cells extending multiple thin processes from a small central cell body. However, *in vivo* 2PLSM recently showed that 'resting' microglial processes are in fact constantly moving, screening their territories, seeking out any signals that may indicate injury or inflammation (Davalos et al. 2005; Nimmerjahn et al. 2005). Like astrocytes, microglia show very little overlap between cells and seem to survey their own domain with their processes (Kettenmann et al. 2011).

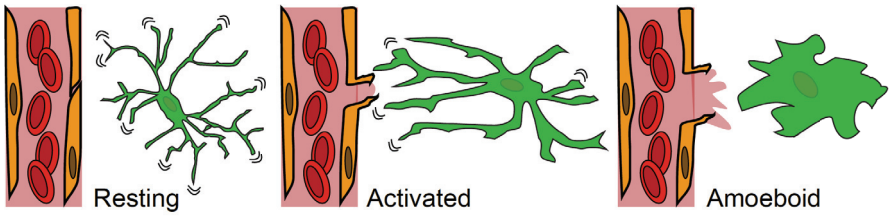

Figure 14. The changing states of microglia. Illustration showing resting microglia (left), microglial activation and BBB opening after a small injury (middle), and severe microglial activation (right) associated with amoeboid morphological appearance and phagocytic behavior in the context of a large injury. Note the surveillance capability of fine processes in resting microglia, thought to constantly scan for foreign antigens.

In response to brain injury, infection or inflammation, microglia are known to change their morphology by transforming through an 'alerted state' to an 'amoeboid state' **(Fig. 14)**. This morphological transition involves retraction of processes, which become fewer but thicker, increase in cell body size and production various cytokines along with other signals (Block et al. 2007; Davalos et al. 2005; Hanisch and Kettenmann 2007; Verkhratsky and Butt 2007). When activated, their morphological change aids phagocytosis and allows the removal of unwanted pathogens or dead host cells. The exact mechanism of how microglial activation is initially triggered is not fully understood, but we do know that microglia possess a number of neurotransmitter (including glutamate, GABA, adenosine and purine) and immune (including complement, cytokine and chemokine) receptors. Many of these receptors are involved in activating microglia during brain injury, but ATP in particular is thought to play a central role (Davalos et al. 2005; Kettenmann et al. 2011; Ohsawa et al. 2007). Brain injury is thought to result in the release of vast amounts of ATP, which microglia respond swiftly to through activation of mainly P2X7 receptors (Burnstock and Verkhratsky 2010; Kettenmann et al. 2011; Verkhratsky and Butt 2007). Activation of these receptors promotes extension of microglial processes towards the perceived site of injury and the release of various cytokines and pro-inflammatory proteins. In addition to releasing pro-inflammatory markers (such as interleukins, tumor necrosis factor-α and transforming growth factor-β), microglia are thought to aid neurons in regeneration post-injury (Kettenmann et al. 2011). For example, they release a number of growth factors, including brain-derived neurotrophic factor and

nerve growth factor, which are thought to aid neurons in overcoming injury (Kettenmann et al. 2011).

In their activated state, microglia have been shown to be effective in phagocytosing unwanted debris, but what happens if this immune response starts targeting host cells? In Alzheimer disease, microglia have been shown to phagocytose neurons, perhaps contributing to loss of cognitive function. Interestingly, knocking out *Cx3Cr1* prevented neuronal loss in mice with Alzheimer (Fuhrmann et al. 2010). Additionally, the Alzheimer disease plaque is formed by amyloid-β deposits, astroglial processes, degenerated neurons and activated microglia. It is therefore poorly understood whether microglial activation is protective in various neurodegenerative diseases or whether they present a target for therapy. Activated microglia are known to be able to trigger robust calcium activity in astrocytes, an observation that may explain some of the neurotoxicity of activated microglia (Agulhon et al. 2012). Activated microglia have been observed following stroke, and it is unclear whether the immune response generated might in fact increase the necrotic infarcted area of brain tissue (Verkhratsky and Butt 2007; Wang et al. 2012c). Interestingly, microglia have also recently been implicated in the role of chronic neuropathic pain. Peripheral nerve damage is known to cause activation of microglia in the spinal cord, which then leads to the activation of purinoreceptors, in particular P2X4 and P2Y12. These receptors have been shown to be necessary in producing allodynia and purinergic inhibition results in reversal of this chronic pain symptom (Inoue et al. 2007; Kobayashi et al. 2008; Tsuda et al. 2003). Additionally, microglia are thought to release brain-derived neurotrophic factor in response to peripheral nerve damage as a signaling molecule to neurons, and inhibiting this release may reverse the symptoms of neuropathic pain (Coull JA 2005). Finally, microglial activation has been shown during the final coma stage in hepatic encephalopathy (HE), coinciding with brain edema and BBB opening. However, these data have been collected using *ex vivo* methods and further investigation using *in vivo* methods to establish the timescale of these changes is warranted (Butterworth 2011; Jiang et al. 2009; Rodrigo et al. 2010). Taken together, these divergent observations regarding the role of microglia in disease may reflect the double role of help and harm that microglia have in the CNS.

Astrocyte ammonia handling in health and disease

Ammonia is a ubiquitous waste product and vital building block in the body that is intimately linked to protein metabolism (Butterworth 2002a). At physiological pH and temperature ammonia exists as 99% NH_4^+ (ammonium) and 1% NH_3 (ammonia) and has an acid dissociation constant (pK_a) of 9.02 (Ott and Larsen 2004). In the brain, ammonia detoxification has a central role as it is necessary for the recycling of the principle excitatory neurotransmitter glutamate, and hence indirectly the generation of the principle inhibitory transmitter, GABA (Bak et al. 2006; Hertz and Kala 2007; Paulsen et al. 1987). The key step of this glutamine-glutamate-GABA cycle happens in astrocytes, which possess glutamine synthetase (GS), the only enzyme capable of detoxifying ammonia in the brain through condensation with glutamate (Hertz and Zielke 2004; Martinez-Hernandez et al. 1977).

One of the major problems with studying ammonia directly is its volatility and the lack of specific tools to detect the molecule (e.g. ammonia-sensitive dyes or electrodes). Consequently, several investigators have used pH as proxy for ammonia movement, as NH_4^+ is a weak acid and NH_3 is a volatile base. For instance, when astrocytes or neurons *in vitro* or *in situ* are exposed to elevated ammonia this causes a rapid intracellular alkalinization, thought to represent volatile NH_3 crossing the lipid bilayer and reaching equilibrium, followed by a prolonged intracellular acidification caused by NH_4^+ entry through ion-channels (Boyarsky et al. 1993; Nagaraja and Brookes 1998). Reciprocal pH changes are usually recorded in the extracellular space, as we found in our study. In a set of very interesting experiments Coles et al. used this pH phenomenon in combination with ammonia ion-sensitive microelectrodes to show that light-stimulated neuronal firing in retina is associated with increased aerobic metabolism and a rapid rise in extracellular ammonia, which is then swiftly taken up by glial cells (Coles et al. 1996; Marcaggi and Coles 2000; Marcaggi et al. 2004). Thus, taken together with related data from cultured astrocytes and acute brain slices it is clear that physiological neuronal firing is associated with a significant release of ammonia along with glutamate into the extracellular space (Alger and Nicoll 1983; Waniewski 1992). Interestingly, glial GS has a higher affinity for ammonia than glutamate, suggesting that astrocytes prioritize the removal of ammonia over the potentially excitotoxic neurotransmitter (Ciani et al. 1996; Waniewski 1992).

Ammonia was relatively widely studied in the 1960s - 80s, as in excess it was found to cause gross brain dysfunction, including encephalopathy and seizures

(Cooper et al. 1979; Lux and Schubert 1969; Martinez-Hernandez et al. 1977; Raabe and Gumnit 1975). The epileptogenic effect of GS inhibitor methionine sulfoximine (MSO) was also observed at this time in dogs accidentally fed MSO via biscuits with bleached flour (dogs are 100-times more sensitive to MSO than rodents and primates) (Paulsen et al. 1988b; Proler and Kellaway 1962). Since the realization that liver failure is characterized by an accumulation of ammonia in the blood (hyperammonemia), the brain dysfunction in this condition, termed hepatic encephalopathy (HE), has also been thought to be largely ammonia-related (Butterworth 2002a). Several different hypotheses have been suggested to explain the neurological effects of ammonia, and these include **(Fig. 15)**: ammonia driving an accumulation of glutamine with secondary osmotic damage to astrocytes (glutamine hypothesis), impaired functional hyperemia or decreased overall blood flow, BBB opening with consequent edema, lactic acidosis or impaired pH homeostasis, a failure of energy (glucose/ATP) metabolism, altered ion homeostasis (intracellular accumulation of Na^+ and Cl^-, and extracellular increase of K^+), microglial activation, glutamate excitotoxicity (although nuclear magnetic resonance, NMR, studies have subsequently shown that there is no net glutamate increase in the brain) and an impairment of GABA function (Alger and Nicoll 1983; Butterworth 2002b; Cooper et al. 1979; Folbergrova et al. 1969; Ganz et al. 1989; Gregorios et al. 1985; Jayakumar et al. 2006; Lux 1971; Norenberg 1977; Raabe 1981; Ratnakumari et al. 1994; Rodrigo et al. 2010).

However, rather surprisingly none of these hypotheses have resulted in viable new therapies, and the current therapy for hyperammonemia still relies on older strategies such as increasing gut elimination with lactulose (Butterworth 2002a). We would suggest that part of the shortcoming in these studies is a failure to appreciate the limitations of reduced experimental preparations when used in isolation. Although most of these studies likely hold important clues to the cause of ammonia neurotoxicity, putting the whole story together may require the use of several methodologies spanning different areas of neuroscience, glial-science, electrophysiology, optical imaging and biochemistry.

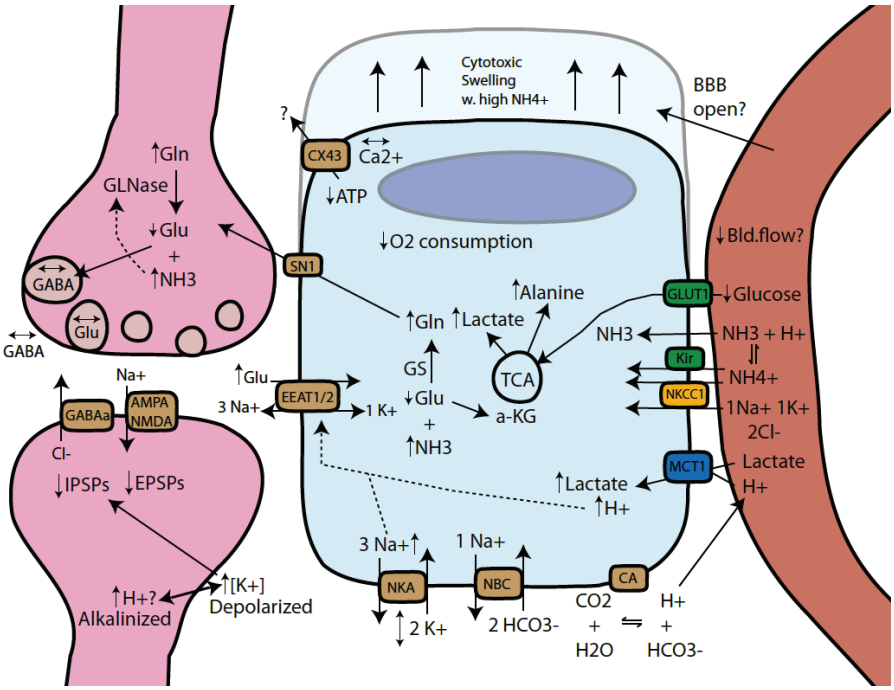

Figure 15. Diagram summarizing the potential mechanisms for acute hyperammonemic encephalopathy based on a systematic review of the literature. Key: Red - blood vessel, blue - astrocyte and pink - neuron (pre- and post-synaptic processes). Excess blood ammonia crosses the BBB and principally enters astrocytes, where it is detoxified by enzyme glutamine synthetase.

6. HYPOTHESES AND AIMS

Two-photon imaging is a technique that has only recently been applied to the study of glial cells *in vivo*. We used this technique to examine the glial regulation of ion and water homeostasis in the brain. Glia are thought to be the principle cell type responsible for regulating these processes. Tight regulation of ion and volume changes is essential for normal neuronal function. We therefore hypothesized that by sensing and regulating local ion and water movement, glial cells can detect and alter physiological neuronal activity. Additionally, we propose that CNS disorders involving an imbalance of water and/or ion regulation might be directly caused by glial dysfunction. Utilizing the strengths of 2PLSM, we aimed to examine these homeostatic mechanisms *in vivo*, at a subcellular level and in real-time. Our ultimate goal was of extending the observations from previous studies to develop new therapies for the neurological disorders studied in our thesis.

Our specific aims were as follows:

I. What is the role of AQP4 in astrocyte calcium signaling elicited by volume changes during brain edema?
II. Does AQP4 affect oxygen micro-distribution during cortical spreading depression?
III. What is the effect of general anesthesia on astrocyte calcium signaling in the cortex of awake behaving animals?
IV. How are lipid molecules transported in the paravascular space and could this specialized gliovascular compartment play a role in astrocyte signaling?
V. Is microglial activation an early feature of HE that can be directly associated with excess ammonia?
VI. What is the role of astrocytes in acute ammonia neurotoxicity and can we identify an early step in this disease pathway that may be targeted for therapy?

7. METHODOLOGICAL CONSIDERATIONS

The goal of our project was to study glial regulation of volume and ion homeostasis in normal and disease settings. To ensure our findings were relevant and translatable to normal adult physiology and pathophysiology we chose to employ largely *in vivo* mouse models. Several recent papers have highlighted the profound difference between cellular dynamics *in vivo* as compared to *in situ*, *in vitro* or histological specimens (Sun et al. 2013; Takano et al. 2006; Wang et al. 2006). For a subset of the experiments we also adapted recently published techniques for awake imaging to avoid the masking effect of anesthesia on endpoints such as seizures, astrocyte calcium activity and cognitive phenotype (Dombeck et al. 2007; Greenberg et al. 2008; Nimmerjahn et al. 2009). To achieve sufficient temporal and spatial resolution *in vivo* without damaging the brain we took advantage of the aforementioned benefits offered by 2PLSM. This type of optical imaging employs a pulsed femtosecond laser to achieve specimen excitation with much longer wavelengths than conventional 1PLSM. However, 2PLSM has some theoretical and practical drawbacks as a consequence of the optics employed, which we will outline below (Christensen and Nedergaard 2011). To achieve a more complete picture of the biology, several adjunct techniques were also used in our studies to complement the 2PLSM findings. The relative merits and shortcomings of these techniques will also be addressed.

Limitations of two-photon imaging

There are three main issues with 2PLSM. First, 2PLSM has a theoretical resolution limit that is close to one-half the wavelength of the exciting light (i.e. diffraction limit = λ / 2 x numerical aperture) (Christensen and Nedergaard 2011). Therefore, 2PLSM theoretically cannot resolve structures smaller than ~ 0.35-45 μm. Practically, 2PLSM imaging of living brain has further limitations due to aberrations along the optic pathway (e.g. optically dense neuropil). The effective resolution can therefore be approximated from the point spread function of an individual 2PLSM set-up, and usually has a radial resolution of ~ 0.6-1.0 and an axial resolution of ~ 3-5 (due to greater dispersion in this axis) (Dong et al. 2003; Drew et al. 2010). This resolution is still not sufficient to address ultrastructural questions, which for instance conventional transmission electron microscopy can address (resolution 0.2 nm) (Denk et al. 2012; Helmstaedter et al. 2008; Mikula et al. 2012). Additionally, new optical techniques

such as stimulated emission depletion (resolution 70-90 nm) microscopy have breached the diffraction limit of light and are currently allowing optical imaging of subcellular protein localization in cultured cells (Blom et al. 2012; Blom et al. 2011; Hell 2003; Willig et al. 2006). However, due to technical limitations such techniques have to our knowledge not yet been applied *in vivo*. The resolution limit of 2PLSM therefore imposes limitations on the questions that can be addressed using this technique, and for instance comparing the subcellular localization or trafficking of proteins between two closely apposed cell membranes is currently beyond the reach of 2PLSM.

Second, 2PLSM has a technical limit on its temporal resolution; as it usually relies on the movement of galvanometric mirrors to raster scan the laser beam across the specimen (similar to confocal microscopy). These mirrors have too much inertia to allow imaging with a temporal resolution < 80-100 ms. Many important processes happen on a timescale that is orders of magnitude faster than the scan rate of most 2PLSM set-ups, including neuronal signaling (Christensen and Nedergaard 2011). Most of the experiments used in this thesis were conducted using galvanometric mirrors, but the recent advent of random access multiphoton microscopy using acousto-optical deflectors is rapidly breaching this temporal resolution barrier (Chen et al. 2011; Duemani Reddy et al. 2008).

Third, due to the optically dense nature of biological material such as brain, 2PLSM is usually unable to image much deeper than 500 μm below the tissue surface. Maximum imaging depth is again a property of the wavelength used to excite the specimen, and recently the use of ultra-long wavelength lasers (e.g. 1280 nm) facilitated imaging as deep as 1 mm below the cortical surface (Kobat et al. 2009). Deeper imaging will undoubtedly open new avenues for discoveries, as most labs are currently limited to imaging down to layer IV of mouse brain cortex. White matter, subcortical nuclei, hippocampus and deeper cortical layers are thus rarely examined *in vivo* due to the technical limitations of imaging (e.g. 2PLSM).

Surgical preparations for *in vivo* imaging

Another critical consideration for imaging involving live animals is the surgical preparation. The typical surgical protocol we employed in our studies involved anesthetizing the animal, sterilizing the skin, fixing the skull to a metal mini-frame, creating a small cranial window (0.5-3 mm diameter), and sealing this window with a

cover glass ± agarose or saline **(Fig. 16)** (Dombeck et al. 2007; Drew et al. 2010; Holtmaat et al. 2009; Wang et al. 2006).

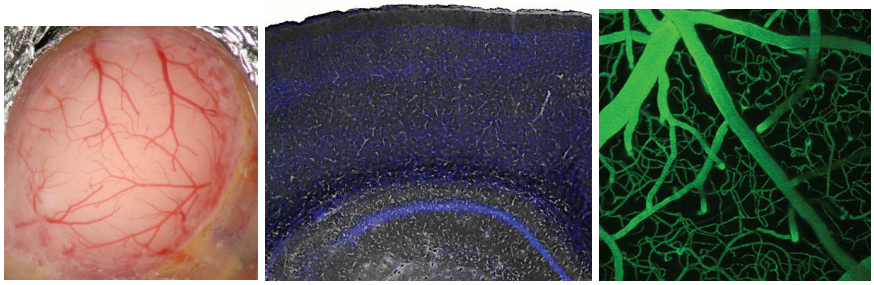

Figure 16. Neurosurgical preparation for *in vivo* 2PLSM imaging. Left: Photograph of a cranial window preparation. Kindly provided by Prof. M. Nedergaard. Middle: Immunofluorescence micrograph showing the layers of the mouse cortex and outlining the microvasculature (white - AQP4, blue - DAPI). Right: Collapsed XYZ stack (25-175 µm depth) of fluorescein isothiocyanate (FITC)-dextran labeled cortical blood vessels imaged using 2PLSM.

Generally, we found two steps to be pivotal in this procedure. First, the cranial window had to be created with extreme caution to avoid injuring the underlying brain. Injuries might not be readily apparent during the surgery, but when we subsequently imaged the animal even minor injuries could significantly confound the processes we wished to study (e.g. calcium signaling) (Xu et al. 2007). One method to circumvent this problem and allow more chronic imaging is to thin the skull instead of generating a full thickness cranial window. This approach may cause more limited resolution, and requires a great amount of technical skill, but can potentially generate less microglial activity, reactive astrogliosis and dendritic spine loss (Drew et al. 2010; Holtmaat et al. 2009). Second, the overall physiological state of the animal strongly influenced many of the endpoints we wished to measure, and we therefore excluded all animals displaying problems with e.g. breathing, hypoxia and hypercapnia (Duffy and MacVicar 1996; Thompson et al. 2006). The latter issue was most critical when experimenting with anesthetized mice, as these small rodents easily develop complications from the anesthesia (e.g. inadequate ventilation).

To address some of the issues mentioned above, we adapted a model to image brain cells in awake behaving mice (Dombeck et al. 2007; Nimmerjahn et al. 2009). Extreme care needed to be taken not to cause pain and stress to the animal, and this model had some issues of its own. Our main concern was to avoid causing any harm to the animal and the experiments were therefore planned and executed with great

care. To address the more specific issue of movement artifacts in awake mice, we developed a method of normalizing fluorescence signals (outlined in more detail in paper II). Related papers that imaged awake mice have also reported alternative methods of circumventing this issue, including post hoc algorithm corrections (Dombeck et al. 2009; Dombeck et al. 2010; Harvey et al. 2009; Ozden et al. 2012). In conclusion, a careful surgical preparation is critical for validity of the results obtained from *in vivo* 2PLSM imaging.

Ethical considerations for *in vivo* imaging

Several key agreements including Nuremberg (1947) and Helsinki (1974) have highlighted the need for an ethical framework to regulate the conduct of medical research. The following is an account of the ethical issues that we encountered during our doctoral research and how we addressed them. We chose to use a mouse experimental model because of the similarity of the brain pathophysiology for the conditions we wished to study between mice and humans (translational potential) and the availability of transgenic mice and the. When designing our experiments we have used the three Rs outlined by Russel and Burch (1959) to minimize both the use of animals and any potential distress inflicted (Wolfensohn and Lloyd 2003). We strongly feel this should be a key priority to emphasize to junior researchers at an early stage. In addition, the ethical treatment of experimental animals is pivotal for both obtaining trustworthy results and the continued existence of basic research. With regards to our thesis work, we encountered the most ethical and practical challenges when it came to designing and implementing the *in vivo* experiments.

Firstly, animal experiments should never be performed if other means exist that will adequately address the research question. Unfortunately, our scientific questions could not be addressed without animal experimentation (**replacement**). Modeling of the glial homeostatic system would for instance not help us test our hypotheses, as the basic properties of this system are still not delineated clearly and clinical outcomes cannot be measured in certain reduced preparations. Secondly, we wished to minimize the number of mice needed to challenge our hypotheses (**reduction**). An important part of achieving this goal was careful planning, including an exhaustive literature search to avoid unnecessary duplication of previous results and statistical power calculations to exactly plan the numbers of animals needed.

Finally, and perhaps most importantly, we spent a long time **refining** our experimental methods. Whenever possible we performed experiments on fully anesthetized animals, which has the benefit that the animal has full analgesia, anesthesia and amnesia. However, for a subset of experiments the use of anesthesia would mask the end-points we wished to examine, and we were forced to adapt a relatively new technique for awake imaging in habituated animals (Dombeck et al. 2007). As awake experiments have the potential of causing significant stress to the animal, they should never be performed without careful consideration of whether the research questions can be addressed in any other way. We found this to be a major ethical burden as well as a practical challenge, also when interpreting the experimental results. We therefore spent extensive efforts when designing these experiments to minimize any pain or distress the animal might experience. Challenges included ensuring adequate anesthesia for the surgical implantation of a cranial window, whilst ensuring the animal could recover completely from the anesthetic. Moreover, adequate postoperative analgesia had to be achieved, and the mice that were imaged multiple times over longer periods had to be carefully assessed for signs of discomfort or distress (Cooper et al. 2000; Langford et al. 2010; Richardson and Flecknell 2005). Finally, during the imaging experiments themselves we had to ensure absolute silence, darkness, adequate warmth and hydration, without the mice getting wet from any of the solutions used (1994). Throughout the design and implementation of these methods we were continuously in contact with the veterinarians at the department of animal health to optimize the animals' well being. We also relied heavily on advice from researchers with previous experience from similar experiments, and previously published protocols on *in vivo* experimentation (Dombeck et al. 2007; Nimmerjahn et al. 2009).

Fluorescent imaging using chemical dyes and transgenic animals

Fluorescent molecules are generally either chemicals (e.g. tetramethylrhodamine derivatives) or proteins (e.g. fluorescent eGFP isolated from jellyfish). The former can frequently be toxic to living cells at high doses, while the latter are better tolerated as they are frequently derived from living animals (Paredes et al. 2008; Regan et al. 2007). The efficiency of two-photon fluorophore excitation and optimal excitation wavelength cannot be directly extrapolated from one-photon spectra, and likely depends on other factors such as the local electric field (Bestvater et al. 2002;

Drobizhev et al. 2011). We used a combination of transgenic mice expressing fluorescent proteins under cell-specific promoters and loading of fluorescent dyes that label cells of interest. The former technique is largely limited by the selectivity and strength of the gene promoter used. *Glt1* is the promoter for the astrocyte specific glutamate transporter GLT1 (mouse ortholog of excitatory amino acid transporter 2), and eGFP expressed by this promoter labels astrocyte soma, principal processes and endfeet sufficiently well **(Fig. 17)** (Regan et al. 2007). However, the finer peri-synaptic processes were less well resolved and this limited our ability to examine these subcellular microdomains in more detail.

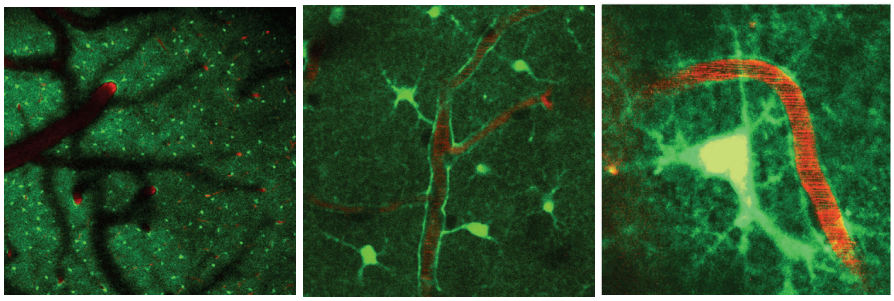

Figure 17. 2PLSM images showing eGFP expressing astrocytes and texas red dextran outlined vasculature at different magnifications. Note the bright eGFP signal in the soma and primary processes, but relatively poor signal-to-noise ratio in the smaller processes.

Several hydrophobic dyes were used to selectively label astrocytes (e.g. SR101 and Texas red hydrazide) or monitor intracellular calcium fluctuations (e.g. rhod-2, fluo-4, Oregon green BAPTA, 1,2-bis(o-aminophenoxy)ethane-N,N,N',N'-tetraacetic acid) **(Table 2)** (Paredes et al. 2008). The former dyes serve as excellent morphological markers (Nimmerjahn et al. 2004), but have relatively recently been shown to trigger epileptiform activity in hippocampal brain slices (Kang et al. 2010). The aforementioned calcium sensitive dyes are acetoxymethyl (AM)-ester linked, allowing the molecule to cross cell membranes by virtue of their lipid solubility. AM-dyes are then trapped inside the cell through the activity of intracellular esterases, which cleave the AM group and render the dye hydrophilic (Paredes et al. 2008). The mechanism for the selective loading of these dyes mainly into astrocytes is still largely a mystery, and one cannot exclude that the dyes themselves have some biological effects on the cells they label (Reeves et al. 2011). The calcium indicators employed in our studies are for instance all BAPTA-based calcium chelators, and

might therefore dampen fluctuations of free Ca^{2+} inside the cell (Paredes et al. 2008; Reeves et al. 2011). Our own experience was therefore to try and minimize the amount of calcium dye loaded, to avoid cell saturation with the dye as this effectively abolished spontaneous calcium transients. Additionally, all chemical calcium indicators need to be loaded over a period of 30 - 45 min into astrocytes either through application on exposed cortex or via pressure injection into the parenchyma. This loading process may itself generate a mild inflammatory response in the brain, adversely effecting recordings (Agulhon et al. 2012). Finally, different calcium indicators have different dissociation constants that determine how long they bind free Ca^{2+} ions, and setting a practical limit on the temporal resolution of imaging. Several investigators have recently found a way to circumvent dye use by generating transgenic mice expressing calcium indicators (e.g. genetically-encoded calcium modulated protein) under astrocyte specific promoters (e.g. GFAP) (Mao et al. 2008; Shigetomi et al. 2010; Tong et al. 2012). In conclusion, both chemical and transgenic fluorescent proteins have inherent limitations that need to be considered when interpreting imaging results.

Table 2. 1PLSM and 2PLSM excitation/emission spectra of relevant fluorophores.

	2P excitation	**1P excitation**	**Emission**
eGFP	927 nm	488 nm	509 nm
Texas red	780 nm	582 nm	602 nm
SR101	905 nm	586 nm	605 nm
Fluorescein	800 nm	508 nm	519 nm
Rhod-2	810 nm	553 nm	576 nm
Fluo-3,4,5	810 nm	493 nm	520 nm
Oregon green BAPTA	810 nm	492 nm	523 nm
Nile red	810 nm	559 nm	640 nm

Data sampling and analysis for 2PLSM

To ensure that all the 2PLSM imaging data we collected were comparable we paid strict attention to maintaining consistent imaging parameters. All 2PLSM images were collected >70 μm below the pial surface in layer I-II of the cerebral cortex. Within individual experiments the depth of imaging, laser power and photomultiplier tube settings were kept within a narrow range. Laser power was generally kept below 40 mW to avoid phototoxicity to the tissue. This is especially important for calcium imaging, as transients can be artificially induced by high laser power (Wang et al.

2006). All the data was analyzed using either ImageJ (National Institute of Health) or custom-made MatLab software (NedLabAnalysis). For calcium imaging, the software allowed simultaneous quantification of fluorescence intensity in multiple regions of interest (ROIs) from an XYT scan with a tracking function (i.e. ROI tracking to correct for XY displacement). To further reduce confounding due to XY or Z displacement (e.g. movement artifact) most calcium indicator intensity traces were also normalized to *Glt1*-eGFP intensity. For volumetric analysis the software used XYZT scans, and quantified the number of pixels over a semi-automated threshold value within a manually defined ROI. The pixels were then added up for each XYZ scan and multiplied by the scale factor to get an estimate of cell volume. The principal limitation of this volumetric analysis was the resolution of 2PLSM, to allow accurate thresholding of the cell. We optimized the resolution by using a high magnification and high numerical aperture lens, adequate laser power, and maximally clear optical media (e.g. thin layer of agarose) in the cranial window.

Electrocorticograms, ion-sensitive microelctrodes (ISMs) and patch clamp

Neuronal activity causes distinct changes in local voltage due to the ion currents associated with action potentials and post-synaptic potentials (Vanderwolf 1992). In most of our 2PLSM experiments we used electrophysiology to monitor neuronal activity in parallel with the astrocyte imaging. However, it is also possible to image both neuronal and astrocyte activity simultaneously with 2PLSM using dyes like Oregon green BAPTA (Dombeck et al. 2007). We largely obtained our recordings by placing a glass microelectrode into the cerebral cortex and completing the circuit with a ground placed in the fluid bathing the brain. The resultant signals were filtered to yield either local field potential or electrocorticogram recordings (Wang et al. 2006). Additionally, electrocorticogram traces can be analyzed both in terms of morphology (e.g. amplitude of whisker electrocorticogram response) and the relative activity in different frequency bands (usually represented as power spectra). Electrocorticogram activity largely represents the sum of pyramidal neuronal activity in the region where the electrode is placed, and increased activity in different frequency bands can represent either wakeful, asleep or anesthetized patterns of neuronal firing **(Table 3)** (Schwilden 2006). These techniques have excellent temporal resolution, and for instance allowed us to record individual EPSPs, but not unexpectedly lack spatial resolution. The accurate placement of electrodes is therefore paramount, as

inconsistent electrode placement between experiments can introduce significant bias. To aid and monitor the placement of these microelectrodes we relied on 2PLSM, which allowed us to visualize the FITC-dextran containing electrodes. It was thus possible to accurately place microelectrodes within a consistent distance of the imaged field.

For a subset of experiments we used ISMs to record changes in extracellular ion homeostasis. ISMs are based on the principle that some hydrophobic resins are selective for certain ion currents (e.g. K^+), and if these resins are placed in the tip of a microelectrode one can record currents that are principally due to the movement of this ion (Nicholson 1993). As with the field electrodes, the ISMs lack spatial resolution and their placement within the brain needs to be accurate. ISMs also have a number of technical issues. For example, over time the resin from the electrode tip leaks, thus reducing sensitivity. It is therefore important to calibrate ISMs before and after each experiment with regard to sensitivity, and discard all recordings where the after-calibration deviates >5%. Moreover, changes in field recordings need to be subtracted from ISM traces to avoid confounding due to local changes in voltage. A field electrode therefore needs to be placed close to, or ideally in the same location as the ISM, which is most frequently achieved by making double-barreled electrodes (Borrelli et al. 1985). Unfortunately, these electrodes have a much higher failure rate than using two single barreled electrodes, as they are more complex to make and the resin can leak out more easily. Finally, ISM resins are never completely selective for the ion they are meant to measure, and can respond to a lesser extent to other ions. This last issue is especially relevant if the ions have a similar hydrated radius and charge. It is therefore important to check the selectivity coefficient for each resin used, and calculate the interference due to the predicted change of other interfering ions so they may be subtracted from the ISM recording (Nicholson 1993). Due to all these pitfalls and limitations we also piloted alternative techniques for measuring extracellular ion changes, including ion- and pH-sensitive dyes (e.g. BCECF, SNARF-4, TAC-Red) (Boyarsky et al. 1993; Mariot et al. 1991; Padmawar et al. 2005). These dyes have the benefit of granting spatial resolution, albeit at the cost of reduced temporal resolution. Although several dyes are commercially available, we were unable to make these chemicals load brain cells sufficiently *in vivo* to allow accurate recordings of ion changes.

Table 3. Characteristics of the different waveforms seen in the electrocorticogram.

Type	Frequency	Physiology	Pathology
δ (delta)	0-4 Hz	Slow wave sleep	Encephalopathy
θ (theta)	4-8 Hz	Drowsiness	Encephalopathy
α (alpha)	8-13 Hz	Relaxed awake	Coma
β (beta)	13-30	Active awake	Sedatives
γ (gamma)	30-100+	Memory	Dementia

For a subset of the experiments experienced electrophysiologists in our lab (Fushun Wang, Qiwu Xu and Ning Kang) performed patch clamp analyses. Briefly, this method that gained its developers Erwin Neher and Bert Sakmann a Nobel Prize in 1991 is based on placing a ~1μm tip glass microelectrode on the cell membrane of e.g. a neuron and applying suction so that a 10^9 (giga) Ω (ohm) resistance seal is formed between the membrane and the electrode (Neher et al. 1978). The high-resistance seal allows the investigator to monitor electrical activity from just a few ion-channels in the little patch of membrane covered by the electrode without interference (noise) from the rest of the cell **(Fig. 18)**. Investigators can either control the membrane potential (voltage clamp) or the movement of ions (current clamp) to measure what changes this induces in the non-clamped parameter, e.g. in voltage-clamp mode you can vary the membrane potential across a range and see what current flow this induces, thus generating an I-V (current-voltage) curve for a particular ion channel (Sakmann and Neher 1984).

There are several variations of patch clamping; including whole-cell where the membrane patch is ruptured allowing the electrode to measure the electrical activity of the whole cell. This method has several advantages over sharp microelectrode recordings used previously (where a very small diameter tip electrode is used to impale the cell); including better electrical access to the cell due to the larger electrode tip diameter. However, the large tip diameter also implies that the whole-cell patch electrode will over a period of >10 min dialyze the contents of the cell (Verkhratsky et al. 2006). Another variation of patch clamping also used in our study is a perforated patch. This is where the electrode is placed on the cell membrane and a giga-Ohm seal is formed, but the membrane patch is not ruptured. Usually agents such as nystatin and gramicidin are used to perforate the membrane patch (as opposed

to antimicrobial agents like amphotericin B), giving the investigator electrical access to the cell that is more selective (depending on what the perforations are permeable to) than with a whole-cell patch (Akaike 1996). A gramicidin patch is for instance very well suited to studying chloride currents, because the perforations are mainly permeable to monovalent cations and uncharged molecules (Kyrozis and Reichling 1995). The drawbacks of a perforated patch are its technical difficulty (the perforated membrane is weakened and a bit unstable), the amount of time it takes for the antibiotics to form adequate perforations (10 - 30 min) and the greater access resistance (= $R_{electrode}$ + $R_{electrode\text{-}cell\ junction}$) that causes less signal-to-noise.

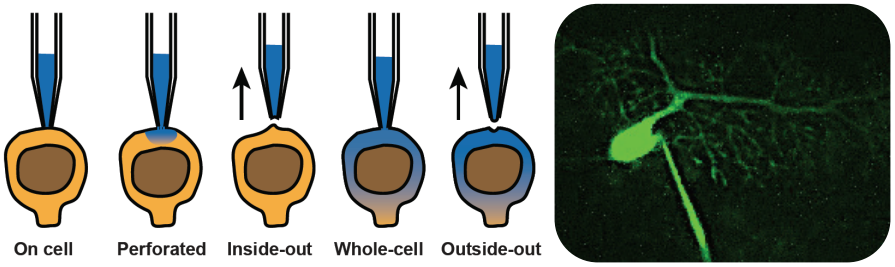

Figure 18. Patch clamp recording. Left: Illustration of various patch clamp techniques outlined in the text. Right: 2PLSM image of a whole-cell patched Purkinje cell outlined with Alexa fluor 488 from the patch micropipette, kindly provided by Qiwu Xu.

Supporting techniques

Gene knock-out or knock-down. Several of the studies in our thesis use gene deletion (KO) or silencing (knock-down) to explore the molecular mechanisms of disease. Generally speaking gene deletion (KO) is accomplished through a sequence of steps, including (Gaveriaux-Ruff and Kieffer 2007): 1) Sequencing and cloning the gene of interest. 2) Altering the sequence of the gene to make it inoperable (that can produce splice variants) or flanking the important exons with sequences (e.g. LoxP) that promote site-specific recombination (e.g. excision or translocation of the flanked exons). 3) Embryonic stem cells are isolated from the mouse blastocyst, grown in vitro, and the altered gene is inserted by homologous recombination using electroporation. At this stage only embryonic stem cells that have taken up the altered gene can be selected if a gene conferring antimicrobial resistance (e.g. to neomycin) has been included in the inserted construct. 4) Embryonic stem cells with the altered gene are then inserted into a recipient mouse blastocyst, generating chimeric offspring, which when bred with wild-type (WT) mice in the next generation will

generate some offspring heterozygous for the deleted or dysfunctional gene. In the case of gene excision using gene floxing (flanked by LoxP sites), a mouse expressing the floxed gene is bred with a mouse expressing Cre-recombinase (potentially under a tissue or cell specific promoter), so that only cells expressing Cre will excise the floxed gene. In contrast to the previous gene deletion strategies where the KO is permanent from birth (called constitutive), it is also possible to make the final recombination step inducible by a drug of choice (e.g. tamoxifen or tetracycline), for instance by using a modified form of Cre-recombinase that requires a drug to activate the enzyme (van der Weyden et al. 2002). The inducible (or conditional) KO strategy has the benefit of allowing deletion of genes that is incompatible with mouse survival into adulthood (Pascual et al. 2005). Additionally, inducible KO avoids the unknown confounding factors associated with developmental adaptation to the constitutive gene deletion.

As an alternative to conventional gene KO, it is also possible to knockdown or silence genes by expressing e.g. short-inhibitory or short-hairpin ribonucleic acid (shRNA), which contain a complimentary sequence to the messenger RNA (mRNA) from the gene of interest (Haas and Sontheimer 2010). There are several benefits to this strategy, including no need to go through multiple generations of mouse breeding, the ability to induce gene knock-down at any stage of development, and gene knock-down often has less cost associated with it than developing and maintaining a separate KO mouse colony. Conversely, the limitations of gene silencing include a much lower and more variable efficiency of 'knock-down' (e.g. 10-70%), challenges with delivery and expression of the silencing RNA construct in the cells of interest (e.g. requires strong highly cell-specific promoter), and relatively high percentage of silencing constructs that work *in situ* not working *in vivo* (Ge et al. 2006; Haas and Sontheimer 2010; Jayakumar et al. 2011a; Koyama et al. 2012). For *in vivo* gene silencing investigators often employ viral vectors that are relatively specific to the cells of interest (e.g. pyramidal neurons), and packaged these with a construct that includes the silencing RNA, a reporter gene (e.g. eGFP), and a sequence recognized by a cell specific promoter (e.g. GFAP). In one of our studies (unpublished), we for instance attempted to use commercially available shRNA to Slc12a2 (coding NKCC1) that has previously been successfully used in glioma cultures. The strategy was to inject mouse pups (e.g. P20) intracortically with high-titer lentivirus (targeting pyramidal cells) expressing Slc12a2 shRNA and eGFP under the pGIPZ promoter (Haas and

Sontheimer 2010). However, eGFP expression was too week to detect, likely due to weak pGIPZ promoter activity *in vivo*. Some authors have circumvented this problem by illustrating not direct eGFP expression in confocal micrographs, but rather antibody against eGFP (Haas and Sontheimer 2010). However, we needed to be able to visualize the eGFP on our electrophysiology set-up so as to patch affected cells, and were thus unsuccessful in this project. Moreover, there is no assurance that reporter gene expression (i.e. eGFP) means effective gene silencing or vice versa, therefore these types of experiments usually require a lot of controls to ensure that observed changes are a result of gene silencing, and e.g. not simply an effect the viral vector. Taken together, although gene silencing is popular in high tier journals as a supplement to pharmacology (to show molecular specificity), this strategy has several pitfalls ensuring that results need to be interpreted with caution.

Whisker stimulation. Unlike humans, mice devote a large proportion of their brain to process information from their whiskers (also called mystifacial vibrissae) (Schubert et al. 2007; Wang et al. 2006). The part of the cerebral cortex in mice that received whisker information has a columnar organization similar to the primate visual cortex, with whisker 'barrels' receiving input from individual whiskers in a 1:1 ratio (Borgdorff et al. 2007). To examine the response of glial cells to physiological sensory stimulation *in vivo*, we therefore adapted a protocol developed by Wang et al. that uses small air puff stimulate the whiskers whilst simultaneously imaging the relevant whisker barrel with 2PLSM (Wang et al. 2006). The benefit of air puff whisker stimulation over for instance electrical stimulation is that it is non-painful, and can thus be used in awake mice. However, other methods such as electromagnetic movement of microbeads or electrical nerve stimulation may be superior overall (Borgdorff et al. 2007). The benefit of whisker stimulation compared to other forms of sensory stimulation (e.g. hindlimb electroshock) is that whisker sensation in mice is a highly developed sensory modality that takes up a large part of the cortex (Winship et al. 2007). Somatotopic mapping of individual whiskers to their respective whisker barrels is also highly specific **(Fig. 19)**. The difficulty with this form of stimulation is to avoid stimulating other whiskers than the one of interest (usually accomplished by trimming them) and to avoid stimulating the face (accomplished by puffing parallel to the snout) (Wang et al. 2006). In conclusion, we found that whisker

stimulation was a good non-invasive way of generating neuronal activation in the sensory cortex.

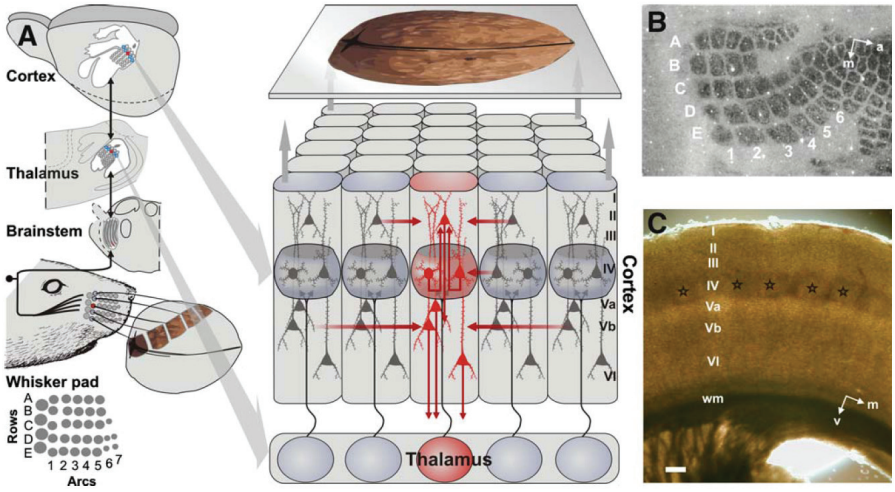

Figure 19. The somatotopic mapping of whiskers to cortical whisker barrels in rodents. **A.** Diagram illustrating the convention for labeling individual whiskers and their projection via trigeminal ganglion cells in the brain stem and thalamic projection neurons to whisker barrels in layer IV of the somatosensory cortex. **B**. Cytochrome oxidase stained tangential section of layer IV barrel cortex. **C.** Dodt gradient contrasted acute coronal section through rodent barrel cortex showing the cortical layers (I-VI) and individual whisker barrels (star). Adapted with permission from Schubert et al. 2007.

Immunohistochemistry. In several of our studies, we used immunohistochemistry to allow the accurate anatomical and cellular localization of putative molecular targets. This technique is based on the principle that when one cuts thin specially preserved slices of brain tissue; these slices can be stained with a primary antibody specific for the molecule of interest. A secondary antibody that binds the primary antibody and is cross-linked to for instance a fluorescent molecule then visualizes the primary antibody (Saper and Sawchenko 2003). Immunohistochemistry has several limitations, including a complete lack of temporal resolution (unless serial immunohistochemistry is performed at different time points). Moreover, the spatial resolution depends directly on the method used to visualize the immunohistochemistry. Confocal immunofluorescence microscopy is, for instance, limited by the aforementioned theoretical limit of resolution for the wavelength of light used. Transmission electron microscopy is, on the other hand, usually only limited by the size of the primary and secondary antibody complex employed for e.g. immunogold labeling (Ottersen et al. 1996). Finally, immunohistochemistry is

primarily limited by the sensitivity and specificity of the antibodies used. Unfortunately, many of antibodies that are commercially available are of poor quality. Several steps are routinely run to control for unspecific labeling, e.g. adding human/bovine serum albumin or milk powder to the antibody solution, omitting primary antibody and reabsorbing the primary antibody solution with the peptide used for immunization (Fritschy 2008). However, many investigators feel one cannot truly know the antibody specificity until tissue from mice where the molecule of interest is knocked out is stained and the staining found to be entirely negative (see paper I).

Laser Doppler Flowmetry. This is an optical technique where a collimated laser beam is split, and the two coherent laser beams are focused on red blood cells passing through blood vessels (Carter 1991). Because the laser scattered from the red blood cells will be Doppler shifted proportionate to the velocity of the cells, it will not be coherent with the incident light and generate interference. This causes the intensity of the reflected light that the device detects to fluctuate with a frequency that is proportional to the Doppler shift and thus the velocity of the red blood cells. The name of this technique is thus a misnomer, as the device actually measures velocity and not flow. Laser Doppler flowmetry as a measure of cerebral blood flow has several sources of error. Most importantly, the optics is dependent on the incident laser light being at right angles to the blood flow that one wishes to measure. Additionally, it is not possible to get an absolute measure of blood flow, but only record changes in blood velocity. Finally, laser Doppler flowmetry is heavily influenced by blood flow in meningeal vessels superficial to the brain, and these vessels may not necessarily directly reflect cerebrovascular changes.

Evans blue extravasation. Evans blue is a chemical dye that has a high affinity for blood albumin, and which fluoresces at 680 nm when excited between 470-540 nm (Vise et al. 1975). The BBB is largely impermeable to macromolecules such as albumin. Systemic administration of Evans blue is therefore frequently used as an assay of BBB opening in disease states (Kaya and Ahishali 2011). The principal limitation of this technique for studying BBB permeability is that not all BBB opening may be characterized by increased permeability to macromolecules such as albumin. A more extensive characterization of BBB permeability thus often involves using other chemicals of different sizes. Finally, it can be beneficial to use Evans blue

pre-bound to albumin as in our study, since some of the chemical may remain unbound to albumin and can cross the BBB.

Brain water content. To obtain a measure of overall brain water content we used the extensively published wet/dry-brain weight method. The method is based on the comparison of brain weight immediately after removal from the animal (wet weight) with the brain weight after all water content has been evaporated in an 80^{o}C oven for 24 hours (dry weight). Percent brain water content can then be computed by: wet weight-dry weight/wet weight. The main issue with this method is the reproducibility depends heavily on brain extraction, drying and weighing having been conducted in the exact same way. Delays in brain extraction can for instance rapidly reduce brain water content through evaporation (Haj-Yasein et al. 2011b).

Intracranial pressure (ICP). When significant brain edema is allowed to accumulate, pressure will begin to build up inside the rigid confines of the skull. This increase in ICP can be monitored clinically in neurosurgical patients by the implantation of pressure probe through a small craniotomy. We employed a similar approach in our mice, and implanted a pressure probe in the cerebral hemisphere to monitor ICP changes during conditions thought to elicit brain edema (Statler et al. 2001). ICP has a characteristic waveform pattern reflecting the pressure fluctuations in the cardiac cycle. The sources for error when using ICP probe include failure to calibrate the probe properly (cannot get absolute reading), failure to allow the ICP recording to stabilize (results in drift) and manipulation of the transducer wire (causes false ICP fluctuations). Finally, to accurately interpret ICP recordings it is essential to also record mean arterial pressure. We did this by implanting a catheter in the femoral artery connected to an external pressure probe. Using ABP it is possible to calculate cerebral perfusion pressure, using the formula: cerebral perfusion pressure = mean arterial pressure – ICP. Normally, cerebral blood flow stays within a narrow range despite variation in blood pressure due to cerebrovascular autoregulation. However, when ICP reaches critical levels cerebral perfusion pressure can become insufficient to supply adequate blood to the brain.

NMR spectroscopy. Atomic isotopes that contain an odd number of protons and neutrons act as small magnets (e.g. ^{1}H). When these isotopes are placed in a strong

externally applied magnetic field, their magnetic poles will tend to align with the field. NMR spectroscopy exploits the principle that if a radiofrequency pulse of a specific frequency is applied to this magnetic field it will tend to disturb the alignment of the isotopes (Behar et al. 1993). The frequency required is the resonance frequency of the isotope, and this will typically bring the isotope to a higher energy state. The isotope will after a time emit the energy in the form of electromagnetic radiation to return to its alignment in the magnetic field. The resonance frequency not only varies from isotope to isotope, but each individual isotope will also have different resonance frequencies depending on their atomic microenvironment. The latter is termed a chemical shift, and can be referenced to a 'standard' where there is little distortion from nearby atoms. In our study, we used ^{1}H-isotope that is abundantly present in biological tissue and water. When the ^{1}H-NMR signal intensity is plotted against chemical shift ('NMR spectrum'), several peaks representing ^{1}H present in different molecules (e.g. lactate, glutamate). A major issue with ^{1}H-NMR is that biological tissues are largely made up of water, generating a large ^{1}H-NMR signal. This is usually addressed by dehydrating tissues and reconstituting them with deuterized (^{2}H) water. Standard ^{1}H-NMR is therefore incompatible with *in vivo* analyses, and is performed on homogenated tissue. Because it uses homogenates, however, care needs to be taken to stop enzymatic reactions immediately after extracting the tissue. This is usually achieved by freezing the tissue, followed by denaturing enzymes with a strong acid. Another source of error is that ^{1}H-NMR spectra are very sensitive pH or free protons, and changes in pH can cause some ^{1}H-NMR peaks to overlap. It is therefore essential to ensure consistent pH between specimens, and use the pH ideal for resolving the peaks of interest without overlaps. Finally, ^{1}H-NMR results are frequently reported as concentrations of molecules of interest per unit brain volume. However, NMR can only detect relative amounts of molecules from the signal intensities, and concentrations need to be inferred e.g. by using a standard. This latter step can also introduce some variability to the results (Zwingmann et al. 2003).

Disease models

Acute hyponatremic brain edema: Hyponatremia is a reduction in the concentration of sodium in the blood. When this occurs acutely it leads to the accumulation of water in the brain; termed osmotic brain edema (Manley et al. 2000; Verbalis 2010). Common causes of hyponatremia in a clinical setting include salt loss in marathon runners,

aggressive intravenous fluid therapy in hospitalized patients and endocrine disorders such as syndrome of inappropriate anti-diuretic hormone (Verbalis 2010). We adapted a method to induce hyponatremic brain edema in mice by acutely injecting 20% (200 mL kg^{-1}) of the mouse body weight as distilled ion-free water i.p. This model generates robust brain edema, and has previously been used by several other groups as a model of osmotic brain edema (Nase et al. 2008). Previous groups have also added anti-diuretic hormone (vasopressin) analogue desmopressin (DDAVP) to the infused water, but in our hands this was unnecessary and might unintentionally alter AQP4 function (Manley et al. 2000; Moeller et al. 2009; Niermann et al. 2001). Our *in vivo* model of hyponatremic brain edema in mice closely resembles related conditions in humans except for one key aspect. Clinical cases of hyponatremia frequently have a more protracted time-course, with more potential for CNS and extra-CNS (e.g. renal) compensation. Unfortunately a longer time course might be more difficult to image accurately, as calcium indicators are internalized and metabolized in the course of 2-3 hours. These sets of experiments therefore represent a compromise between a more ideal model of hyponatremia, and a model that progresses rapidly enough to allow study by 2PLSM.

Hepatic encephalopathy (HE): HE is brain impairment, ranging from confusion to coma, caused by the accumulation of waste products including ammonia in liver failure (Butterworth et al. 2009). In a clinical setting, hepatic encephalopathy is most frequently seen as a complication of alcoholic liver disease or as acute drug-induced liver failure (e.g. paracetamol overdose). We used the liver toxin azoxymethane to induce acute liver failure and consequent hepatic encephalopathy in mice. Azoxymethane was first discovered in 1960 in Guam, and was isolated as the active ingredient that causes ingested cycad palm nuts to be carcinogenic and hepatotoxic (Bélanger et al. 2006; Matkowskyj et al. 1999). This chemical model of HE has several benefits, in that it is very reproducible and encompasses all the relevant clinical and biochemical features of human HE. Azoxymethane is also one of the few models of HE that can be used in mice, which was an important prerequisite for our study that intended to use transgenic animals **(Fig. 20)** (i.e. *Cx3Cr1*-eGFP) (Bélanger et al. 2006). Conversely, surgical models of HE (e.g. portocaval anastomosis) usually require the use of larger animals (Butterworth et al. 2009). However, in all chemical models of HE one cannot exclude that the drug itself has some CNS effects.

Moreover, most human HE is due to entirely different liver toxins (e.g. alcohol, paracetamol), and different toxic substances can generate quite disparate phenotypes. Finally, alcohol related HE frequently occurs in the context of acute-on-chronic liver failure, which again this model does not adequately depict (Butterworth et al. 2009).

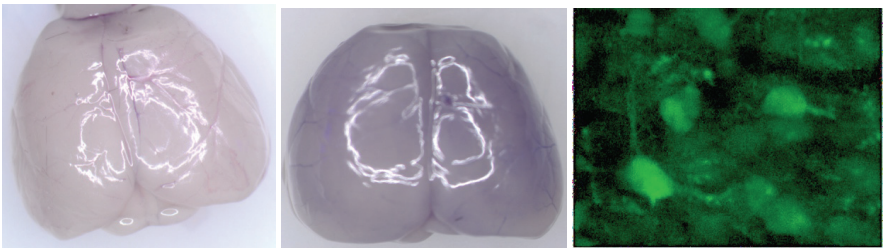

Figure 20. The phenotype of azoxymethane-induced hepatic encephalopathy. Photographs of Evans blue injected mouse brains illustrating the increased BBB permeability in azoxymethane-induced HE; left (control) and middle (hepatic encephalopathy). Right: Hyperbilirubinemia in hepatic encephalopathy causes autofluorescent labeling of brain cells that can be imaged by 2PLSM *in vivo* (unpublished observation).

Acute hyperammonemia encephalopathy: Hyperammonemic encephalopathy is neurological dysfunction that results from elevated blood ammonia levels, and in a clinical setting this is most frequently seen in patients with liver disease (Cagnon and Braissant 2007). However, patients with liver failure also have a plethora of other biochemical disturbances, which likely contribute to the neurological phenotype and make it difficult to dissect out the role of ammonia. We therefore chose to examine a model of isolated acute hyperammonemia using a X-linked recessive condition called ornithine transcarbamylase (*Otc*) deficiency (Ratnakumari et al. 1992). Because the enzymatic detoxification of ammonia in the liver via the urea cycle is compromised, both mice and humans with this condition are prone to developing rapid rises in plasma ammonia. Although these *Otc* mice can develop spontaneous hyperammonemic episodes, or dietary-induced episodes (e.g. protein load), we chose to induce acute hyperammonemic encephalopathy by giving a parenteral ammonia load (Moscioni et al. 2006; Ye et al. 1997). This ensured both reproducibility and a short time course ideal for 2PLSM imaging. The plasma ammonia concentrations we recorded using this model was within the range reported for clinical cases (Cagnon and Braissant 2007). However, a major limitation of this model is that time course ammonia intoxication may be more hyperacute than that seen in human cases.

8. SUMMARY OF RESULTS

I. Critical role of aquaporin-4 (AQP4) in astrocytic Ca^{2+} signaling events elicited by cerebral edema

Hypo-osmotic brain edema is a potentially fatal condition where swelling occurs as a result of a decreased concentration of osmolytes such as sodium. We used 2PLSM to explore the role of astrocyte swelling and volume related calcium signaling in this condition.

First, we showed that acute hypo-osmotic stress causes brief (5-10 min) astrocyte swelling *in situ*, followed by a prolonged regulatory volume decrease. The initial swelling, but not the volume decrease, was AQP4-dependent. Additionally, severe osmotic stress led to irreversible astrocyte swelling and cell lysis. Second, we demonstrated that hypo-osmotic brain edema increased the frequency and prolonged the duration of astrocyte calcium transients, which was also AQP4-dependent. We therefore hypothesized that *Aqp4* deletion suppressed the calcium response by limiting water influx and thus volume changes associated with hypo-osmotic stress. Third, we found that applying purinergic P2 receptor antagonists suppressed calcium transients evoked by astrocyte swelling. Finally, we showed that cultured $Aqp4^{+/+}$ but not $Aqp4^{-/-}$ astrocytes exposed to hypo-osmotic stress released significant amounts of ATP.

We concluded that during hypo-osmotic brain edema AQP4 is necessary for astrocytes to sense osmotic changes and generate volume related signals. These included calcium transients evoked by ATP release that would contribute to a worse clinical outcome by triggering the release of excitotoxic neurotransmitters.

II. *NADH fluorescence imaging indicates effect of aquaporin-4 deletion on oxygen microdistribution in cortical spreading depression*

CSD is a wave of tissue depolarization linked to migraine, which is accompanied by tissue hypoxia in regions furthest away from the vasculature (microwatershed areas). We used 2PLSM imaging of intrinsic NADH fluorescence during CSD to reveal a previously unrecognized role of AQP4 in cortical oxygen distribution.

We found that deletion of the astrocyte water channel *Aqp4* causes a selective increase of NADH fluorescence in microwatershed areas, indicating greater hypoxia in these regions. Using laser Doppler flowmetry and oxygen sensitive microelectrodes we demonstrated that this hypoxia is not a result of decreased overall oxygen or blood supply. Next, we tested whether *Aqp4* deletion worsens oxygenation through increasing the metabolic demand. The profound increase in $[K^+]_o$ that is the hallmark of CSD is believed to cause a unique strain on ion and volume homeostasis in the brain. Using potassium ion sensitive microelectrodes we show that *Aqp4* deletion slows $[K^+]_o$ recovery, which might cause oxygen overuse. Alternatively, our data could indicate that AQP4 acts as a gas channel, facilitating oxygen diffusion from the vasculature to microwatershed regions.

In conclusion, our results suggest a novel role for AQP4 in oxygen micro-distribution during CSD. Our data indicate that this AQP4 related hypoxia is either a result of AQP4 mediated gas diffusion or AQP4 facilitated potassium ion transport.

III. *General anesthesia selectively disrupts astrocyte calcium signaling in the awake mouse cortex*

General anesthesia is thought to induce sedation and unconsciousness by exclusively interfering with neuronal signaling. However, the effects of anesthesia on glial cells have not previously been systematically explored. We therefore proceeded to use 2PLSM to explore the effect of several commonly used anesthetics on astrocyte calcium signals in awake behaving mice.

We found that all three anesthetics tested in our study potently suppressed spontaneous calcium signals both in the soma and processes of neocortical astrocytes. The anesthetics also altered the pattern of astrocyte calcium signaling; from highly synchronized in the awake state to largely unsynchronized with anesthesia. Additionally, we demonstrated that calcium signals evoked by physiological sensory (whisker) stimulation were also strongly suppressed by anesthesia. Several lines of evidence indicate that our observations were not secondary effects of the anesthetics silencing neuronal activity: a) Astrocyte signals were suppressed by lower doses of anesthesia than those required to block neuronal activity. b) A local blockade of neuronal activity using TTX or CNQX/AP5 completely suppressed neuronal but not glial signals. c) Similar to previous studies we observed a delay of 0.5-5s between cortical neuronal activation and the astrocyte calcium transients. This delay suggests that astrocyte signaling may be mediated by extra-synaptic events. Finally, we show that the anesthetic effect on astrocytes could be explained by a direct impairment of calcium mobilization via IP_3R2-dependent mechanisms, as astrocyte calcium signaling in response to local agonist (ATP) was also selectively reduced by anesthesia.

In conclusion, anesthetics appear to selectively suppress astrocyte calcium signals. It is therefore possible that some of the sedative effects of these drugs may be mediated via glial targets that are not fully exploited by current pharmacology.

IV. *Paravascular microcirculation facilitates rapid lipid transport and astrocyte signaling in the brain*

Unlike peripheral organs, the brain is entirely devoid of a separate lymphatic system to resorb interstitial fluid and transport lipids. A recent study identified a paravascular circulation of hydrophilic molecules in the anatomically distinct PVS. However, the paravascular transport of lipophilic substances has not been explored *in vivo*. Our study aimed to address two related unanswered questions: does the PVS mediate rapid lipid transport and can the PVS act as a separate signaling compartment to coordinate glial communication?

We administered lipid tracers into subarachnoid CSF via the cisterna magna and demonstrated that they move rapidly through the brain parallel to blood vessels. We found that the circulation of lipid tracer was highly restricted to the PVS, indicating that the PVS may serve as a dynamic barrier to lipid diffusion into the brain parenchyma. The lipid tracer entered the brain via a para-arterial and exited via a para-venous route. We were able to enhance the intra-cellular delivery of lipophilic tracer molecules by surgically depressurizing the subarachnoid space. Finally, depressurizing the PVS caused an impairment of desynchronized calcium signaling. To further test this hypothesis of the PVS acting as signaling compartment, we took advantage of one of the most widely used astrocytic calcium wave agonists - ATP. ATP was injected into both the PVS and surrounding parenchyma. Interestingly, the propagation of the calcium wave in astrocytes elicited by PVS ATP administration was much faster and covered a larger diameter than intraparenchymal administration.

Taken together, we demonstrated a novel pathway for the rapid and highly selective microcirculation of lipophilic molecules through paravascular CSF. We show that the PVS acts as a signaling highway between astrocytes, and when knocked causes a pathological pattern of glial communication.

V. *Real-time analysis of microglial activation and motility in hepatic and hyperammonemic encephalopathy*

The role of microglial activation and/or dysfunction in hepatic encephalopathy is incompletely understood and has only been studied *ex vivo*. We used 2PLSM in *Cx3cr1*-eGFP mice to image dynamic changes in microglial morphology and surveillance behavior in real-time.

We used a model of isolated hyperammonemia that generated robust but reversible encephalopathy (lethargy, ataxia and myoclonic seizures). Contrary to some previous reports, we found no BBB opening or brain edema in this condition. Additionally, we were unable to detect any microglial activation or change in surveillance behavior. Next, we adapted a chemical mouse model of hepatic encephalopathy using azoxymethane, characterized by a slower plasma ammonia increase. Phenotypically the mice progressed through successive stages of encephalopathy including lethargy, ataxia and finally coma, but no seizures. Contrary to the acute hyperammonemia model, we found both increased BBB permeability (leakage) and brain edema at the coma stage. Using 2PLSM imaging, we demonstrated microglial activation and decreased microglial surveillance during the coma stage, but not prior to the onset of neurological dysfunction.

In conclusion, our data suggest that microglial activation does not contribute to the initial neurological dysfunction seen in isolated hyperammonemia. Conversely microglial activation is present during the coma stage of hepatic encephalopathy, where it coincides with BBB opening and brain edema. Microglial activation may therefore contribute to overall mortality in hepatic encephalopathy by accelerating the progression to brain edema and coma.

VI. *Ammonia compromises astrocyte potassium buffering and impairs neuronal inhibition without causing swelling in vivo*

Ammonia is both a vital building block and a lethally neurotoxic compound if allowed to accumulate. To explore the molecular mechanisms underlying the acute neurotoxicity of ammonia we employed a combination of biochemical, electrophysiological, genetic and optical imaging methods *in vivo*.

We chose to use a mouse model of congenital *Otc* deficiency, a childhood condition in which liver ammonia detoxification is dysfunctional, causing elevated plasma ammonia. *Otc*$^{spf\text{-}ash}$ mice have cognitive and motor deficits at baseline that significantly worsened following an ammonia challenge and were accompanied by generalized seizures. We showed that ammonia induced seizures originate in the cortex, and are associated with a dysfunction of inhibitory neurotransmission. Using *in vivo* 2PLSM we demonstrated that this neuronal dysfunction was secondary to an impairment of astrocyte calcium signaling, $[K^+]_o$ handling, but not astrocyte swelling (as previously hypothesized). This severe dysfunction of astrocyte potassium buffering was likely due to the competition of ammonium with potassium for membrane transport. Finally, we showed that the elevated $[K^+]_o$ and/or $[NH_4^+]_o$ increase the electrochemical gradient Cl^- import via NKCC1, depolarizing the reversal potential of $GABA_A$ receptor (E_{GABA}). Using either the highly selective NKCC1 antagonist bumetanide or *Slc12a2* KO, we were able to rescue the shift in E_{GABA} and reverse the disease phenotype.

In conclusion, we demonstrate a novel molecular mechanism for the acutely neurotoxic effects of ammonia, which are primarily results of a profound dysfunction astrocyte ion homeostasis. By specifically targeting this disease mechanism we were able to treat this fatal childhood neurological disorder.

9. DISCUSSION AND FUTURE DIRECTION

In the last 20 years the application of new experimental tools such as calcium imaging and 2PLSM has revealed that normal brain function requires both neuronal and glial cells acting in concert (Nedergaard and Verkhratsky 2012). The late realization that glial cells play an active role in brain function likely reflects the unique challenges faced when studying glial neurobiology. For instance, glial research requires techniques offering both high temporal and spatial resolution, as well as being sensitive to tissue distortion or injury (Agulhon et al. 2012). Although several new techniques such as 2PLSM have been applied to glial research in recent years, many of the basic disease models that have been studied are adaptations of neurocentric research paradigms. Such models, including acute hippocampal slices and primary cell culture, may not be equally representative of glial physiology (Sun et al. 2013). In an attempt to overcome these obstacles and increase the translational potential of our research, we primarily employed *in vivo* animal models. The following is a discussion of what our studies add to current understanding of glial neurobiology, the critical limitations of the data and the important questions that remain open for future study.

AQP4 and astrocyte volume homeostasis. Since the Nobel-prize winning set of first experiments, it has been known that cells expressing aquaporins undergo rapid volume change in response to osmotic stress (Preston et al. 1992). Several prominent studies have subsequently suggested that by virtue of their high AQP4 expression, astrocytes are more likely to swell than other brain cells. AQP4 has therefore been suggested as a novel therapeutic target in brain edema (Amiry-Moghaddam and Ottersen 2003; Manley et al. 2000). However, the data supporting this hypothesis have several limitations, including using reduced preparations (e.g. cultured astrocytes) and post-mortem studies of cell volume (e.g. electron microscopy). Additionally, studies of *Aqp4* KO mice have revealed that the water channel may be either beneficial or detrimental depending on the type of brain edema elicited (Papadopoulos and Verkman 2007). Finally, imaging studies that have attempted to show astrocyte swelling in living tissue have either had technical limitations (Nase et al. 2008) (did not assess tissue perfusion) or have not found significant volume change (Risher et al. 2012; Takano et al. 2007; Zhou et al. 2010). Could there more to the story than AQP4 rendering astrocytes prone to passive swelling? Since the 1980s

it has been known that primary cultured astrocytes respond dynamically to hypo-osmotic stress, first swelling and then undergoing regulatory volume decrease (RVD) (Kimelberg 1987; Olson et al. 1986). The latter process is incompletely understood, but believed to involve the activation of volume-regulated channels, leading to the efflux of amino acids, ATP, glutamate, K^+ and Cl^-. Although volume-regulated anion channels can be inferred using electrophysiology, their actual molecular identity is still unknown (Okada et al. 2009; Takano et al. 2005).

In an attempt to address the role of AQP4 in astrocyte volume regulation, we developed a method for high-resolution astrocyte volumetry in acute cortical slices using 2PLSM. Similar to the original *in vitro* studies, we found that the response of astrocytes to hypo-osmotic stress is dynamic. We observed a very brief AQP4-dependent initial swelling, followed by robust RVD that was nominally AQP4-independent. The volume dynamics we observed *in situ* were even faster and smaller than those previously reported *in vitro*. Thus at least in the context of healthy brain slices, astrocytes are capable of very tight volume control that is AQP4-dependent. Conversely, when the degree of osmotic stress was increased, astrocytes underwent passive AQP4-dependent swelling before inevitable cell lysis.

However, our study has several limitations. First, we employed an *in situ* and not *in vivo* model to achieve higher-resolution volume measurements in a setting where we could control osmotic stress precisely. Conversely, the astrocytes were exposed to trauma in the cutting process, had depressurized blood circulation and were derived from young mice that express a different subset of proteins (Sun et al. 2013). Our results also showed that the type of astrocyte response depended on the degree of osmotic stress and the health of the tissue. All of these factors may contribute to altered astrocyte volume dynamics, perhaps resulting in a slower RVD than *in vivo*. We suggest that the lack of direct evidence of astrocyte swelling and RVD *in vivo* may reflect the high speed at which these events occur in intact perfused brain (Takano et al. 2007; Zhou et al. 2010).

Our results raise several new questions. First, do astrocytes swell and/or undergo RVD *in vivo?* As the temporal and spatial resolution of imaging improves, we may be able to better address this question, and also examine volume changes in microdomains (i.e. individual processes) (Haj-Yasein et al. 2012). The polarized AQP4 distribution in endfeet could indicate that this microdomain senses or modulates volume changes associated with fluctuations in blood flow. Additionally,

the high AQP4 expression in astrocytes but not neurons could imply a specialized function in rapid and tight volume regulation, instead of the aforementioned interpretation that astrocytes swell easily. Hence, if astrocyte swelling is not responsible for the brain edema observed in hypo-osmotic conditions, could the increase in tissue water content reflect neuronal swelling? It is conceivable that in the evolutionary division of labor between astrocytes and neurons, that the latter have sacrificed tight volume regulation to attain more specialized signaling functions. Astrocytic RVD may represent a compensatory mechanism for this and avoid detrimental extracellular space shrinkage (with increased ion and neurotransmitter concentrations)? If AQP4 does not solely mediate increased brain edema through facilitating astrocyte swelling, then why is *Aqp4* deletion beneficial in these conditions? Could the increased and pathological astrocyte calcium activity observed in our study, with associated release of excitotoxic transmitters, explain some of this phenotype? The answers to these questions will be essential when designing new therapies for brain edema targeting AQP4 (Amiry-Moghaddam and Ottersen 2003). Finally, what is the molecular identity of volume-regulated anion channels in astrocytes? The answer to this question may be closely related to current contention around the notion of gliotransmission and connexin hemichannels, as neuronal firing causes brisk extracellular space shrinkage and several of the molecules released by volume-regulated anion channels have direct actions on neurons (Okada et al. 2009).

AQP4 and cerebral oxygen microdistribution. CSD is a curious and highly reproducible phenomenon where a self-sustaining cortical wave of neurodepression and depolarization can be elicited by focal cortical application of concentrated KCl (Leao 1947). Although the relationship is not clear, CSD has been linked the initiation of migraine headaches, often being cited as an electrochemical correlate of the migraine aura (Lauritzen et al. 2011). Similar self-sustaining waves of spreading depolarization can also be elicited in a range of other neurological conditions, including stroke (anoxic depolarization), traumatic brain injury, intracerebral and subarachnoid hemorrhage (Lauritzen et al. 2011). Additionally, CSD pathophysiology shares several features with epilepsy. Both are episodic disorders that have been linked to mutations in ion channels or transporters that alter neuronal excitability (Takano and Nedergaard 2009). Experimentally, it is possible to trigger either seizures or CSD *in vivo* with intermediate (10-20 mM) or high (>50 mM) potassium

concentrations, respectively (unpublished observations). CSD therefore appears to occur only when local $[K^+]_o$ reaches a threshold that is such a large strain on ion homeostasis that all neurons in an area remain depolarized and refractory for a sufficient time to prevent recurrent excitatory loops arising.

Several studies have suggested that vasoconstriction and impaired neurovascular coupling may explain parts of the hypoxia and potassium dyshomeostasis seen in CSD (Chuquet et al. 2007; Piilgaard and Lauritzen 2009). However, CSD is initially characterized by significant global and capillary-level hyperemia when the tissue is most hypoxic in animal studies (Lauritzen and Fabricius 1995; Takano et al. 2007). The almost therapeutic effects of anesthesia in CSD might explain part of this inconsistency between awake human and anesthetized animal studies. General anesthesia reduces neuronal exciteability, decreases cerebral metabolic rate and likely as a consequence reduces baseline blood flow so that the initial hyperemia response to CSD becomes more obvious (Lauritzen et al. 2011; Sonn and Mayevsky 2006). Taken together, insufficient blood supply does not appear to cause the initial hypoxia seen in CSD.

As tissue depolarization precedes the hypoxia this in turn suggests that the inadequate oxygenation is a result of the large the metabolic strain of potassium re-uptake (presumably via the NKA). NADH imaging demonstrates that this excess metabolic activity occurs primarily close to blood vessels, effectively depriving areas far from the circulation of oxygen (i.e. microwatersheds). Conversely in anoxia, tissue hypoxia precedes the wave of depolarization and there is no characteristic biphasic pattern of NADH signals, such as that seen in CSD (Takano et al. 2007). Subsequent NADH studies have also shown that mild hypoxemia or increased neuronal activity can also be used to reveal these geometrically shaped biphasic NADH responses. These fundamental observations are likely a biochemical (NADH) correlate of the theoretical Krogh oxygen diffusion cylinders that surround oxygen-rich vessels (i.e. arterioles). Moreover, these limits of oxygen tissue diffusion likely explain key aspects of microvascular anatomy, such the ‘cylinder’ of low capillary density surrounding oxygen rich arterioles in brain and retina (Kasischke et al. 2011). Since the physical limitations of oxygen diffusion and potassium re-uptake are so fundamental to the vascular microanatomy of nervous tissue, we therefore asked whether any molecular adaptations exist to improve microwatershed oxygenation.

Using *in vivo* NADH imaging we showed that during the unique metabolic strain elicited by CSD, AQP4 is necessary for efficient oxygenation of watershed areas. Our observations have several limitations and potential explanations. First, this study was carried out in anesthetized animals, where neuronal excitability would be strongly affected by the choice of anesthetic (i.e. urethane in this case), which might confound the results (Sonn and Mayevsky 2006). However, CSD is arguably such an overwhelming phenomenon that it should be less biased by anesthetics than for instance seizures (Sonn and Mayevsky 2006). Second, ours and other recent NADH-studies have unfortunately lacked cellular resolution, so we are unable to say what cell types become most metabolically compromised. Conversely, the morphological data from Takano et al. seem to indicate that neurons, which show swelling and loss of dendritic spines, are more severely affected than astrocytes (Takano et al. 2007). Third, our study was conducted in constitutive *Aqp4* KO mice, and AQP4 expression in other cells or organs could hypothetically explain the excess hypoxia. On the other hand, recent work on glial conditional *Aqp4* KO has revealed that these mice have an almost identical phenotype (although CSD has not been explored) (Haj-Yasein et al. 2011c).

Finally, given that we detected a hyperemic response similar to Takano et al. (i.e. adequate blood supply), there are two competing hypothesis that could explain our results. 1) AQP4 may be necessary for the energy efficient function of potassium transporters, such as NKA, by rapidly dissipating any osmotic gradients that are built up. Other forms of AQP4-facilitated potassium transport (e.g. Kir4.1 mediated spatial buffering) are likely to play a lesser role, as the $[K^+]_o$ increase is so global that redistribution would be ineffective (Padmawar et al. 2005). 2) Alternatively, the central pore formed by AQP4 tetramers may enhance the O_2 permeability of astrocyte membranes. Aquaporin-assisted gas diffusion is a controversial hypothesis, but one that may be particularly relevant in a subset of membrane microdomains such as the astrocytic endfeet. The protein density in endfoot membranes is extremely high, mainly due to AQP4 orthogonal arrays, and this may decrease the rate of O_2 diffusion across the lipid bilayer (Wang et al. 2007). Per unit weight brain and retinal tissue have the highest oxygen consumption in the body (Kur et al. 2012). The AQP4 central pore could therefore represent an evolutionary adaptation to enhance oxygen diffusion across protein-enriched membranes such as astrocytic endfeet. Hypothetically AQP4-

assisted O_2 diffusion would increase the size of arterial Krogh cylinders, and improve watershed oxygenation (**Fig. 21**). However, the hypothesis that aquaporins increase gas diffusion across the lipid bilayer is still very contentious, and unfortunately our data cannot conclusively differentiate this hypothesis from the alternative ion-transport model (Fang et al. 2002; Musa-Aziz et al. 2009; Wang and Tajkhorshid 2010).

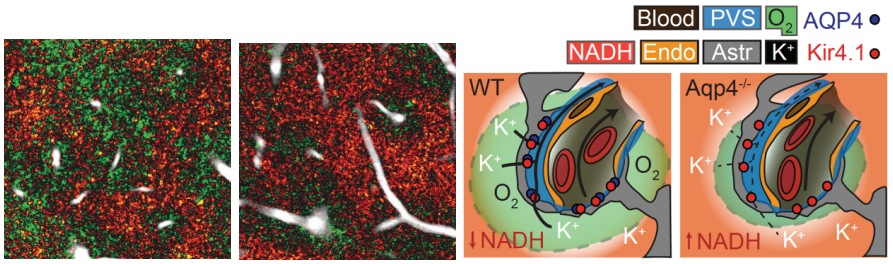

Fig 21. Effect of AQP4 deletion on cortical oxygenation. Left 2 panels: Representative false color images of NADH signal intensity in cortex of WT and AQP4 KO mice during CSD. FITC-dextran labeled vasculature is shown in white. Key: red represents +60% and green -60% NADH signal intensity normalized to baseline. Right 2 panels: Illustration of the hypothetical interplay between AQP4, potassium buffering and microwatershed oxygenation in CSD.

Astrocyte calcium signaling in wakefulness and anesthesia. In 1990 Cornell-Bell et al. showed that astrocytes respond to glutamate by generating waves of increased intracellular calcium (Cornell-Bell et al. 1990). This seminal study opened the possibility that astrocytes might contribute to synaptic signaling on an equal footing to neurons, leading to the tripartite synapse hypothesis (Araque et al. 1999). Using 2PLSM imaging this hypothesis has subsequently been tested in *in vivo*, where it was demonstrated that astrocytes respond to physiological sensory stimulation in a glutamate-dependent fashion (Wang et al. 2006; Winship et al. 2007). However, most of our current understanding of astrocyte calcium signaling still derives from cultured astrocytes, brain slices or anesthetized whole animals. Because of inherent limitations in each of these methods, several investigators have recently begun to question the fundamental tenets of the tripartite synapse model (Agulhon et al. 2008; Nedergaard and Verkhratsky 2012). The main receptor (mGluR5) implicated in astrocyte-neuronal signaling is, for instance, only expressed in young mice used for acute brain slices (Sun et al. 2013). More recently, two groups have independently developed methods to image glial calcium signals in the cerebellum and motor cortex of awake head-restrained mice (Dombeck et al. 2007; Nimmerjahn et al. 2009). Both these studies found greater spontaneous calcium activity that was highly synchronized, in

stark contrast to the individual infrequent calcium signals seen in anesthetized mice. We therefore proceeded to image astrocyte calcium activity in the sensory cortex of awake and anesthetized mice, to see if this would provide further clues as to 1) the direct effects of anesthetics on astrocytes and 2) the nature and mediators of physiological astrocyte calcium signals.

To start with the first question, we asked whether anesthetics might mediate some of their sedative effects via astrocytes, instead of neurons. General anesthetics are a class of sedative drugs used to induce a reversible sleep-like loss of consciousness (hypnosis), amnesia, immobility and insensitivity to painful stimuli (analgesia). The principal targets for the sedative effects of these drugs are thought to be neuronal receptors or channels, but recently some anesthetics have also been reported to affect astrocyte signaling *ex vivo* (Mantz et al. 1993; Miyazaki et al. 1997; Tian et al. 2005; Yang et al. 2008). Our data demonstrate that: 1) Three commonly used anesthetics with putatively different neuronal targets all cause a similar global suppression and desynchronization of astrocyte calcium signals. 2) Anesthesia begins to affect astrocyte before neuronal signaling, although this result should be interpreted a bit more cautiously as we are comparing astrocyte calcium imaging with electrical neuronal activity. 3) Anesthesia also suppresses astrocyte calcium signals elicited by sensory stimulation and direct agonist (ATP) application.

The biggest challenge with interpreting our data is distinguishing the direct effects of anesthesia on astrocytes from those that occur secondary to neuronal changes. Perhaps the strongest argument supporting a direct effect of anesthesia on astrocytes, was the marked suppression of agonist-evoked calcium responses. ATP application is known to trigger astrocyte calcium transients without requiring neuronal firing (Cotrina et al. 1998). Our results are also supported by previous *in vitro* work that has demonstrated anesthesia can directly impair astrocyte calcium mobilization and signal propagation (Mantz et al. 1993; Miyazaki et al. 1997; Yang et al. 2008). Thus, in conclusion, our findings have two important implications with regards to future research: 1) Further study on the effects of anesthesia on astrocyte signaling is needed, as this could lead to a better understanding of current anesthetic agents and more important reveal novel glial pharmacological targets. 2) We also strongly suggest that future studies of astrocyte calcium signaling approach the use of anesthesia cautiously, as they can fundamentally confound results.

Another question we addressed in our study is what characterizes physiological calcium signaling in the awake cortex. Our study revealed a more than 10-fold greater frequency of spontaneous calcium transients in awake than anesthetized animals, which were highly synchronized, and appeared more like sudden bursts than the typical waves described *in vitro*. The pattern of calcium activity we observed in the somatosensory cortex was very consistent with what the two previous awake imaging studies from motor cortex and cerebellum (Dombeck et al. 2007; Nimmerjahn et al. 2009). Moreover, similar synchronized bursts across hundreds of astrocytes can also be elicited in lightly anesthetized animals with whisker stimulation (Wang et al. 2006). In our study we expand on these observations, and showed that sensory-evoked astrocyte calcium signals disappear altogether with increasing doses of anesthesia (Schummers et al. 2008). Additionally, we found that sensory-evoked calcium signals occur at a delay of 1-5 s relative to the firing of cortical neurons, and that these responses are entirely dependent on IP_3R2 signaling (Dombeck et al. 2007; Nimmerjahn et al. 2009; Wang et al. 2006). Conversely, spontaneous and evoked astrocyte calcium signals were highly resistant to a blockade of local purinergic or glutamatergic activity (using TTX, PPADS/suramin or CNQX/AP5), as has also been reported in cerebellar Bergman glia (Nimmerjahn et al. 2009). At first glance these observations appear to challenge several key elements of the tripartite synapse model, which predict that a local neuronal or purinergic blockade abrogates astrocyte signals.

However, there are several important considerations with ours and the previous two awake imaging studies, which may help explain these results. First, our imaging was conducted only in layers 1 and 2 of the cortex, and our electrophysiology suggested that surface drug application primarily affected these layers. It is therefore possible that astrocyte calcium signals originating deeper in the cortex can propagate radially via mediators that act on IP_3R2 receptors, but are not dependent on axonal transmission, glutamate or ATP (Nimmerjahn et al. 2009). This form of radial propagation could also explain the faster bursts observed in awake cortex, as compared to the slower waves seen *ex vivo*. Second, several diffuse neuromodulatory systems exist that are activated concurrently with salient stimuli (e.g. whisker stimulation) and release neurotransmitters diffusely and synchronously via varicosities throughout the cortex. Stimulation of brain stem nuclei for noradrenergic and cholinergic systems have, for instance, both been shown to elicit robust cortical

astrocyte calcium responses in anesthetized animals (Bekar et al. 2008; Navarrete et al. 2012; Takata et al. 2011). Third, the puzzling 1-5 s astrocyte-neuronal delay could imply either a very slow response to local neuronal firing (e.g. slow neurotransmitter spillover from the synaptic cleft) or that a slower indirect pathway (e.g. noradrenergic system) triggers the calcium responses. The delay could for instance also serve a purpose if it reflects the time it takes for neuronal firing to deplete ATP stores, when astrocyte calcium signals might be required promote neurovascular or neuro-metabolic coupling (Takano et al. 2006). Fourth, our first study (**Paper I**) revealed that astrocyte volume changes evoke calcium signals *in vivo*. Since astrocyte endfeet have the highest AQP4 expression and thus would be the most volume sensitive, it is possible that astrocyte calcium signals occur in response to the mechanical distortion caused by functional hyperemia, which occurs on a 1-5 s timescale (Takano et al. 2006). Finally, two recent *in situ* studies that used high-resolution 2PLSM have revisited the interesting idea that calcium signals in individual processes may be more relevant to brain or synaptic function the signals in the cell body (Di Castro et al. 2011; Wang et al. 2006). Although the conclusions of these studies need to be interpreted cautiously due to the ontogenic changes in mGluR5 expression (Sun et al. 2013), the general idea of processes signaling independent of the soma is potentially important. We therefore also examined calcium signals in the processes in the awake mouse cortex, and found that although all processes were generally involved in the synchronized bursts, individual processes would also display more frequent isolated signals (Wang et al. 2006). Further exploration of the kinetics and function(s) of these localized calcium signals in awake cortex will be an important next step for our understanding of astrocyte signaling.

In conclusion, our study demonstrates that anesthesia can directly suppress astrocyte signaling. More importantly, we show that calcium signals in the awake cortex are faster, more frequent and synchronized than those observed *in situ* and *in vitro*. Our observations highlight important questions regarding the tripartite synapse model, as it is based on studies carried out primarily in reduced preparations or anesthetized mice. We would therefore suggest that the fundamental question of how astrocytes and neurons communicate at the level of the individual synapse still remains unanswered (Nedergaard and Verkhratsky 2012; Perea and Araque 2007). Do astrocytes contribute to synaptic transmission by vesicular or non-vesicular neurotransmitter release (Hamilton and Attwell 2010)? How can astrocytes contribute

to signal transmission if their response time is so slow? Could some of the previous observations of astrocyte-neuronal signaling be artifacts of the experimental preparations (e.g. pup brain slices, traumatic cranial windows) (Agulhon et al. 2012; Sun et al. 2013)? Are synaptic signals somehow integrated within astrocytic microdomains, individual astrocytes or do we need to consider whole astrocytic syncytia (Rouach et al. 2008)?

Rapid microcirculation of water and lipids through the PVS. The brain is one of the few organs entirely devoid of a lymphatic system parallel to the blood circulation (Abbott 2004). Macroscopically, the circulation of CSF through the subarachnoid space and ventricles is known to serve many of the functions of peripheral lymphatics. However, the microcirculation within the brain parenchyma is incompletely understood. It is unclear how excess interstitial fluid, waste products and signaling molecules are circulated (Abbott 2004). A recent study by Iliff et al. has shown that water and hydrophilic compounds circulate rapidly through the brain parenchyma via the PVS (Iliff et al. 2012; Rennels et al. 1990). In our study, we address two essential functions of peripheral lymphatics – the transport of lipids and signal molecules. We found that lipophilic tracers injected into subarachnoid CSF were rapidly transported via the PVS with very little diffusion out of this space into the brain parenchyma. This observation was surprising given the small size (<1 kDa) and cell permeability of these tracers. It is possible that the restricted lipid transport is a consequence of lipoprotein binding within the PVS. Indeed, the lipophilic tracers behaved more like large molecular weight hydrophilic tracers, similar in size to lipoproteins (Fagan and Holtzman 2000; Koch et al. 2001). Unlike the results of Iliff et al. we did not find that this lipid transport pathway was affected by AQP4-deletion, indicating that other mechanisms may govern lipid bulk-flow (Iliff et al. 2012).

Moreover, we found that compromising the hydraulic integrity of the PVS enhanced the intracellular accumulation of lipophilic tracers and caused an abnormal pattern of astrocyte calcium signaling. Temporarily knocking out the PVS using a cisterna magna puncture, caused a desynchronization and increased frequency of calcium transients in astrocytes that may represent pathology. The second aim of our study was to examine whether the PVS can act as a separate astrocyte-astrocyte signaling compartment. The PVS is tightly ensheathed by astrocyte endfeet not more than 20 nm apart (Mathiisen et al. 2010). It has previously been shown that a large

proportion of calcium transients initiate and propagate along the vasculature (Simard et al. 2003). When we injected ATP agonist into the PVS *in situ*, we similarly observed a propagation of astrocyte calcium transients along the vasculature before spreading outwards. Interestingly, these paravascular calcium waves were faster and spread over a larger area than when ATP was injected directly into the parenchyma.

Our data indicate that the PVS may act as an efficient highway for astrocyte-astrocyte signaling. However, there are several limitations of our findings. First, the lipophilic molecules used, with the exception of palmitic acid, are chemical tracers and we can only infer that similar sized endogenous lipids circulate in the same manner. It is therefore possible that unknown chemical properties of these tracers interfere with their transport. On the other hand, we tested a range of chemical lipophilic tracers along with a biologically relevant lipid (palmitic acid) and received reproducible results. Second, in our model to assess intracellular delivery we had to apply tracers directly on the cortex on inject them intraparenchymally via a cranial window. As discussed previously, the surgical creation of a cranial window is associated with molecular, cellular and mechanical changes that may confound the results (e.g. inflammation, brain herniation, depressurized local subarachnoid CSF flow) (Holtmaat et al. 2009). Third, in our attempt to look at global movement of tracers through the brain we were forced to use serial slicing of perfusion fixed tissue. The data from these sets of experiments reveal some of the inherent issues with this technique, such as the post-perfusion diffusion of lipid soluble compounds. Having acknowledged these limitations, our observations could still have important implications for current understanding of paravascular lipid circulation, membrane lipid metabolism (e.g. cholesterol and palmitoylation) and diseases involving lipoprotein mutations (e.g. Alzheimer disease). Further studies are clearly warranted to explore the effects of lipid transport in the PVS (Leoni et al. 2010; Takano et al. 2006). Although we demonstrated that the PVS is likely involved in astrocyte-astrocyte signaling, an important question that remains unanswered in our study is whether this lipid microcirculation facilitates astrocyte-vascular communication. Additionally, it is possible that defining the molecular mechanisms responsible for the putatively AQP4-independent restricted lipid microcirculation might open new avenues for intracellular drug delivery across the BBB (Merian et al. 2012).

Microglial activation in hepatic encephalopathy. Microglia are innate immune cells that clear unwanted debris and mediate inflammatory responses in the brain. Microglia transition from a resting to an active state, and finally become phagocytic (amoeboid) when they detect brain injury or infection (Kettenmann et al. 2011). Microglial involvement in HE is incompletely understood. Different HE models have generated conflicting data, and almost all previous studies have been conducted *in vitro*, *in situ* or histologically (Bruck et al. 2011; Jover et al. 2006; Rodrigo et al. 2010; Zemtsova et al. 2011). When microglial cells become activated by a perceived pathogen they alter morphology to aid migration and phagocytosis, expressing fewer and thicker processes. This microglial activation is correlated with increased secretion of pro-inflammatory cytokines (e.g. TNF-α), proteolytic enzymes (e.g. matrix metalloproteinase-9) in addition to displaying phagocytic behavior (Kettenmann et al. 2011).

Microglial activation has been identified histologically in bile duct ligation and hepatic devascularization models of HE (Jover et al. 2006; Rodrigo et al. 2010; Zemtsova et al. 2011). However, microglia did not become activated in a study of portal vein ligation, despite the mice experiencing severe encephalopathy (Bruck et al. 2011). Furthermore, activation of microglia in HE has not previously been explored *in vivo* or in the azoxymethane induced model, which has the added benefit of being one of the most reliable and reproducible models also useable in transgenic mice. We therefore chose to investigate and compare microglial activation and motility in real-time using 2PLSM imaging of *Cx3cr1*-eGFP mice in azoxymethane-induced HE with acute isolated hyperammonemia. Contrary to some previous reports, we found that microglia only become activated in the later stage of HE, after the onset of symptoms, but coincident with the onset of BBB opening and brain edema. Additionally, we found no change in microglia morphology or motility during isolated hyperammonemia. Thus, our study indicates that microglial activity may be involved in the onset of potentially fatal brain edema late in HE, but that it is not necessary for the neurological dysfunction seen in early HE or acute hyperammonemic encephalopathy.

Our study has several limitations that one needs to consider when interpreting the results. Since *in vivo* 2PLSM of microglial activation has only been performed in few studies to date, the sensitivity of this method is unfortunately not completely known (Fuhrmann et al. 2010; Marker et al. 2010; Nimmerjahn et al. 2005). On the

other hand, 2PLSM has several benefits with regard to identifying microglial activation, such as improved anatomical resolution, the ability to compose 3D-stacks and the possibility to follow changes in the same cell over time. However, immunohistochemistry has the advantage of being able to detect the expression of surface markers of microglial activation that could be more sensitive (e.g. Iba1). Microglial motility or turnover rate (TOR) of processes is an incompletely understood behavior that microglia display in living brain tissue. It is thought to represent physiological surveillance of the surrounding environment but may also be associated with trauma from the cranial window itself (Fuhrmann et al. 2010; Nimmerjahn et al. 2005). Hence the decreased TOR we observed in late HE needs to be interpreted cautiously until further studies shed light on this phenomenon. Regarding the mouse model of azoxymethane induced HE, it is well characterized both in our study and previous work. It also has a phenotypic and biochemical profile that is comparable to common forms of HE seen in humans. However, this chemically induced disease model presents some issues regarding possible confounding effects of the drug on the CNS directly. In summary, we believe there are several important questions that remain unanswered for future study including: Is real-time 2PLSM morphometric imaging of microglia an accurate and sensitive measure of activation? What is the function of microglial surveillance behavior in living brains and to what extent is the high turnover rate we observe an artifact of the surgical preparation? Does chronic low-grade hyperammonemia cause microglial activation, e.g. through prolonged reactive oxygen stress, and would inhibition of this improve clinically relevant outcomes in HE (Agusti et al. 2011; Cauli et al. 2007)?

Ammonia – a ubiquitous building block and deadly toxin. Ammonia is known to be acutely neurotoxic in humans, and is thought to exert its toxic effects on the brain by causing astrocyte swelling and dysfunction (Brusilow et al. 2010; Cagnon and Braissant 2007). Astrocytes are thought to be most extremely sensitive to ammonia toxicity because of their privileged role as the only cell in the CNS able to detoxify ammonia via the enzyme GS (Martinez-Hernandez et al. 1977). Our first goal was therefore to characterize the extent of astrocyte involvement in ammonia toxicity and image for the first time *in vivo* the volume changes associated with this condition. We chose to address these questions in the $Otc^{spf\text{-}ash}$ model of hyperammonemia with no liver failure, which allowed us to study the CNS effects of ammonia in isolation (cf.

hepatic encephalopathy). Furthermore, following a detailed characterization of the symptomatology we chose to focus on the pathology in the cerebral cortex. This was because electrophysiology findings (myoclonic seizures) led us to suspect this as a major target of the ammonia toxicity. To our great surprise, doses of ammonia sufficient to trigger significant symptoms such as ataxia and seizures did not induce any astrocyte swelling *in vivo*. Additionally, deleting the main route of water influx into astrocytes, AQP4, had no effect on disease outcome in isolated ammonia toxicity, contrary to contemporary hypotheses (Rama Rao et al. 2010). Our data are therefore consistent with the previously discussed much tighter astrocyte volume regulation *in vivo* than for instance *in vitro*. Since the brain edema reported in ammonia toxicity could also be due to water accumulation in other compartments we measured overall brain water content. We found that moderate ammonia doses did not cause any overall brain edema in the acute setting (Brusilow et al. 2010). To ensure our volume assay was sufficiently sensitive, we then administered higher doses of ammonia and were able to replicate the previously described ammonia-induced astrocyte swelling and brain edema. The presence of symptoms with doses of ammonia insufficient to cause swelling led us to conclude that astrocyte swelling is not prerequisite for ammonia neurotoxicity.

Given our negative findings with regards to astrocyte swelling, we next wanted to explore alternative molecular mechanisms for the toxicity of ammonia. First, we used 2PLSM to look for signs of astrocyte dysfunction and chose to examine calcium signaling, which as discussed previously is linked to key homeostatic functions. Consistent with our initial hypothesis that ammonia is selectively toxic to astrocytes, we found a marked increase and desynchronization of astrocyte calcium signals following ammonia administration. Astrocyte calcium signals have recently been shown to be critical for buffering of $[K^+]_o$ via the NKA in both cerebrum and cerebellum (Wang et al. 2012a; Wang et al. 2012b). Additionally, several studies from kidney, bee retina, acute brain slice and astrocyte cultures have indicated that ammonia may directly interfere with potassium homeostasis (Alger and Nicoll 1983; Brookes and Turner 1993; Marcaggi et al. 2004; Stephan et al. 2012; Sugimoto et al. 1997). We therefore hypothesized that ammonia sequestered into astrocytes for GS detoxification might selectively impair potassium homeostasis in these cells causing an increase in $[K^+]_o$. Using K^+ ISMs we were able to demonstrate the $[K^+]_o$ increase *in vivo* (Alger and Nicoll 1983). However, the mechanism for the ammonia induced

$[K^+]_o$ increase was still unknown, as it likely was not be mediated by the swelling-related mechanisms proposed in the previous studies. Using *in situ* assays we demonstrated that the physical similarities of ammonium (NH_4^+) and potassium (K^+) ions cause them to directly compete for transport across astrocyte membranes. This fundamental biochemical aspect of ammonia might explain why toxicity is observed in bacteria, to fish and ultimately humans (Marcaggi et al. 2004).

To further explore the link between a failure of astrocyte potassium buffering and neurological impairment, we proceeded to correlate the kinetics of the $[K^+]_o$ increase with symptom onset and severity. Consistent with our previous hypothesis, we found that $[K^+]_o$ increased robustly prior to symptom onset *in vivo*, and that the magnitude of the potassium increase correlated closely with encephalopathy grade. Seminal previous studies between 1970-80 showed that neurons exposed to excess ammonia rapidly develop impaired post-synaptic inhibition (Aickin et al. 1982; Alger and Nicoll 1983; Lux 1971; Lux and Loracher 1970; Lux et al. 1970; Lux and Schubert 1969; Meyer and Lux 1974; Raabe and Gumnit 1975; Raabe 1981). To explore this hypothesis *in vivo*, we used paired-pulse whisker stimulation to show that ammonia toxicity is associated with a failure of cortical inhibitory transmission. Additionally, using *in situ* electrophysiology we were able to show that the failure of inhibitory transmission was due to excess extracellular NH_4^+ and K^+ driving chloride influx via NKCC1 and causing a depolarizing shift in the Cl^--based GABA equilibrium potential (E_{GABA}) of pyramidal neurons. NKCC1 can be selectively inhibited by the clinically used diuretic bumetanide, which we found significantly reduced the severity of the ammonia phenotype and increased survival following lethal ammonia injections. Bumetanide has also recently been shown to improve clinical outcomes in HE, though the authors suggested this occurred due to an amelioration of astrocyte swelling (Jayakumar et al. 2008; Jayakumar et al. 2011b). Moreover, recent studies of neonatal and febrile seizures have revealed an important role of potassium and NKCC1 mediated E_{GABA} depolarization that can be treated with bumetanide (Dzhala et al. 2005; Koyama et al. 2012).

The molecular pathway delineated above led us to suspect that potassium alone might be sufficient to replicate many of the neurotoxic effects of ammonia. Since potassium is largely impermeable to the BBB (Hansen et al. 1977), we developed a model whereby either potassium or ammonia was superfused directly onto the cerebral cortex. Interestingly, we found that increasing $[K^+]_o$ alone was

sufficient to depolarize E_{GABA} and trigger myoclonic seizures. This observation is supported by recent studies showing that impaired potassium buffering in reactive astrocytes can mediate seizures in mesial temporal lobe epilepsy, neonatal and febrile seizures (Dzhala et al. 2005; Heuser et al. 2012; Koyama et al. 2012).

In conclusion, we arrived at a novel molecular mechanism for ammonia and potassium neurotoxicity and isolated a molecular target with clear translational applications. We were able to describe how acute hyperammonemia causes a rapid increase in basal $[K^+]_o$, leading to myoclonic seizures. A major limitation of our study was the short timescale of hyperammonemia. Congenital hyperammonemia in children often leads to acute increases in plasma ammonia, though this frequently occurs on top of a low-grade encephalopathy and cognitive impairment (Cagnon and Braissant 2007; Lichter-Konecki et al. 2008). There has been limited experimentation regarding how chronic hyperammonemia might affect learning and memory in young animals. Additionally, it would be interesting to test whether NKCC1 antagonist bumetanide might improve any cognitive phenotype. Finally as ours and other recent studies have highlighted the link between impaired astrocytic $[K^+]_o$ homeostasis, NKCC1 and seizures, further *in vivo* experiments are required to address whether this causal pathway might be involved in other types of seizure disorders, e.g. post-traumatic and hypoglycemic seizures (Dzhala et al. 2005; Haj-Yasein et al. 2011a; Heuser et al. 2012; Koyama et al. 2012).

10. CONCLUSIONS

In summary, exploiting the strengths of 2PLSM *in vivo* imaging we chose to examine several key aspects of glial function and dysfunction in the context of water and ion homeostasis. Our results demonstrate that glial cells perform homeostatic and signaling roles that are essential for effective brain function. Additionally, we found that early breakdown of these glial mechanisms was a hallmark of neurological dysfunction across the broad range of conditions examined in our studies. Our data thus illustrate that therapies targeting glial cells have the potential to create a paradigm change in the current clinical approach to treating neurological disorders.

I. AQP4 is critical for calcium signaling evoked by swelling of astrocytes in response to hyponatremic brain edema. AQP4 thus increases astrocyte sensitivity to small osmotic changes and may therefore mediate volume related signaling.

II. AQP4 deletion selectively worsens microwatershed hypoxia in cortical spreading depression, without affecting overall oxygenation or blood flow. This can be explained by either a role of AQP4 in O_2 transport or AQP4 facilitating energy-efficient potassium homeostasis.

III. Several commonly used general anesthetics with nominally different molecular mechanisms selectively suppress astrocyte calcium signaling, prior to having a detectable effect on neurons. These observations raise the important question of whether anesthetics may exert some of their sedative actions via astrocytes, and not just neurons.

IV. The paravascular space formed between astrocyte endfeet and the vasculature represents a novel lymphatic-like route for lipid transport and glial signaling in the brain.

V. Microglial activation coincides with the onset of brain edema in the late stages of hepatic encephalopathy, which may increase mortality in this condition. Neurotoxic levels of ammonia alone were insufficient to activate microglia.

VI. Neurotoxic levels of ammonia selectively short-circuit astrocyte potassium buffering, and secondarily impairs neuronal inhibitory activity by decreasing inward NKCC1-dependent $GABA_A$-currents. Pharmacological inhibition with the clinically used diuretic bumetanide reverses this phenotype, improving clinically relevant end-points such as seizures and encephalopathy.

11. REFERENCES

Abbott NJ. 2004. Evidence for bulk flow of brain interstitial fluid: significance for physiology and pathology. Neurochem Int 45(4):545-52.

Agre P, Nielsen S, Ottersen OP. 2004. Towards a molecular understanding of water homeostasis in the brain. Neuroscience 129(4):849-50.

Agulhon C, Fiacco TA, McCarthy KD. 2010. Hippocampal short- and long-term plasticity are not modulated by astrocyte Ca2+ signaling. Science 327(5970):1250-4.

Agulhon C, Petravicz J, McMullen AB, Sweger EJ, Minton SK, Taves SR, Casper KB, Fiacco TA, McCarthy KD. 2008. What is the role of astrocyte calcium in neurophysiology? Neuron 59(6):932-46.

Agulhon C, Sun MY, Murphy T, Myers T, Lauderdale K, Fiacco TA. 2012. Calcium Signaling and Gliotransmission in Normal vs. Reactive Astrocytes. Front Pharmacol 3:139.

Agusti A, Cauli O, Rodrigo R, Llansola M, Hernandez-Rabaza V, Felipo V. 2011. p38 MAP kinase is a therapeutic target for hepatic encephalopathy in rats with portacaval shunts. Gut 60(11):1572-9.

Aickin CC, Deisz RA, Lux HD. 1982. Ammonium action on post-synaptic inhibition in crayfish neurones: implications for the mechanism of chloride extrusion. J Physiol 329:319-39.

Akaike N. 1996. Gramicidin perforated patch recording and intracellular chloride activity in excitable cells. Prog Biophys Mol Biol 65(3):251-64.

Alger BE, Nicoll RA. 1983. Ammonia does not selectively block IPSPs in rat hippocampal pyramidal cells. J Neurophysiol 49(6):1381-91.

Amiry-Moghaddam M, Frydenlund DS, Ottersen OP. 2004. Anchoring of aquaporin-4 in brain: molecular mechanisms and implications for the physiology and pathophysiology of water transport. Neuroscience 129(4):999-1010.

Amiry-Moghaddam M, Otsuka T, Hurn PD, Traystman RJ, Haug FM, Froehner SC, Adams ME, Neely JD, Agre P, Ottersen OP and others. 2003a. An alpha-syntrophin-dependent pool of AQP4 in astroglial end-feet confers bidirectional water flow between blood and brain. Proc Natl Acad Sci U S A 100(4):2106-11.

Amiry-Moghaddam M, Ottersen OP. 2003. The molecular basis of water transport in the brain. Nat Rev Neurosci 4(12):991-1001.

Amiry-Moghaddam M, Williamson A, Palomba M, Eid T, de Lanerolle NC, Nagelhus EA, Adams ME, Froehner SC, Agre P, Ottersen OP. 2003b. Delayed K+ clearance associated with aquaporin-4 mislocalization: phenotypic defects in brains of alpha-syntrophin-null mice. Proc Natl Acad Sci U S A 100(23):13615-20.

Andersson RM, Aizman O, Aperia A, Brismar H. 2004. Modulation of Na+,K+-ATPase activity is of importance for RVD. Acta Physiol Scand 180(4):329-34.

Araque A, Parpura V, Sanzgiri RP, Haydon PG. 1999. Tripartite synapses: glia, the unacknowledged partner. Trends Neurosci 22(5):208-15.

Arcuino G, Lin JH, Takano T, Liu C, Jiang L, Gao Q, Kang J, Nedergaard M. 2002. Intercellular calcium signaling mediated by point-source burst release of ATP. Proc Natl Acad Sci U S A 99(15):9840-5.

Attwell D, Buchan AM, Charpak S, Lauritzen M, Macvicar BA, Newman EA. 2010. Glial and neuronal control of brain blood flow. Nature 468(7321):232-43.
Aukland K, Reed RK. 1993. Interstitial-lymphatic mechanisms in the control of extracellular fluid volume. Physiol Rev 73(1):1-78.
Bak LK, Schousboe A, Waagepetersen HS. 2006. The glutamate/GABA-glutamine cycle: aspects of transport, neurotransmitter homeostasis and ammonia transfer. J Neurochem 98(3):641-53.
Barres BA. 2008. The mystery and magic of glia: a perspective on their roles in health and disease. Neuron 60(3):430-40.
Behar KL, Fitzpatrick SM, Hetherington HP, Shulman RG. 1993. Cerebral metabolic studies in vivo by combined 1H/31P and 1H/13C NMR spectroscopic methods. Acta Neurochir Suppl (Wien) 57:9-20.
Bekar LK, He W, Nedergaard M. 2008. Locus coeruleus alpha-adrenergic-mediated activation of cortical astrocytes in vivo. Cerebr Cortex 18(12):2789-2795.
Bélanger M, Côté J, Butterworth RF. 2006. Neurobiological characterization of an azoxymethane mouse model of acute liver failure. Neurochem Int 48(6-7):434-440.
Bestvater F, Spiess E, Stobrawa G, Hacker M, Feurer T, Porwol T, Berchner-Pfannschmidt U, Wotzlaw C, Acker H. 2002. Two-photon fluorescence absorption and emission spectra of dyes relevant for cell imaging. J Microsc 208(Pt 2):108-15.
Bezzi P, Gundersen V, Galbete JL, Seifert G, Steinhauser C, Pilati E, Volterra A. 2004. Astrocytes contain a vesicular compartment that is competent for regulated exocytosis of glutamate. Nat Neurosci 7(6):613-20.
Binder DK, Oshio K, Ma T, Verkman AS, Manley GT. 2004. Increased seizure threshold in mice lacking aquaporin-4 water channels. Neuroreport 15(2):259-62.
Binder DK, Yao X, Zador Z, Sick TJ, Verkman AS, Manley GT. 2006. Increased seizure duration and slowed potassium kinetics in mice lacking aquaporin-4 water channels. Glia 53(6):631-6.
Bjorkhem I. 2007. Rediscovery of cerebrosterol. Lipids 42(1):5-14.
Block ML, Zecca L, Hong JS. 2007. Microglia-mediated neurotoxicity: uncovering the molecular mechanisms. Nat Rev Neurosci 8(1):57-69.
Blom H, Ronnlund D, Scott L, Spicarova Z, Rantanen V, Widengren J, Aperia A, Brismar H. 2012. Nearest neighbor analysis of dopamine D1 receptors and Na(+)-K(+)-ATPases in dendritic spines dissected by STED microscopy. Microsc Res Tech 75(2):220-8.
Blom H, Ronnlund D, Scott L, Spicarova Z, Widengren J, Bondar A, Aperia A, Brismar H. 2011. Spatial distribution of Na+-K+-ATPase in dendritic spines dissected by nanoscale superresolution STED microscopy. BMC Neurosci 12:16.
Board F. 1994. Pain and distress in laboratory rodents and lagomorphs. Report of the Federation of European Laboratory Animal Science Associations (FELASA) Working Group on Pain and Distress accepted by the FELASA Board of Management November 1992. Lab Anim 28(2):97-112.
Borgdorff AJ, Poulet JF, Petersen CC. 2007. Facilitating sensory responses in developing mouse somatosensory barrel cortex. J Neurophysiol 97(4):2992-3003.

Borrelli MJ, Carlini WG, Dewey WC, Ransom BR. 1985. A simple method for making ion-selective microelectrodes suitable for intracellular recording in vertebrate cells. J Neurosci Methods 15(2):141-54.
Bowman CL, Kimelberg HK. 1984. Excitatory amino acids directly depolarize rat brain astrocytes in primary culture. Nature 311(5987):656-9.
Boyarsky G, Ransom B, Schlue WR, Davis MB, Boron WF. 1993. Intracellular pH regulation in single cultured astrocytes from rat forebrain. Glia 8(4):241-248.
Brookes N, Turner RJ. 1993. Extracellular potassium regulates the glutamine content of astrocytes: mediation by intracellular pH. Neurosci Lett 160(1):73-6.
Bruck J, Gorg B, Bidmon HJ, Zemtsova I, Qvartskhava N, Keitel V, Kircheis G, Haussinger D. 2011. Locomotor impairment and cerebrocortical oxidative stress in portal vein ligated rats in vivo. J Hepatol 54(2):251-7.
Brusilow SW, Koehler RC, Traystman RJ, Cooper AJ. 2010. Astrocyte glutamine synthetase: importance in hyperammonemic syndromes and potential target for therapy. Neurotherapeutics 7(4):452-470.
Burnstock G, Verkhratsky A. 2010. Long-term (trophic) purinergic signalling: purinoceptors control cell proliferation, differentiation and death. Cell Death Dis 1:e9.
Butterworth RF. 2002a. Pathophysiology of hepatic encephalopathy: a new look at ammonia. Metab Brain Dis 17(4):221-227.
Butterworth RF. 2002b. Pathophysiology of hepatic encephalopathy: a new look at ammonia. Metab Brain Dis 17(4):221-7.
Butterworth RF. 2011. Hepatic encephalopathy: a central neuroinflammatory disorder? Hepatology 53(4):1372-6.
Butterworth RF, Norenberg MD, Felipo V, Ferenci P, Albrecht J, Blei AT. 2009. Experimental models of hepatic encephalopathy: ISHEN guidelines. Liver Int 29(6):783-788.
Caesar K, Hashemi P, Douhou A, Bonvento G, Boutelle MG, Walls AB, Lauritzen M. 2008. Glutamate receptor-dependent increments in lactate, glucose and oxygen metabolism evoked in rat cerebellum in vivo. J Physiol 586(5):1337-49.
Cagnon L, Braissant O. 2007. Hyperammonemia-induced toxicity for the developing central nervous system. Brain Res Rev 56:183-197.
Carter LP. 1991. Surface monitoring of cerebral cortical blood flow. Cerebrovasc Brain Metab Rev 3(3):246-61.
Cauli O, Rodrigo R, Piedrafita B, Boix J, Felipo V. 2007. Inflammation and hepatic encephalopathy: ibuprofen restores learning ability in rats with portacaval shunts. Hepatology 46(2):514-9.
Chan WY, Kohsaka S, Rezaie P. 2007. The origin and cell lineage of microglia: new concepts. Brain Res Rev 53(2):344-54.
Chen KC, Nicholson C. 2000. Spatial buffering of potassium ions in brain extracellular space. Biophys J 78(6):2776-97.
Chen X, Leischner U, Rochefort NL, Nelken I, Konnerth A. 2011. Functional mapping of single spines in cortical neurons in vivo. Nature 475(7357):501-5.

Chever O, Djukic B, McCarthy KD, Amzica F. 2010. Implication of Kir4.1 channel in excess potassium clearance: an in vivo study on anesthetized glial-conditional Kir4.1 knock-out mice. J Neurosci 30(47):15769-77.
Christensen DJ, Nedergaard M. 2011. Two-photon in vivo imaging of cells. Pediatr Nephrol 26(9):1483-9.
Chuquet J, Hollender L, Nimchinsky EA. 2007. High-resolution in vivo imaging of the neurovascular unit during spreading depression. J Neurosci 27(15):4036-44.
Ciani E, Groneng L, Voltattorni M, Rolseth V, Contestabile A, Paulsen RE. 1996. Inhibition of free radical production or free radical scavenging protects from the excitotoxic cell death mediated by glutamate in cultures of cerebellar granule neurons. Brain Res 728(1):1-6.
Coles JA, Marcaggi P, Vega C, Cotillon N. 1996. Effects of photoreceptor metabolism on interstitial and glial cell pH in bee retina: evidence of a role for NH4+. J Physiol 495 (Pt 2):305-18.
Cooper AJ, McDonald JM, Gelbard AS, Gledhill RF, Duffy TE. 1979. The metabolic fate of 13N-labeled ammonia in rat brain. J Biol Chem 254(12):4982-4992.
Cooper DM, McIver R, Bianco R. 2000. The thin blue line: a review and discussion of aseptic technique and postprocedural infections in rodents. Contemp Top Lab Anim Sci 39(6):27-32.
Cornell-Bell AH, Finkbeiner SM, Cooper MS, Smith SJ. 1990. Glutamate induces calcium waves in cultured astrocytes: long-range glial signaling. Science 247(4941):470-3.
Cotrina ML, Lin JH, Alves-Rodrigues A, Liu S, Li J, Azmi-Ghadimi H, Kang J, Naus CC, Nedergaard M. 1998. Connexins regulate calcium signaling by controlling ATP release. Proc Natl Acad Sci U S A 95(26):15735-40.
Coull JA BS, Boudreau D, Boivin D, Tsuda M, Inoue K, Gravel C, Salter MW, De Koninck Y. 2005. BDNF from microglia causes the shift in neuronal anion gradient underlying neuropathic pain. Nature 438(7070):1017-1021.
Cserr HF, Cooper DN, Suri PK, Patlak CS. 1981. Efflux of radiolabeled polyethylene glycols and albumin from rat brain. Am J Physiol 240(4):F319-28.
Cserr HF, Depasquale M, Patlak CS, Pullen RG. 1986. Convection of cerebral interstitial fluid and its role in brain volume regulation. Ann N Y Acad Sci 481:123-34.
Davalos D, Grutzendler J, Yang G, Kim JV, Zuo Y, Jung S, Littman DR, Dustin ML, Gan WB. 2005. ATP mediates rapid microglial response to local brain injury in vivo. Nat Neurosci 8(6):752-8.
Delpire E, Lu J, England R, Dull C, Thorne T. 1999. Deafness and imbalance associated with inactivation of the secretory Na-K-2Cl co-transporter. Nat Genet 22(2):192-5.
Denk W, Briggman KL, Helmstaedter M. 2012. Structural neurobiology: missing link to a mechanistic understanding of neural computation. Nat Rev Neurosci 13(5):351-8.
Denk W, Strickler JH, Webb WW. 1990. Two-photon laser scanning fluorescence microscopy. Science 248(4951):73-6.

Di Castro MA, Chuquet J, Liaudet N, Bhaukaurally K, Santello M, Bouvier D, Tiret P, Volterra A. 2011. Local Ca2+ detection and modulation of synaptic release by astrocytes. Nat Neurosci 14(10):1276-84.
Dirnagl U. 2006. Bench to bedside: the quest for quality in experimental stroke research. J Cereb Blood Flow Metab 26(12):1465-78.
Djukic B, Casper KB, Philpot BD, Chin LS, McCarthy KD. 2007. Conditional knock-out of Kir4.1 leads to glial membrane depolarization, inhibition of potassium and glutamate uptake, and enhanced short-term synaptic potentiation. J Neurosci 27(42):11354-65.
Dombeck DA, Graziano MS, Tank DW. 2009. Functional clustering of neurons in motor cortex determined by cellular resolution imaging in awake behaving mice. J Neurosci 29(44):13751-60.
Dombeck DA, Harvey CD, Tian L, Looger LL, Tank DW. 2010. Functional imaging of hippocampal place cells at cellular resolution during virtual navigation. Nat Neurosci 13(11):1433-40.
Dombeck DA, Khabbaz AN, Collman F, Adelman TL, Tank DW. 2007. Imaging large-scale neural activity with cellular resolution in awake, mobile mice. Neuron 56(1):43-57.
Dominguez DC. 2004. Calcium signalling in bacteria. Mol Microbiol 54(2):291-7.
Dong CY, Koenig K, So P. 2003. Characterizing point spread functions of two-photon fluorescence microscopy in turbid medium. J Biomed Opt 8(3):450-9.
Drew PJ, Shih AY, Driscoll JD, Knutsen PM, Blinder P, Davalos D, Akassoglou K, Tsai PS, Kleinfeld D. 2010. Chronic optical access through a polished and reinforced thinned skull. Nat Methods 7(12):981-4.
Drobizhev M, Makarov NS, Tillo SE, Hughes TE, Rebane A. 2011. Two-photon absorption properties of fluorescent proteins. Nat Methods 8(5):393-9.
Duemani Reddy G, Kelleher K, Fink R, Saggau P. 2008. Three-dimensional random access multiphoton microscopy for functional imaging of neuronal activity. Nat Neurosci 11(6):713-20.
Duffy S, MacVicar BA. 1996. In vitro ischemia promotes calcium influx and intracellular calcium release in hippocampal astrocytes. J Neurosci 16(1):71-81.
Dzhala VI, Talos DM, Sdrulla DA, Brumback AC, Mathews GC, Benke TA, Delpire E, Jensen FE, Staley KJ. 2005. NKCC1 transporter facilitates seizures in the developing brain. Nat Med 11(11):1205-1213.
Enger R, Gundersen GA, Haj-Yasein NN, Eilert-Olsen M, Thoren AE, Vindedal GF, Petersen PH, Skare O, Nedergaard M, Ottersen OP and others. 2012. Molecular scaffolds underpinning macroglial polarization: An analysis of retinal Muller cells and brain astrocytes in mouse. Glia 60(12):2018-26.
Fagan AM, Holtzman DM. 2000. Astrocyte lipoproteins, effects of apoE on neuronal function, and role of apoE in amyloid-beta deposition in vivo. Microsc Res Tech 50(4):297-304.
Fang X, Yang B, Matthay MA, Verkman AS. 2002. Evidence against aquaporin-1-dependent CO2 permeability in lung and kidney. J Physiol 542(Pt 1):63-9.
Folbergrova J, Passonneau JV, Lowry OH, Schulz DW. 1969. Glycogen, ammonia and related metabolites in the brain during seizures evoked by methionine sulfoximine. J Neurochem 16(2):191-203.

Frigeri A, Nicchia GP, Nico B, Quondamatteo F, Herken R, Roncali L, Svelto M. 2001. Aquaporin-4 deficiency in skeletal muscle and brain of dystrophic mdx mice. FASEB J 15(1):90-98.
Fritschy JM. 2008. Is my antibody-staining specific? How to deal with pitfalls of immunohistochemistry. Eur J Neurosci 28(12):2365-70.
Frydenlund DS, Bhardwaj A, Otsuka T, Mylonakou MN, Yasumura T, Davidson KG, Zeynalov E, Skare O, Laake P, Haug FM and others. 2006. Temporary loss of perivascular aquaporin-4 in neocortex after transient middle cerebral artery occlusion in mice. Proc Natl Acad Sci U S A 103(36):13532-6.
Fuhrmann M, Bittner T, Jung CK, Burgold S, Page RM, Mitteregger G, Haass C, LaFerla FM, Kretzschmar H, Herms J. 2010. Microglial Cx3cr1 knockout prevents neuron loss in a mouse model of Alzheimer's disease. Nat Neurosci 13(4):411-3.
Fukata Y, Fukata M. 2010. Protein palmitoylation in neuronal development and synaptic plasticity. Nat Rev Neurosci 11(3):161-75.
Ganz R, Swain M, Traber P, DalCanto M, Butterworth RF, Blei AT. 1989. Ammonia-induced swelling of rat cerebral cortical slices: implications for the pathogenesis of brain edema in acute hepatic failure. Metab Brain Dis 4(3):213-223.
Gaveriaux-Ruff C, Kieffer BL. 2007. Conditional gene targeting in the mouse nervous system: Insights into brain function and diseases. Pharmacol Ther 113(3):619-34.
Ge S, Goh EL, Sailor KA, Kitabatake Y, Ming GL, Song H. 2006. GABA regulates synaptic integration of newly generated neurons in the adult brain. Nature 439(7076):589-93.
Giaume C, Koulakoff A, Roux L, Holcman D, Rouach N. 2010. Astroglial networks: a step further in neuroglial and gliovascular interactions. Nat Rev Neurosci 11(2):87-99.
Grande PO, Romner B. 2012. Osmotherapy in brain edema: a questionable therapy. J Neurosurg Anesthesiol 24(4):407-12.
Greenberg DS, Houweling AR, Kerr JN. 2008. Population imaging of ongoing neuronal activity in the visual cortex of awake rats. Nat Neurosci 11(7):749-51.
Gregorios JB, Mozes LW, Norenberg LO, Norenberg MD. 1985. Morphologic effects of ammonia on primary astrocyte cultures. I. Light microscopic studies. J Neuropathol Exp Neurol 44(4):397-403.
Grisar T, Franck G, Delgado-Escueta AV. 1983. Na+ K+-ATPase within neurons and glia in the generation of seizures. Adv Neurol 34:199-208.
Gunnarson E, Song Y, Kowalewski JM, Brismar H, Brines M, Cerami A, Andersson U, Zelenina M, Aperia A. 2009. Erythropoietin modulation of astrocyte water permeability as a component of neuroprotection. Proc Natl Acad Sci U S A 106(5):1602-7.
Gunnarson E, Zelenina M, Axehult G, Song Y, Bondar A, Krieger P, Brismar H, Zelenin S, Aperia A. 2008. Identification of a molecular target for glutamate regulation of astrocyte water permeability. Glia 56(6):587-96.
Haas BR, Sontheimer H. 2010. Inhibition of the Sodium-Potassium-Chloride Cotransporter Isoform-1 reduces glioma invasion. Cancer Res 70(13):5597-606.

Haj-Yasein NN, Jensen V, Ostby I, Omholt SW, Voipio J, Kaila K, Ottersen OP, Hvalby O, Nagelhus EA. 2012. Aquaporin-4 regulates extracellular space volume dynamics during high-frequency synaptic stimulation: a gene deletion study in mouse hippocampus. Glia 60(6):867-74.
Haj-Yasein NN, Jensen V, Vindedal GF, Gundersen GA, Klungland A, Ottersen OP, Hvalby O, Nagelhus EA. 2011a. Evidence that compromised K+ spatial buffering contributes to the epileptogenic effect of mutations in the human Kir4.1 gene (KCNJ10). Glia 59(11):1635-42.
Haj-Yasein NN, Vindedal GF, Eilert-Olsen M, Gundersen GA, Skare O, Laake P, Klungland A, Thoren AE, Burkhardt JM, Ottersen OP and others. 2011b. Glial-conditional deletion of aquaporin-4 (Aqp4) reduces blood-brain water uptake and confers barrier function on perivascular astrocyte endfeet. Proc Natl Acad Sci U S A 108(43):17815-20.
Haj-Yasein NN, Vindedal GF, Ellert-Olsen M, Gundersen GA, Skare O, Laake P, Klungland A, Thorén AE, Burkhardt JM, Ottersen OP and others. 2011c. Glial-conditional deletion of aquaporin-4 (Aqp4) reduces blood-brain water uptake and confers barrier function on perivascular astrocyte endfeet. Proc Natl Acad Sci U S A 108(43):17815-17820.
Hamilton NB, Attwell D. 2010. Do astrocytes really exocytose neurotransmitters? Nat Rev Neurosci 11(4):227-38.
Hanisch UK, Kettenmann H. 2007. Microglia: active sensor and versatile effector cells in the normal and pathologic brain. Nat Neurosci 10(11):1387-94.
Hansen AJ, Lund-Andersen H, Crone C. 1977. K+-permeability of the blood-brain barrier, investigated by aid of a K+-sensitive microelectrode. Acta Physiol Scand 101(4):438-445.
Hartline DK, Colman DR. 2007. Rapid conduction and the evolution of giant axons and myelinated fibers. Curr Biol 17(1):R29-35.
Harvey CD, Collman F, Dombeck DA, Tank DW. 2009. Intracellular dynamics of hippocampal place cells during virtual navigation. Nature 461(7266):941-6.
Hell SW. 2003. Toward fluorescence nanoscopy. Nat Biotechnol 21(11):1347-55.
Helmchen F, Denk W. 2005. Deep tissue two-photon microscopy. Nat Methods 2(12):932-40.
Helmstaedter M, Briggman KL, Denk W. 2008. 3D structural imaging of the brain with photons and electrons. Curr Opin Neurobiol 18(6):633-41.
Hertz L, Kala G. 2007. Energy metabolism in brain cells: effects of elevated ammonia concentrations. Metab Brain Dis 22(3-4):199-218.
Hertz L, Zielke HR. 2004. Astrocytic control of glutamatergic activity: astrocytes as stars of the show. Trends Neurosci 27(12):735-43.
Heuser K, Eid T, Lauritzen F, Thoren AE, Vindedal GF, Tauboll E, Gjerstad L, Spencer DD, Ottersen OP, Nagelhus EA and others. 2012. Loss of Perivascular Kir4.1 Potassium Channels in the Sclerotic Hippocampus of Patients With Mesial Temporal Lobe Epilepsy. J Neuropathol Exp Neurol.
Holtmaat A, Bonhoeffer T, Chow DK, Chuckowree J, De Paola V, Hofer SB, Hubener M, Keck T, Knott G, Lee WC and others. 2009. Long-term, high-resolution imaging in the mouse neocortex through a chronic cranial window. Nat Protoc 4(8):1128-44.
Iadecola C, Nedergaard M. 2007. Glial regulation of the cerebral microvasculature. Nat Neurosci 10(11):1369-76.

Iliff JJ, Wang M, Liao Y, Plogg BA, Peng W, Gundersen GA, Benveniste H, Vates GE, Deane R, Goldman SA and others. 2012. A Paravascular Pathway Facilitates CSF Flow Through the Brain Parenchyma and the Clearance of Interstitial Solutes, Including Amyloid beta. Sci Transl Med 4(147):147ra111.

Illarionova NB, Gunnarson E, Li Y, Brismar H, Bondar A, Zelenin S, Aperia A. 2010. Functional and molecular interactions between aquaporins and Na,K-ATPase. Neuroscience 168(4):915-25.

Inoue K, Tsuda M, Tozaki-Saitoh H. 2007. Modification of neuropathic pain sensation through microglial ATP receptors. Purinergic Signal 3(4):311-6.

Jayakumar AR, Liu M, Moriyama M, Ramakrishnan R, Forbush B, 3rd, Reddy PV, Norenberg MD. 2008. Na-K-Cl Cotransporter-1 in the mechanism of ammonia-induced astrocyte swelling. J Biol Chem 283(49):33874-82.

Jayakumar AR, Panickar KS, Curtis KM, Tong XY, Moriyama M, Norenberg MD. 2011a. Na-K-Cl cotransporter-1 in the mechanism of cell swelling in cultured astrocytes after fluid percussion injury. J Neurochem 117(3):437-48.

Jayakumar AR, Rao KV, Murthy CR, Norenberg MD. 2006. Glutamine in the mechanism of ammonia-induced swelling. Neurochem Int 48(6-7):623-628.

Jayakumar AR, Valdes V, Norenberg MD. 2011b. The Na-K-Cl cotransporter in the brain edema of acute liver failure. J Hepatol 54(2):272-278.

Jiang W, Desjardins P, Butterworth RF. 2009. Minocycline attenuates oxidative/nitrosative stress and cerebral complications of acute liver failure in rats. Neurochem Int 55(7):601-5.

Jourdain P, Bergersen LH, Bhaukaurally K, Bezzi P, Santello M, Domercq M, Matute C, Tonello F, Gundersen V, Volterra A. 2007. Glutamate exocytosis from astrocytes controls synaptic strength. Nat Neurosci 10(3):331-9.

Jover R, Rodrigo R, Felipo V, Insausti R, Saez-Valero J, Garcia-Ayllon MS, Suarez I, Candela A, Compan A, Esteban A and others. 2006. Brain edema and inflammatory activation in bile duct ligated rats with diet-induced hyperammonemia: A model of hepatic encephalopathy in cirrhosis. Hepatology 43(6):1257-66.

Kang J, Jiang L, Goldman SA, Nedergaard M. 1998. Astrocyte-mediated potentiation of inhibitory synaptic transmission. Nat Neurosci 1(8):683-92.

Kang J, Kang N, Yu Y, Zhang J, Petersen N, Tian GF, Nedergaard M. 2010. Sulforhodamine 101 induces long-term potentiation of intrinsic excitability and synaptic efficacy in hippocampal CA1 pyramidal neurons. Neuroscience 169(4):1601-9.

Karowski CJ, Proenza LM. 1977. Relationship between Muller cell responses, a local transretinal potential, and potassium flux. J Neurophysiol 40(2):244-59.

Kasischke KA, Lambert EM, Panepento B, Sun A, Gelbard HA, Burgess RW, Foster TH, Nedergaard M. 2011. Two-photon NADH imaging exposes boundaries of oxygen diffusion in cortical vascular supply regions. J Cereb Blood Flow Metab 31(1):68-81.

Kasischke KA, Vishwasrao HD, Fisher PJ, Zipfel WR, Webb WW. 2004. Neural activity triggers neuronal oxidative metabolism followed by astrocytic glycolysis. Science 305(5680):99-103.
Kaya M, Ahishali B. 2011. Assessment of permeability in barrier type of endothelium in brain using tracers: Evans blue, sodium fluorescein, and horseradish peroxidase. Methods Mol Biol 763:369-82.
Kettenmann H, Backus KH, Schachner M. 1984. Aspartate, glutamate and gamma-aminobutyric acid depolarize cultured astrocytes. Neurosci Lett 52(1-2):25-9.
Kettenmann H, Hanisch UK, Noda M, Verkhratsky A. 2011. Physiology of microglia. Physiol Rev 91(2):461-553.
Kimelberg HK. 1987. Anisotonic media and glutamate-induced ion transport and volume responses in primary astrocyte cultures. J Physiol (Paris) 82(4):294-303.
Kimelberg HK, Nedergaard M. 2010. Functions of astrocytes and their potential as therapeutic targets. Neurotherapeutics 7(4):338-53.
King LS, Kozono D, Agre P. 2004. From structure to disease: the evolving tale of aquaporin biology. Nat Rev Mol Cell Biol 5(9):687-98.
Kirischuk S, Parpura V, Verkhratsky A. 2012. Sodium dynamics: another key to astroglial excitability? Trends Neurosci 35(8):497-506.
Kobat D, Durst ME, Nishimura N, Wong AW, Schaffer CB, Xu C. 2009. Deep tissue multiphoton microscopy using longer wavelength excitation. Opt Express 17(16):13354-64.
Kobayashi K, Yamanaka H, Fukuoka T, Dai Y, Obata K, Noguchi K. 2008. P2Y12 receptor upregulation in activated microglia is a gateway of p38 signaling and neuropathic pain. J Neurosci 28(11):2892-902.
Koch S, Donarski N, Goetze K, Kreckel M, Stuerenburg HJ, Buhmann C, Beisiegel U. 2001. Characterization of four lipoprotein classes in human cerebrospinal fluid. J Lipid Res 42(7):1143-51.
Kofuji P, Newman EA. 2004. Potassium buffering in the central nervous system. Neuroscience 129(4):1045-56.
Koyama R, Tao K, Sasaki T, Ichikawa J, Miyamoto D, Muramatsu R, Matsuki N, Ikegaya Y. 2012. GABAergic excitation after febrile seizures induces ectopic granule cells and adult epilepsy. Nat Med.
Kur J, Newman EA, Chan-Ling T. 2012. Cellular and physiological mechanisms underlying blood flow regulation in the retina and choroid in health and disease. Prog Retin Eye Res 31(5):377-406.
Kyrozis A, Reichling DB. 1995. Perforated-patch recording with gramicidin avoids artifactual changes in intracellular chloride concentration. J Neurosci Methods 57(1):27-35.
Langford DJ, Bailey AL, Chanda ML, Clarke SE, Drummond TE, Echols S, Glick S, Ingrao J, Klassen-Ross T, Lacroix-Fralish ML and others. 2010. Coding of facial expressions of pain in the laboratory mouse. Nat Methods 7(6):447-9.
Largo C, Ibarz JM, Herreras O. 1997. Effects of the gliotoxin fluorocitrate on spreading depression and glial membrane potential in rat brain in situ. J Neurophysiol 78(1):295-307.

Larrosa B, Pastor J, Lopez-Aguado L, Herreras O. 2006. A role for glutamate and glia in the fast network oscillations preceding spreading depression. Neuroscience 141(2):1057-68.
Lauritzen M. 1994. Pathophysiology of the migraine aura. The spreading depression theory. Brain 117 (Pt 1):199-210.
Lauritzen M. 2001. Cortical spreading depression in migraine. Cephalalgia 21(7):757-60.
Lauritzen M. 2005. Reading vascular changes in brain imaging: is dendritic calcium the key? Nat Rev Neurosci 6(1):77-85.
Lauritzen M, Dreier JP, Fabricius M, Hartings JA, Graf R, Strong AJ. 2011. Clinical relevance of cortical spreading depression in neurological disorders: migraine, malignant stroke, subarachnoid and intracranial hemorrhage, and traumatic brain injury. J Cereb Blood Flow Metab 31(1):17-35.
Lauritzen M, Fabricius M. 1995. Real time laser-Doppler perfusion imaging of cortical spreading depression in rat neocortex. Neuroreport 6(9):1271-3.
Lauritzen M, Mathiesen C, Schaefer K, Thomsen KJ. 2012. Neuronal inhibition and excitation, and the dichotomic control of brain hemodynamic and oxygen responses. Neuroimage 62(2):1040-50.
Leao AA. 1947. Further observations on the spreading depression of activity in the cerebral cortex. J Neurophysiol 10(6):409-14.
Leo L, Gherardini L, Barone V, De Fusco M, Pietrobon D, Pizzorusso T, Casari G. 2011. Increased susceptibility to cortical spreading depression in the mouse model of familial hemiplegic migraine type 2. PLoS Genet 7(6):e1002129.
Leoni V, Caccia C. 2011. Oxysterols as biomarkers in neurodegenerative diseases. Chem Phys Lipids 164(6):515-24.
Leoni V, Solomon A, Kivipelto M. 2010. Links between ApoE, brain cholesterol metabolism, tau and amyloid beta-peptide in patients with cognitive impairment. Biochem Soc Trans 38(4):1021-5.
Lichter-Konecki U, Mangin JM, Gordish-Dressman H, Hoffman EP, Gallo V. 2008. Gene expression profiling of astrocytes from hyperammonemic mice reveals altered pathways for water and potassium homeostasis in vivo. Glia 56(4):365-377.
Lovatt D, Sonnewald U, Waagepetersen HS, Schousboe A, He W, Lin JH, Han X, Takano T, Wang S, Sim FJ and others. 2007. The transcriptome and metabolic gene signature of protoplasmic astrocytes in the adult murine cortex. J Neurosci 27(45):12255-66.
Lux HD. 1971. Ammonium and chloride extrusion: hyperpolarizing syntaptic inhibition in spinal motor neurons. Science 173(996):555-557.
Lux HD, Loracher C. 1970. Postsynaptic disinhibition by ammonium. Naturwissenschaften 57(9):456-7.
Lux HD, Loracher C, Neher E. 1970. The action of ammonium on postsynaptic inhibition of cat spinal motoneurons. Exp Brain Res 11(5):431-47.
Lux HD, Schubert P. 1969. Postsynaptic inhibition: intracellular effects of various ions in spinal motoneurons. Science 166(3905):625-6.
MacAulay N, Zeuthen T. 2010. Water transport between CNS compartments: contributions of aquaporins and cotransporters. Neuroscience 168(4):941-56.

Maiman TH. 1960. Stimulated Optical Radiation in Ruby. Nature 187(4736):493-494.
Manley GT, Fujimura M, Ma T, Noshita N, Filiz F, Bollen AW, Chan P, Verkman AS. 2000. Aquaporin-4 deletion in mice reduces brain edema after acute water intoxication and ischemic stroke. Nat Med 6(2):159-163.
Mantz J, Cordier J, Giaume C. 1993. Effects of general anesthetics on intercellular communications mediated by gap junctions between astrocytes in primary culture. Anesthesiology 78(5):892-901.
Mao T, O'Connor DH, Scheuss V, Nakai J, Svoboda K. 2008. Characterization and subcellular targeting of GCaMP-type genetically-encoded calcium indicators. PLoS One 3(3):e1796.
Marcaggi P, Coles JA. 2000. A Cl(-) cotransporter selective for NH(4)(+) over K(+) in glial cells of bee retina. J Gen Physiol 116(2):125-42.
Marcaggi P, Jeanne M, Coles JA. 2004. Neuron-glial trafficking of NH4+ and K+: separate routes of uptake into glial cells of bee retina. Eur J Neurosci 19(4):966-976.
Mariot P, Sartor P, Audin J, Dufy B. 1991. Intracellular pH in individual pituitary cells: measurement with a dual emission pH indicator. Life Sci 48(3):245-52.
Marker DF, Tremblay ME, Lu SM, Majewska AK, Gelbard HA. 2010. A thin-skull window technique for chronic two-photon in vivo imaging of murine microglia in models of neuroinflammation. J Vis Exp(43).
Martinez-Hernandez A, Bell KP, Norenberg MD. 1977. Glutamine synthetase: glial localization in brain. Science 195(4284):1356-1358.
Mathiesen C, Brazhe A, Thomsen K, Lauritzen M. 2012. Spontaneous calcium waves in Bergman glia increase with age and hypoxia and may reduce tissue oxygen. J Cereb Blood Flow Metab.
Mathiisen TM, Lehre KP, Danbolt NC, Ottersen OP. 2010. The perivascular astroglial sheath provides a complete covering of the brain microvessels: an electron microscopic 3D reconstruction. Glia 58(9):1094-103.
Matkowskyj KA, Marrero JA, Carroll RE, Danilkovich AV, Green RM, Benya RV. 1999. Azoxymethane-induced fulminant hepatic failure in C57BL/6J mice: characterization of a new animal model. Am J Physiol 277:G455-G462.
Matyash V, Kettenmann H. 2010. Heterogeneity in astrocyte morphology and physiology. Brain Res Rev 63(1-2):2-10.
Mauch DH, Nagler K, Schumacher S, Goritz C, Muller EC, Otto A, Pfrieger FW. 2001. CNS synaptogenesis promoted by glia-derived cholesterol. Science 294(5545):1354-7.
Meeks JP, Mennerick S. 2007. Astrocyte membrane responses and potassium accumulation during neuronal activity. Hippocampus 17(11):1100-8.
Merian J, Gravier J, Navarro F, Texier I. 2012. Fluorescent nanoprobes dedicated to in vivo imaging: from preclinical validations to clinical translation. Molecules 17(5):5564-91.
Meyer H, Lux HD. 1974. Action of ammonium on a chloride pump. Removal of hyperpolarizing inhibition in an isolated neuron. Pflugers Arch 350(2):185-95.
Mikula S, Binding J, Denk W. 2012. Staining and embedding the whole mouse brain for electron microscopy. Nat Methods 9(12):1198-201.

Misgeld T, Kerschensteiner M. 2006. In vivo imaging of the diseased nervous system. Nat Rev Neurosci 7(6):449-63.
Mitsuma T, Tani K, Hiroaki Y, Kamegawa A, Suzuki H, Hibino H, Kurachi Y, Fujiyoshi Y. 2010. Influence of the cytoplasmic domains of aquaporin-4 on water conduction and array formation. J Mol Biol 402(4):669-81.
Miyakawa-Naito A, Uhlen P, Lal M, Aizman O, Mikoshiba K, Brismar H, Zelenin S, Aperia A. 2003. Cell signaling microdomain with Na,K-ATPase and inositol 1,4,5-trisphosphate receptor generates calcium oscillations. J Biol Chem 278(50):50355-61.
Miyazaki H, Nakamura Y, Arai T, Kataoka K. 1997. Increase of glutamate uptake in astrocytes: a possible mechanism of action of volatile anesthetics. Anesthesiology 86(6):1359-66; discussion 8A.
Moeller HB, Fenton RA, Zeuthen T, Macaulay N. 2009. Vasopressin-dependent short-term regulation of aquaporin 4 expressed in Xenopus oocytes. Neuroscience 164(4):1674-84.
Moeller HB, Olesen ET, Fenton RA. 2011. Regulation of the water channel aquaporin-2 by posttranslational modification. Am J Physiol Renal Physiol 300(5):F1062-73.
Mori S, Oishi K, Faria AV. 2009. White matter atlases based on diffusion tensor imaging. Curr Opin Neurol 22(4):362-9.
Moscioni D, Morizono H, McCarter RJ, Stern A, Cabrera-Luque J, Hoang A, Sanmiguel J, Wu D, Bell P, Gao GP and others. 2006. Long-term correction of ammonia metabolism and prolonged survival in ornithine transcarbamylase-deficient mice following liver-directed treatment with adeno-associated viral vectors. Mol Ther 14(1):25-33.
Musa-Aziz R, Chen LM, Pelletier MF, Boron WF. 2009. Relative CO2/NH3 selectivities of AQP1, AQP4, AQP5, AmtB, and RhAG. Proc Natl Acad Sci U S A 106(13):5406-11.
Nagaraja TN, Brookes N. 1998. Intracellular acidification induced by passive and active transport of ammonium ions in astrocytes. Am J Physiol 274(4 Pt 1):C883-91.
Nagelhus EA, Horio Y, Inanobe A, Fujita A, Haug FM, Nielsen S, Kurachi Y, Ottersen OP. 1999. Immunogold evidence suggests that coupling of K+ siphoning and water transport in rat retinal Muller cells is mediated by a coenrichment of Kir4.1 and AQP4 in specific membrane domains. Glia 26(1):47-54.
Nagelhus EA, Mathiisen TM, Ottersen OP. 2004. Aquaporin-4 in the central nervous system: cellular and subcellular distribution and coexpression with KIR4.1. Neuroscience 129(4):905-13.
Nase G, Helm PJ, Enger R, Ottersen OP. 2008. Water entry into astrocytes during brain edema formation. Glia 56(8):895-902.
Navarrete M, Perea G, Fernandez de Sevilla D, Gomez-Gonzalo M, Nunez A, Martin ED, Araque A. 2012. Astrocytes mediate in vivo cholinergic-induced synaptic plasticity. PLoS Biol 10(2):e1001259.
Nedergaard M. 1994. Direct signaling from astrocytes to neurons in cultures of mammalian brain cells. Science 263(5154):1768-71.
Nedergaard M, Rodriguez JJ, Verkhratsky A. 2010. Glial calcium and diseases of the nervous system. Cell Calcium 47(2):140-9.

Nedergaard M, Verkhratsky A. 2012. Artifact versus reality--how astrocytes contribute to synaptic events. Glia 60(7):1013-23.
Neher E, Sakmann B, Steinbach JH. 1978. The extracellular patch clamp: a method for resolving currents through individual open channels in biological membranes. Pflugers Arch 375(2):219-28.
Newman EA. 1985. Voltage-dependent calcium and potassium channels in retinal glial cells. Nature 317(6040):809-11.
Newman EA, Frambarch DA, Odette LL. 1984. Control of extracellular potassium levels by retinal glial cell K+ siphoning. Science 225(4667):1174-1175.
Newman EA, Zahs KR. 1998. Modulation of neuronal activity by glial cells in the retina. J Neurosci 18(11):4022-8.
Nicholson C. 1993. Ion-selective microelectrodes and diffusion measurements as tools to explore the brain cell microenvironment. J Neurosci Methods 48(3):199-213.
Nielsen S, Nagelhus EA, Amiry-Moghaddam M, Bourque C, Agre P, Ottersen OP. 1997. Specialized membrane domains for water transport in glial cells: high-resolution immunogold cytochemistry of aquaporin-4 in rat brain. J Neurosci 17(1):171-180.
Niermann H, Amiry-Moghaddam M, Holthoff K, Witte OW, Ottersen OP. 2001. A novel role of vasopressin in the brain: modulation of activity-dependent water flux in the neocortex. J Neurosci 21(9):3045-51.
Nieweg K, Schaller H, Pfrieger FW. 2009. Marked differences in cholesterol synthesis between neurons and glial cells from postnatal rats. J Neurochem 109(1):125-34.
Nimmerjahn A, Kirchhoff F, Helmchen F. 2005. Resting microglial cells are highly dynamic surveillants of brain parenchyma in vivo. Science 308(5726):1314-8.
Nimmerjahn A, Kirchhoff F, Kerr JN, Helmchen F. 2004. Sulforhodamine 101 as a specific marker of astroglia in the neocortex in vivo. Nat Methods 1(1):31-7.
Nimmerjahn A, Mukamel EA, Schnitzer MJ. 2009. Motor behavior activates Bergman glial networks. Neuron 62(3):400-412.
Norenberg MD. 1977. A light and electron microscopic study of experimental portal-systemic (ammonia) encephalopathy. Progression and reversal of the disorder. Lab Invest 36(6):618-627.
O'Brien JS, Sampson EL. 1965a. Fatty acid and fatty aldehyde composition of the major brain lipids in normal human gray matter, white matter, and myelin. J Lipid Res 6(4):545-51.
O'Brien JS, Sampson EL. 1965b. Lipid composition of the normal human brain: gray matter, white matter, and myelin. J Lipid Res 6(4):537-44.
Oberheim NA, Goldman SA, Nedergaard M. 2012. Heterogeneity of astrocytic form and function. Methods Mol Biol 814:23-45.
Oberheim NA, Tian GF, Han X, Peng W, Takano T, Ransom B, Nedergaard M. 2008. Loss of astrocytic domain organization in the epileptic brain. J Neurosci 28(13):3264-76.
Oberheim NA, Wang X, Goldman S, Nedergaard M. 2006. Astrocytic complexity distinguishes the human brain. Trends Neurosci 29(10):547-53.

Ohsawa K, Irino Y, Nakamura Y, Akazawa C, Inoue K, Kohsaka S. 2007. Involvement of P2X4 and P2Y12 receptors in ATP-induced microglial chemotaxis. Glia 55(6):604-16.
Okada Y, Sato K, Numata T. 2009. Pathophysiology and puzzles of the volume-sensitive outwardly rectifying anion channel. J Physiol 587(Pt 10):2141-9.
Olson JE, Sankar R, Holtzman D, James A, Fleischhacker D. 1986. Energy-dependent volume regulation in primary cultured cerebral astrocytes. J Cell Physiol 128(2):209-15.
Ott P, Larsen FS. 2004. Blood-brain barrier permeability to ammonia in liver failure: a critical reappraisal. Neurochem Int 44(4):185-98.
Ottersen OP, Laake JH, Reichelt W, Haug FM, Torp R. 1996. Ischemic disruption of glutamate homeostasis in brain: quantitative immunocytochemical analyses. J Chem Neuroanat 12(1):1-14.
Ozden I, Dombeck DA, Hoogland TM, Tank DW, Wang SS. 2012. Widespread state-dependent shifts in cerebellar activity in locomoting mice. PLoS One 7(8):e42650.
Padmawar P, Yao X, Bloch O, Manley GT, Verkman AS. 2005. K+ waves in brain cortex visualized using a long-wavelength K+-sensing fluorescent indicator. Nat Methods 2(11):825-7.
Panatier A, Vallee J, Haber M, Murai KK, Lacaille JC, Robitaille R. 2011. Astrocytes are endogenous regulators of basal transmission at central synapses. Cell 146(5):785-98.
Papadopoulos MC, Manley GT, Krishna S, Verkman AS. 2004. Aquaporin-4 facilitates reabsorption of excess fluid in vasogenic brain edema. FASEB J 18(11):1291-3.
Papadopoulos MC, Verkman AS. 2005. Aquaporin-4 gene disruption in mice reduces brain swelling and mortality in pneumococcal meningitis. J Biol Chem 280(14):13906-12.
Papadopoulos MC, Verkman AS. 2007. Aquaporin-4 and brain edema. Pediatr Nephrol 22(6):778-84.
Paredes RM, Etzler JC, Watts LT, Zheng W, Lechleiter JD. 2008. Chemical calcium indicators. Methods 46(3):143-51.
Parpura V, Basarsky TA, Liu F, Jeftinija K, Jeftinija S, Haydon PG. 1994. Glutamate-mediated astrocyte-neuron signalling. Nature 369(6483):744-7.
Parpura V, Verkhratsky A. 2012. Homeostatic function of astrocytes: Ca(2+) and Na(+) signalling. Transl Neurosci 3(4):334-344.
Pascual O, Casper KB, Kubera C, Zhang J, Revilla-Sanchez R, Sul JY, Takano H, Moss SJ, McCarthy K, Haydon PG. 2005. Astrocytic purinergic signaling coordinates synaptic networks. Science 310(5745):113-6.
Paulsen RE, Contestabile A, Villani L, Fonnum F. 1987. An in vivo model for studying function of brain tissue temporarily devoid of glial cell metabolism: the use of fluorocitrate. J Neurochem 48(5):1377-85.
Paulsen RE, Contestabile A, Villani L, Fonnum F. 1988a. The effect of fluorocitrate on transmitter amino acid release from rat striatal slices. Neurochem Res 13(7):637-41.
Paulsen RE, Odden E, Fonnum F. 1988b. Importance of glutamine for gamma-aminobutyric acid synthesis in rat neostriatum in vivo. J Neurochem 51(4):1294-9.

Pellerin L, Bouzier-Sore AK, Aubert A, Serres S, Merle M, Costalat R, Magistretti PJ. 2007. Activity-dependent regulation of energy metabolism by astrocytes: an update. Glia 55(12):1251-62.
Perea G, Araque A. 2007. Astrocytes potentiate transmitter release at single hippocampal synapses. Science 317(5841):1083-6.
Piilgaard H, Lauritzen M. 2009. Persistent increase in oxygen consumption and impaired neurovascular coupling after spreading depression in rat neocortex. J Cereb Blood Flow Metab 29(9):1517-27.
Preston GM, Agre P. 1991. Isolation of the cDNA for erythrocyte integral membrane protein of 28 kilodaltons: member of an ancient channel family. Proc Natl Acad Sci U S A 88(24):11110-4.
Preston GM, Carroll TP, Guggino WB, Agre P. 1992. Appearance of water channels in Xenopus oocytes expressing red cell CHIP28 protein. Science 256(5055):385-7.
Proler M, Kellaway P. 1962. The methionine sulfoximine syndrome in the cat. Epilepsia 3:117-30.
Raabe W, Gumnit RJ. 1975. Disinhibition in cat motor cortex by ammonia. J Neurophysiol 38(2):347-55.
Raabe WA. 1981. Ammonia and disinhibition in cat motor cortex by ammonium acetate, monofluoroacetate and insulin-induced hypoglycemia. Brain Res 210(1-2):311-322.
Rama Rao KV, Jayakumar AR, Tong X, Curtis KM, Norenberg MD. 2010. Brain aquaporin-4 in experimental acute liver failure. J Neuropathol Exp Neurol 69(9):869-79.
Ransom B, Behar T, Nedergaard M. 2003. New roles for astrocytes (stars at last). Trends Neurosci 26(10):520-2.
Rash JE, Davidson KG, Yasumura T, Furman CS. 2004. Freeze-fracture and immunogold analysis of aquaporin-4 (AQP4) square arrays, with models of AQP4 lattice assembly. Neuroscience 129(4):915-34.
Ratnakumari L, Qureshi IA, Butterworth RF. 1992. Effects of congenital hyperammonemia on the cerebral and hepatic levels of the intermediates of energy metabolism in spf mice. Biochem Biophys Res Commun 184(2):746-51.
Ratnakumari L, Qureshi IA, Butterworth RF. 1994. Evidence for cholinergic neuronal loss in brain in congenital ornithine transcarbamylase deficiency. Neurosci Lett 178(1):63-5.
Reeves AM, Shigetomi E, Khakh BS. 2011. Bulk loading of calcium indicator dyes to study astrocyte physiology: key limitations and improvements using morphological maps. J Neurosci 31(25):9353-8.
Regan MR. 2007. Variations in promoter activity reveal a differential expression and physiology of glutamate transporters by glia in developing and mature CNS. J Neurosci 27:6607.
Regan MR, Huang YH, Kim YS, Dykes-Hoberg MI, Jin L, Watkins AM, Bergles DE, Rothstein JD. 2007. Variations in promoter activity reveal a differential expression and physiology of glutamate transporters by glia in the developing and mature CNS. J Neurosci 27(25):6607-19.
Reichenbach A, Dettmer D, Reichelt W, Eberhardt W. 1987. High Na+ affinity of the Na+,K+ pump in isolated rabbit retinal Muller (glial) cells. Neurosci Lett 75(2):157-62.

Reichenbach A, Wurm A, Pannicke T, Iandiev I, Wiedemann P, Bringmann A. 2007. Muller cells as players in retinal degeneration and edema. Graefes Arch Clin Exp Ophthalmol 245(5):627-36.
Rennels ML, Blaumanis OR, Grady PA. 1990. Rapid solute transport throughout the brain via paravascular fluid pathways. Adv Neurol 52:431-9.
Richardson CA, Flecknell PA. 2005. Anaesthesia and post-operative analgesia following experimental surgery in laboratory rodents: are we making progress? Altern Lab Anim 33(2):119-27.
Riddell DR, Zhou H, Atchison K, Warwick HK, Atkinson PJ, Jefferson J, Xu L, Aschmies S, Kirksey Y, Hu Y and others. 2008. Impact of apolipoprotein E (ApoE) polymorphism on brain ApoE levels. J Neurosci 28(45):11445-53.
Risher WC, Croom D, Kirov SA. 2012. Persistent astroglial swelling accompanies rapid reversible dendritic injury during stroke-induced spreading depolarizations. Glia 60(11):1709-20.
Rivera C, Voipio J, Kaila K. 2005. Two developmental switches in GABAergic signalling: the K+-Cl- cotransporter KCC2 and carbonic anhydrase CAVII. J Physiol 562(Pt 1):27-36.
Rivera C, Voipio J, Payne JA, Ruusuvuori E, Lahtinen H, Lamsa K, Pirvola U, Saarma M, Kaila K. 1999. The K+/Cl- co-transporter KCC2 renders GABA hyperpolarizing during neuronal maturation. Nature 397(6716):251-5.
Rodrigo R, Cauli O, Gomez-Pinedo U, Agusti A, Hernandez-Rabaza V, Garcia-Verdugo JM, Felipo V. 2010. Hyperammonemia induces neuroinflammation that contributes to cognitive impairment in rats with hepatic encephalopathy. Gastroenterology 139(2):675-84.
Rouach N, Koulakoff A, Abudara V, Willecke K, Giaume C. 2008. Astroglial metabolic networks sustain hippocampal synaptic transmission. Science 322(5907):1551-5.
Sakka L, Coll G, Chazal J. 2011. Anatomy and physiology of cerebrospinal fluid. Eur Ann Otorhinolaryngol Head Neck Dis 128(6):309-16.
Sakmann B, Neher E. 1984. Patch clamp techniques for studying ionic channels in excitable membranes. Annu Rev Physiol 46:455-72.
Saper CB, Sawchenko PE. 2003. Magic peptides, magic antibodies: guidelines for appropriate controls for immunohistochemistry. J Comp Neurol 465(2):161-3.
Schafer K, Blankenburg F, Kupers R, Gruner JM, Law I, Lauritzen M, Larsson HB. 2012. Negative BOLD signal changes in ipsilateral primary somatosensory cortex are associated with perfusion decreases and behavioral evidence for functional inhibition. Neuroimage 59(4):3119-27.
Schmid-Schonbein GW. 1990. Microlymphatics and lymph flow. Physiol Rev 70(4):987-1028.
Schubert D, Kotter R, Staiger JF. 2007. Mapping functional connectivity in barrel-related columns reveals layer- and cell type-specific microcircuits. Brain Struct Funct 212(2):107-19.
Schummers J, Yu H, Sur M. 2008. Tuned responses of astrocytes and their influence on hemodynamic signals in the visual cortex. Science 320(5883):1638-43.
Schwilden H. 2006. Concepts of EEG processing: from power spectrum to bispectrum, fractals, entropies and all that. Best Pract Res Clin Anaesthesiol 20(1):31-48.

Shigetomi E, Kracun S, Khakh BS. 2010. Monitoring astrocyte calcium microdomains with improved membrane targeted GCaMP reporters. Neuron Glia Biol 6(3):183-91.
Simard M, Arcuino G, Takano T, Liu QS, Nedergaard M. 2003. Signaling at the gliovascular interface. J Neurosci 23(27):9254-9264.
Simard M, Nedergaard M. 2004. The neurobiology of glia in the context of water and ion homeostasis. Neuroscience 129(4):877-96.
Song Y, Gunnarson E. 2012. Potassium dependent regulation of astrocyte water permeability is mediated by cAMP signaling. PLoS One 7(4):e34936.
Sonn J, Mayevsky A. 2006. Effects of anesthesia on the responses to cortical spreading depression in the rat brain in vivo. Neurol Res 28(2):206-19.
Statler KD, Jenkins LW, Dixon CE, Clark RS, Marion DW, Kochanek PM. 2001. The simple model versus the super model: translating experimental traumatic brain injury research to the bedside. J Neurotrauma 18(11):1195-206.
Stephan J, Haack N, Kafitz KW, Durry S, Koch D, Hochstrate P, Seifert G, Steinhauser C, Rose CR. 2012. Kir4.1 channels mediate a depolarization of hippocampal astrocytes under hyperammonemic conditions in situ. Glia 60(6):965-78.
Strohschein S, Huttmann K, Gabriel S, Binder DK, Heinemann U, Steinhauser C. 2011. Impact of aquaporin-4 channels on K+ buffering and gap junction coupling in the hippocampus. Glia 59(6):973-80.
Sugimoto H, Koehler RC, Wilson DA, Brusilow SW, Traystman RJ. 1997. Methionine sulfoximine, a glutamine synthetase inhibitor, attenuates increased extracellular potassium activity during acute hyperammonemia. J Cereb Blood Flow Metab 17(1):44-49.
Sun W, McConnell E, Pare JF, Xu Q, Chen M, Peng W, Lovatt D, Han X, Smith Y, Nedergaard M. 2013. Glutamate-dependent neuroglial calcium signaling differs between young and adult brain. Science 339(6116):197-200.
Szentistvanyi I, Patlak CS, Ellis RA, Cserr HF. 1984. Drainage of interstitial fluid from different regions of rat brain. Am J Physiol 246(6 Pt 2):F835-44.
Takano T, Kang J, Jaiswal JK, Simon SM, Lin JH, Yu Y, Li Y, Yang J, Dienel G, Zielke HR and others. 2005. Receptor-mediated glutamate release from volume sensitive channels in astrocytes. Proc Natl Acad Sci U S A 102(45):16466-71.
Takano T, Nedergaard M. 2009. Deciphering migraine. J Clin Invest 119(1):16-9.
Takano T, Tian GF, Peng W, Lou N, Libionka W, Han X, Nedergaard M. 2006. Astrocyte-mediated control of cerebral blood flow. Nat Neurosci 9(2):260-7.
Takano T, Tian GF, Peng W, Lou N, Lovatt D, Hansen AJ, Kasischke KA, Nedergaard M. 2007. Cortical spreading depression causes and coincides with tissue hypoxia. Nat Neurosci 10(6):754-762.
Takata N, Mishima T, Hisatsune C, Nagai T, Ebisui E, Mikoshiba K, Hirase H. 2011. Astrocyte calcium signaling transforms cholinergic modulation to cortical plasticity in vivo. J Neurosci 31(49):18155-65.
Tfelt-Hansen PC, Koehler PJ. 2011. One hundred years of migraine research: major clinical and scientific observations from 1910 to 2010. Headache 51(5):752-78.
Thompson RJ, Zhou N, MacVicar BA. 2006. Ischemia opens neuronal gap junction hemichannels. Science 312(5775):924-7.

Thorne RG, Nicholson C. 2006. In vivo diffusion analysis with quantum dots and dextrans predicts the width of brain extracellular space. Proc Natl Acad Sci U S A 103(14):5567-72.
Tian GF, Azmi H, Takano T, Xu Q, Peng W, Lin J, Oberheim N, Lou N, Wang X, Zielke HR and others. 2005. An astrocytic basis of epilepsy. Nat Med 11(9):973-81.
Tong X, Shigetomi E, Looger LL, Khakh BS. 2012. Genetically Encoded Calcium Indicators and Astrocyte Calcium Microdomains. Neuroscientist.
Torres A, Wang F, Xu Q, Fujita T, Dobrowolski R, Willecke K, Takano T, Nedergaard M. 2012. Extracellular Ca(2)(+) acts as a mediator of communication from neurons to glia. Sci Signal 5(208):ra8.
Tsuda M, Shigemoto-Mogami Y, Koizumi S, Mizokoshi A, Kohsaka S, Salter MW, Inoue K. 2003. P2X4 receptors induced in spinal microglia gate tactile allodynia after nerve injury. Nature 424(6950):778-83.
Vajda Z, Pedersen M, Doczi T, Sulyok E, Nielsen S. 2004. Studies of mdx mice. Neuroscience 129(4):993-8.
van der Weyden L, Adams DJ, Bradley A. 2002. Tools for targeted manipulation of the mouse genome. Physiol Genomics 11(3):133-64.
Vanderwolf CH. 1992. The electrocorticogram in relation to physiology and behavior: a new analysis. Electroencephalogr Clin Neurophysiol 82(3):165-75.
Verbalis JG. 2010. Brain volume regulation in response to changes in osmolality. Neuroscience 168(4):862-70.
Verkhratsky A, Butt A. 2007. Glial Neurobiology. England: John Wiley & Sons, Ltd.
Verkhratsky A, Krishtal OA, Petersen OH. 2006. From Galvani to patch clamp: the development of electrophysiology. Pflugers Arch 453(3):233-47.
Verkhratsky A, Rodriguez JJ, Parpura V. 2012a. Calcium signalling in astroglia. Mol Cell Endocrinol 353(1-2):45-56.
Verkhratsky A, Sofroniew MV, Messing A, deLanerolle NC, Rempe D, Rodriguez JJ, Nedergaard M. 2012b. Neurological diseases as primary gliopathies: a reassessment of neurocentrism. ASN Neuro 4(3).
Vise WM, Liss L, Yashon D, Hunt WE. 1975. Astrocytic processes: A route between vessels and neurons followingblood-brain barrier injurt. J Neuropathol Exp Neurol 34(4):324-34.
Walz W. 2000. Role of astrocytes in the clearance of excess extracellular potassium. Neurochem Int 36(4-5):291-300.
Wang F, Smith NA, Xu Q, Fujita T, Baba A, Matsuda T, Takano T, Bekar L, Nedergaard M. 2012a. Astrocytes modulate neural network activity by Ca(2)(+)-dependent uptake of extracellular K(+). Sci Signal 5(218):ra26.
Wang F, Xu Q, Wang W, Takano T, Nedergaard M. 2012b. Bergmann glia modulate cerebellar Purkinje cell bistability via Ca2+-dependent K+ uptake. Proc Natl Acad Sci U S A 109(20):7911-6.
Wang M, Iliff JJ, Liao Y, Chen MJ, Shinseki MS, Venkataraman A, Cheung J, Wang W, Nedergaard M. 2012c. Cognitive deficits and delayed neuronal loss in a mouse model of multiple microinfarcts. J Neurosci 32(50):17948-60.
Wang X, Lou N, Xu Q, Tian GF, Peng WG, Han X, Kang J, Takano T, Nedergaard M. 2006. Astrocytic Ca2+ signalling evoked by sensory stimulation in vivo. Nat Neurosci 9(6):816-823.

Wang Y, Cohen J, Boron WF, Schulten K, Tajkhorshid E. 2007. Exploring gas permeability of cellular membranes and membrane channels with molecular dynamics. J Struct Biol 157(3):534-44.
Wang Y, Tajkhorshid E. 2010. Nitric oxide conduction by the brain aquaporin AQP4. Proteins 78(3):661-70.
Waniewski RA. 1992. Physiological levels of ammonia regulate glutamine synthesis from extracellular glutamate in astrocyte cultures. J Neurochem 58(1):167-174.
Willig KI, Kellner RR, Medda R, Hein B, Jakobs S, Hell SW. 2006. Nanoscale resolution in GFP-based microscopy. Nat Methods 3(9):721-3.
Winship IR, Plaa N, Murphy TH. 2007. Rapid astrocyte calcium signals correlate with neuronal activity and onset of the hemodynamic response in vivo. J Neurosci 27(23):6268-72.
Wolfensohn S, Lloyd M. 2003. Handbook of laboratory animal management and welfare. Oxford: Wiley-Blackwell.
Xiong ZQ, Stringer JL. 2000. Sodium pump activity, not glial spatial buffering, clears potassium after epileptiform activity induced in the dentate gyrus. J Neurophysiol 83(3):1443-51.
Xu HT, Pan F, Yang G, Gan WB. 2007. Choice of cranial window type for in vivo imaging affects dendritic spine turnover in the cortex. Nat Neurosci 10(5):549-51.
Yang H, Liang G, Hawkins BJ, Madesh M, Pierwola A, Wei H. 2008. Inhalational anesthetics induce cell damage by disruption of intracellular calcium homeostasis with different potencies. Anesthesiology 109(2):243-50.
Ye X, Robinson MB, Pabin C, Quinn T, Jawad A, Wilson JM, Batshaw ML. 1997. Adenovirus-mediated in vivo gene transfer rapidly protects ornithine transcarbamylase-deficient mice from an ammonium challenge. Pediatr Res 41(4):527-535.
Zemtsova I, Gorg B, Keitel V, Bidmon HJ, Schror K, Haussinger D. 2011. Microglia activation in hepatic encephalopathy in rats and humans. Hepatology 54(1):204-15.
Zhang Q, Fukuda M, Van Bockstaele E, Pascual O, Haydon PG. 2004. Synaptotagmin IV regulates glial glutamate release. Proc Natl Acad Sci U S A 101(25):9441-6.
Zhou N, Gordon GR, Feighan D, MacVicar BA. 2010. Transient swelling, acidification, and mitochondrial depolarization occurs in neurons but not astrocytes during spreading depression. Cereb Cortex 20(11):2614-24.
Zwingmann C, Chatauret N, Leibfritz D, Butterworth RF. 2003. Selective increase of brain lactate synthesis in experimental acute liver failure: results of a [1H-13C] nuclear magnetic resonance study. Hepatology 37(2):420-428.

I

II

***In vivo* NADH fluorescence imaging indicates effect of aquaporin-4 deletion on oxygen microdistribution in cortical spreading depression**

Alexander Stanley Thrane[1,2,3*], Takahiro Takano[1*], Vinita Rangroo Thrane[1,2,3*], Fushun Wang[1], Weiguo Peng[1], Ole Petter Ottersen[2], Maiken Nedergaard[1], Erlend A. Nagelhus[1,2,3,4]

[1]Division of Glial Disease and Therapeutics, Center for Translational Neuromedicine, University of Rochester Medical Center, Rochester, New York 14642.

[2]Centre for Molecular Biology and Neuroscience, Letten Centre, Institute of Basic Medical Sciences, University of Oslo, 0317 Oslo, Norway.

[3]Centre for Molecular Medicine Norway, Nordic EMBL Partnership, University of Oslo, 0318 Oslo, Norway.

[4]Department of Neurology, Oslo University Hospital, 0027 Oslo, Norway

* These authors contributed equally to this work

Correspondence: Maiken Nedergaard, MD PhD, Center for Translational Neuromedicine, 601 Elmwood Avenue, Rochester, New York 14642, USA. E-mail: nedergaard@urmc.rochester.edu. Phone: (585) 273-2868. **Funding:** This work was supported by the US National Institutes of Health (NS075177 and NS078304 to M.N.), Research Council of Norway (NevroNor, and FUGE grants), Letten Foundation, and Fulbright Foundation. **Disclosure:** The authors declare no conflict of interest. **Running headline:** Aquaporin-4 effects oxygenation in spreading depression.

Abstract

Using *in vivo* two-photon imaging we show that mice deficient in aquaporin-4 (AQP4) display increased fluorescence of nicotinamide adenine dinucleotide (NADH) when subjected to cortical spreading depression (CSD). The increased NADH signal, a proxy of tissue hypoxia, was restricted to micro-watershed areas remote from the vasculature. *Aqp4* deletion had no effects on the hyperemia response, but slowed $[K^+]_o$ recovery. These observations suggest that K^+ uptake is suppressed in *Aqp4*$^{-/-}$ mice as a consequence of decreased oxygen delivery to tissue located furthest away from the vascular source of oxygen, although increased oxygen consumption may also contribute to our observations.

Key words

AQP4, astrocytes, glia, NADH, metabolic.

Introduction

Aquaporin-4 (AQP4) is the principal brain water channel and is concentrated in astrocytic endfoot membranes at the brain-blood and brain-liquor interfaces.[1] It is surprising that our understanding of the physiological roles of AQP4 has evolved so slowly given its abundance in brain. Although AQP4 is engaged in interstitial fluid dynamics under physiological conditions,[2, 3] several lines of work show that animals must be subjected to severe stress for a clear *Aqp4*$^{-/-}$ phenotype to become apparent. The role of AQP4 in mediating water exchange across the blood-brain interface was for instance initially demonstrated in models of brain edema that entail pronounced osmotic stress.[4]

Here we used cortical spreading depression (CSD) as a model of severe metabolic stress to resolve whether oxygenation of brain neuropil depends on the presence of AQP4. Drawing on experience from studies of brain edema, we hypothesized that severe stress would be needed to disclose a link between AQP4 expression and tissue oxygenation.[4] CSD is a slowly spreading wave of depressed neuronal activity associated with a massive buildup of extracellular concentration of K^+ ions ($[K^+]_o$), thought to occur during migraine headaches. The recovery of $[K^+]_o$ involves several mechanisms, including inward rectifying K^+-channels, (Na^+)-K^+-Cl^- cotransporters and the Na^+,K^+-ATPase.[5-7]

Two-photon imaging of nicotinamide adenine dinucleotide (NADH) fluorescence can be used to provide high-resolution maps of tissue redox state *in vivo*. Increased NADH signal is a sensitive non-linear proxy of tissue hypoxia.[8] Our analysis shows that *Aqp4* deletion leads to a more pronounced oxygen deficit in microwatershed areas and a

protracted $[K^+]_o$ recovery. The most parsimonious explanation of these observations is that removal of AQP4 reduces oxygen supply and hence slows K^+ re-uptake.

Materials and Methods

Mouse preparation. *Aqp4*$^{-/-}$ and *Aqp4*$^{+/+}$ mice of either sex were generated as previously described and anesthetized using intraperitoneal urethane (1 g/kg) and α-chloralose (50 mg/kg).[9] The mice were prepared for *in vivo* 2-photon imaging as previously described.[7] CSD was evoked by either pressure injecting 1M KCl through a micropipette or surface application of 1M KCl (5 µl) through a small secondary craniotomy. Fixation of mice, preparation of tissue slices and immunohistochemistry were performed as described previously.[9] All animal experiments were conducted in accordance with the ARRIVE guidelines and approved by the Animal Care and Use Committee of the University of Rochester.

***In vivo* recordings.** A Mai Tai laser (SpectraPhysics) attached to a confocal scanning system (Fluoview 300, Olympus) and an upright microscope (IX51W) with a 20X objective (0.95 NA, Olympus) was used. We performed combined imaging of NADH and intravascular fluorescein isothiocyanate (FITC)-dextran (2000 kDa, 5%, i.v.).[7] NADH was excited at 740 nm and emission was detected using a 460 nm filter (50 nm bandwidth), whilst FITC-dextran emission was detected using a 515 nm filter (50 nm bandwidth). The images were taken every 3 s at 50-150 µm depth. Images were filtered and converted to percent changes from baseline using ImageJ software (NIH) as described previously.[7] The NADH fluorescence changes during CSD reveal a

characteristic biphasic response.[7] This response has a complex geometry, and perivascular "cylinders" of low NADH signal can be seen whose size depends both on their vascular oxygen content and diameter.[8] We therefore calculated the change in signal intensity of individual pixels normalized to values in a baseline image ($\Delta F/F_0$), before the onset of CSD. By convention the regions where pixel values became more negative ($\Delta F/F_0 < 0$) and positive ($\Delta F/F_0 > 0$) during the CSD wave were defined as "Dip" and "Overshoot", respectively.[7] Direct current (DC) potentials and $[K^+]_o$ were recorded using glass microelectodes and tissue pO_2 (tpO_2) was measured using a Clark-type polarographic oxygen microelectrode (OX-4, Unisense) as outlined before.[7, 10] Cerebral blood flow was assessed using a fiberoptic laser Doppler probe (PF5010, Perimed) and connected to an infrared laser Doppler flowmeter. All signals were digitized (Digidata 1332A, Axon Instruments) and analyzed (pClamp 10.2, Axon Instruments).

Results

Deletion of *Aqp4* increases microwatershed NADH fluorescence during CSD

We measured tissue NADH fluorescence, cerebral blood flow, tissue oxygen tension (tpO_2), local field potentials (LFP), and $[K^+]_o$ in living wild type and *Aqp4*$^{-/-}$ mice following induction of CSD (**Figure 1A)**. Immunofluorescence confirmed high perivascular AQP4 expression in wild type mice and confirmed the efficacy of the gene knockout strategy (**Figure 1B**). The total and perivascular dip NADH responses in *Aqp4*$^{-/-}$ animals did not differ from that in wild type during CSD **(Figure 1C,D)**. However, the overshoot region of the NADH response was greater in the *Aqp4*$^{-/-}$ animals than in wild types almost from the onset of CSD, and became significantly higher ~ 2 min after onset

(Total neuropil: wild type 14.36 ± 4.02% vs. *Aqp4*$^{-/-}$ 19.61 ± 6.21%. Dip: wild type 17.33 ± 3.43% vs. *Aqp4*$^{-/-}$ 23.23 ± 4.78%. Overshoot: wild type 17.09 ± 3.71% vs. *Aqp4*$^{-/-}$ 39.48 ± 6.43%, all peak values, $p<0.05$ for 145 to 250 s post-CSD onset) **(Figure 1E,F)**. The rising phase of NADH fluorescence overshoot lasted 187.50 ± 36.54 s in wild type and 133.33 ± 49.09 s in *Aqp4*$^{-/-}$ animals, and was not significantly different (data not shown). Thus, our data suggest that *Aqp4* deletion selectively impairs tissue oxygenation in areas furthest away from the vasculature.

Deletion of *Aqp4* does not influence hyperemia and vascular oxygen supply in CSD

Cerebral blood flow is critical for maintaining adequate tissue oxygenation. Due to the strong AQP4 expression around blood vessels, we tested whether *Aqp4* deletion influenced the vascular response to CSD. Neither the amplitude nor the duration of the hyperemia phase differed between wild type and *Aqp4*$^{-/-}$ animals (Peak: wild type 164.50 ± 4.57% vs. *Aqp4*$^{-/-}$ 162.57 ± 7.54%. Duration: wild type 174.50 ± 11.56 s vs. *Aqp4*$^{-/-}$ 178.06 ± 6.09 s) **(Figure 2A-C)**. Additionally, *Aqp4* deletion did not affect overall tissue oxygen supply, which we assessed using oxygen sensitive microelectrodes that integrate tpO_2 from a ~ 268-524 μm^3 volume encompassing both NADH dip and overshoot regions (Baseline: wild type 38.60 ± 3.14 mmHg vs. *Aqp4*$^{-/-}$ 45.98 ± 4.88 mmHg. CSD: wild type 9.14 ± 2.05 mmHg vs. *Aqp4*$^{-/-}$ 11.53 ± 3.03 mmHg. **(Figure 2D)**.[7] The kinetics of these tpO_2 recordings was not significantly different **(Figure 2E,F)** (ΔtpO_2: wild type -29.46 ± 4.98 vs. *Aqp4*$^{-/-}$ -34.45 ± 3.13. Declining slope: wild type -2.79 ± 1.22 mmHg/s vs. *Aqp4*$^{-/-}$ -3.44 ± 0.74 mmHg/s. Recovery slope: wild type +0.67 ± 0.38 mmHg/s vs. *Aqp4*$^{-/-}$ +0.58 ± 0.12 mmHg/s). Finally, when we used tpO_2 and blood flow recordings to

approximate the cerebral metabolic rate of oxygen ($\Delta CMRO_2$) this was not significantly different between the two genotypes during CSD (wild type 281.50 ± 21.62 μmol/100g/min vs. *Aqp4*$^{-/-}$ 292.50 ± 23.40 μmol/100g/min, data not shown). However, this calculation uses equivalent coefficients for oxygen diffusion through brain in both genotypes, which may be an incorrect assumption if AQP4 alters gas diffusion. Taken together, we found no evidence that deleting *Aqp4* altered hyperemia or overall oxygen supply during CSD.

Deletion of *Aqp4* delays $[K^+]_o$ recovery in CSD

The amplitude of the DC potential shift, which is dependent on $[K^+]_o$, was significantly lower in *Aqp4*$^{-/-}$ than in wild type mice (Amplitude: wild type -18.71 ± 2.11 mV vs. *Aqp4*$^{-/-}$ -12.80 ± 1.16 mV) **(Figure 2G,H)**. In line with these data and the finding that *Aqp4* deletion increases basal ECS volume,[11] the amplitude of the $[K^+]_o$ increase was significantly lower in *Aqp4*$^{-/-}$ animals (Amplitude: wild type 75.54 ± 1.86 mM vs. *Aqp4*$^{-/-}$ 64.49 ± 1.73 mM) **(Figure 2I,J)**. The rising phase of $[K^+]_o$ in CSD lasted 30.53 ± 1.76 s in wild type and 31.61 ± 4.75 s in *Aqp4*$^{-/-}$ animals, not significantly different **(Figure 2K)**. However, *Aqp4*$^{-/-}$ mice showed a slower $[K^+]_o$ recovery compared to wild types (Recovery rate: wild type 1.79 ± 0.12 mM/s vs. *Aqp4*$^{-/-}$ 1.27 ± 0.08 mM/s. Duration of $[K^+]_o$ elevation: wild type 130.32 ± 5.42 s vs. *Aqp4*$^{-/-}$ 153.86 ± 7.54 s) **(Figure 2L,M)**, suggesting that the capacity for $[K^+]_o$ clearance is reduced by *Aqp4* deletion.

Discussion

Our study provides the first line of evidence that AQP4 impacts oxygenation of brain tissue. Using CSD as a model of severe metabolic stress, we show that *Aqp4* deletion increases NADH fluorescence in areas furthest away from cerebral microvessels. NADH fluorescence is a sensitive indicator of tissue hypoxia with a p_{50} of 3.4 mmHg,[8] and our data thus demonstrate that *Aqp4* deletion enhances the already critical microwatershed hypoxia seen in CSD.[7] Measurements with laser Doppler flowmetry show that this impaired oxygenation was not due to inadequate blood supply, as *Aqp4*$^{-/-}$ and wild type mice had a comparable hyperemia response. Moreover, oxygen sensitive microelectrodes showed that the observed NADH changes did not reflect overall differences in tissue oxygenation, but were spatially restricted to microwatershed regions.

The observed increase of microwatershed hypoxia in *Aqp4*$^{-/-}$ mice can be explained by either enhanced oxygen consumption or reduced oxygen diffusion. *Aqp4* deletion has previously been shown to impair $[K^+]_o$ clearance during CSD, seizures and neuronal stimulation.[2, 3, 5, 6, 12] AQP4 can impact $[K^+]_o$ clearance in several ways, including regulating extracellular space volume, dissipating osmotic gradients arising from ion transport and enhancing interstitial bulk flow.[2, 3, 6, 12] *Aqp4* deletion might therefore increase microwatershed hypoxia by making perivascular $[K^+]_o$ homeostasis less efficient and consume excess oxygen. However, this hypothesis would imply that *Aqp4*$^{-/-}$ mice have a larger perivascular NADH signal dip and a higher overall oxygen uptake, neither of which we found in our study. Additionally, the hypothesis would predict that $[K^+]_o$ increases in the *Aqp4*$^{-/-}$ mice prior to the observed NADH changes, whereas our data indicate the opposite.

The alternative hypothesis entails *Aqp4* deletion impairing oxygen diffusion across perivascular endfoot membranes. Experimental analyses in oocytes and modeling studies have suggested that AQP4 might serve as a gas channel.[13, 14] Wang & Tajkhorshid suggested that the central pore of the AQP4 tetramer could conduct NO and O_2.[13] However, the membrane permeability for gasses likely varies significantly depending on the type of gas studied (O_2, CO_2, NO), lipid composition of the membrane (e.g. endfoot vs. oocyte), and macromolecular organization of transmembrane proteins (e.g. AQP4 tetramers). Aquaporin-facilitated gas transport is therefore an unresolved topic, where several studies have presented evidence for and against the hypothesis.[13-15] If oxygen diffusion were rate limiting in our study we would hypothesize that microwatershed hypoxia would be increased and involve a larger area, which the NADH imaging supports. We might also expect that inadequate oxygenation precedes and potentially causes the slowed $[K^+]_o$ clearance seen in *Aqp4*$^{-/-}$ mice, and our data show a tendency towards this. Finally, NADH is an indirect and non-linear indicator of tissue hypoxia that can be influenced by factors unrelated to oxygenation (e.g. cell swelling, hypoglycemia). As we were unable to detect an overall difference in tissue oxygenation using microelectrodes, our data therefore does not directly show that mitochondrial oxygen uptake is inadequate or rate limiting in the *Aqp4*$^{-/-}$ mice.

In conclusion, our data suggest that *Aqp4* deletion in CSD impairs the oxygenation of areas remote from brain microvessels. These observations are consistent with the hypothesis that AQP4 facilitates oxygen diffusion, but due to methodological limitations we cannot conclusively differentiate this from the alternative explanation that

Aqp4 deletion increases metabolic demand. Our study thus provides the first evidence to suggest that AQP4 is involved in facilitating oxygen diffusion *in vivo*.

References

1. Nielsen S, Nagelhus EA, Amiry-Moghaddam M, Bourque C, Agre P and Ottersen OP. Specialized membrane domains for water transport in glial cells: high-resolution immunogold cytochemistry of aquaporin-4 in rat brain. *J Neurosci*. 1997; 17: 171-80.
2. Iliff JJ, Wang M, Liao Y, Plogg BA, Peng W, Gundersen GA, et al. A Paravascular Pathway Facilitates CSF Flow Through the Brain Parenchyma and the Clearance of Interstitial Solutes, Including Amyloid beta. *Sci Transl Med*. 2012; 4: 147ra11.
3. Strohschein S, Huttmann K, Gabriel S, Binder DK, Heinemann U and Steinhauser C. Impact of aquaporin-4 channels on K+ buffering and gap junction coupling in the hippocampus. *Glia*. 2011; 59: 973-80.
4. Manley GT, Fujimura M, Ma T, Noshita N, Filiz F, Bollen AW, et al. Aquaporin-4 deletion in mice reduces brain edema after acute water intoxication and ischemic stroke. *Nat Med*. 2000; 6: 159-63.
5. Mazel T, Richter F, Vargova L and Sykova E. Changes in extracellular space volume and geometry induced by cortical spreading depression in immature and adult rats. *Physiological research / Academia Scientiarum Bohemoslovaca*. 2002; 51 Suppl 1: S85-93.
6. Padmawar P, Yao X, Bloch O, Manley GT and Verkman AS. K+ waves in brain cortex visualized using a long-wavelength K+-sensing fluorescent indicator. *Nature methods*. 2005; 2: 825-7.
7. Takano T, Tian GF, Peng W, Lou N, Lovatt D, Hansen AJ, et al. Cortical spreading depression causes and coincides with tissue hypoxia. *Nat Neurosci*. 2007; 10: 754-62.
8. Kasischke KA, Lambert EM, Panepento B, Sun A, Gelbard HA, Burgess RW, et al. Two-photon NADH imaging exposes boundaries of oxygen diffusion in cortical vascular supply regions. *Journal of cerebral blood flow and metabolism : official journal of the International Society of Cerebral Blood Flow and Metabolism*. 2011; 31: 68-81.
9. Thrane AS, Rappold PM, Takumi F, Ottersen OP, Nedergaard M and Nagelhus EA. Critical role of aquaporin-4 (AQP4) in astrocytic Ca2+ signaling events elicited by cerebral edema. *Proc Natl Acad Sci U S A*. 2010; 108: 846-51.
10. Wang F, Xu Q, Wang W, Takano T and Nedergaard M. Bergmann glia modulate cerebellar Purkinje cell bistability via Ca2+-dependent K+ uptake. *Proceedings of the National Academy of Sciences of the United States of America*. 2012; 109: 7911-6.
11. Yao X, Hrabetova S, Nicholson C and Manley GT. Aquaporin-4-deficient mice have increased extracellular space without tortuosity change. *J Neurosci*. 2008; 28: 5460-4.
12. Binder DK, Yao X, Zador Z, Sick TJ, Verkman AS and Manley GT. Increased seizure duration and slowed potassium kinetics in mice lacking aquaporin-4 water channels. *Glia*. 2006; 53: 631-6.
13. Wang Y and Tajkhorshid E. Nitric oxide conduction by the brain aquaporin AQP4. *Proteins*. 2010; 78: 661-70.

14. Musa-Aziz R, Chen LM, Pelletier MF and Boron WF. Relative CO2/NH3 selectivities of AQP1, AQP4, AQP5, AmtB, and RhAG. *Proceedings of the National Academy of Sciences of the United States of America*. 2009; 106: 5406-11.
15. Fang X, Yang B, Matthay MA and Verkman AS. Evidence against aquaporin-1-dependent CO2 permeability in lung and kidney. *J Physiol*. 2002; 542: 63-9.

Figure legends. "*In vivo* NADH fluorescence imaging…". Thrane AS, Takano T, Rangroo Thrane V, Wang F, Peng W, Ottersen OP, Nedergaard M and Nagelhus EA

Figure 1. Deletion of *Aqp4* increased NADH fluorescence in microwatershed areas during CSD. (**A**) Experimental setup. Following induction of CSD in living *Aqp4*$^{-/-}$ and wild type (WT) mice, we measured changes in NADH fluorescence with 2PLSM, cerebral blood flow (CBF) with laser Doppler flowmetry (LDF), extracellular concentration of K^+ ($[K^+]_o$) with K^+-ion-sensitive microelectrodes (ISM), DC potential, and tissue partial pressure of oxygen (tpO2) (not illustrated). (**B**) Immunofluorescence micrographs from WT and *Aqp4*$^{-/-}$ mice illustrating AQP4 expression in cerebral cortex. AQP4 (green), GFAP (red) and DAPI (blue). (**C**) Endogenous NAD^+ and its reduced counterpart NADH are key coenzymes in glycolysis, the citric acid cycle, and the mitochondrial respiratory chain. Since only NADH is fluorescent (and not NAD^+), two-photon NADH imaging offers maps of tissue redox state that can be used as a proxy of tissue oxygenation. (**D**) *Left*: NADH fluorescence images of cerebral cortex in WT (75 μm depth) and *Aqp4*$^{-/-}$ (105 μm depth) mice. Green is FITC-dextran labeled blood vessels. NADH fluorescence is largely uniform, except where NADH is made less visible by the presence of large pial vessels at the surface of the brain. *Right*: Representative false color images of change in NADH fluorescence ($\Delta F/F_0$) from baseline intensity, during the early (CSD wave) and late phase of CSD (hypoxic phase), and after recovery. In the early phase of CSD, when DC potential dropped, cortical tissue showed a complex pattern of NADH decrease (dip, shown in green) and increase (overshoot, shown in red/orange), (8). At a later stage, when DC potential had normalized, all regions showed

increased NADH fluorescence (hypoxic phase), before gradually returning to baseline level. Scale bar represents 50 μm. (**E**) Running average traces ($\Delta F/F_0$) for the biphasic NADH response during CSD, showing whole field ("total"), dip and overshoot in WT and *Aqp4*$^{-/-}$ mice. Duration of DC shift is indicated. $^{*}P < 0.05$, $n = 5$ animals in each group, unpaired *t* test. (**F**) Bar graph representing the peak change in NADH fluorescence in WT and *Aqp4*$^{-/-}$ mice. $P = 0.394$ (total), 0.329 (dip) and 0.00762 (overshoot), $n = 5$ animals in each group, unpaired *t* test. Data are shown as mean ± SEM.

Figure 2. Deletion of *Aqp4* did not affect vascular oxygen supply but delayed extracellular K^+ clearance in CSD. (**A**) Representative laser Doppler recordings (black) and a running average of these recordings (red) demonstrating the hyperemic response during CSD in *Aqp4*$^{-/-}$ and WT mice. (**B**, **C**) Bar graphs summarizing the effect of *Aqp4* deletion on peak amplitude and duration of the CSD hyperemic response. $P = 0.876$ (peak), 0.794 (duration), $n = 22$ (WT) and 41 (*Aqp4*$^{-/-}$) stimulations from 7 (WT) and 12 (*Aqp4*$^{-/-}$) animals, unpaired *t* test. (**D**) Line graph showing mean cortical tpO_2 before (basal) and during CSD in WT and *Aqp4*$^{-/-}$ mice, measured using oxygen sensitive microelectrodes. $P = 0.264$ (base), 0.555 (trough), $n = 6$ (WT) and 8 (*Aqp4*$^{-/-}$) animals, unpaired *t* test. (**E, F**) Bar graphs showing mean cortical tpO_2 slope decline and recovery. $P = 0.641$ (decline), $P = 0.818$ (recovery), $n = 6$ (WT) and 8 (*Aqp4*$^{-/-}$) animals, unpaired *t* test. (**G, H**) Representative traces and bar graphs summarizing the effects of *Aqp4* deletion on amplitude of the DC-shift. $^{*}P = 0.0223$, $n = 6$ (WT) and 8 (*Aqp4*$^{-/-}$) animals, unpaired *t* test. (**I**) Running averages of extracellular concentration of K^+($[K^+]_o$) during CSD for WT (black) and *Aqp4*$^{-/-}$ mice (red), acquired using K^+-ion-sensitive-

microelectrodes (ISM). Inset: K^+-ISM calibration curve. n = 7 (WT) and 12 (*Aqp4*$^{-/-}$). (**J-M**) Bar graphs summarizing the effect of *Aqp4* deletion on peak $[K^+]_o$, time to peak, $[K^+]_o$ recovery rate, and duration of $[K^+]_o$ elevation in CSD. $[K^+]_o$ peak is reduced and $[K^+]_o$ recovery is delayed in *Aqp4*$^{-/-}$ mice. $^*P$ = 0.0459 (duration), $^{**}P < 0.001$ (peak and recovery rate), P = 0.855 (time to peak), n = 22 (WT) and 41 (*Aqp4*$^{-/-}$) CSD responses from 7 (WT) and 12 (*Aqp4*$^{-/-}$) animals, unpaired t test. Data are shown as mean ± SEM.

Fig. 1

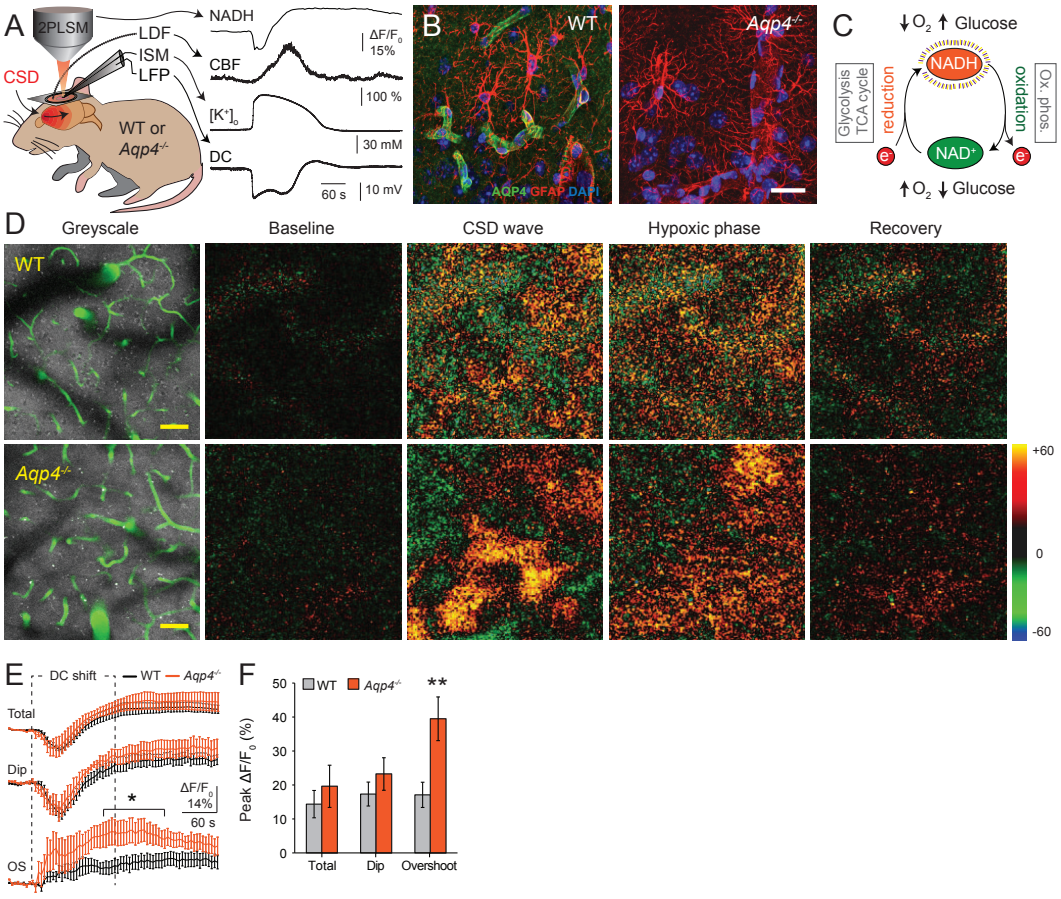
A
2PLSM
CSD
LDF
ISM
LFP
WT or Aqp4-/-
NADH
CBF
[K+]o
DC
ΔF/F0 15%
100 %
30 mM
60 s
10 mV
B
WT
Aqp4-/-
AQP4 GFAP DAPI
C
↓O2 ↑ Glucose
Glycolysis TCA cycle
reduction
NADH
NAD+
oxidation
Ox. phos.
e-
↑O2 ↓ Glucose
D
Greyscale
Baseline
CSD wave
Hypoxic phase
Recovery
WT
Aqp4-/-
+60
0
-60
E
DC shift
WT
Aqp4-/-
Total
Dip
OS
ΔF/F0 14%
60 s
*
F
WT
Aqp4-/-
**
Peak ΔF/F0 (%)
50
40
30
20
10
0
Total
Dip
Overshoot

Fig. 2

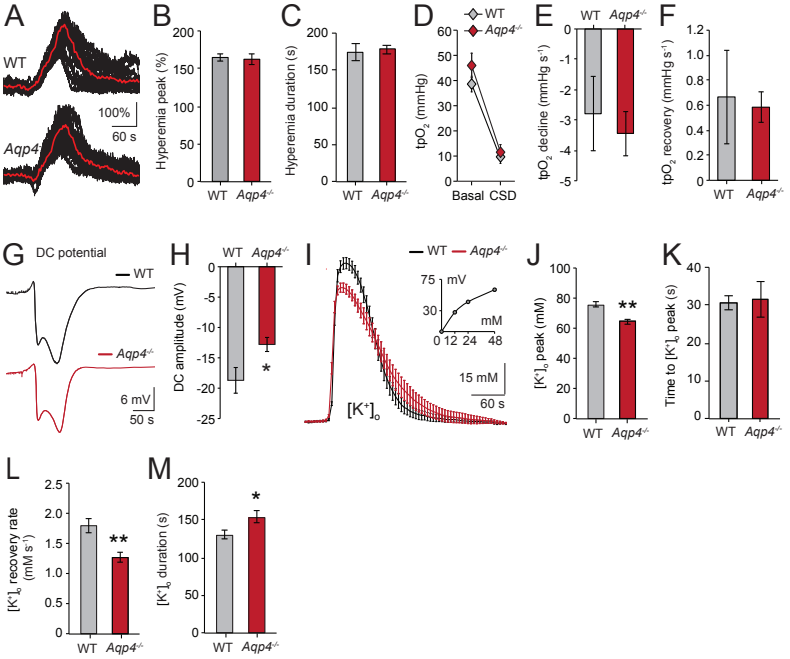
A
WT
Aqp4-/-
100%
60 s
B
Hyperemia peak (%)
C
Hyperemia duration (s)
D
WT
Aqp4-/-
tpO2 (mmHg)
Basal CSD
E
tpO2 decline (mmHg s-1)
F
tpO2 recovery (mmHg s-1)
G
DC potential
6 mV
50 s
H
DC amplitude (mV)
I
[K+]o
75 mV
30
mM
0 12 24 48
15 mM
60 s
J
[K+]o peak (mM)
K
Time to [K+]o peak (s)
L
[K+]o recovery rate (mM s-1)
M
[K+]o duration (s)

III

IV

Paravascular microcirculation facilitates rapid lipid transport and astrocyte signaling in the brain

Vinita Rangroo Thrane[1,2,3]†*, Alexander S. Thrane[1,2,3]†, Benjamin A. Plog, Meenakshisundaram Thiyagarajan[1], Jeffrey J. Iliff[1], Rashid Deane[1], Erlend A. Nagelhus[2,3], Maiken Nedergaard[1]

Key words: lipophilic, glia, endfoot, cerebrospinal fluid, calcium

[1]Division of Glia Disease and Therapeutics, Center for Translational Neuromedicine, Department of Neurosurgery, University of Rochester Medical Center, Rochester, New York 14642.

[2]Letten Institute of Basic Medical Sciences, University of Oslo, 0317 Oslo, Norway.

[3]Centre for Molecular Medicine Norway, Nordic EMBL Partnership, University of Oslo, 0318 Oslo, Norway.

†These authors contributed equally to the paper

Correspondence: Vinita Rangroo Thrane, MD, Centre for Molecular Medicine Norway, Nordic EMBL Partnership, University of Oslo, P.O. Box 1137 Blindern, N-0318 Oslo, Norway. E-mail: vrangroo@gmail.com. Phone: +47 999126007.

Acknowledgements: We thank Jeffrey Rothstein and Ole Petter Ottersen for the transgenic animals, and Georg A. Gundersen for the electron micrograph. This work was supported by the US National Institutes of Health (NS075177 and NS078304 to M.N., and F31NS073390 to N.A.S.), Research Council of Norway (NevroNor, and FUGE grants), Letten Foundation, and Fulbright Foundation. **Disclosure:** The authors declare no conflict of interest.

Abstract

The paravascular circulation of cerebrospinal fluid (CSF) may serve as a lymphatic system in the brain. Using *in vivo* two-photon imaging we demonstrate that the paravascular space facilitates selective movement of small lipophilic molecules and rapid glial calcium signaling in the brain. Depressurizing the paravascular system leads to unselective lipid diffusion, intracellular lipid accumulation and pathological signaling in astrocytes.

The brain, unlike other organs, lacks a separate lymphatic system to clear interstitial fluid, transport lipids and facilitate diffusion of signaling molecules. The extracellular space is narrow and highly tortuous in neuropil, and is incompatible with rapid fluid and solute movement[1, 2]. Hydrophilic tracers have recently been shown to circulate through the brain in cerebrospinal fluid (CSF) via the paravascular space (PVS)[3]. This anatomical space is completely ensheathed by astrocyte endfeet and is well-positioned to serve as a highway for glial-glial and glial-vascular communication[2]. However, the role of the PVS in lipid transport and signal transduction has not been investigated *in vivo*. Two related questions therefore remain unanswered: can the PVS facilitate rapid lipid transport and might the PVS act as a separate compartment for astrocyte signaling?

To outline the CSF microcirculation, tracers were infused via the cisterna magna **(Fig. 1a)**. Both the fixable lipophilic tracer Texas red hydrazide (TXR, 0.621 kDa) and the hydrophilic tracer tetramethylrhodamine (TMR, 3 kDa) moved rapidly through the brain along cerebral blood vessels (tracer penetration: TXR 12.57 ± 4.41 and TMR 38.71 ± 7.70% brain area at 30 min). Surprisingly, lipophilic tracers of small molecular weight showed as limited parenchymal penetration as large hydrophilic tracers (fluorescein isothiocyanate dextran, FITC, 2000 kDa) in cortical grey matter (tracer penetration 15.56 ± 2.81% brain area) **(Fig. 1b)**[3].

We used *in vivo* two-photon laser scanning microscopy (2PLSM) to further explore the highly selective paravascular movement of lipophilic tracers. This restricted movement is unexpected as biologically relevant lipid molecules, such as prostaglandins, cholesterol and palmitic acid, are small (< 1 kDa) and cell permeable [4-8]. We demonstrated that the movement of small (< 1 kDa) lipophilic tracers was highly selective to the PVS (palmitic acid, rhod-2, TXR, sulforhodamine SR101 and

Oregon green BAPTA-1 OGB) **(Fig. 2a, Supplementary Fig. 1a)**. Intra-arterial Texas red dextran or FITC were used to morphologically distinguish cortical surface arteries and veins as well as penetrating arterioles and venules **(Supplementary Fig. 1a)**[3]. Cross-sectional intensity projections of penetrating arterioles confirmed paravascular tracer selectivity **(Fig. 2b)**. By analyzing regions of interest representing the PVS and the surrounding tissue **(Fig. 2c)**, we showed that the lipophilic tracers were rapidly cleared via the PVS without gaining access to the surrounding tissue (normalized tracer fluorescence ratio of PVS to surround at 60 min: OGB 3.36 ± 0.79, SR101 3.50 ± 0.88, rhod-2 4.21 ± 1.35) **(Fig. 2d)**. Deletion of the astrocyte water channel aquaporin-4 has recently been shown to slow the circulation of hydrophilic tracers in CSF, but did not affect lipophilic tracer movement (PVS to surround ratio in *Aqp4*$^{-/-}$ at 60 min: 4.83 ± 1.42) [3].

We next examined whether lipopohilic tracers enter and exit the brain via similar arterio-venous paravascular routes as hydrophilic molecules[3]. Using NG2-DsRed mice that have fluorescently labeled vascular smooth muscle in arterioles, we showed that the biologically relevant tracer palmitic acid entered via a para-arterial route **(Fig. 2e)**. Moreover, using 2PLSM imaging we showed that lipophilic tracer (rhod-2) moved sequentially in the PVS surrounding surface arteries, penetrating arterioles, capillaries and venules following cisterna magna infusion (normalized fluorescence of rhod-2 to eGFP expressed under the astrocyte specific *Glt1* promoter: 30 min: arteriole 1.90 ± 0.38, capillary 0.45 ± 0.247, venule 0.23 ± 0.172; 60 min: arteriole 2.34 ± 0.44, capillary 0.94 ± 0.21, venule 0.44 ± 0.25; 90 min: arteriole 1.74 ± 0.32, capillary 0.72 ± 0.27, venule 1.33 ± 0.34) **(Fig. 2f, g)**. These observations indicate that lipophilic molecules enter the brain via para-arterial and exit via para-venous routes.

To investigate the consequences of disrupting the paravascular microcirculation, we temporarily depressurized the PVS by puncturing the cisterna magna (CMP) **(Fig 3a)**. We took advantage of astrocyte specific calcium indicators (such as rhod-2), which are lipophilic tracers that become concentrated inside cells due to their acetoxymethyl group[9, 10]. This improved the sensitivity for detecting parenchymal influx. CMP accelerated intracellular accumulation of lipophilic tracer rhod-2 when applied to the cortical surface or injected intraparenchymally (eGFP normalized fluorescence of rhod-2 astrocyte labeling intensity at 30 min for sham control: 1.54 ± 0.36 vs. CMP: 4.01 ± 0.57) **(Fig. 3b, c)**. Conversely, *Aqp4* deletion, which slows paravascular water movement, did not enhance cellular tracer uptake (*Aqp4*$^{-/-}$ control at 30 min: 1.56 ± 0.27) **(Fig. 3d)**. Thus, an intact PVS restricts lipid diffusion and cellular uptake.

To investigate the role of the PVS as a signaling compartment, we compared spontaneous astrocyte calcium activity in the cortex of awake mice subjected to CMP or sham surgery. Interestingly, depressurizing the PVS caused increased frequency and decreased synchronization of calcium signaling (ctrl 2.21 ± 0.19 vs. CMP 3.08 ± 0.29 mHz cell^{-1}; cell-cell correlation: ctrl 0.69 ± 0.03 vs. CMP 0.60 ± 0.03) **(Fig. 3e-g)**[10]. Other aspects of astrocyte signaling were not affected (amplitude: ctrl 39.08 ± 2.10% vs. CMP 39.98 ± 2.18%; duration: ctrl 21.29 ± 1.29 s vs. CMP 24.74 ± 1.62 s; P(active over 15 min): ctrl 75.83 ± 4.20% vs. CMP 7981.05 ± 4.18%) **(Supplementary Fig. 1b-d)**. Astrocyte calcium activity has been shown to propagate along blood vessels and the waves are largely ATP mediated[11-13]. We therefore inserted a microelectrode into the PVS *in situ* and stimulated calcium transients by injecting ATP. The rapid movement of agonist in the PVS stimulated a brisk calcium wave spreading outwards from the blood vessel, which propagated faster and over a

larger area than when ATP was injected intraparenchymally (wave propagation: parenchyma 4.47 ± 0.56 vs. PVS 8.89 ± 1.22 μm s^{-1}; wave diameter: parenchyma 142.86 ± 12.50 vs. PVS 315.81 ± 51.42 μm) **(Fig. 3h)**.

To summarize, we show that the brain has a distinct paravascular compartment for lipid transport and glial signaling within the narrow confines of the neuropil. Lipid transport follows the arterio-venous circulation and is highly selective to the PVS. Compromising paravascular transport causes increased intracellular lipid accumulation and abnormal astrocyte calcium signaling. We speculate that lipid transport in the brain may be spatially restricted due to the high concentration of astrocyte secreted lipoproteins in CSF. Interestingly, lipoprotein mutations are the largest known risk factor for developing Alzheimer disease[14, 15]. Ours and previous data therefore suggest that the paravascular compartment may represent a lymphatic equivalent in the brain that resorbs interstitial fluid, selectively transports small lipid molecules and can act as a signaling highway for coordinated astrocyte communication.

References

1. Abbott, N.J. Evidence for bulk flow of brain interstitial fluid: significance for physiology and pathology. *Neurochemistry international* **45**, 545-552 (2004).
2. Sykova, E. & Nicholson, C. Diffusion in brain extracellular space. *Physiological reviews* **88**, 1277-1340 (2008).
3. Abbott, N.J., Patabendige, A.A., Dolman, D.E., Yusof, S.R. & Begley, D.J. Structure and function of the blood-brain barrier. *Neurobiology of disease* **37**, 13-25 (2010).
4. Iliff, J.J.*, et al.* A Paravascular Pathway Facilitates CSF Flow Through the Brain Parenchyma and the Clearance of Interstitial Solutes, Including Amyloid beta. *Sci Transl Med* **4**, 147ra111 (2012).
5. Iliff, J.J.*, et al.* Brain-wide pathway for waste clearance captured by contrast-enhanced MRI. *The Journal of clinical investigation* (2013).
6. Attwell, D.*, et al.* Glial and neuronal control of brain blood flow. *Nature* **468**, 232-243 (2010).
7. Slezak, M. & Pfrieger, F.W. New roles for astrocytes: regulation of CNS synaptogenesis. *Trends in neurosciences* **26**, 531-535 (2003).
8. Fukata, Y. & Fukata, M. Protein palmitoylation in neuronal development and synaptic plasticity. *Nature reviews. Neuroscience* **11**, 161-175 (2010).
9. Takano, T.*, et al.* Astrocyte-mediated control of cerebral blood flow. *Nat Neurosci* **9**, 260-267 (2006).
10. Higashimori, H., Blanco, V.M., Tuniki, V.R., Falck, J.R. & Filosa, J.A. Role of epoxyeicosatrienoic acids as autocrine metabolites in glutamate-mediated K+ signaling in perivascular astrocytes. *American journal of physiology. Cell physiology* **299**, C1068-1078 (2010).
11. Moore, C.I. & Cao, R. The hemo-neural hypothesis: on the role of blood flow in information processing. *Journal of neurophysiology* **99**, 2035-2047 (2008).
12. Paredes, R.M., Etzler, J.C., Watts, L.T., Zheng, W. & Lechleiter, J.D. Chemical calcium indicators. *Methods (San Diego, Calif.)* **46**, 143-151 (2008).
13. Thrane, A.S.*, et al.* General anesthesia selectively disrupts astrocyte calcium signaling in the awake mouse cortex. *Proceedings of the National Academy of Sciences of the United States of America* **109**, 18974-18979 (2012).
14. Simard, M., Arcuino, G., Takano, T., Liu, Q.S. & Nedergaard, M. Signaling at the gliovascular interface. *J. Neurosci.* **23**, 9254-9264 (2003).
15. Thrane, A.S.*, et al.* Critical role of aquaporin-4 (AQP4) in astrocytic Ca2+ signaling events elicited by cerebral edema. *Proc. Natl. Acad. Sci. U. S. A.* **108**, 846-851 (2010).
16. Koizumi, S., Fujishita, K. & Inoue, K. Regulation of cell-to-cell communication mediated by astrocytic ATP in the CNS. *Purinergic signalling* **1**, 211-217 (2005).
17. Parpura, V. & Verkhratsky, A. Homeostatic function of astrocytes: Ca(2+) and Na(+) signalling. *Translational neuroscience* **3**, 334-344 (2012).
18. Leoni, V., Solomon, A. & Kivipelto, M. Links between ApoE, brain cholesterol metabolism, tau and amyloid beta-peptide in patients with cognitive impairment. *Biochemical Society transactions* **38**, 1021-1025 (2010).
19. Castellano, J.M.*, et al.* Low-density lipoprotein receptor overexpression enhances the rate of brain-to-blood Abeta clearance in a mouse model of beta-amyloidosis. *Proceedings of the National Academy of Sciences of the United States of America* **109**, 15502-15507 (2012).

Figure legends

Figure 1 Rapid paravascular movement of lipophilic tracers. **(a)** Experimental design for studying tracer (red) movement in paravascular space via cisterna magna. Inset: electron micrograph of penetrating arteriole (PA) with surrounding paravascular space (PVS). Scale bar represents 2.5 μm. **(b)** Epifluorescence montages illustrate distribution of Texas red hydrazide (TXR), fluorescein isothiocyanate dextran (FITC) and tetramethylrhodamine dextran (TMR). Top insets display auto-thresholded images. Scale bar represents 200 μm. **(c)** Quantification of brain parenchymal penetration. $^{**}P < 0.01$, $n = 6$ animals for all groups, Mann-Whitney *U*. Data are shown as mean ± SEM.

Figure 2 Lipophilic tracers selectively enter and exit brain via paravascular space surrounding arterioles and venules. **(a)** Left: *in vivo* two-photon image of rhod-2 circulation via the paravascular space in *Glt1*-eGFP mouse. White circles indicate penetrating arterioles. Surface artery (SA). Scale bar represents 100 μm. Right: high magnification images of the paravascular space surrounding penetrating arteriole at serial depths. **(b)** Cross sectional intensity traces illustrating the paravascular space (rhod-2, red) and intravascular space (Texas red dextran) around a penetrating arteriole (PA). Endfoot (EF). Scale bar represents 7.5 (top) and 5 (bottom) μm. **(c)** Region of interest (left) and analysis of tracer intensity (right) in the paravascular space and surrounding parenchyma. Scale bar represents 10 μm. $n = 24$ arterioles from 7 animals, paired *t* test. **(d)** Ratio of lipophilic tracer fluorescence in paravascular space to surrounding parenchyma at 60 min. Sulforhodamine (SR101), Oregon green BAPTA (OGB). $n = 11$ (OGB), 15 (SR101), 24 (rhod-2) and 12 (*Aqp4*$^{-/-}$ rhod-2) arterioles from 16 animals (total), unpaired *t* test. **(e)** Immunofluorescence

micrographs from NG2-DsRed mouse show entry of palmitic acid lipid along the paravascular space. Antibody against lectin outlines vascular endothelium. White arrows indicate arterioles. Scale bar represents 100 μm. **(f, g)** Representative images and quantification of rhod-2 tracer in the paravascular space surrounding an arteriole, a capillary and venule. Scale bars represent 7.5 μm. n = 24 (arterioles), 14 (capillaries) and 12 (venules) from 7 animals, paired t test. ***$P < 0.001$. Data are shown as mean ± SEM.

Figure 3 Depressurizing the paravascular space impairs lipid transport and astrocyte signaling. **(a)** Cisterna magna puncture (CMP) temporarily depressurizes the paravascular space. Lipophilic tracer was applied to cortical surface or injected into parenchyma. **(b, c)** Two-photon images and quantification of lipid tracer labeling in eGFP expressing cortical astrocytes (circled) following sham control and cisterna magna puncture (CMP). Scale bars represent 75 μm. n = 45 cells from 5 animals for both groups, unpaired t test. **(d)** Normalized rhod-2 astrocyte labeling intensity. n = 45 (Ctrl), 32 ($Aqp4^{-/-}$) and 45 (CMP) cells from 14 animals (total), one-way ANOVA. **(e)** Representative traces of spontaneous calcium activity from cortical astrocytes in awake mice. Synchronized (red) and individual (green) transients. **(f, g)** CMP increases frequency and reduces synchronization of astrocyte calcium signals. n = 60 (ctrl) and 52 (CMP) cells from 10 animals (total), unpaired t test. **(h, i)** ATP injection (visualized with FITC-dextran) into the paravascular space stimulates rapid and widespread astrocyte calcium wave spreading outwards from the blood vessel. n = 16 (intraparenchymal, IP) and 9 (paravascular space, PVS) slices from 11 animals (total), unpaired t test. Scale bar represents 40 μm. *$P < 0.05$, **$P < 0.01$, ***$P < 0.001$. Data are shown as mean ± SEM.

Fig. 1

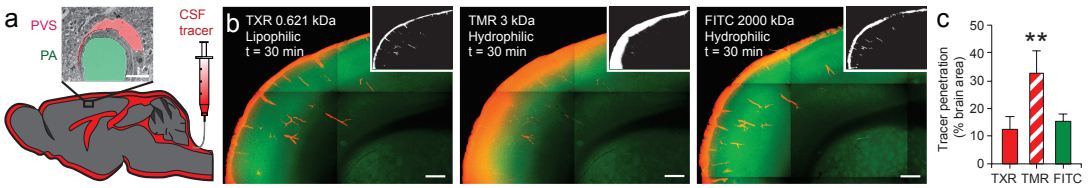

Fig. 2

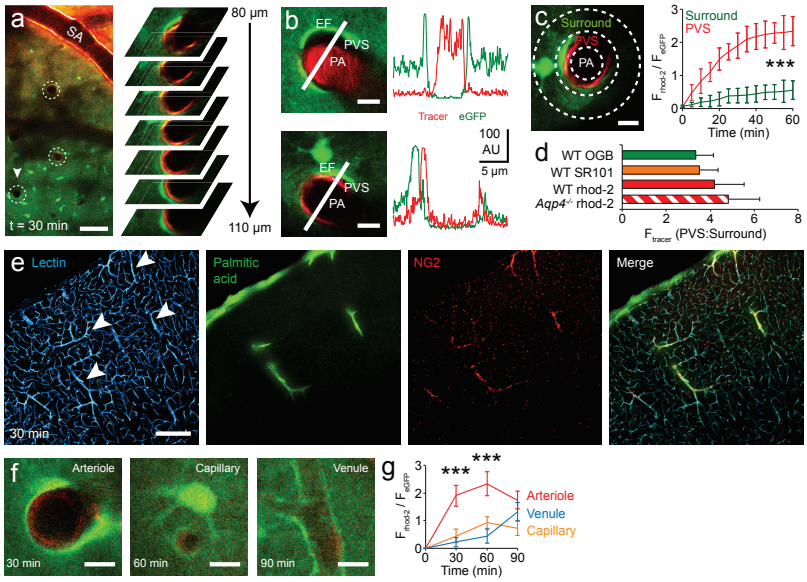

Fig. 3

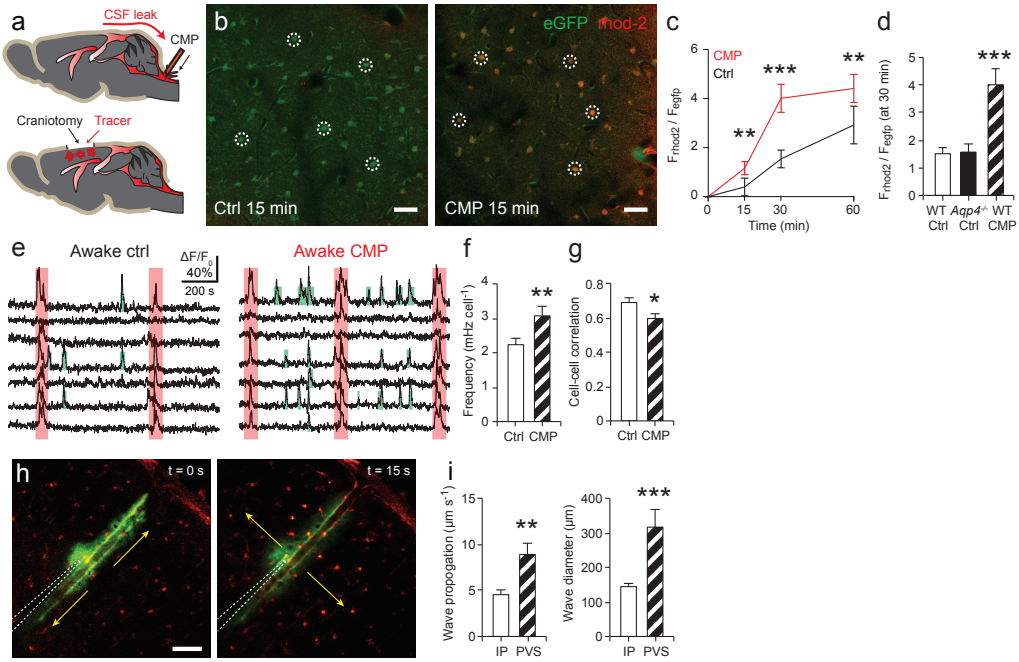

Paravascular microcirculation facilitates rapid lipid transport and astrocyte signaling in the brain

Vinita Rangroo Thrane[1,2,3]†*, Alexander S. Thrane[1,2,3]†, Benjamin A. Plog, Meenakshisundaram Thiyagarajan[1], Jeffrey J. Iliff[1], Rashid Deane[1], Erlend A. Nagelhus[2,3], Maiken Nedergaard[1]

Supplemetary Figure 1 (a) *In vivo* two-photon image of the cortical vascular tree outlined using Texas red dextran. Collapsed z-stack from 0 - 200 μm, surface arteries (SA), surface veins (SV), penetrating arterioles (PA), penetrating venules (PV). Scale bar represents 100 μm. **(b-d)** Cisterna magna puncture (CMP) causes no alteration in amplitude (n = 54 ctrl and 49 CMP cells from 6 and 5 animals, respectively), duration (n = 55 ctrl and 49 CMP cells from 6 and 5 animals, respectively) and percent of active cells (n = 60 ctrl and 52 CMP cells from 6 and 5 animals, respectively) in astrocyte calcium signaling. Unpaired t test. Data are shown as mean ± SEM.

Supplemental Figure 1

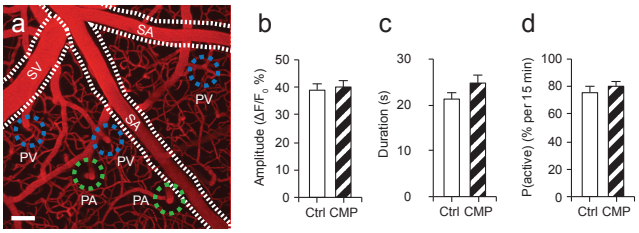

Materials and Methods

Animals. *Glt-1*-eGFP, NG2-DsRed and *Aqp4*$^{-/-}$ mice were generated as outlined previously,[1, 2] and mice of either sex from 6-12 weeks used in conjunction with C57BL/6J wild-types (Jackson Laboratories) were used for experiments. All animals, except those used for awake imaging, were anesthetized with ketamine (0.12 mg g^{-1}) and xylazine (0.01 mg g^{-1}) intraperitoneally (i.p.). All animal experiments were approved by the Animal Care and Use Committee of the University of Rochester.

Tracer preparation and intracisternal infusion. The hydrophilic tracers fluorescein isothiocyanate (FITC) dextran (0.5%, 2000 kDa) and tetramethylrhodamine (TMR) dextran (0.5%, 3 kDa) and the lipophilic, cell-permeant tracers palmitic acid (BODIPY® FL C_{16} 1 mg ml^{-1}, 0.474 kDa, Molecular Probes), Texas red hydrazide (0.4-2 mM, 0.621 kDa), sulforhodamine SR101 acid chloride (0.2 mM, 0.607 kDa), rhod-2 AM (acetoxymethyl ester) (0.45-4.5 mM, 1.124 kDa) and Oregon-green BAPTA-1 OGB AM (0.5 mM, 1.258 kDa, acquired from Invitrogen and Sigma-Aldrich) were constituted in artificial cerebrospinal fluid (aCSF).[1] These tracers were chosen because of their small size (comparable to endogenous lipids), relevance to *in vivo* imaging (e.g. as calcium indicators) and ability to cross cell membranes, such as the endfoot membrane that encases the PVS.[1, 3] The mice were secured in a stereotaxic frame, and a 30G needle was inserted into the cisterna magna. Tracer dissolved in aCSF was delivered at a rate of 2 µL min^{-1} over 5 minutes with a syringe pump (Harvard Apparatus). The dyes were used at higher concentrations to allow the approximate dilution factor of 1:5 when 10 µL was infused into the total mouse CSF volume of 40 µL.[4] The cisterna magna was punctured

with a 30G needle to drain the CSF and depressurize the PVS. In sham control animals the cisterna magna was exposed without puncturing it.

***Ex vivo* imaging.** Mouse preparation was modified from published protocols.[2] The animals were perfused transcardially with 4% paraformaldehyde in 0.1M phosphate buffered saline (pH 7.4) and post-fixed overnight. 100 μm vibratome brain sections were then cut and mounted on slides using PROLONG anti-fade gold with DAPI (Invitrogen). Epifluorescence multi-channel whole-brain montages were collected using a virtual slice module (Microlucida Software, Microbrightfield). Exposure and gain levels were maintained constant throughout the study. The percentage of brain tracer penetration was calculated using the area fraction function in ImageJ (NIH) on consistently thresholded images, as described previously.[2] For EM experiments 0.1% glutaraldehyde was added to the perfusate/fixation solution and the ultra-thin Lowicryl sections were prepared as outlined previously.[5] Images were obtained 125 μm below the surface in the barrel cortex.

***In vivo* imaging.** Anesthetized animals were intubated and artificially ventilated with a small animal ventilator (CWE), their temperature was maintained using a heating pad, and blood gasses were collected via a femoral arterial cannula to ensure physiological hemodynamic parameters.[1] To visualize the cerebral vasculature FITC or Texas red dextran (Invitrogen) were administered intra-arterially. A steel frame was secured to the skull using dental cement, and a 2 mm craniotomy was opened over the somatosensory cortex with particular care being taken not to puncture the dura mater. To stabilize

imaging, the craniotomy was then sealed with agarose (1.5%, type III-A, Sigma) and a coverslip. A Mai Tai laser (SpectraPhysics) attached to a confocal scanning system (Fluoview 300, Olympus) and an upright microscope (IX51W) were used. Tracers and eGFP were excited at 850 - 890 nm and emission was collected at 575 - 645 nm using a 20x (0.95NA) lens. 512x512 pixel frames were collected from the pial surface to 200 μm depth at 20 μm z-steps. Superficial arteries and veins were distinguished based on morphology (e.g. arteries pass more superficially, and have fewer branches near the surface).[2] Tracer movement was analyzed as outlined previously by defining doughnut shaped ROIs around penetrating arterioles.[2]

Awake calcium imaging. Animal preparation was performed as described by the authors previously.[3] Briefly, mice were anesthetized with isoflurane (1.0 - 1.5%), head-restrained with a steel mini-frame, and habituated to imaging through training sessions. The craniotomy was made as outlined above and rhod-2 (2 mM, Invitrogen) was loaded onto exposed cortex before applying the coverslip. Calcium signaling was imaged 75 - 125 μm depth and dual channel (rhod-2 and eGFP) frames were collected at 0.2 or 1 Hz. Calcium transients were analysed using previously described custom-made software (MatLab Inc.) and Image J (NIH)[1, 3].

***In situ* calcium imaging.** Acute cortical slices were prepared from P10-20 mice as described previously.[1, 6] Briefly, 400 um acute cortical slices were incubated with rhod-2 (2 mM) for 20 min, before being transferred to a recording chamber where they were imaged and analyzed as outlined before.

Statistical analyses. All analysis was performed using IBM SPSS Statistics 19 and all tests were two-tailed where significance was achieved at $\alpha = 0.05$ level (for details see supporting information). Wherever necessary a Bonferroni correction for multiple testing was done.

1. Thrane, A.S.*, et al.* Critical role of aquaporin-4 (AQP4) in astrocytic Ca2+ signaling events elicited by cerebral edema. *Proc. Natl. Acad. Sci. U. S. A.* **108**, 846-851 (2010).
2. Iliff, J.J.*, et al.* A Paravascular Pathway Facilitates CSF Flow Through the Brain Parenchyma and the Clearance of Interstitial Solutes, Including Amyloid beta. *Sci Transl Med* **4**, 147ra111 (2012).
3. Thrane, A.S.*, et al.* General anesthesia selectively disrupts astrocyte calcium signaling in the awake mouse cortex. *Proceedings of the National Academy of Sciences of the United States of America* **109**, 18974-18979 (2012).
4. Oshio, K., Watanabe, H., Song, Y., Verkman, A.S. & Manley, G.T. Reduced cerebrospinal fluid production and intracranial pressure in mice lacking choroid plexus water channel Aquaporin-1. *FASEB journal : official publication of the Federation of American Societies for Experimental Biology* **19**, 76-78 (2005).
5. Nielsen, S.*, et al.* Specialized membrane domains for water transport in glial cells: high-resolution immunogold cytochemistry of aquaporin-4 in rat brain. *J. Neurosci.* **17**, 171-180 (1997).
6. Simard, M., Arcuino, G., Takano, T., Liu, Q.S. & Nedergaard, M. Signaling at the gliovascular interface. *J. Neurosci.* **23**, 9254-9264 (2003).

V

VI

Ammonia compromises astrocyte potassium buffering and impairs neuronal inhibition without causing swelling *in vivo*

Vinita Rangroo Thrane[1,2,3]†*, Alexander S. Thrane[1,2,3]†, Fushun Wang[1], Maria L. Cotrina[1], Nathan A. Smith[1], Michael Chen[1], Ning Kang[1], Takumi Fujita[1], Erlend A. Nagelhus[2,3], Maiken Nedergaard[1]

Key words: ammonia, astrocyte, potassium, seizure, bumetanide

[1]Division of Glial Disease and Therapeutics, Center for Translational Neuromedicine, Department of Neurosurgery, University of Rochester Medical Center, Rochester, New York 14642.

[2]Center for Molecular Biology and Neuroscience, Department of Anatomy, Institute of Basic Medical Sciences, University of Oslo, 0317 Oslo, Norway.

[3]Center for Molecular Medicine Norway, Nordic EMBL Partnership, University of Oslo, 0318 Oslo, Norway.

†These authors contributed equally to the paper

*To whom correspondence should be adressed:

Vinita R. Thrane, MD, Center for Molecular Medicine Norway, Nordic EMBL Partnership, University of Oslo, P.O. Box 1137 Blindern, N-0318 Oslo, Norway.

E-mail: vrangroo@gmail.com

Phone: +47 999126007

One sentence summary

Ammonia impairs neural inhibition by compromising astrocyte potassium buffering, and inhibiting Na+-K+-2Cl- cotransporter 1 (NKCC1) can effectively block this neurotoxic process.

Abstract

Ammonia is a ubiquitous waste product that accumulates in numerous metabolic disorders, causing neurological dysfunction ranging from learning impairment, to tremor, ataxia, seizures and coma. The brain is particularly vulnerable to ammonia as it readily crosses the blood-brain barrier and rapidly saturates its only removal pathway, glutamine synthetase, located in astrocytes. Although ammonia is believed to exert its neurotoxic effects through astrocyte swelling, here we show that swelling is only a terminal feature of ammonia toxicity *in vivo*. Instead, our data indicate that ammonia rapidly compromises astrocyte potassium buffering, leading to an increase in extracellular potassium. The potassium overload in turn increases Na^+-K^+-$2Cl^-$ cotransporter isoform 1 (NKCC1) activity and depolarizes the neuronal GABA reversal potential, thus impairing cortical inhibitory networks and causing severe neurological impairment. Inhibiting NKCC1 with the clinically used diuretic, bumetanide, potently treats the ammonia-induced neurological dysfunction. These data identify failure of potassium buffering in astrocytes as a central mechanism in ammonia neurotoxicity, and suggest that bumetanide may constitute a novel therapeutic option for disorders of ammonia handling.

[Main Text:]

Introduction

Ammonia is a waste product of cellular metabolism that is constantly generated throughout the body. Existing as 99% NH_4^+ and 1% NH_3 at physiological pH, ammonia is thus able to cross the blood-brain barrier by diffusing in its gas phase (NH_3) (*1*). If allowed to accumulate, ammonia causes brain dysfunction ranging from mild cognitive impairment, to seizures, coma and death (*2*).

Ammonia homeostasis is particularly important in the brain, as an equimolar amount of ammonia is simultaneously released with glutamate during neuronal firing (Fig. 1A) (*3*). Brain ammonia is almost exclusively detoxified by condensation with glutamate to form glutamine, a reaction catalyzed by glutamine synthetase (GS) with a rapid half-life of less than 3 s (*4*). GS has a higher affinity for ammonia than glutamate, suggesting that the removal of ammonia is prioritized over an excitotoxic neurotransmitter (*5*).

The current literature points to astrocytes as the primary target of ammonia toxicity, as they are the only cell type in the brain that express GS (*6*). Histological preparations from animals exposed to elevated ammonia in the context of liver failure display astrocyte pathology in the form of swelling (*7*). However, it remains unclear whether astrocyte swelling contributes to the initial deterioration of neurological functions characteristic of acute ammonia toxicity (*8*).

In order to elucidate the mechanisms responsible for ammonia toxicity in the brain, we use the *Otc*$^{spf\text{-}ash}$ mouse model. These mice have an X-linked mutation in the gene encoding ornithine transcarbamylase (*Otc*), a urea cycle enzyme essential for liver detoxification of

ammonia. *Otc*$^{spf\text{-}ash}$ mice are prone to developing rapid rises in plasma ammonia leading to severe neurological dysfunction and coma (*9*). Clinically relevant ammonia neurotoxicity can be studied in the absence of hepatic complications using the *Otc*$^{spf\text{-}ash}$ mouse model. Ammonia neurotoxicity in the context of acute liver failure, on the other hand, is associated with numerous ammonia-independent changes (e.g. neuroinflammation) that alter the neurological phenotype (*8*). *Otc*$^{spf\text{-}ash}$ mice thus provide an optimal model to study the direct effects of ammonia on the brain.

In this study we used *in vivo* optical imaging and electrophysiology in awake behaving *Otc*$^{spf\text{-}ash}$ mice and found that astrocyte swelling is only observed during the terminal stages of ammonia neurotoxicity. The earlier stages are, instead, characterized by a failure of astrocyte potassium buffering. The consequent increase in extracellular potassium ($[K^+]_o$) drives a Na^+-K^+-$2Cl^-$ cotransporter isoform 1 (NKCC1)-dependent depolarizing shift in the neuronal γ-aminobutyric acid (GABA) reversal potential (E_{GABA}). GABA, the main inhibitory transmitter in the brain, principally exerts its rapid hyperpolarizing (inhibitory) action via anion-permeable $GABA_A$ receptors (*10*). The depolarized E_{GABA} in ammonia neurotoxicity thus leads to a rapid impairment of neuronal inhibition. Bumetanide is a specific inhibitor of NKCC1 that is routinely used in clinical practice to treat fluid retention, with a favorable side-effect profile (*11*). In our awake mouse model, we found that inhibiting NKCC1 with bumetanide restored inhibitory transmission and protected the mice from ammonia-related neurological dysfunction.

Results

The *Otc*$^{spf\text{-}ash}$ mouse model is characterized by acute ammonia neurotoxicity

To characterize the effects of ammonia on brain function, we subjected awake adult male *Otc*$^{spf\text{-}ash}$ mice to an acute systemic ammonia load (NH_4Cl or NH_4Ac, 7.5 mmol kg^{-1} i.p.). Shortly after the injection, the mice developed a stereotypical sequence of neurological impairments, including decreased spontaneous movement, hypersensitivity to sound (hyperacusis), imbalance, tremor, ataxia, seizures, and in severe cases coma followed by death (Fig. 1A) (*12*).

The neurological phenotype in our model of OTC deficiency was accompanied by a brisk increase in the extracellular ammonia concentration ($[NH_4^+]_o$) in plasma (from 0.32 ± 0.7 to 4.21 ± 0.59 mM) and brain (from 0.54 ± 0.18 to 4.83 ± 0.52 mM) (Fig. 1B,C, Fig. S1A). The excess ammonia, in turn, caused an accumulation of glutamine in the brain via enzymatic trapping in astrocytes by GS (9.25 ± 0.34 μmol g^{-1}) (Fig. 1D, Fig. S1B) (*1, 6*). Similar to children born with OTC deficiency, the *Otc*$^{spf\text{-}ash}$ mice also had a baseline excess of both ammonia (plasma 0.32 ± 0.073 mM, brain 0.54 ± 0.19 mM) and glutamine (7.58 ± 0.52 μmol g^{-1}), and displayed some milder features of ammonia neurotoxicity, such as impaired learning (Fig.1 B-E, Fig. S1C, D) (*2, 9, 13*).

Next, we examined whether our disease model was characterized by any global hemodynamic changes, as this can occur in very severe ammonia toxicity (*2*). Cerebral perfusion pressure (CPP), cerebral blood flow (CBF), and intracranial pressure (ICP) were, however, all unchanged following the acute ammonia challenge (Fig. 1F). Finally, we employed several behavioral measures to track the progression and severity of ammonia neurotoxicity in a clinically relevant fashion. Using automated video tracking we found that spontaneous mouse movement decreased sensitively and early following the ammonia challenge (13.69 ± 1.48 vs. 0.42 ± 0.22 m min^{-1}) (Fig. 1H). We also developed a sensory-motor phenotype score that

allowed us to both track the onset of specific phenotypes (e.g. ataxia) and also grade their severity (0.53 ± 0.28 vs. 9.00 ± 0.46 out of 11) (Fig. 1H, Fig. S1E) (*9, 14*).

Acute ammonia exposure causes a robust seizure phenotype

In addition to cognitive, sensory, and motor impairment, children with OTC deficiency typically also develop seizures during episodes of transient increases in ammonia (*2, 12*). We used cortical, subcortical and muscle electrodes in awake mice to further explore this phenotype (Fig. 2A) (*8*). Around weaning *Otc*$^{spf\text{-}ash}$ mice occasionally developed spontaneous myoclonuses, which are brief (< 2 s) involuntary jerk-like movements that can be caused by seizure activity in either the cortex or subcortical structures (*15*). However, these events were scarce and too variable to allow careful study. We therefore used the aforementioned acute ammonia challenge to precipitate a more robust seizure phenotype. The intermediate doses (7.5 mmol kg^{-1}) employed in most of our study caused numerous myoclonic events (ME), whilst a lethal dose (10 mmol kg^{-1}) of ammonia also induced longer lasting generalized tonic-clonic seizures (Fig. 2B).

We proceed to examine the ME in more detail, and found several lines of evidence indicated that these events were a form of centrally generated seizures. Firstly, we found that the myoclonic electroencephalogram (EEG) discharges consistently preceded the electromyogram (EMG) discharges by 19.42 ± 4.78 s, indicating that these events originated in the brain (Fig. 2C). Secondly, we were able to detect 3-9 Hz poly-spike and wave (SWD) discharges typical of myoclonic epilepsy using EEG and the associated myoclonic jerks using video-analysis and EMG (Fig. S2A-C and Video 1) (*16, 17*). Finally, we found that the frequency of ME closely correlated with overall disease severity (assessed by the aforementioned phenotype score), which both showed similar dose-response curve (Fig. 2D). Importantly, both overall phenotype and ME

were entirely masked by anesthesia, emphasizing the need for recordings in awake animals in our study.

Direct cortical application of ammonia reproduces the disease phenotype

Next, we wanted to examine the anatomical origin of the ammonia-induced seizures. To do this we generated a new model where we applied ammonia (10 mM) directly on the cortex of awake mice. We found that the resultant cortical ammonia elevation was sufficient to reproduce the disease phenotype of systemic ammonia toxicity (Fig. 2E, F). The lower ME frequency in this compared to the systemic model likely relates to small area of cortex (1.5 mm cranial window) being exposed to ammonia. To define how deep into the brain the locally applied ammonia permeated we used NH_4^+ ion-sensitive microelectrodes (ISM). We found that the ammonia diffusion was surprisingly restricted, affecting mainly the superficial cortex (Fig. 2E). Seen in the context of previously radio-isotope studies, this observation most likely relates to the rapid metabolic trapping of ammonia in astrocytes by the enzyme GS (*1*). Consistent with this idea, when we inhibited GS with L-methionine sulfoximine (MSO, 1.5 mM) the cortical $[NH_4^+]_o$ gradient was reduced. It is therefore likely that cortical astrocytes take up most of the excess $[NH_4^+]_o$ in our model of focal ammonia toxicity. The importance of astrocyte ammonia sequestration is further illustrated by the increased ME frequencies we recorded when MSO was co-administered with ammonia (MSO 1.06 ± 0.26 vs. NH_4Cl 2.66 ± 0.14 vs. NH_4Cl + MSO 3.29 ± 0.19) (Fig. 2F). Astrocyte uptake of excess $[NH_4^+]_o$ in the cortex thus appears to play a critical role in generating the neurological dysfunction seen in ammonia neurotoxicity.

Using both our systemic and cortical disease models, we proceeded to explore whether ammonia-related ME arise in the cortex or thalamus. Recent studies in humans and rodents have

suggested that several generalized seizure types, such as SWD (including ME and absence seizures) and tonic-clonic, may primarily originate in the cortex and secondarily invade the thalamus (*18-20*). To establish the origin of ammonia-induced seizures, we placed extracellular electrodes in the cortex and thalamus of awake mice. The dual recordings showed that ammonia-induced SWD in the cortex preceded those in the thalamus by 7.87 ± 2.15 ms when ammonia was administered systemically, and 8.26 ± 2.11 ms when ammonia was applied cortically (Fig. 2G) (*21*). In conclusion, several lines of evidence suggest cortical ammonia toxicity may be sufficient and necessary for ME generation, which in turn correlated closely with overall disease severity.

Cortical ammonia exposure causes rapid disinhibition of neuronal firing

Different and often inconsistent neuronal effects of ammonia have been described in the context of different disease models (*in vitro*, *in situ* and *in vivo*) and different time courses (acute, subacute and chronic) (*22*). Similar to previous ^{1}H-NMR studies, we found no net change in the levels of neurotransmitters glutamate and GABA that could explain the neurotoxicity of ammonia (Table S1) (*13, 23*). In one of the few previous *in vivo* studies Lux et al. showed that inhibitory GABAergic neurotransmission is impaired when cats receive an acute ammonia challenge. However, this study looked primarily at spinal motor neurons and did not actually measure seizure activity. To extend these observations into a more clinically relevant analysis, we examined the effect of ammonia superfusion on cortical inhibitory networks in awake animals using paired-pulse whisker stimulation. This method has previously been used to study the maturation of inhibitory networks (*24*). The whisker stimulation paradigm we employed elicits two successive field excitatory post-synaptic potentials (fEPSP). The amplitude of the

second fEPSP is normally smaller than the first one, owing to activation of cortical inhibitory networks that suppress the second fEPSP. This is quantified by a paired-pulse ratio (PPR) of less than one. Ammonia superfusion, however, increased the PPR from 0.64 ± 0.13 in the control setting to 1.56 ± 0.24 (paired-pulse facilitation), which recovered to 0.61 ± 0.15 upon washout (Fig. 2H, I). For the first time we therefore demonstrate that ammonia causes a significant disinhibition of excitatory neuronal firing in the cortex and thereby provide a direct link to cortical seizure generation.

Astrocyte swelling is only a terminal feature of acute ammonia neurotoxicity

We next asked what role astrocytes might play in ammonia neurotoxicity. Much of recent literature has suggested ammonia-induced astrocyte swelling and brain edema are an important cause of the neurological impairment seen in ammonia neurotoxicity (*7, 25-27*). However, astrocyte swelling has to our knowledge never been demonstrated *in vivo*. We used two-photon laser scanning microscopy (2PLSM) in awake $Otc^{spf\text{-}ash}$ mice expressing eGFP in astrocytes under the *Glt-1* promoter to examine real-time volume changes following an acute ammonia challenge (Fig. 3A). We found that ammonia caused no significant astrocyte swelling *in vivo*, but rather a transient yet significant shrinkage of 5.04 ± 0.85% (Fig. 3B). In addition, cortical slices acutely exposed to ammonia (10 mM) failed to show astrocyte swelling unless concentrations high enough to cause cell lysis (50 mM) were applied (Fig. 3C).

To further investigate the role of astrocyte swelling, we examined mice deficient in aquaporin-4 (AQP4) water channels. AQP4 is the major influx pathway for water into astrocytes and knocking out this protein reduces astrocyte swelling (*28*). AQP4 has also been shown to be upregulated in ammonia neurotoxicity (*29*). However, when injected with ammonia, $Aqp4^{-/-}$ mice

displayed no improvement in the severity of phenotype or ME frequency (Fig. S3A, B). Finally, to determine whether global brain swelling is necessarily associated with all levels of ammonia neurotoxicity, we measured brain water content in *Otc*$^{spf\text{-}ash}$ and WT mice following different doses of ammonia. We found that 5-7.5 mmol kg^{-1} of ammonia did not cause brain edema despite causing the previously illustrated significant neurological phenotype (Fig 3D, Fig. S3C). Swelling was only observed with a lethal ammonia dose of 10 mmol kg^{-1}, consistent with data from patients with fatal ammonia toxicity (*30*). Taken together, our results indicate that astrocyte swelling is not a critical event in acute ammonia neurotoxicity. Moreover, the data demonstrate that the *Otc*$^{spf\text{-}ash}$ model used in our study is not associated with significant edema, even though the mice exhibit all the clinical and biochemical signs of ammonia neurotoxicity.

Astrocytes calcium signaling: an early sign of impaired glia-neuronal crosstalk in ammonia neurotoxicity

Having not yet found any sign of astrocyte dysfunction, despite strong evidence suggesting astrocytes bear the brunt of the ammonia load, we proceeded to explore astrocyte signaling. Since astrocytes are electrically silent, we used 2PLSM to image intracellular calcium transients in cortical astrocytes of *Otc*$^{spf\text{-}ash}$ mice loaded with calcium indicator rhod-2. The indicator selectively loaded astrocytes, as shown by co-localization with eGFP expressed in astrocytes as described above. To allow direct correlation of imaging to clinical phenotype these animals were again awake (Fig. 3F, Fig. S3D). Astrocyte calcium signaling is believed to modulate a range of functions including cerebral blood flow, synaptic activity and extracellular ion homeostasis (*31-33*). However, most data has been collected from anesthetized mice or *in situ* preparations, and the role of spontaneous calcium transients in awake behaving mice is not well characterized (*34*).

We recorded several distinct patterns of spontaneous calcium transients during control conditions (Fig. 3F). The most striking observation in awake mice was a higher frequency of spontaneous calcium transients compared to anesthetized animals (Table S2, Video 2). The predominant pattern of signaling in awake mice was synchronous bursts, whereas anesthetized animals largely displayed individual calcium transients. This observation is consistent with the only other study that explored calcium activity in the awake cortex, which concluded that the synchronous bursting exhibited a delayed and variable correlation with neuronal activity (*34*).

We next examined astrocyte calcium transients in awake *Otc*$^{spf\text{-}ash}$ mice receiving a systemic ammonia challenge. Following the ammonia administration the mice experienced a prolonged increase in overall calcium transient frequency from 2.67 ± 0.36 to 9.03 ± 1.16 Hz cell^{-1} 10^{-3} (Fig. 3E, F). The increase in calcium signaling preceded the onset of ME by 1.58 ± 0.37 min. Surprisingly, however, calcium transient frequency decreased when ME frequency peaked (Fig. 3E, F). Additionally, individual ME showed a weak temporal correlation of 0.15 ± 0.10 with calcium transients (Fig. 3G, Fig. S3E). Moreover, the ammonia challenge also caused a pathological desynchronization of cortical calcium transients, with a reduced cell-cell ($\Delta F/F_0$) correlation from 0.65 ± 0.06 to 0.26 ± 0.08 compared to baseline (Fig. 3H, Video 3). Finally, both ammonia and saline injection triggered a brief burst of transients one minute after administration, likely due to animal arousal (*35*). Taken together, these observations indicate astrocytes signaling distress early in ammonia neurotoxicity, and perhaps experience an overall failure of signaling during the most severe clinical stage of the disorder. The decreased and desynchronized signaling when ME activity is peaking could represent pathological neuron-to-glia signaling evoked by excessive neuronal firing (*32*).

Astrocytes overloaded with ammonia fail to buffer potassium

Using awake intact mouse models we have so far shown that acute ammonia toxicity is associated with 1) severe neurological impairment, 2) neuronal disinhibition and 3) astrocyte distress and/or dysfunction, but not swelling. We therefore proceeded to examine the link between astrocyte and neuronal dysfunction. Extracellular potassium homeostasis ($[K^+]_o$) is a vital function of astrocytes with important implications for neuronal function (*36-41*). Previous *in situ* and *in vitro* studies have also indicated that ammonia may compromise astrocyte potassium buffering (*42, 43*). Using NH_4^+ and K^+-ISM electrodes in awake mice we found that both systemically (7.5 mmol kg^{-1}) and cortically (10 mM) applied ammonia directly impaired potassium homeostasis in the cortex (Fig. 4A-C). Systemic administration caused a 1.93 ± 0.19 mM $[K^+]_o$ increase in the $Otc^{spf\text{-}ash}$ mice (subtracted for NH_4^+ interference), above a resting level of 3.91 ± 0.27 mM (Fig. 4B) (*44*). Direct cortical administration caused a 2.24 ± 0.17 mM increase in $[K^+]_o$, which recovered to a level slightly below baseline upon washout as the neurological manifestations including ME subsided (Fig. 4C, Fig. S4C). More importantly, this $[K^+]_o$ increase preceded ME onset by 4.91 ± 0.35 min and 2.875 ± 0.201 min in the systemic and cortical models, respectively (Fig. S4A-C). Additionally, the $[K^+]_o$ increase we observed showed a strong correlation with ME frequency (Fig. 4D). Similar observations could be reproduced in wild-type mice, indicating that the is not an artifact of the $Otc^{spf\text{-}ash}$ strain (Fig. S4D).

Next, we wanted to assess the role of astrocyte ammonia sequestration (via GS) in the potassium accumulation. Reduced activity of GS in gliotic brain tissue has previously been implicated in the initiation of temporal lobe epilepsy (*45*). Similarly, we found that administering MSO prior to the ammonia challenge exacerbated both the $[NH_4^+]_o$ and the $[K^+]_o$ increase (Fig. S4DE, F). This observation may reflect that decreasing the influx of ammonia into astrocytes

with MSO increases the overall cation load (NH_4^+ or K^+) on neurons, as less NH_4^+ is trapped in glutamine. Finally, ammonia is also known to exert pH effects in brain (*46*). We therefore used H^+ ISMs and found an extracellular alkalization following ammonia injection. However, this effect was mild, delayed and correlated poorly with clinical phenotype (Fig. S4G). Thus, we confirmed that astrocytes play a key role in enzymatic ammonia removal, and show that ammonia neurotoxicity causes a profound cortical $[K^+]_o$ increase that precedes and correlates strongly disease severity.

Potassium replicates the neuronal impairment in ammonia toxicity

Our data indicate that ammonia-related neurological changes are preceded by an increase in cortical $[K^+]_o$. We therefore superfused KCl (12.5 mM) across the cortex of awake mice to explore whether increased $[K^+]_o$ is sufficient by itself to replicate the adverse effects of ammonia (Fig. 4A). Strikingly, when $[K^+]_o$ was increased by 2.37 ± 0.03 mM using KCl superfusion, the mice developed ME similar to our ammonia superfusion model (Fig. 4E, F). With higher doses (20 mM) they would also develop tonic-clonic seizures (Fig. 4F). We subsequently proceeded to explore whether potassium-related seizures were also associated with disinhibition of neuronal firing. Using the paired-pulse paradigm we described above, we demonstrated that KCl superfusion caused a disinhibition similar to ammonia with a mean PPR of 1.48 ± 0.22, which recovered to 0.63 ± 0.14 after washout (Fig. 4G). In conclusion, for the first time *in vivo* we show that increasing $[K^+]_o$ alone is sufficient to generate neuronal disinhibition, seizures, and thus replicate the neuronal impairment seen in ammonia toxicity. These observations were entirely dependent on using awake intact animals, as the clinical phenotype was masked by anesthesia.

Ammonia competes with potassium for uptake in astrocytes

We subsequently used a combination of *in vitro* assays to determine the mechanism of the ammonia-induced $[K^+]_o$ increase. Interestingly, previous radioisotope studies revealed that almost immediately following an acute ammonia load, 4x as much ^{13}N-labelled ammonia is fixed in glutamine than exists as the free ionized form NH_4^+ (*1*). Given that glutamine is only formed in astrocytes (via GS), this observation means that >4x as much ammonia crosses astrocyte membranes than any other cell type (including neurons). Previous studies have used this insight to focus principally on the toxic effects of excess ammonia and/or glutamine in the astrocyte cytosol (*25*). However, the >4x higher flux of ammonia across astrocyte membranes provides perhaps the most bioenergetically challenging load, and this is often overlooked.

To explain how the excess ammonia load on astrocyte membranes could lead to decreased K^+ uptake we hypothesized that ammonia would either indirectly impair (pump failure) or directly compete (pump overactivity) for uptake with K^+. Because the gradients driving astrocyte uptake of potassium inevitably all depend on Na^+-K^+-ATPase (NKA) activity, we chose to focus on this transporter as a proof of principle. NKA-mediated potassium clearance, but not clearance via K^+-channels or (Na^+)-K^+-Cl^-cotransporters, is for instance known to be most important during epileptic activity (*47*). Surprisingly, when NH_4Cl was substituted KCl in a cell-free NKA assay, we found that NH_4Cl alone was able to maintain normal NKA activity, indicating that K^+ can be substituted by NH_4^+ without an effect on ATPase function (Fig. 4I). This observation is further supported by previous studies in kidney showing that NH_4^+ can replace K^+ as a substrate for the renal NKA (*48, 49*). Notably, NH_4^+ and K^+ ions have a similar

hydrated radius and charge, and can also permeate potassium channels with similar efficacy (*3, 50*).

Given that both K^+ and NH_4^+ ions can bind to the Na^+-K^+-ATPase, we would predict that Na^+-K^+-ATPase activity is increased during ammonia toxicity, as there is more overall substrate ($[NH4^+]_o$ and $[K^+]_o$) available for transport. Interestingly, increased Na^+-K^+-ATPase activity has been shown in both congenital and acquired ammonia disorders (*51*). Indeed, the transient shrinkage of ammonia-exposed astrocytes shown above is consistent with increased activity of the Na^+-K^+-ATPase, which exports 3 Na^+ and imports 2 K^+ ions. Furthermore, we would predict that ammonia decreases potassium uptake in a dose-dependent fashion. Consistent with this hypothesis we found that biologically relevant ammonia concentrations (0.5-10 mM) inhibited NKA-dependent (ouabain-sensitive) potassium analogue rubidium ($^{86}Rb^+$) uptake in cultured astrocytes in a dose-dependent fashion (Fig. 4H). In contrast, neuronal $^{86}Rb^+$ uptake was more inconsistently reduced, compatible with the hypothesis that neurons play a less prominent role in potassium buffering than astrocytes (Fig. S4H) (*37*). Combined, our observations indicate that NH_4^+ short circuits the astrocytic K^+ buffering, causing the sustained increase in $[K^+]_o$ observed *in vivo* (Fig. 4J).

Ammonia depolarizes E_{GABA} in cortical neurons

We next wanted to explore the link between impaired astrocyte potassium buffering and neuronal disinhibition by using neuronal patch clamping in cortical slices perfused with ammonia. Adding 7 mM ammonia to the perfusate reproduced the increase in $[NH_4^+]_o$ and $[K^+]_o$ observed *in vivo* (3.67 ± 0.53 mM and 1.88 ± 0.13 mM respectively) (Fig. 5A).

The inhibitory action of GABA is dependent on a hyperpolarized E_{GABA} (*10*). Using whole-cell patch clamping of pyramidal neurons with ramp voltage and GABA application we found that ammonia depolarized E_{GABA} by 12.33 ± 3.66 mV (Fig. 5B). This effect was $GABA_A$-receptor dependent as bicuculline, a $GABA_A$-receptor antagonist, completely blocked the GABA-induced current (Fig. S5A, B). Similar to previous studies using moderate ammonia concentrations, we found no consistent change in neuronal resting membrane potential or input resistance (*22, 52*).

Because E_{GABA} is heavily dependent on chloride transporters, we next tested the diuretic bumetanide, a highly specific NKCC1 inhibitor used in clinical practice to treat heart failure (*11*). In our study, bumetanide (5 μM) pre-incubation successfully prevented the depolarizing effect of ammonia on E_{GABA} (Fig. 5B). Using immunohistochemistry we found that NKCC1 is present in cortex (Fig 5C), confirming previous studies indicating NKCC1 expression in adult brain, although at lower levels than in developing tissue (*53-55*). We observed no obvious differences in the expression pattern of NKCC1 between wild-type and *Otc*$^{spf\text{-}ash}$ mice throughout the cortex. Interestingly, chronic low elevations of ammonia similar to the resting levels seen in our *Otc*$^{spf\text{-}ash}$ mice have been shown to increase NKCC1 activity up to 3 fold, perhaps explaining some of the baseline learning deficit in these mice (*56*). On the basis of these observations, we hypothesize that elevated $[K^+]_o$ and $[NH_4^+]_o$ overactivate neuronal NKCC1, leading to an intracellular accumulation of chloride that depolarizes E_{GABA} (Fig. 5D). Supporting this conclusion, previous *in vivo*, *in situ* and *in vitro* work has shown that neurons exposed to elevated ammonia levels have significantly increased intracellular chloride content (*52, 57, 58*).

NKCC1 inhibition improves clinically relevant features of ammonia neurotoxicity

To test the validity of our *in situ* model we returned to awake animals, and asked whether blocking NKCC1 with bumetanide reducing disinhibition *in vivo* (Fig. 6A). Using the previously described paired-pulse paradigm, we found that adding bumetanide to the superfusate significantly improved disinhibition following cortical application of both ammonia and potassium (Fig. 6B-C, Fig. S6A). With ammonia application PPR increased maximally to 0.88 ± 0.15 when bumetanide was co-administered, and recovered to a control level of 0.59 ± 0.17 after washout of both ammonia and bumetanide. Similarly, when potassium alone was co-applied with bumetanide the mean PPR only increased to 0.92 ± 0.18. Taken together, these data indicate that bumetanide effectively treats the neuronal dysfunction seen in ammonia neurotoxicity.

Next, we wanted to investigate whether this improvement of neuronal function translated into a clinically relevant improvement in disease phenotype. Employing the same phenotype measures outline in Figure 1 we demonstrated that NKCC1 inhibition increases spontaneous mouse movement, reduces the sensory-motor phenotype score, decreases ME frequency and increases survival following an ammonia overdose (Fig. 6E-H). Spontaneous movement increased from 0.42 ± 0.22 to 3.17 ± 0.46 m min^{-1} and phenotype score was reduced from 9.00 ± 0.46 to 6.00 ± 0.72 (Fig. 6E, F). ME frequency was reduced from 0.78 ± 0.05 to 0.13 ± 0.03 (with cortical KCl), 1.02 ± 0.07 to 0.10 ± 0.02 (with cortical NH_4Cl) and 2.66 ± 0.14 to 0.32 ± 0.02 ME min^{-1} (with systemic NH_4Cl) (Fig. 6G). Survival over a 45 min period after ammonia overdose (10 mmol kg^{-1}) increased by a factor of 3.87 (hazard rate ratio 0.26, 95% confidence interval 0.08 to 0.87). These clinically relevant improvements were observed both when bumetanide was administered systemically (i.p., 30 mg kg^{-1}) and cortically (5 μM), indicating that the drug exerts its beneficial action principally in the cortex. Moreover, the therapeutic effect

of bumetanide could not be attributed to a normalization of $[K^+]_o$, $[NH_4^+]_o$ or brain amino acids, which were unaltered by the treatment (Fig. 6I, J, Table S1 and Table S3).

These *in vivo* data demonstrate that an elevation of ammonia in the cortex is sufficient to induce NKCC1-dependent and bumetanide-sensitive neuronal impairment, supporting the model developed from the *in situ* data **(see Fig. 4g)**.

Discussion

Ammonia neurotoxicity is an almost universal phenomenon that occurs in all animals from fish to humans, and has previously been extensively studied *in vitro, in situ*, and using biochemical or histological methods. This work has produced important clues as to the cellular mechanisms underlying ammonia neurotoxicity, but the continued lack of treatment illustrates clearly that the overall picture is still incomplete. What we have tried to do in our study is to test and extend individual *ex vivo* observations using *in vivo* models, where we can continuously correlate experimental observations with clinical phenotype. In this way we attempted to piece together a more complete picture of what cellular and subcellular changes are necessary and sufficient to produce the neurological dysfunction seen in acute ammonia neurotoxicity (e.g. elevated $[K^+]_o$), and which are not (e.g. astrocyte swelling). All anesthetics tested in our study masked the ammonia-induced neurological phenotype and disrupted normal astrocyte signaling. Thus, the use of awake animals in our *in vivo* models was critical to identify the pathological chain of events involving both astrocytes and neurons that leads to ammonia neurotoxicity.

First, we chose a childhood disorder, X-linked OTC deficiency, and used this to develop a clean mouse model of acute ammonia neurotoxicity that was unconfounded by hemodynamic or hepatic complications (*9*). Using behavioral and biochemical methods we show that this

model replicates all the pathognomic features of ammonia neurotoxicity. This relatively rare disorder thus represents an important opportunity to try and understand the larger phenomenon of ammonia toxic effects on neural tissue.

Second, using paired-pulse whisker stimulation in awake mice we show that an acute ammonia challenge causes disinhibition of neuronal firing and consequently ME similar to those observed in children with OTC deficiency (*2*). Additionally, we provide evidence suggesting that these ME originate in the cortex, likely due to the rapid influx of ammonia into cortical astrocytes driven by the enzyme GS. Finally, we show that the neurological phenotype in ammonia neurotoxicity can be reproduced using a novel model where we apply ammonia directly to cortex of awake mice.

Third, due to the putatively four times larger ammonia-load on astrocyte membranes than all other cell type, we next asked how astrocytes contribute to or cause the neuronal dysfunction. Extensive *ex vivo* literature suggests that ammonia causes brisk astrocyte swelling (*7, 25-27*). To our surprise, however, we found that ammonia does not cause astrocyte swelling, but instead produces novel changes in astrocyte calcium signaling. We suggest that the signaling changes represent astrocytic responses to neuronal hyperexciteability, astrocyte distress and/or dysfunction of astrocytes early in the disease process. To our knowledge this is the first examination of astrocyte volume and signaling changes *in vivo* during ammonia neurotoxicity.

Fourth, we proceeded to explore whether dysfunctional astrocyte signaling was indicative of impaired astrocyte potassium uptake, as the two are closely linked (*36*). Using our awake mouse models of systemic and direct cortical ammonia neurotoxicity we observed that a ~2 mM $[K^+]_o$ increase preceded symptom onset. Notably, the magnitude of the $[K^+]_o$ increase correlated closely with disease severity. We were also able to reproduce the neural and clinical features of

ammonia neurotoxicity by cortical application of potassium alone. We thus provide the first direct link between potassium and neural dysfunction, including seizures, in ammonia intoxication.

Fifth, we demonstrate that NH_4^+ can compete with K^+ ions for active uptake on astrocyte membranes. This competition short circuits the astrocytic Na^+-K^+-ATPase pump with severe consequences, including compromised $[K^+]_o$ buffering and seizures. A similar competition has been shown in kidney and retina, suggesting that an accumulation of ammonia may act as a universal hazard that can disrupt potassium homeostasis in any organ and almost any animal (*3, 48*).

Finally, we show that there is currently no effective way (e.g. MSO) of protecting astrocytes from ammonia without increasing the ammonia-load on neurons. Instead, we find that inhibiting the downstream effects of ammonia and potassium on neurons is the most effective therapeutic strategy. These downstream effects appear to depend most critically on a potassium-driven depolarizing shift in E_{GABA} that impairs neural inhibition. We show that inhibiting the chloride importer NKCC1 with the clinically used diuretic bumetanide not only rescues the shift in E_{GABA}, but also improves all aspects of the neurological phenotype.

ME are characterized by generalized SWD on the EEG (*16*). SWD are observed in a group of seizure disorders, including childhood absence seizures, which have recently been shown to involve early cortical activation (*18*). This led to the hypothesis that SWD originate from a focus in the cortex, before recruiting the thalamus leading to generalized seizures. Notably, during SWD, injection of lidocaine into the cortex to locally inhibit neuronal firing is able to suppress all seizure activity in the brain (*19*). In our study, two lines of evidence suggest that the ME we observed during ammonia neurotoxicity are cortical in origin. First, we recorded

SWD in the cortex ~8 ms prior to the thalamus. Second, direct application of ammonia or potassium on the cortex replicated the SWD activity seen in systemic ammonia toxicity. Taken together, these data suggest that an impairment of potassium homeostasis in the cortex is sufficient to generate ME in our model.

In our study we find that ammonia- and potassium-induced neurological impairment is preceded by a depolarizing shift in neuronal E_{GABA}. A similar shift in E_{GABA} has been shown in resected hippocampi from patients with temporal lobe epilepsy (*59*). Interestingly, administration of the astrocyte toxin fluoroacetate or insulin-induced hypoglycemia also depolarize E_{GABA} (*60*). In adults, the inhibitory action of GABA is dependent on a hyperpolarized E_{GABA}. In early development, however, cortical neurons have a depolarized E_{GABA} due to the high activity of NKCC1, which causes an intracellular accumulation of chloride (*61*). Early studies using radiolabelled $^{36}Cl^-$ and intracellular electrodes found a similar chloride accumulation during acute ammonia exposure, although the mechanism was not known (*52, 57*). Later in development, decreased activity of NKCC1 and increased activity of K^+-Cl^- cotransporter isoform 2 (KCC2), cause a developmental switch in E_{GABA} making it hyperpolarized (*62*). Inhibition of NKCC1 has therefore been suggested as a therapy for seizures in early development (neonates) (*53*). Moreover, KCC2 expression is reduced following nerve injury in adults, depolarizing E_{GABA}, causing inappropriate neuronal firing and neuropathic pain (*63*). In our model, increased $[NH_4^+]_o$ and $[K^+]_o$ drive an NKCC1-dependent depolarizing shift in E_{GABA}, resembling early development. Using awake behaving adult mice, we demonstrate that this depolarizing shift is followed by a severe impairment of cortical inhibitory neurotransmission and seizures.

The FDA-approved diuretic bumetanide considerably improved clinically relevant behavioral measures in our awake models of ammonia- and potassium-induced neurotoxicity. During childhood an accumulation of ammonia is most frequently caused by enzyme deficiencies such as the *Otc* mutation explored in our study. These devastating conditions have attracted limited research focus, and consequently the disease mechanisms are incompletely understood (*7, 29*). Few mechanism-specific therapies have been developed for acute ammonia neurotoxicity, and bumetanide may bridge the gap in ammonia-related translational research, providing a safe, effective and mechanism-targeted therapeutic option. Our results provide clear impetus for the initiation of clinical trials investigating the therapeutic potential of bumetanide in ammonia neurotoxicity.

Materials and Methods

Rodent breeding and behavioral studies

All animal experiments were approved by the Animal Care and Use Committee of the University of Rochester. $Otc^{spf\text{-}ash}$ B6C3-F1 mice were bred as described previously, and males from 8-12 weeks were used (*9*). $Otc^{spf\text{-}ash}$ mice were crossed with *Glt-1*-eGFP mice for imaging experiments. C57BL/6J mouse and Wistar rat pups were obtained from Jackson Laboratories. To analyze cognitive abilities in OTC mice, two commercial conditioning chambers (H10-11M-TC, Coulbourn Instruments) were adapted for contextual fear conditioning. Over the course of 4 days, mice were trained via a tone/shock protocol and trained to fear contextual and auditory cues. Better trained mice exhibited higher freezing percentages in the precesense of auditory or contextual cues (*64, 65*). Automated movement analysis was performed using AnyMaze™

software analysis of CCD-camera recordings in a standard mouse cage. We developed a sensory-motor phenotype score to quantify the severity of ammonia neurotoxicity based on two previous studies (*9, 14*). Each animal gets scored every 15 minutes based on the severity of the following phenotypes: hyperacusis (0-2), imbalance (0-3), ataxia / tremor (0-3) and level of consciousness (0-3). A maximum score of 11 represents deep coma (no corneal reflex) whilst 0 represents normal wakefulness.

Animal preparation for awake *in vivo* recordings

Mouse preparation was modified from published protocols (*8, 34*). Briefly, mice were anesthetized using isoflurane (1.5% mixed with 1-2 L/min O_2), head restrained with a custom-made mini-frame, habituated over 2 days, a 1.5 mm craniotomy was then opened over the somatosensory cortex, and the mice were allowed 60 min recovery prior to conducting the experiments. Body temperature was maintained with a heating pad. For systemic drug treatment, a polyethylene intraperitoneal (i.p.) catheter was surgically implanted to deliver drugs accurately and with minimal manipulation. For cortical drug application artificial cerebrospinal fluid (aCSF) was perfused across the cortex of awake mice at a rate of 2 mL/min, into a custom-made well with ~200 µL volume, through tubing with ~100 µL volume, meaning the entire volume bathing the brain was exchanged every ~9 s. The aCSF solution contained (in mM) 126 NaCl, 2.5 KCl, 1.25 NaH_2PO_4, 2 $MgCl_2$, 2 $CaCl_2$, 10 glucose, and 26 $NaHCO_3$, pH 7.4. For imaging, calcium indicator rhod-2 AM (Invitrogen, 2 mM) was loaded onto exposed cortex for 45 min before applying agarose (1.5%, type III-A, Sigma) and a coverslip (*28*).

Biochemical and hemodynamic analysis

Plasma ammonia analysis was performed on blood samples collected using 50 µL heparinized tubes from the femoral artery. A L-glutamate dehydrogenase based kit (Sigma) was used for the quantification of ammonia in plasma. For ^{1}H-NMR mouse forebrains were extracted, frozen, homogenized and lyophilized before being reconstituted with D_2O as described previously (*23*). ^{1}H-NMR spectra were acquired at 25^{o}C using a 600 mHz Varian UnityINOVA spectrometer (7200 Hz spectral width, 32K data points, 64 signals averaged for each spectrum). For hemodynamic recordings an intracranial pressure probe (Millar) was inserted through a small 0.5 mm craniotomy over the somatosensory cortex. Cerebral blood flow was assessed using a fiberoptic laser Doppler probe (PF5010, Perimed) and connected to an infrared laser doppler flowmeter. Blood pressure was monitored through the femoral artery cannula (SYS-BP1, WPI), and cerebral perfusion pressure was deduced by subtracting ICP from blood pressure. All signals were digitized (Digidata 1332A, Axon Instruments) and analyzed (pClamp 10.2). Brain water content was assessed using wet-to-dry ratios (WDR) of brain weight as described previously.(*66*)

Electrophysiological recordings

In vivo recordings were obtained from layer II somatosensory cortex. *In situ* recordings were obtained from layer II in coronal cortical slices prepared from P21-30 mice. ISMs of K^+ and $NH4^+$ were pulled from double-barreled pipette glass (PB150-6, WPI) with a tip of 1-3 µm. The pipettes were silanized (coated) with dimethylsilane I (Fluka, Sigma) and filled with either K^+ ionophore I cocktail B (Fluka, selectivity coefficient -1.8 $\log(K^+/NH_4^+)$) or NH4+ ionophore I cocktail B (Fluka, -0.9 $\log(NH_4^+/K^+)$). All ISMs were calibrated before and after each experiment (a < 5% difference was acceptable) using standard solutions and the calibration data were fitted to the Nikolsky equation to determine electrode slope and interference (*44*). Whole-

cell patch-clamp recordings were performed as described previously (*67*). Electroencephalogram (EEG) signals were externally filtered at 6 Hz (Filter Butterworth Model by Encore, Axopatch 200B by Axon Instruments), bandpass filtered at 1-100 Hz and digitized (Digidata 1440A by Axon Instruments). Ion-sensitive microelectrode (ISM) signals were amplified (FD223a by WPI), externally filtered and digitized as above, and reference field potential traces were subtracted. In selected experiments, wireless electromyogram (EMG) and electroencephalogram (EEG) electrodes were implanted (DSI Physiotel®), and an extracellular microelectrode was placed in the thalamus (ventrobasal complex). Recordings were analyzed offline using pClamp 10.2. Myoclonic events (ME) were defined on the EEG as single or multiple 3-9 Hz polyspike and wave discharges (SWD) of 0.2-2 s duration associated with myoclonic jerks determined by video recording, EMG or direct observation. Whisker stimulation was delivered using a picospritzer III (Parken Instrumentation) and Master 8 (A.M.P.I.). Stimuli consisted of paired 50 μs air pulses with an inter-stimulus interval of 150 ms, and paired-pulse ratio (PPR) was calculated as previously described (*24*). NH_4Cl/NH_4Ac solutions were pH (7.4) and osmolarity adjusted.

Two-photon laser scanning microscopy

A Mai Tai laser (SpectraPhysics) attached to a confocal scanning system (Fluoview 300, Olympus) and an upright microscope (IX51W) was used. *In vivo* volume changes and calcium activity were imaged in cortex 100 μm below the pial surface, using a 60x (1.1NA) and a 20x (0.95NA) lens, respectively. For *in vivo* volumetry we collected xyzt image series (z-step 1.5 μm, every 5 min) with acquisition time <20 seconds and laser power <40 mW. For *in vivo* calcium imaging we collected dual channel (rhod-2 and eGFP) frames at 0.2 or 1 Hz. A low sampling

rate and <20 mW laser were used to avoid photodamage. A calcium transient was defined as an event where the relative ratio between the rhod-2 and eGFP signal intensities ($\Delta F/F_0$) was >2 standard deviations (σ) from baseline. Beginning and end were defined as $\Delta F/F_0$ >0.5 σ and <0.5 σ respectively. Amplitude was taken as the peak $\Delta F/F_0$ in this interval. For *in situ* volumentric imaging acute cortical slices were loaded with texas red hydrazide (1.5 µM, a fixable sulforhodamine 101 derivative) in aCSF for 50 minutes. Volume and calcium recordings were analyzed using previously described custom-made software (MatLab Inc.) (*28*).

Cell culture assays

Cultured neocortical astrocytes were prepared from P1-2 mouse and rat pups as previously described (*36, 68*). For $^{86}Rb^+$ experiments the cultures were incubated for 10 min ± ouabain (1 mM). The potassium analogue $^{86}Rb^+$ was then added to each well plate for 15 min (1 µCi, Perkin Elmer). The reaction was stopped by placing the cells on ice and washed with ice-cold aCSF. The cells were lysed and $^{86}Rb^+$ uptake quantified by liquid scintillation counting (Beckman Coulter). For Na^+-K^+-ATPase activity, astrocyte cultures were utilized as previously described, and enzyme activity was quantified using the malachite green reaction (Sigma) and analyzed using spectrophotometry (*69*).

Immunohistochemistry

Mice were anesthesized and perfused transcardially with 4% paraformaldehyde, and the brains were post-fixed overnight. Serial 16 µm sagittal cryostat sections were cut after overnight cryoprotection in 30% sucrose. Sections were incubated with goat anti-NKCC1 primary antibody (1:200, Sta. Cruz Biotechnology) overnight at 4°C, followed by incubation with an Alexa-488

donkey anti-goat secondary antibody (1:500, Invitrogen). Vectashield containing DAPI (Vector) was used for mounting. Images were taken with a 10x lens in a BX53 Olympus system microscope attached to a DP72 Olympus digital camera.

Statistical analysis

All analysis was performed using IBM SPSS Statistics 19 and all tests were two-tailed where significance was achieved at $\alpha = 0.05$ level. Where $n \geq 10$ for normally distributed data, the unpaired *t* test or ANOVA were used for independent samples, and paired *t* test for paired samples. Where $n < 10$ non-parametric tests including Mann-Whitney *U* and Kruskall-Wallis were used for independent samples, and Wilcoxon signed ranks test for paired samples. Overdose survival was compared using Cox regression model (controlling for the confounding effect of mouse weight).

Supplementary Materials

Materials and methods

Fig. S1. Behavioral and biochemical characterization of acute ammonia neurotoxicity.

Fig. S2. Myoclonic phenotype associated with ammonia intoxication.

Fig. S3. Deletion of astrocyte water channel aquaporin 4 (AQP4) is not protective in acute ammonia toxicity.

Fig. S4. Ammonia impairs cortical potassium buffering.

Fig. S5. GABA-currents recorded during ramp voltage are entirely $GABA_A$-receptor dependent.

Fig. S6. Bumetanide treats potassium-induced neural disinhibition.

Table S1. Biochemical changes during acute ammonia neurotoxicity.

Table S2. Astrocyte calcium signaling during acute ammonia neurotoxicity in awake mice.

Table S3. Bumetanide treatment does not affect cortical ammonia or potassium concentrations.

Movie S1. Myoclonic phenotype induced by 7.5 mmol kg^{-1} ammonia injection in an *Otc*$^{spf\text{-}ash}$ mice.

Movie S2. Spontaneous calcium transients in cortical astrocytes prior to 7.5 mmol kg^{-1} ammonia injection (control).

Movie S3. Calcium transients in cortical astrocytes after 7.5 mmol kg^{-1} ammonia injection.

References

1. A. J. Cooper, J. M. McDonald, A. S. Gelbard, R. F. Gledhill, T. E. Duffy, The metabolic fate of 13N-labeled ammonia in rat brain. *J. Biol. Chem.* **254**, 4982 (1979).
2. L. Cagnon, O. Braissant, Hyperammonemia-induced toxicity for the developing central nervous system. *Brain Res. Rev.* **56**, 183 (2007).
3. P. Marcaggi, M. Jeanne, J. A. Coles, Neuron-glial trafficking of NH4+ and K+: separate routes of uptake into glial cells of bee retina. *Eur. J. Neurosci.* **19**, 966 (2004).
4. A. J. Cooper, 13N as a tracer for studying glutamate metabolism. *Neurochemistry international* **59**, 456 (Sep, 2011).
5. R. A. Waniewski, Physiological levels of ammonia regulate glutamine synthesis from extracellular glutamate in astrocyte cultures. *J. Neurochem.* **58**, 167 (1992).
6. A. Martinez-Hernandez, K. P. Bell, M. D. Norenberg, Glutamine synthetase: glial localization in brain. *Science* **195**, 1356 (1977).
7. R. F. Butterworth, Pathophysiology of hepatic encephalopathy: a new look at ammonia. *Metab. Brain Dis.* **17**, 221 (2002).
8. V. R. Thrane *et al.*, Real-time analysis of microglial activation and motility in hepatic and hyperammonemic encephalopathy. *Neuroscience*, (Jun 21, 2012).
9. X. Ye *et al.*, Adenovirus-mediated in vivo gene transfer rapidly protects ornithine transcarbamylase-deficient mice from an ammonium challenge. *Pediatr. Res.* **41**, 527 (1997).
10. Z. J. Zhang, T. A. Valiante, P. L. Carlen, Transition to seizure: From "macro"- to "micro"-mysteries. *Epilepsy Res* **97**, 290 (Dec, 2011).
11. P. Hannaert, M. Alvarez-Guerra, D. Pirot, C. Nazaret, R. P. Garay, Rat NKCC2/NKCC1 cotransporter selectivity for loop diuretic drugs. *Naunyn Schmiedebergs Arch. Pharmacol.* **365**, 193 (2002).
12. P. C. Rowe, S. L. Newman, S. W. Brusilow, Natural history of symptomatic partial ornithine transcarbamylase deficiency. *The New England journal of medicine* **314**, 541 (Feb 27, 1986).
13. L. Ratnakumari, I. A. Qureshi, R. F. Butterworth, Effects of congenital hyperammonemia on the cerebral and hepatic levels of the intermediates of energy metabolism in spf mice. *Biochemical and biophysical research communications* **184**, 746 (Apr 30, 1992).
14. S. J. Guyenet *et al.*, A simple composite phenotype scoring system for evaluating mouse models of cerebellar ataxia. *Journal of visualized experiments : JoVE*, (2010).
15. J. F. Russell *et al.*, Familial cortical myoclonus with a mutation in NOL3.
16. H. Blumenfeld, Cellular and network mechanisms of spike-wave seizures. *Epilepsia* **46**, 21 (2005).
17. H. M. Hamer *et al.*, Electrophysiology of focal clonic seizures in humans: a study using subdural and depth electrodes. *Brain* **126**, 547 (2003).
18. X. Bai *et al.*, Dynamic time course of typical childhood absence seizures: EEG, behavior, and functional magnetic resonance imaging. *J. Neurosci.* **30**, 5884 (2010).
19. E. Sitnikova, G. van Luijtelaar, Cortical control of generalized absence seizures: effect of lidocaine applied to the somatosensory cortex in WAG/Rij rats. *Brain Res.* **1012**, 127 (2004).

20. M. N. DeSalvo *et al.*, Focal BOLD fMRI changes in bicuculline-induced tonic-clonic seizures in the rat. *NeuroImage* **50**, 902 (Apr 15, 2010).
21. H. K. Meeren, J. P. Pijn, E. L. Van Luijtelaar, A. M. Coenen, F. H. Lopes da Silva, Cortical focus drives widespread corticothalamic networks during spontaneous absence seizures in rats. *J. Neurosci.* **22**, 1480 (2002).
22. J. C. Szerb, R. F. Butterworth, Effect of ammonium ions on synaptic transmission in the mammalian central nervous system. *Prog. Neurobiol.* **39**, 135 (1992).
23. C. Zwingmann, N. Chatauret, D. Leibfritz, R. F. Butterworth, Selective increase of brain lactate synthesis in experimental acute liver failure: results of a [1H-13C] nuclear magnetic resonance study. *Hepatology* **37**, 420 (2003).
24. A. J. Borgdorff, J. F. Poulet, C. C. Petersen, Facilitating sensory responses in developing mouse somatosensory barrel cortex. *J. Neurophysiol.* **97**, 2992 (2007).
25. A. R. Jayakumar, K. V. Rao, C. R. Murthy, M. D. Norenberg, Glutamine in the mechanism of ammonia-induced swelling. *Neurochem. Int.* **48**, 623 (2006).
26. K. V. Rama Rao, A. R. Jayakumar, X. Tong, K. M. Curtis, M. D. Norenberg, Brain aquaporin-4 in experimental acute liver failure. *Journal of neuropathology and experimental neurology* **69**, 869 (Sep, 2010).
27. M. Zielińska, R. O. Law, J. Albrecht, Excitotoxic mechanism of cell swelling in rat cerebral cortical slices treated acutely with ammonia. *Neurochem. Int.* **43**, 299 (2003).
28. A. S. Thrane *et al.*, Critical role of aquaporin-4 (AQP4) in astrocytic Ca2+ signaling events elicited by cerebral edema. *Proc. Natl. Acad. Sci. U. S. A.* **108**, 846 (2010).
29. U. Lichter-Konecki, J. M. Mangin, H. Gordish-Dressman, E. P. Hoffman, V. Gallo, Gene expression profiling of astrocytes from hyperammonemic mice reveals altered pathways for water and potassium homeostasis in vivo. *Glia* **56**, 365 (2008).
30. J. P. Donovan, D. F. Schafer, B. W. J. Shaw, M. F. Sorrell, Cerebral oedema and increased intracranial pressure in chronic liver disease. *Lancet.* **351**, 719 (1998).
31. S. Koizumi, K. Fujishita, M. Tsuda, Y. Shigemoto-Mogami, K. Inoue, Dynamic inhibition off excitatory synaptic transmission by astrocyte-derived ATP in hippocampal cultures. *Proc. Natl. Acad. Sci. U. S. A.* **100**, 11023 (2003).
32. X. Wang *et al.*, Astrocytic Ca2+ signalling evoked by sensory stimulation in vivo. *Nat. Neurosci.* **9**, 816 (2006).
33. A. V. Gourine *et al.*, Astrocytes control breathing through pH-dependent release of ATP. *Science* **329**, 571 (Jul 30, 2010).
34. D. A. Dombeck, A. N. Khabbaz, F. Collman, T. L. Adelman, D. W. Tank, Imaging large-scale neural activity with cellular resolution in awake, mobile mice. *Neuron* **56**, 43 (Oct 4, 2007).
35. L. K. Bekar, W. He, M. Nedergaard, Locus coeruleus alpha-adrenergic-mediated activation of cortical astrocytes in vivo. *Cerebr. Cortex* **18**, 2789 (2008).
36. F. Wang *et al.*, Astrocytes modulate neural network activity by Ca(2)(+)-dependent uptake of extracellular K(+). *Science signaling* **5**, ra26 (Apr 3, 2012).
37. N. N. Haj-Yasein *et al.*, Evidence that compromised K+ spatial buffering contributes to the epileptogenic effect of mutations in the human Kir4.1 gene (KCNJ10). *Glia* **59**, 1635 (Nov, 2011).
38. W. Walz, in *Advanced Molecular Cell Biology: Non-Neuronal Cells of the Nervous System: Function and Dysfunction,* L. Hertz, Ed. (Elsevier, Gilmour, Ontario., 2004), vol. 31, pp. 595-609.

39. M. V. Sofroniew, Molecular dissection of reactive astrogliosis and glial scar formation. *Trends in neurosciences* **32**, 638 (Dec, 2009).
40. K. C. Chen, C. Nicholson, Spatial buffering of potassium ions in brain extracellular space. *Biophysical journal* **78**, 2776 (Jun, 2000).
41. M. Simard, M. Nedergaard, The neurobiology of glia in the context of water and ion homeostasis. *Neuroscience* **129**, 877 (2004).
42. B. E. Alger, R. A. Nicoll, Ammonia does not selectively block IPSPs in rat hippocampal pyramidal cells. *J. Neurophysiol.* **49**, 1381 (1983).
43. N. Allert, H. Koller, M. Siebler, Ammonia-induced depolarization of cultured rat cortical astrocytes. *Brain research* **782**, 261 (Jan 26, 1998).
44. C. Nicholson, Ion-selective microelectrodes and diffusion measurements as tools to explore the brain cell microenvironment. *J. Neurosci. Methods* **48**, 199 (1993).
45. T. Eid *et al.*, Loss of glutamine synthetase in the human epileptogenic hippocampus: possible mechanism for raised extracellular glutamate in mesial temporal lobe epilepsy. *Lancet* **363**, 28 (2004).
46. M. Chesler, Regulation and modulation of pH in the brain. *Physiol. Rev.* **83**, 1183 (2003).
47. Z. Q. Xiong, J. L. Stringer, Sodium pump activity, not glial spatial buffering, clears potassium after epileptiform activity induced in the dentate gyrus. *Journal of neurophysiology* **83**, 1443 (Mar, 2000).
48. S. M. Wall, L. M. Koger, NH4+ transport mediated by Na(+)-K(+)-ATPase in rat inner medullary collecting duct. *Am. J. Physiol.* **267**, F660 (1994).
49. I. Kurtz, R. S. Balaban, Ammonium as a substrate for Na+-K+-ATPase in rabbit proximal tubules. *Am. J. Physiol.* **250**, F497 (1986).
50. J. Stephan *et al.*, Kir4.1 channels mediate a depolarization of hippocampal astrocytes under hyperammonemic conditions in situ. *Glia* **60**, 965 (May, 2012).
51. L. Ratnakumari, R. Audet, I. A. Qureshi, R. F. Butterworth, Na+,K(+)-ATPase activites are increased in brain in both congenital and acquired hyperammonemic syndromes. *Neurosci. Lett.* **197**, 89 (1995).
52. H. D. Lux, Ammonium and chloride extrusion: hyperpolarizing syntaptic inhibition in spinal motor neurons. *Science* **173**, 555 (1971).
53. V. I. Dzhala *et al.*, NKCC1 transporter facilitates seizures in the developing brain. *Nat. Med.* **11**, 1205 (2005).
54. C. Kanaka *et al.*, The differential expression patterns of messenger RNAs encoding K-Cl cotransporters (KCC1,2) and Na-K-2Cl cotransporter (NKCC1) in the rat nervous system. *Neuroscience* **104**, 933 (2001).
55. H. Chen, J. Luo, D. B. Kintner, G. E. Shull, D. Sun, Na(+)-dependent chloride transporter (NKCC1)-null mice exhibit less gray and white matter damage after focal cerebral ischemia. *J. Cereb. Blood Flow Metab.* **25**, 54 (Jan, 2005).
56. A. R. Jayakumar, V. Valdes, M. D. Norenberg, The Na-K-Cl cotransporter in the brain edema of acute liver failure. *J. Hepatol.* **54**, 272 (2011).
57. A. M. Benjamin, Effects of ammonium ions on spontaneous action potentials and on contents of sodium, potassium, ammonium, and chloride ions in brain in vitro. *J. Neurochem.* **30**, 131 (1978).
58. T. Irie *et al.*, Chloride concentration in cultured hippocampal neurons increases during long-term exposure to ammonia through enhanced expression of an anion exchanger. *Brain research* **806**, 246 (Sep 28, 1998).

59. G. Huberfeld *et al.*, Perturbed chloride homeostasis and GABAergic signaling in human temporal lobe epilepsy. *J. Neurosci.* **27**, 9866 (2007).
60. W. A. Raabe, Ammonia and disinhibition in cat motor cortex by ammonium acetate, monofluoroacetate and insulin-induced hypoglycemia. *Brain. Res.* **210**, 311 (1981).
61. J. Yamada *et al.*, Cl- uptake promoting depolarizing GABA actions in immature rat neocortical neurones is mediated by NKCC1. *J Physiol* **557**, 829 (Jun 15, 2004).
62. P. Blaesse, M. S. Airaksinen, C. Rivera, K. Kaila, Cation-chloride cotransporters and neuronal function. *Neuron* **61**, 820 (Mar 26, 2009).
63. B. S. Coull JA, Boudreau D, Boivin D, Tsuda M, Inoue K, Gravel C, Salter MW, De Koninck Y., BDNF from microglia causes the shift in neuronal anion gradient underlying neuropathic pain. *Nature* **438**, 1017 (2005).
64. S. G. Anagnostaras, S. A. Josselyn, P. W. Frankland, A. J. Silva, Computer-assisted behavioral assessment of Pavlovian fear conditioning in mice. *Learning & memory (Cold Spring Harbor, N.Y.)* **7**, 58 (Jan, 2000).
65. B. J. Wiltgen, A. J. Silva, Memory for context becomes less specific with time. *Learning & memory (Cold Spring Harbor, N.Y.)* **14**, 313 (Apr, 2007).
66. N. N. Haj-Yasein *et al.*, Glial-conditional deletion of aquaporin-4 (Aqp4) reduces blood-brain water uptake and confers barrier function on perivascular astrocyte endfeet. *Proc. Natl. Acad. Sci. U. S. A.* **108**, 17815 (2011).
67. F. Wang, C. Xiao, J. H. Ye, Taurine activates excitatory non-synaptic glycine receptors on dopamine neurones in ventral tegmental area of young rats. *J. Physiol.* **1**, 503 (2005).
68. J. H. Lin *et al.*, Gap-junction-mediated propagation and amplification of cell injury. *Nat. Neurosci.* **1**, 494 (1998).
69. H. V. Anupama Adya, B. N. Mallick, Comparison of Na-K ATPase activity in rat brain synaptosome under various conditions. *Neurochem. Int.* **33**, 283 (1998).

Acknowledgements: We thank S. Kennedy for help with ^{1}H-NMR experiments, L. K. Bekar for his much appreciated comments and help with electrophysiology, J. Chang for designing MatLab software, D. Wang for helpful advice and for EEG analysis, J. M. Wilson (University of Pennsylvania) for providing the *Otc*$^{spf\text{-}ash}$ mice and J. D. Rothstein (Johns Hopkins University) for providing *Glt-1*-eGFP BAC transgenic mice. **Funding:** This work was supported by the US National Institutes of Health (grants P01NS050315 and R01NS056188 to M.N., and F31NS073390 to N.A.S.), Research Council of Norway (STORFORSK, NevroNor, and FUGE grants), Nordic Center of Excellence Program, Letten Foundation and Fulbright Foundation. **Author contributions:** V.R.T., A.S.T., E.A.N., M.L.C. and M.N. planned the project. V.R.T., A.S.T., M.L.C., E.A.N. and M.N. wrote the manuscript. V.R.T. and A.S.T. performed *in vivo* electrophysiology, imaging and data analysis. F.W. performed *in situ* electrophysiology. A.S.T., V.R.T. and M.C. performed behavioral experiments. A.S.T. and V.R.T. performed *in situ* imaging. N.A.S. performed rubidium experiments. T.F. performed ATPase experiments. M.L.C. performed immunohistochemistry. **Competing interests:** The authors declare that there are no competing financial interests.

Figure legends

Fig. 1. Acute ammonia neurotoxicity is characterized by severe neurological impairment and pathognomic biochemical changes. (**A**) $Otc^{spf\text{-}ash}$ mice deficient in the liver enzyme ornithine transcarbamylase (OTC) are unable to metabolize ammonia to urea and excrete it via the kidney. Following an acute systemic ammonia load the $Otc^{spf\text{-}ash}$ mice therefore accumulate ammonia in the brain, where it is only metabolized in astrocytes via the amination of glutamate (Glu) to glutamine (Gln) catalyzed by glutamine synthetase (GS). Ammonia neurotoxicity progresses through stages characterized by stereotypical neurological features (e.g. ataxia). (**B**) Ammonia levels in blood plasma and (**C**) brain before and after 7.5 mmol kg^{-1} NH_4Cl. ***$P < 0.001$, $n = 7$ for each group, Mann-Whitney *U* test. (**D**) Brain [glutamine] measured by ^{1}H-NMR 30 minutes after saline (ctrl) or ammonia. *$P = 0.015$, $n = 6$ for each group, Kruskall-Wallis test. (**E**) Baseline deficit in spatial learning in $Otc^{spf\text{-}ash}$ mice shown using fear chamber conditioning. *$P = 0.014$, $n = 5$ for each group, Mann-Whitney *U* test. (**F**) No significant change in global hemodynamic parameters in our model of acute ammonia neurotoxicity (cerebral perfusion pressure: CPP, cerebral bloodflow: CBF and intracranial pressure: ICP). (**G**) Left panel, diagram illustrating automated video movement analysis. Right panel, decreased spontaneous mouse movement is an early feature of ammonia neurotoxicity. ***$P < 0.001$, $n = 8$ (NH_4Cl) and 5 (Ctrl), Mann-Whitney *U* test. (**H**) Left panel, diagrams illustrating elements of the sensory-motor phenotype score we developed to follow disease severity after the ammonia load. Right panel, phenotype score increases sensitively after the ammonia load (7.5 mmol kg^{-1}) in $Otc^{spf\text{-}ash}$ mice, followed by a slow recovery. ***$P < 0.001$, $n = 8$ (NH_4Cl) and 5 (Ctrl), Mann-Whitney *U* test. Data are shown as mean ± SEM.

Fig. 2. Ammonia potently triggers seizure activity by causing an impairment of neural inhibition (disinhibition). (**A**) Double-barreled ion-sensitive microelectrodes (ISM), electroencephalogram (EEG) and electromyogram (EMG) electrodes were used to record seizure activity during acute ammonia neurotoxicity in awake mice. The ammonia was either applied systemically (7.5 mmol kg^{-1}) or cortically (10 mM), and EEG electrodes were placed in both cortex (Ctx) and thalamus (Tha). (**B**) Acute ammonia administration triggers tonic-clonic seizures and myoclonic events (ME). (**C**) ME are associated with polyspike and wave discharges (SWD) on EEG that are occasionally followed by a delayed EMG discharge. $n = 10$. (**D**) ME and behavioral phenotypes worsen with increasing doses of ammonia, but are suppressed when animals are anesthetized (pooled data for ketamine, isoflurane, urethane). $*P < 0.01$, $n = 6$ for each group, Kruskall-Wallis test. (**E**) $[NH_4^+]_o$ at different depths in the brain during direct cortical application of ammonia. The ammonia gradient in the brain dissipates when glutamine synthetase is inhibited with 1.5 mM MSO. Depth 0 μm represents ISM in the solution. $*P = 0.019$, $**P < 0.01$, $n = 5$ for each depth, Mann-Whitney *U* test. (**F**) Inhibiting GS with MSO (0.83 mmol kg^{-1} i.p.) induces ME in awake mice. The ME phenotype was exacerbated when ammonia is co-administered. $*P = 0.00022$, $n = 7$ (MSO), 22 (NH_4Cl) and 7 (NH_4Cl + MSO), Kruskall-Wallis test. (**G**) Extracellular recordings demonstrate that SWD in the cortex (Ctx) precede those in the thalamus (Tha). $n = 478$ events, 6 mice. (**H**) 10 consecutive sweeps of field excitatory post-synaptic potentials (fEPSP) elicited by paired-pulse whisker stimulation before, during, and after cortical NH_4Cl application (10 mM, red box). (**I**) The paired-pulse ratio (PPR) increases during ammonia superfusion, indicating an impairment of cortical inhibitory networks. $*P < 0.001$, $n = 10$, paired *t* test. Data are shown as mean ± SEM.

Fig. 3. Astrocyte ammonia toxicity is associated with impaired calcium signaling, but not swelling *in vivo*. (**A**) Two-photon laser scanning microscopy (2PLSM) was performed following a systemic ammonia load (7.5 mmol kg^{-1}) in awake $Otc^{spf\text{-}ash}$ mice expressing eGFP under the *Glt-1* promoter. (**B**) 3D real-time volume analysis using xyzt scans of eGFP expressing astrocytes during ammonia neurotoxicity reveals no astrocyte swelling, only transient shrinkage. Representative images are shown below. Red outline represents volume at time 0. Scale bar represents 5 μm. ***$P < 0.001$, $n = 12$ for each group, unpaired *t* test. (**C**) Equivalent volume analysis of texas red hydrazide (TxR) loaded astrocytes in cortical slices. Left panel, texas red selectively labels astrocytes expressing eGFP under the *Glt-1* promoter. Scale bar represents 10 μm. Right panel, 10 mM NH_4Cl is not associated with acute astrocyte swelling, which was only observed in conjunction with cell lysis when 50 mM NH_4Cl was applied. **$P = 0.0019$ (50 mM NH_4Cl vs. Ctrl), $n = 13$ (Control), 12 (10 mM), 10 (50 mM), unpaired *t* test. (**D**) Brain water content is not increased 30 min after mild to moderate ammonia intoxication, but is elevated when a lethal dose is administered. **$P = 0.0025$, n.s. = not significant, $n = 7$ (0 mmol kg^{-1}), 5 (5 mmol kg^{-1}), 6 (7.5 mmol kg^{-1}), 5 (10 mmol kg^{-1}), Mann-Whitney *U* test. (**E**) Left panel, representative image showing eGFP expressing astrocytes loaded with calcium indicator rhod-2 imaged 100 μm below the pial surface using 2PLSM. Scale bar represents 30 μm. Right panel, corresponding rhod-2 intensity traces showing calcium transients. (**F**) Increased calcium activity is an early sign of ammonia neurotoxicity, but calcium activity paradoxically decreases during the period with peak ME frequency, before increasing again. Red box indicates time of i.p. injection. Heat bar indicates mean ME frequency per minute. ***$P < 0.0001$, $n = 52$ (ammonia) and 62 (control) cells sampled from 12 animals, unpaired *t* test with Bonferroni correction. (**G**)

Representative calcium ($\Delta F/F_0$) and corresponding EEG trace demonstrate a weak temporal correlation between individual ME and calcium transients (coefficient < 0.3). (**H**) Ammonia injection desynchronizes calcium transients, as assessed by Pearson correlation of $\Delta F/F_0$. **P* < 0.0001, *n* = 52 (ammonia) and 62 (control) cells, paired *t* test. Data are shown as mean ± SEM.

Fig. 4. Ammonia compromises astrocyte potassium buffering by competing with potassium for uptake. (**A**) Double-barreled ISM were used to record $[NH_4^+]_o$, $[K^+]_o$ and electroencephalogram (EEG) from layer II cortex of awake mice either receiving 7.5 mmol kg^{-1} i.p. or 10 mM cortical NH_4Cl. The calibration curves for NH_4^+ and K^+ ISMs are shown. (**B**) Representative NH_4^+ (top panel) and K^+ (bottom panel) ISM traces following i.p. injection (red box) of either ammonia (NH_4Cl) or saline (Ctrl). Vertical red lines indicate individual ME. (**C**) Representative ISM trace (top panel) and scatterplot (bottom panel) showing an increase in $[K^+]_o$ during cortical application of ammonia (red box) in an awake mouse. Red lines indicate individual ME. Red arrow indicates mean onset of ME. $[K^+]_o$ increases prior to seizure onset. **P* < 0.001, *n* = 10 (ammonia) and 7 (control), Mann-Whitney *U* test. (**D**) Linear regression showing that seizure frequency correlates strongly with $[K^+]_o$ concentrations recorded during ammonia neurotoxicity. *n* = 8 (NH_4Cl i.p.) and 10 (cortical NH_4Cl application, Ctx). (**E**) Representative K^+ ISM trace (top panel) during direct potassium application to the cortex of an awake mouse. KCl application (red box) causes multiple ME (red lines). Line graph (bottom panel) showing that cortical application of 12.5 mM KCl replicates the cortical $[K^+]_o$ increase seen following 10 mM NH_4Cl application at different depths in the brain. *n* = 5 for each depth. (**F**) Representative traces illustrating tonic-clonic (top) and ME (bottom) induced by direct cortical application of KCl in awake mice. Seizure discharges are detect in the cortex (Ctx) prior to the thalamus (Tha) and

muscle (EMG). (**G**) 10 consecutive sweeps of fEPSP elicited by paired-pulse whisker stimulation before, during, and after cortical KCl application (12.5 mM, red box). **P* = 0.028, *n* = 6, Wilcoxon signed ranks test. (**H**) NH_4Cl (15 mM) can substitute KCl (15 mM) as a substrate for the Na^+-K^+-ATPase in a cell-free assay of astrocyte cultures. n.s. = not significant, *P* = 0.49, *n* = 4 for each group, Mann-Whitney *U* test. (**I**) Na^+-K^+-ATPase-dependent (ouabain-sensitive) uptake of potassium analogue rubidium ($^{86}Rb^+$) in cultured astrocytes, normalized to vehicle. **P* < 0.0001, *n* = 23 (0 mM), 17 (0.5 mM), 16 (2 mM), 10 (5 mM), 10 (10 mM), one-way analysis of variance (ANOVA). (**J**) Diagram illustrating how excess ammonia would anatomically (via end-feet, e.f.) and enzymatically (via glutamine synthetase, GS) be drawn into astrocytes and trapped as glutamine (Gln). This cation influx compromises the ability of astrocytes to buffer potassium generated by normal neuronal firing. Data are shown as mean ± SEM.

Fig. 5. Excess ammonia and potassium cause a depolarization of the neuronal GABA reversal potential (E_{GABA}). (**A**) Top panel, cortical slices from WT mice (>P21) were superfused with 7 mM NH_4Cl. Bottom panel, representative ISM recordings for $[NH_4^+]_o$ and $[K^+]_o$ illustrating similar ionic changes observed *in vivo*. (**B**) Mean $\Delta[ion]_o$ recorded following ammonia superfusion. $[NH_4^+]_o$ (*n* = 9) and $[K^+]_o$ (*n* = 18). (**C**) Representative traces show that ammonia reduces the chloride current induced by ramp voltage with application of GABA. (**D**) Ammonia causes a right shift of the I-V curve. NKCC1 antagonist bumetanide (BUM) reverses this effect. (**E**) Bumetanide prevents the ammonia-induced depolarization of E_{GABA}. ***P* = 0.0034, *n* = 11 (control), 11 (NH_4Cl), 7 (BUM), 7 (NH_4Cl + BUM), Wilcoxon signed ranks test. (**F**) Immunofluorescence micrograph of adult *Otc*$^{spf\text{-}ash}$ and wild-type mouse cortex labeled with primary antibody against NKCC1 and DAPI-stained nuclei. Scale bar represents 100 μm. Inset

shows NKCC1 labeling in choroid plexus (positive control). Scale bar represents 250 μm. (**G**) Diagram showing the proposed mechanism for ammonia neurotoxicity. NH_4^+ competes with K^+ ions for active uptake, impairing astrocyte potassium buffering. This leads to an increase in $[K^+]_o$, overactivating neuronal NKCC1, which depolarizes E_{GABA} rendering GABAergic (inhibitory) neurotransmission less effective. Na^+-K^+-ATPase (NKA), glutamate (Glu), glutamine synthetase (GS), glutamine (Gln), Na^+-K^+-$2Cl^-$cotransporter isoform 1 (NKCC1), $GABA_A$ receptor ($GABA_AR$), K^+-Cl^- cotransporter isoform 2 (KCC2), bumetanide (BUM), membrane potential (V_m), GABA reversal potential (E_{GABA}). Data are shown as mean ± SEM.

Fig. 6. NKCC1 inhibition with bumetanide (BUM) potently treats the electrophysiological and clinical features of ammonia neurotoxicity. (**A**) Awake mice were treated with either systemic NH_4Cl (7.5 mmol kg^{-1}), cortical NH_4Cl (10 mM), or cortical KCl (12.5 mM) ± bumetanide (30 mg kg^{-1} i.p. or 5 μM cortically), while electrophysiological and behavioral changes were recorded. (**B**) 10 consecutive sweeps of field excitatory post-synaptic potentials (fEPSP) elicited by paired-pulse whisker stimulation before, during, and after cortical application of NH_4Cl with (blue box). (**C**) The facilitating (increased) paired-pulse ratio (PPR) induced by NH_4Cl cortical application (blue box) is reversed by bumetanide. ***$P < 0.001$, $n = 10$ for both groups, unpaired *t* test. (**D**) The PPR facilitation seen following KCl cortical application (blue box) is similarly reduced by bumetanide. **$P = 0.0022$, $n = 6$ (KCl) and 5 (KCl + BUM), Mann-Whitney *U* test. (**E**) Bumetanide improves spontaneous mouse movement after a systemic NH_4Cl load (blue box) in *Otc*$^{spf\text{-}ash}$ mice. **$P < 0.01$, $n = 8$ (NH_4Cl) and 7 (NH_4Cl + BUM), Mann-Whitney *U* test. (**F**) Following a systemic NH_4Cl load in *Otc*$^{spf\text{-}ash}$ mice sensory-motor phenotype score is reduced by bumetanide treatment. **$P < 0.01$, $n = 8$ (NH_4Cl) and 7 (NH_4Cl + BUM), Mann-Whitney *U* test.

(**G**) Frequency of MEs induced by ammonia and/or potassium is reduced by bumetanide treatment. ***$P < 0.001$, **$P < 0.01$, $n = 10$ (systemic NH_4Cl), 10 (cortical NH_4Cl) and 6 (cortical KCl). Mann-Whitney *U* test. (**H**) Cox regression analysis of *Otc*$^{spf\text{-}ash}$ mouse survival time after a NH_4Cl overdose (10 mmol kg^{-1}). *$P = 0.021$, $n = 9$ (NH_4Cl) and 10 (NH_4Cl + bumetanide). (**I**) Increase in cortical $[K^+]_o$ following a systemic NH_4Cl load in *Otc*$^{spf\text{-}ash}$ mice is unchanged by bumetanide. (**J**) Increase in cortical $[K^+]_o$ following a cortical NH_4Cl is unchanged by bumetanide. Data are shown as mean ± SEM.

Fig. 1.

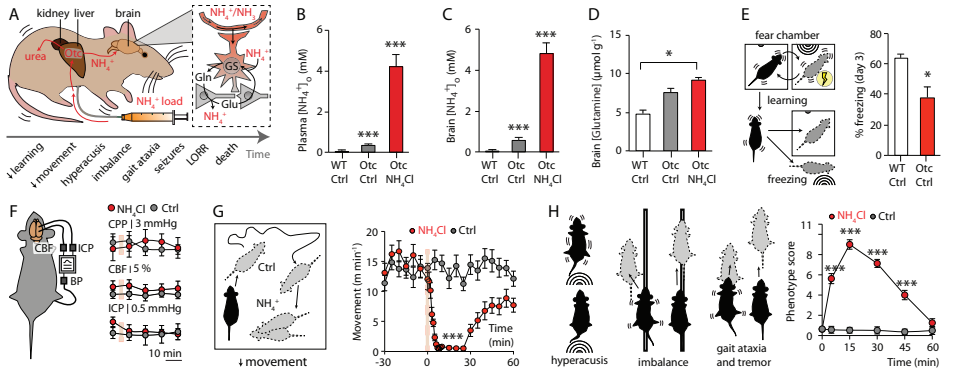

Fig. 2.

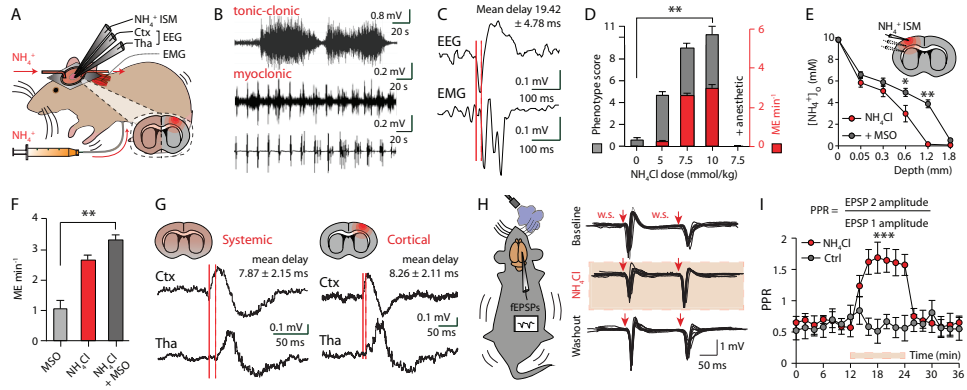

Fig. 3.

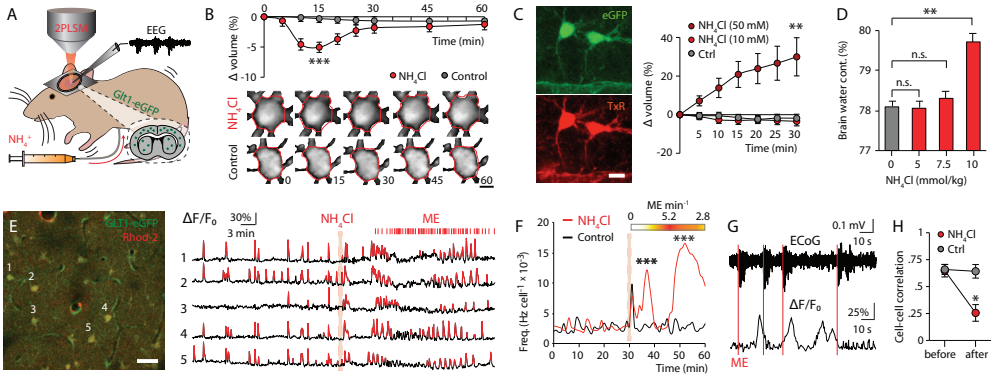

Fig. 4.

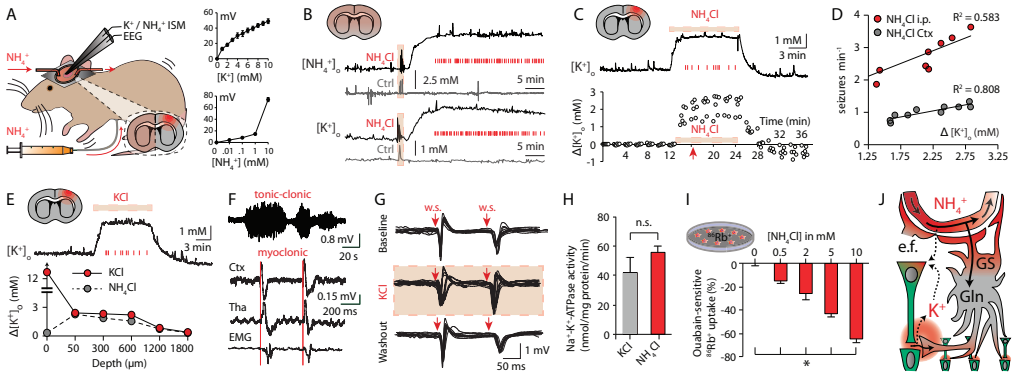

Fig. 5.

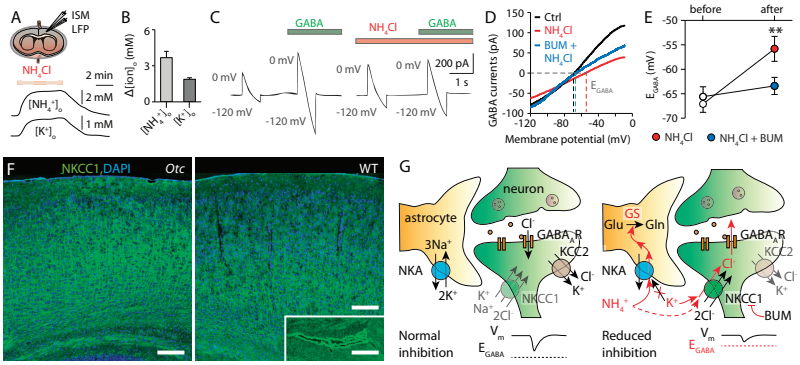

Fig. 6.

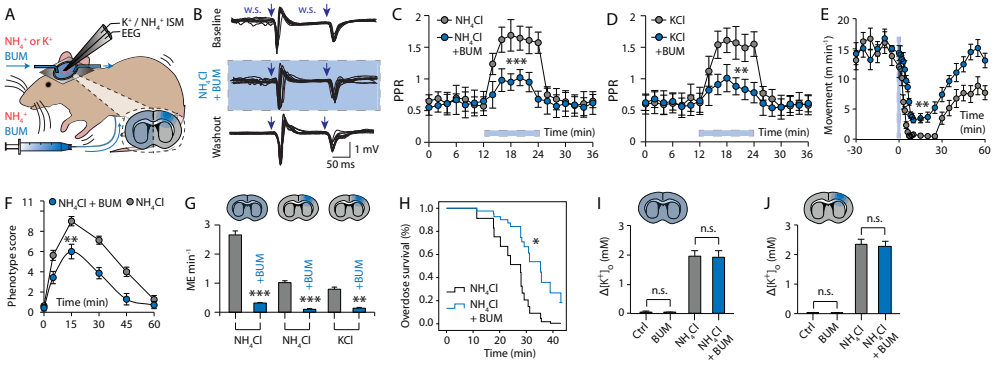

Supplementary Materials

Title: Ammonia compromises astrocyte potassium buffering and impairs neuronal inhibition without causing swelling *in vivo*. **Authors:** V. Rangroo Thrane, A. S. Thrane, F. Wang, M. L. Cotrina, N. A. Smith, T. Fujita, M. Chen, E. A. Nagelhus, M. Nedergaard

Materials and Methods

Animal preparation

Otc$^{spf\text{-}ash}$ mice and wild-type littermates were generated as outlined by Wilson et al. (*1*). *Aqp4*$^{-/-}$ mice and wild-type littermates were generated as described previously (*2*). Mice subjected to studies were males from 8 to 12 weeks of age. Mice were anesthetized with isoflurane (1.5% mixed with 1-2 L/min O_2) via nose cone. A custom-made mini-frame was secured to the skull. The animals were habituated to the head-restraint for 3-4 hours, in multiple sessions over 2 days. The mice were then re-anesthetized and a craniotomy was opened, 1.5 mm in diameter, 3 mm lateral and 1.5 mm posterior to the bregma with the dura carefully removed. The latter procedure lasted <20 minutes. Animals were then head-restrained, placed in a behavioral tube and moved to the set-up located in a dark quiet room, where they were allowed to recover from the anesthetic for 60 minutes prior to commencing recordings. The short surgery time and multiple recovery periods were used to minimize the effects of isoflurane on cortical electrical activity.

Sensory-motor phenotype score

We developed composite sensory-motor phenotype score based on two previous studies (*1, 3*). Mouse movement and seizure activity were omitted from this score, because we wanted to represent these manifestations independently and more quantitatively. The score thus consisted of 4 elements:

hyperacusis, imbalance, ataxia/tremor and level of consciousness. Each animal was scored after the first 5 min and then every 15 min as they progressed through the stereotypical stages of ammonia neurotoxicity. Hyperacusis was score from 0 if the mouse did not display a startle response to 30-60 dB sound, 1 if the mouse responded to only 60 dB and 2 if it responded to 30 dB as well. Imbalance was scored using a ledge test, and the mice were given 0 if the balanced on the ledge and let themselves down in a controlled fashion, 1 if they loose their footing whilst walking on the ledge, 2 if it does not effectively walk on or let itself down from the ledge, and 3 if it is unable to walk, get down, or just falls off. Ataxia/tremor was scored using a gait test, where the mouse is encouraged to walk for a short distance. The mouse gets 0 if it walks effectively, 1 if it has a slight tremor, 2 if it has a broad based gait or severe tremor, 3 if it drags its abdomen on the ground or is unable to walk. Consciousness was scored as either 0 for awake, 1 loss of scatter reflex, 2 loss of righting reflex (LORR), 3 loss of corneal reflex.

Ion sensitive microelectrode (ISM) fabrication

ISMs of K^+, $NH4^+$ and H^+ were made from double-barreled pipette glass (PB150-6, WPI) and pulled to a tip of 1-3 μm. The pipettes were silanized (coated) with dimethylsilane I (Fluka, Sigma). The ionophore used for K^+ was Fluka 60398 (potassium ionophore I cocktail B), for NH4+ was Fluka 09882 (ammonium ionophore I cocktail B) and for H^+/pH was Fluka 95291 (hydrogen ionophore I cocktail A) all obtained from Sigma. The K^+ ionophore has a selectivity coefficient relative to NH_4^+ of -1.8 $\log(K^+/NH_4^+)$, and the NH_4^+ ionophore has a selectivity coefficient relative to K^+ of -0.9 $\log(NH_4^+/ K^+)$. The backfill solutions for the K^+, $NH4^+$ and H^+ ISMs were 0.15 M KCl, 0.5 M NH_4Cl and phosphate-buffered saline (PBS) with a pH of 7.4 respectively. The reference barrels were used to record the DC potentials and were filled with 0.15 M NaCl. In selected experiments, single barrel

electrodes were also used in combination with single reference electrodes. K^+ and NH_4^+ ISM traces were subtracted for interference by calculating the mV response to the increase of the other ion in calibration solutions. All ISMs were calibrated before and after each experiment. K+ calibrations were done in 150 mM NaCl that contained doubling steps of K+ over a range of concentrations appropriate for the experiment, usually from 3-48 mM. $NH4^+$ calibrations were carried out in 150 mM NaCl and aCSF from 0.1-10 mM to determine the sensitivity during the *in vivo* environment. H^+ calibrations were carried out in phosphate buffers from pH 5 to 9, where >90% had a response time of 1-5 seconds and a 51-59 mV response to 1 pH unit change. Calibration data were fitted to the Nikolsky equation to determine electrode slope and interference (*4*). In all experiments, recordings were used only if the post-experiment calibration did not differ >5% from the pre-experiment calibration.

Two-photon laser scanning microscopy (2PLSM)

Normal calcium signaling was easily abolished if the astrocytes were loaded too long with calcium indicator, the craniotomy diameter was too large and with laser or mechanical injury. We therefore tested each animal for optimal loading by performing whisker stimulation, to verify a physiological calcium response (*5*).

^{1}H-NMR spectroscopy

Mice were anesthetized using 1.5% isoflurane and decapitated. Forebrains (whole brain minus cerebellum/brainstem) were quickly extracted, frozen in liquid nitrogen, and homogenized in 7.5 mL 12% PCA at 0^{o}C using a micro-sonicator. The homogenate was centrifuged at 25,000G for 15 minutes, and the supernatants were neutralized to pH 7.0 with KOH over an ice bath. A further 15-

minute centrifugation (25,000G) separated the resultant $KClO_4$, and the supernatant was lyophilized before being reconstituted with 0.65 ml D_2O. ^{1}H-NMR spectra were acquired using a 600 mHz Varian UnityINOVA spectrometer equipped with a triple-axis gradient HCN probe (standard room temperature). Signals were acquired following a 90^o pulse with a spectral width of 7200 Hz and 32K data points. The time between pulses was 15 seconds and 64 signals were averaged for each spectrum. The sample temperature was 25^{o}C. Integrals of the relevant peaks were converted to μmol/gram wet-weight and normalized NAA (methyl) to increase inter-sample consistency.

***In situ* electrophysiology**

Coronal cortical slices were prepared from P21-30 mice as described previously (*6*). This age was chosen as in younger pups the GABA reversal potential can be depolarizing (excitatory) (*7*). Whole-cell patch-clamp recordings were done using electrodes with 3-5 MΩ resistance, and an intracellular solution containing 135 mM K-methylsulfate, 10 mM KCl, 10 mM hepes, 5 mM NaCl, 2.5 mM Mg-ATP, 0.3 mM Na-GTP (pH 7.3), containing Alexa Fluor® 350 (Invitrogen). Signals were low-pass filtered at 2 kHz and digitized at 10 kHz using Axopatch MultiClamp 700A and Digidata 1320A (Axon Instruments).

Fig. S1. Behavioral and biochemical characterization of acute ammonia neurotoxicity. (**A**) Cortical $[NH_4^+]_o$ increase in NH_4Cl and NH_4Ac injected mice. $P = 0.88$, $n = 7$ (NH_4Cl) and 5 (NH_4Ac), Mann-Whitney *U* test. (**B**) Representative ^{1}H-NMR spectra 30 minutes after injection with saline or ammonia in *Otc*$^{spf\text{-}ash}$ mice. ppm (parts per million), aspartate (Asp), glutamine (Gln), glutamate (Glu), γ-aminobutyric acid (GABA), glutamine + glutamate (Glx), N-acetylaspartic acid (NAA), N-acetylaspartylglutamate (NAAG), alanine (Ala), lactate (Lac). (**C**) *Otc*$^{spf\text{-}ash}$ and WT mouse freezing behavior upon being placed in the fear chamber where they receive a shock through 4 days of training. (**D**) *Otc*$^{spf\text{-}ash}$ and WT mouse freezing behavior upon hearing the noise associated wtih shock treatment through 4 days of training. (**E**) Ammonium chloride (NH_4Cl) and ammonium acetate (NH_4Ac) induce a similar phenotype in *Otc*$^{spf\text{-}ash}$ mice (7.5 mmol kg^{-1} i.p.). Data are shown as mean ± SEM.

Fig. S2. Seizure phenotype associated with ammonia intoxication. (**A**) Representative EEG and EMG trace showing myoclonic seizures in an *Otc*$^{spf\text{-}ash}$ mouse following 7.5 mmol kg^{-1} NH_4Cl. (**B**) Myoclonic seizure frequency in *Otc*$^{spf\text{-}ash}$ and WT littermates following 7.5 mmol kg^{-1} ammonia injection. ***$P < 0.001$, $n = 22$ (*Otc*$^{spf\text{-}ash}$) and 10 (WT), unpaired *t* test. (**C**) Seizure frequency following 7.5 mmol kg^{-1} NH_4Cl and NH_4Ac intraperitoneally (i.p.). $P = 0.83$, $n = 22$ (NH_4Cl) and 5 (NH_4Ac), Mann-Whitney *U* test. Data are shown as mean ± SEM.

Fig. S3. Deletion of astrocyte water channel aquaporin 4 (AQP4) is not protective in acute ammonia toxicity. (**A**) Seizure frequency and phenotype score in wild-type (WT) and *Aqp4*$^{-/-}$ mice injected with 7.5 mmol kg^{-1} NH_4Cl i.p. $P = 0.829$ (seizures), $P = 0.357$ (encephalopathy), $n = 10$ (ctrl) and 9 (*Aqp4*$^{-}$

$^{-/-}$), Mann-Whitney *U* test. (**B**) Cortical $[NH_4^+]_o$ in WT and *Aqp4*$^{-/-}$ mice before and after ammonia injection. $P = 0.94$, $n = 6$ for each group, Mann-Whitney *U* test. (**C**) Brain water content measured by wet-to-dry ratios in control and ammonia injected WT and *Aqp4*$^{-/-}$ mice. Ammonia injection does not cause increased brain water content. *Aqp4*$^{-/-}$ mice have increased brain water content in the control setting as we have described previously (*8*). $P = 0.59$ (WT), $P = 0.69$ (*Aqp4*$^{-/-}$), $n = 10$ (WT ctrl), 5 (WT NH_4Cl), 5 (*Aqp4*$^{-/-}$ ctrl) and 5 (*Aqp4*$^{-/-}$ NH_4Cl), Mann-Whitney *U* test. (**D**) For awake calcium imaging change in rhod-2 flourescence ($\Delta F/F_0$) was normalized to eGFP to reduce movement artifacts. Calcium transients were defined as $\Delta F/F_0 > 2$ standard deviations (σ) from baseline. (**E**) Pearson correlation of astrocyte calcium transients (cell) and ECoG seizure recordings. $n = 52$ cells. Data are shown as mean ± SEM.

Fig. S4. Ammonia impairs cortical potassium buffering. (**A**) Scatterplot of $[NH_4^+]_o$ increase following ammonia (7.5 mmol kg^{-1}) or saline administration (red box). $n = 7$ for each group. Red arrow indicates mean onset of seizures. (**B**) Scatterplot of $[K^+]_o$ increase following ammonia (7.5 mmol kg^{-1}) or saline administration (red box). $n = 10$ (ammonia) and 7 (control). (**C**) Scatterplot of $[NH_4^+]_o$ increase following cortical application of ammonia (10 mM, red box). $n = 4$. (**D**) $[K^+]_o$ increase following ammonia injection in *Otc*$^{spf\text{-}ash}$ and WT littermates. ***$P < 0.001$, $n = 10$ (*Otc*$^{spf\text{-}ash}$) and 5 (WT), Mann-Whitney *U* test. (**E**) Glutamine synthetase inhibition further compromises potassium buffering by preventing ammonia removal in astrocytes. $[NH_4^+]_o$ increase following ammonia ± L-methionine sulfoximine (MSO) (0.83 mmol kg^{-1}, administered 3 h before the ammonia) i.p. in *Otc*$^{spf\text{-}ash}$ mice. *$P = 0.0043$, **$P = 0.048$, $n = 6$ (Ctrl), 6 (MSO), 7 (NH_4Cl) and 5 (NH_4Cl + MSO), Mann-Whitney *U* test. (**F**) $[K^+]_o$ increase following ammonia injection and/or MSO in *Otc*$^{spf\text{-}ash}$ mice. *$P =$ 0.0016, **$P = 0.013$, $n = 9$ (Ctrl), 6 (MSO), 10 (NH_4Cl) and 5 (NH_4Cl + MSO), Mann-Whitney *U*

test. (**G**) Ammonia-induced pH effects are mild and delayed. Linear regression of seizure frequency on pH_o. *Otc*$^{spf\text{-}ash}$ mice show a mild extracellular brain alkalinization and peripheral (blood) acidosis, following 7.5 mmol kg^{-1} ammonia i.p. Both pH changes correlate weakly with seizure frequency. (**H**) Ammonia causes a variable reduction in the potassium uptake of neurons. Na^+-K^+-ATPase-dependent (ouabain-sensitive) uptake of potassium analogue $^{86}Rb^+$ in cultured neurons, normalized to vehicle (0 mM NH_4Cl). **P* <0.0001, *n* = 20 (0 mM), *n* = 4 (0.5 mM), *n* = 4 (2 mM), *n* = 16 (5 mM), *n* = 4 (10 mM), Kruskall-Wallis test. Data are shown as mean ± SEM.

Fig. S5. GABA-currents recorded during ramp voltage are entirely $GABA_A$-receptor dependent. (**A**) Representative traces show that bicuculline blocks the current induced by ramp voltage after GABA application. (**B**) I-V curve shows that bicuculline blocks all GABA-induced current.

Fig. S6. Bumetanide treats potassium-induced neural disinhibition. (**A**) 10 consecutive sweeps following paired-pulse whisker stimulation shows KCl superfusion (12.5 mM, blue box) no longer evokes a facilitating sensory response (disinhibition) when co-administered with bumetanide (BUM, 5 μM).

Table S1. Biochemical changes during acute ammonia neurotoxicity. ^{1}H-NMR was used to determine amino acid concentrations (μmol g^{-1} wet weight) 30 minutes after saline (Ctrl) or ammonia administration (7.5 mmol kg^{-1} i.p.). Data are shown as mean ± SEM.

Genotype: **Exposure:**	WT Ctrl	WT BUM	WT NH_4	*Otc*$^{spf\text{-}ash}$ Ctrl	*Otc*$^{spf\text{-}ash}$ BUM	*Otc*$^{spf\text{-}ash}$ NH_4	*Otc*$^{spf\text{-}ash}$ BUM NH_4
Glutamate	14.29 ± 0.19	14.38 ± 0.22	12.49 ± 0.15	14.67 ± 0.68	14.27 ± 0.23	13.24 ± 0.33	12.51 ± 0.37

Glutamine	4.85 ± 0.47	4.52 ± 0.18	8.69 ± 0.33	7.58 ± 0.52	8.70 ± 1.54	9.25 ± 0.34	11.44 ± 0.46
GABA	2.00 ± 0.13	2.55 ± 0.05	2.19 ± 0.12	2.53 ± 0.12	2.39 ± 0.13	2.46 ± 0.13	2.23 ± 0.08

Table S2. Astrocyte calcium signaling during acute ammonia neurotoxicity in awake mice. Data from analysis of 2PLSM xyt series, where calcium indicator rhod-2 was used to detect astrocyte calcium transients 100 μm below the pial surface. Data are shown as mean ± SEM

	Ctrl (*n* = 62)	**NH_4Cl** (*n* = 52)
Freq. (Hz $cell^{-1}$ x $10^{-3)}$	2.67 ± 0.36	9.03 ± 1.16
Amplitude ($\Delta F/F_0$)	0.48 ± 0.11	0.47 ± 0.32
Duration (s)	18.98 ± 3.05	21.51 ± 4.55
Cell-cell correlation	0.65 ± 0.06	0.26 ± 0.08

Table S3. Bumetanide treatment does not affect cortical ammonia or potassium concentrations. NH_4^+ and K^+ ISMs recordings from cortex of awake *Otc*$^{spf\text{-}ash}$ mice. Data are shown as mean ± SEM.

CORTICAL SUPERFUSION						
	$[NH_4^+]_o$ (mM)	**n (animals)**	***P* value Mann-Whitney *U* test**	**$\Delta[K^+]_o$ (mM)**	**n (animals)**	***P* value Mann-Whitney *U* test**
Control	0.45 ± 0.17	6		0.0058±0.019	6	
BUM	0.52 ± 0.11	6	0.59	0.0025±0.018	6	0.94
NH_4Cl	5.82 ± 0.18	6		2.24 ± 0.17	10	
NH_4Cl + BUM	5.78 ±0.13	6	0.87	2.17 ± 0.12	9	0.66
INTRAPERITONEAL INJECTION						
	$[NH_4^+]_o$ (mM)	**n (animals)**	***P* value Mann-Whitney *U* test**	**$\Delta[K^+]_o$ (mM)**	**n (animals)**	***P* value Mann-Whitney *U* test**
Control	0.48 ± 0.12	6		0.015 ± 0.025	9	
BUM	0.42 ± 0.16	6	0.39	0.0073± 0.015	6	0.53

NH_4Cl	4.83 ± 0.52	7		1.93 ± 0.19	10	
NH_4Cl + BUM	4.70 ± 0.32	6	0.83	1.97 ± 0.17	6	0.92

Supplementary Movies

Movie S1. Seizure phenotype induced by 7.5 mmol kg^{-1} ammonia injection in an *Otc*$^{spf\text{-}ash}$ mice.

Movie S2. Spontaneous calcium transients in cortical astrocytes prior to 7.5 mmol kg^{-1} ammonia injection (control).

Movie S3. Calcium transients in cortical astrocytes after 7.5 mmol kg^{-1} ammonia injection.

Supplementary References

1. X. Ye *et al.*, Adenovirus-mediated in vivo gene transfer rapidly protects ornithine transcarbamylase-deficient mice from an ammonium challenge. *Pediatr. Res.* **41**, 527 (1997).
2. A. S. Thrane *et al.*, Critical role of aquaporin-4 (AQP4) in astrocytic Ca2+ signaling events elicited by cerebral edema. *Proc. Natl. Acad. Sci. U. S. A.* **108**, 846 (2010).
3. S. J. Guyenet *et al.*, A simple composite phenotype scoring system for evaluating mouse models of cerebellar ataxia. *Journal of visualized experiments : JoVE*, (2010).
4. C. Nicholson, Ion-selective microelectrodes and diffusion measurements as tools to explore the brain cell microenvironment. *J. Neurosci. Methods* **48**, 199 (1993).
5. X. Wang *et al.*, Astrocytic Ca2+ signalling evoked by sensory stimulation in vivo. *Nat. Neurosci.* **9**, 816 (2006).
6. M. Simard, G. Arcuino, T. Takano, Q. S. Liu, M. Nedergaard, Signaling at the gliovascular interface. *J. Neurosci.* **23**, 9254 (2003).
7. V. I. Dzhala *et al.*, NKCC1 transporter facilitates seizures in the developing brain. *Nat. Med.* **11**, 1205 (2005).
8. N. N. Haj-Yasein *et al.*, Glial-conditional deletion of aquaporin-4 (Aqp4) reduces blood-brain water uptake and confers barrier function on perivascular astrocyte endfeet. *Proc. Natl. Acad. Sci. U. S. A.* **108**, 17815 (2011).

Fig. S1.

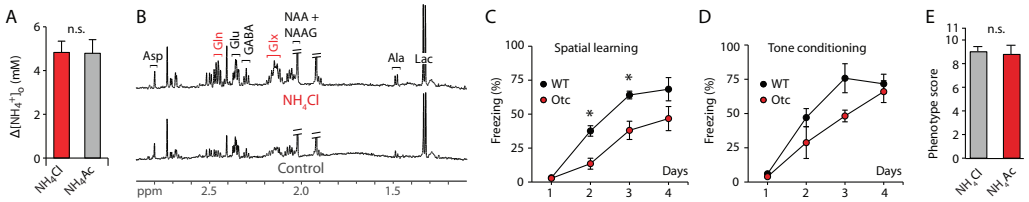

Fig. S2.

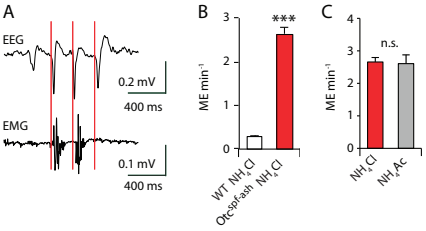

Fig. S3.

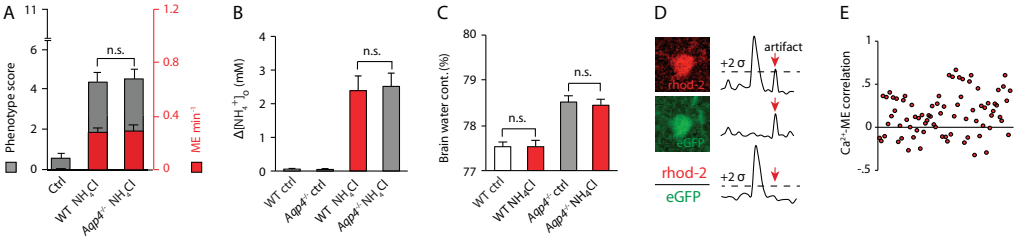

Fig. S4.

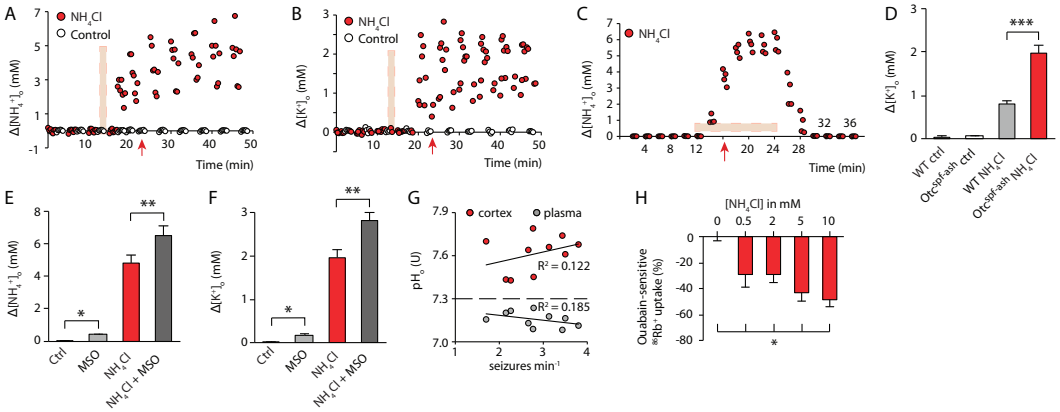

Fig. S5.

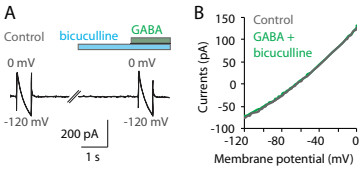
A
Control
bicuculline
GABA
0 mV
0 mV
-120 mV
-120 mV
200 pA
1 s
B
Control
GABA +
bicuculline
Currents (pA)
150
100
50
0
-50
-100
-120
-80
-40
0
Membrane potential (mV)

Fig. S6.

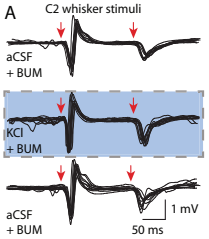
A
C2 whisker stimuli
aCSF
+ BUM
KCl
+ BUM
aCSF
+ BUM
1 mV
50 ms

References

1. Thorne, R.G. & Nicholson, C. In vivo diffusion analysis with quantum dots and dextrans predicts the width of brain extracellular space. *Proceedings of the National Academy of Sciences of the United States of America* **103**, 5567-5572 (2006).
2. Abbott, N.J. Evidence for bulk flow of brain interstitial fluid: significance for physiology and pathology. *Neurochemistry international* **45**, 545-552 (2004).
3. Iliff, J.J*., et al.* A Paravascular Pathway Facilitates CSF Flow Through the Brain Parenchyma and the Clearance of Interstitial Solutes, Including Amyloid beta. *Sci Transl Med* **4**, 147ra111 (2012).
4. Slezak, M. & Pfrieger, F.W. New roles for astrocytes: regulation of CNS synaptogenesis. *Trends in neurosciences* **26**, 531-535 (2003).
5. Fukata, Y. & Fukata, M. Protein palmitoylation in neuronal development and synaptic plasticity. *Nature reviews. Neuroscience* **11**, 161-175 (2010).
6. Takano, T*., et al.* Astrocyte-mediated control of cerebral blood flow. *Nat Neurosci* **9**, 260-267 (2006).
7. Higashimori, H., Blanco, V.M., Tuniki, V.R., Falck, J.R. & Filosa, J.A. Role of epoxyeicosatrienoic acids as autocrine metabolites in glutamate-mediated K+ signaling in perivascular astrocytes. *American journal of physiology. Cell physiology* **299**, C1068-1078 (2010).
8. Moore, C.I. & Cao, R. The hemo-neural hypothesis: on the role of blood flow in information processing. *Journal of neurophysiology* **99**, 2035-2047 (2008).
9. Paredes, R.M., Etzler, J.C., Watts, L.T., Zheng, W. & Lechleiter, J.D. Chemical calcium indicators. *Methods (San Diego, Calif.)* **46**, 143-151 (2008).
10. Thrane, A.S*., et al.* General anesthesia selectively disrupts astrocyte calcium signaling in the awake mouse cortex. *Proceedings of the National Academy of Sciences of the United States of America* **109**, 18974-18979 (2012).
11. Simard, M., Arcuino, G., Takano, T., Liu, Q.S. & Nedergaard, M. Signaling at the gliovascular interface. *J. Neurosci.* **23**, 9254-9264 (2003).
12. Thrane, A.S*., et al.* Critical role of aquaporin-4 (AQP4) in astrocytic Ca2+ signaling events elicited by cerebral edema. *Proc. Natl. Acad. Sci. U. S. A.* **108**, 846-851 (2010).
13. Koizumi, S., Fujishita, K. & Inoue, K. Regulation of cell-to-cell communication mediated by astrocytic ATP in the CNS. *Purinergic signalling* **1**, 211-217 (2005).
14. Leoni, V., Solomon, A. & Kivipelto, M. Links between ApoE, brain cholesterol metabolism, tau and amyloid beta-peptide in patients with cognitive impairment. *Biochemical Society transactions* **38**, 1021-1025 (2010).
15. Castellano, J.M*., et al.* Low-density lipoprotein receptor overexpression enhances the rate of brain-to-blood Abeta clearance in a mouse model of beta-amyloidosis. *Proceedings of the National Academy of Sciences of the United States of America* **109**, 15502-15507 (2012).